University of Nevada, Reno

GEOLOGY OF THE CHUKAR FOOTWALL MINE, MAGGIE CREEK DISTRICT, CARLIN TREND, NEVADA

A Thesis submitted in partial fulfillment of the requirements for the degree of Master of Science in Geology

By

Juan Antonio Ruiz Párraga

Dr. Tommy Thompson, Thesis Advisor

May, 2007

University of Nevada, Reno
Statewide • Worldwide

THE GRADUATE SCHOOL

We recommend that the thesis
prepared under our supervision by

JUAN ANTONIO RUIZ PARRAGA

Entitled

Geology Of The Chukar Footwall Mine, Maggie Creek District,
Carlin Trend, Nevada

be accepted in partial fulfillment of the
requirements for the degree of

MASTER OF SCIENCE

Tommy B. Thompson, Ph.D., Advisor

Richard A. Schweikert, Ph. D., Committee Member

Victor Vasquez, Ph.D., Graduate School Representative

Marsha H. Read, Ph. D., Associate Dean, Graduate School

May, 2007

ABSTRACT

The Chukar Footwall mine forms part of the NW striking Carlin trend in northern Nevada, and lies beneath the southwest highwall of the Gold Quarry, a world-class deposit with total 1999 reserves, resources, and mineral inventories in excess of 24M oz gold. The Chukar Footwall orebodies are hosted in the planar to wispy silty limestone and calc-silicates of the Silurian-Devonian Roberts Mountains Formation (SDrm). The Devonian Popovich Formation (Dp), a micritic package locally hosting economic gold mineralization, structurally overlies the SDrm. The Raven dike intrudes the DSrm at several mine levels along northwest- trending structures. The dike is composed of abundant dark green, millimeter sized subhedral-anhedral phenocrysts in a light colored aphanitic groundmass. It is altered to clay and pyrite, but does not appear to be an ore fluid feeder structure. The time of the Raven dike emplacement into NNW-trending structures has been determined by U-Pb zircon geochronology, producing an age of 200.3±5.1 Ma (early Jurassic). Apatite separates from the Raven dike yielded a fission track pooled age of 17.7±3.7 Ma for a thermal event that may have been associated with mineralization at Chukar Footwall; however, initial cooling began at 26.2±5.5 Ma.

These rocks were probably deformed during the Antler orogeny, generating the Chukar anticline, a northeast trending open structure with a subhorizontal plunge. High gold grades are commonly situated along the hinge and the southeast limb and in small parasitic folds. A conjugate system of

structures is represented by northwest and northeast striking faults, where the former cuts the latter.

Kinematic indicators denote predominantly oblique normal slips for both fault sets.

The Chukar Footwall mine exhibits the hydrothermal alteration assemblages typical of Carlin-type gold deposits: (a) decalcification, (b) dolomitization, (c) silicification, (d) argillization, and (e) baritization. The uniqueness of this deposit relative to the more typical Carlin-type is the (1) sharp boundaries between fresh and altered rocks, and (2) presence of abundant visible gold. Gold mineralization is spatially related with strong decalcification in the vicinity of intersections of northeasterly structures with the Chukar anticline. Coarse, visible gold occurs in decarbonatized silty limestone along fractures of all orientations as well as along bedding planes. Also, visible gold is present in late barite veinlets, coprecipitating with the latter phase.

Stable isotope transects reveal systematic $\delta^{18}O$ and $\delta^{13}C$ shifts in wall rocks where approaching structures and/or changes of intensity of hydrothermal alteration. At a mine scale, these shifts define a generalized trend toward lighter oxygen and heavier carbon values for the wallrocks from the higher to the deeper mine levels, with a negative correlation between oxygen and carbon. Late stage calcite veins $\delta^{13}C$ values lie within the values of the nearby altered limestone, suggesting the carbon could have been derived from the wallrocks. Isotope and fluid inclusion data point to gangue precipitation from interaction between meteoric water and the wallrocks. $\delta^{34}S$ from sulfides and sulfates are consistent

with a sulfur derivation from sedimentary sources. A correlation has been found between the presence of visible gold and the isotopic signature of barite. Barite precipitated from meteoric water as it descended into open structures.

Microthermometric data from late stage barite±gold veins indicate significant variation in both homogenization temperatures and salinities with depth. Mean salinities and mean homogenization temperatures from the deeper mine levels range from 3.03 to 3.18 wt % NaCl equiv and between 183.2° and 179.7° C. In contrast, lower salinities (~1.16 wt % NaCl equiv) and homogenization temperatures (177.3°C) were recorded in samples from shallower levels. Similarly, recorded data from late calcite yielded very low salinities (up to 0.71 wt % NaCl equiv) and low homogenization temperatures (between 87.6° to 117° C). Neither CO_2 nor CH_4 were detected in calcites. These data suggest the participation of, at least, two contrasting fluids.

The Chukar Footwall orebody forms part of the Gold Quarry gold system to which same basic genetic ideas may apply. The metallogenic evolution of the Chukar Footwall deposit began with a significant pre-ore episode of dissolution-collapse breccia between the Roberts Mountains Formation and the Popovich Formation that formed a semi-impermeable cap for later hydrothermal fluids. During ore-stage, ore fluids were channelized along major active NE-striking structures, and probably micron-size Au and base metals precipitation took place as a result of sulfidation and a shift toward higher pH values. During Late Miocene extension, NW-striking faults were open for descending cool, weakly saline meteoric fluids and ascending relatively hotter, more saline hydrothermal

fluids, possibly producing metal remobilization and visible gold precipitation along structures. It seems that the common link among the Gold Quarry gold systems is its structural relation to the Deep Sulfide Feeder and Chukar Gulch faults, which served as a major conduits for hydrothermal fluids.

ACKNOWLEDGEMENTS

I would like to thank Dr. Tommy Thompson and Dr. Richard Schweickert for being my M.S. thesis advisors, and for their insights on the geological aspects of north-central Nevada. Dr. Thompson gave me the opportunity and the appropriate financial assistance for this research through the Ralph J. Roberts Center for Research in Economic Geology (CREG).

Thanks to the Chukar Footwall geologists Joe Sagar, Kevin Creel, and Mike Robinson for their logistical support, patience, and ideas about Chukar Footwall's geology during underground mapping. My appreciation is extended to Newmont for letting me work at Chukar Footwall, giving me free access to information, and conducting the ICP-MS analyses.

I would also like to thank to Dr. John McCormack (UNR) for the SEM analyses and comments, Dr. Ray Donelick and Paul O'Sullivan for performing the critical U/Pb zircon data and apatite fission track dating from the Raven dike. Also thanks to Dianna Neff for sharing the splendid view of Gold Quarry.

Finally, discussions with my fellow students Keith Campbell, Craig Mach, and Robert Wood are greatly appreciated.

¡ Salud a todos!

TABLE OF CONTENTS **Page**

LIST OF FIGURES

LIST OF TABLES

LIST OF PLATES

What was once baffling is now clear, what seemed absurdly important is now simply childish, yet still the journey is unfinished.

Simon Conway Morris, *Life's Solution*, 2003

GEOLOGY OF THE CHUKAR FOOTWALL MINE, MAGGIE CREEK DISTRICT, CARLIN TREND, NEVADA

1. INTRODUCTION

The discovery in 1995 of the Chukar Footwall orebody beneath the southwest highwall of the Gold Quarry mine brought out the potential to explore for deep blind deposits along the Carlin trend in northeastern Nevada (Fig. 1). The Carlin Trend is a north-northwest trending belt with a mineral endowment of more than 50 million ounces gold produced between 1965 and 2002 (Teal and Jackson, 2002). After a period of near-surface exploration, current exploration projects are focused on deeper, blind orebodies through both direct and indirect methods. No geological data about the blind orebodies can be inferred from surface outcrops, thus the structure and geochemistry of the orebody is deduced from drill data (i.e., West Leeville, Chukar Footwall).

The detailed stratigraphy, structure, and metallogeny of the Carlin trend are well known at both regional scale and deposit scale. The tectonic evolution of this area indicates a complex scenario through time involving widespread Early Silurian to Late Devonian-Mississippian shallow to deep water carbonate depositional environments deposited onto the Cordilleran passive margin; traditionally this package of rocks

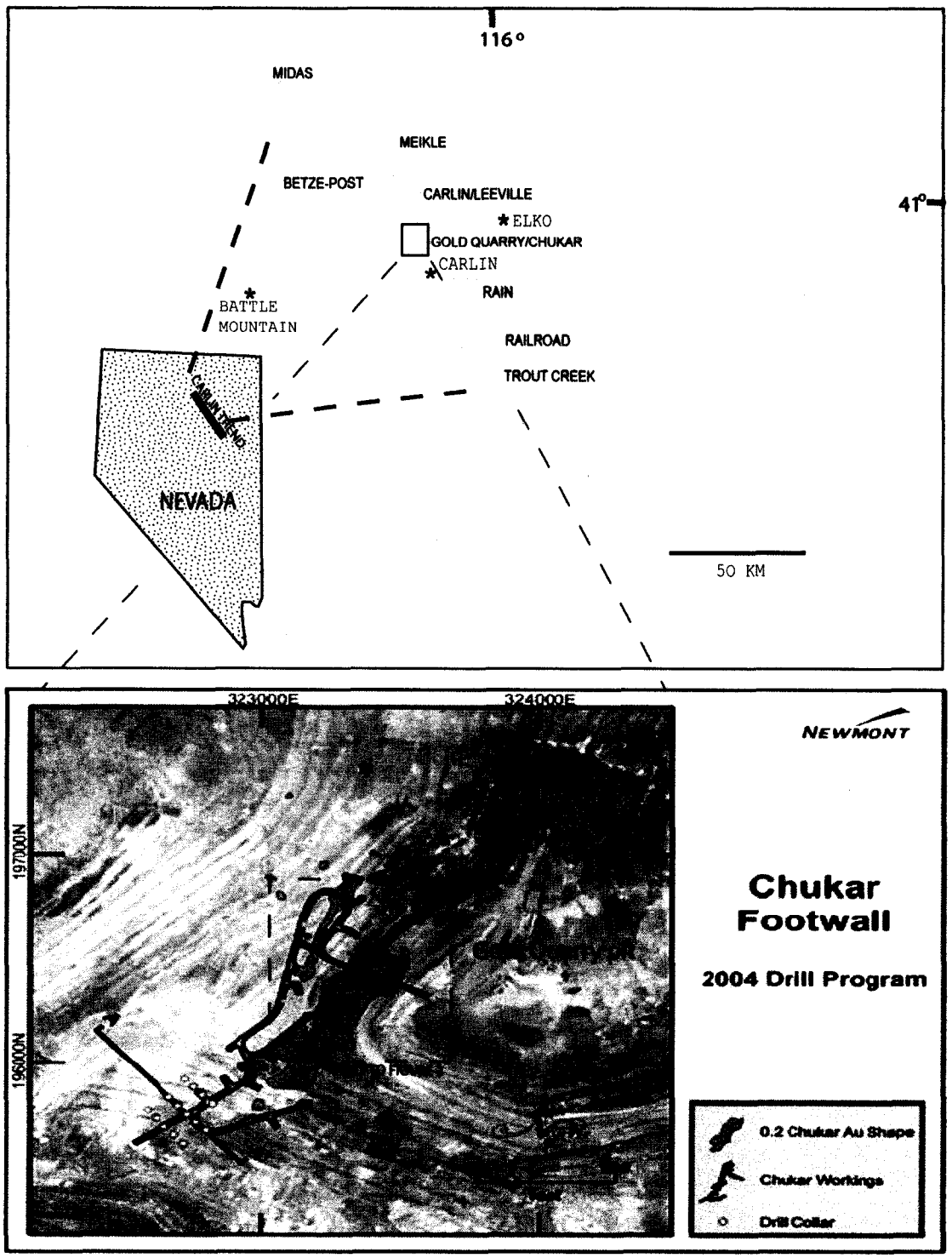

FIGURE 1. Location map of the Carlin trend in northeastern Nevada, a NNW- trending series of gold deposits hosted in Paleozoic carbonate rocks and mined by open pits and underground methods. The Chukar Footwall underground mine is located beneath the southwest highwall of the Gold Quarry pit.

has been referred to as miogeoclinal strata. Coeval eugeoclinal strata were deposited further west from the margin, and thrust over the miogeoclinal sequences during the Late Devonian-Early Mississippian Antler orogeny along the Roberts Mountains thrust (Roberts et al., 1958; Cook and Corboy, 2002). During pre-Tertiary times, this region underwent several compressional phases giving rise to large WNW to NNW trending folds (i.e., Post anticline, Tuscarora anticline, and Betze anticline) with associated minor structures (Lewis, 2001). Dioritic, quartz-dioritic, and granodioritic bodies and associated sills and dike swarms were emplaced at 158 Ma and 106 Ma (Evans, 1980; Emsbo et al., 1996) producing significant contact metamorphism and metasomatism in the host lithologies. Tectonic history is mainly represented by the (1) reactivation of older structures, (2) emplacement of Eocene dikes, which are interpreted to be contemporaneous with gold mineralization in some districts, and (3) Miocene Basin and Range extension (Emsbo et al., 1996; Henry and Ressel, 2000; Arehart, 1996).

The Carlin Trend displays several general metallogenic characteristics (Roberts, 1960; Hofstra and Cline, 2000; Thompson, 2000): (1) the host rocks are lower plate Paleozoic carbonates, which are exposed along an north-northwest alignment through several tectonic windows; however, some orebodies occur in different lithologies; (2) temporally and spatially linked with gold orebodies, the hydrothermal alteration assemblages are represented by decarbonatization±

dolomitization ± silicification ± argillization ± sulfidation and baritization ± alunitization and supergene processes; and (3) gold occurs as submicroscopic grains disseminated along arsenian rims on iron sulfides minerals. Common ore and gangue mineralogies are represented by barite, calcite, quartz, stibnite, iron sulfides, fluorite, realgar, and orpiment.

There are currently several competing models attempting to explain the genesis of the Carlin-type gold deposits. Central to this controversy is the question of the metal source and heat mechanisms: (1) fluids and metals were derived during regional metamorphism of crustal rocks during an Eocene extensional event (Seedorff, 1991), (2) meteoric fluids were heated and convected during rapid crustal extension during Basin and Range extension (Ilchick and Barton, 1997), (3) due to the spatial association of some Carlin-type deposits with igneous rocks some authors suggested a magmatic provenance of fluids and metals (Arehart et al., 1993, Radke, 1985, Thompson, 2000), and (4) recently, Johnston and Ressel (2004) suggested the possibility that Carlin-type deposits may be interpreted as distal and shallow expression of a deeper magmatic system(s) underlying the trend due to their temporal coincidence with regional Eocene magmatism.

PURPOSE AND OBJECTIVES

The purpose of this study is to gain a better understanding of the geology and metallogeny of the Chukar Footwall underground mine, an unoxidized, deep-seated sedimentary rock-hosted disseminated gold deposit, through systematic studies on the geochemistry, wallrock alteration, stable isotopes, paragenesis, and fluid inclusions to propose a metallogenic model. Consequently, this research will focus on key issues like: (1) What are the main geological parameters that control gold mineralization? (2) Is there any spatial and/or temporal relationship between wallrock alteration and gold grades? (3) What was the nature and evolution of the ore fluids? (4) What is the age of gold mineralization at Chukar Footwall? and (5) What is the geochemical and isotopic signature of mineralized rocks? The main objectives of this research were to develop a geological framework of the Chukar Footwall mine through specific projects such as:

- Geological mapping of all mine levels that were accesible during the field component of this research.
- Petrographic analyses to identify and characterize mineral paragenesis and hydrothermal alteration assemblages.
- Geochemical and stable isotopic studies to identify possible zonation patterns and fluid flow paths.

- Fluid inclusion analyses on late stage minerals provide constraints on temperature and salinities of hydrothermal fluids.
- Fission-track dating on apatite from the Raven dike may provide data about the timing of hydrothermal alteration that is assumed to be related to gold deposition.

METHODOLOGY

Underground mapping and sampling, combined with laboratory studies, were conducted from June, 2004 to May, 2005 to generate the body of data that is presented in the following chapters. Underground mapping of levels 4770, 4740, 4730, 4720, 4710, 4680, 4650, 4610, 4590, and Tracker Decline was done at 1:240 scale. About two hundred samples were collected. Forty-two were selected for petrographic descriptions, and fifty-two samples were analyzed for 32-elements by ICP-MS by Newmont at the Gold Quarry lab. Additionally, about ten kilos of dike rocks were collected from the 4580 level for both apatite-fission and U-Pb zircon dating and submitted for analysis to Donelick Analytical labs. Finally, sixty-seven stable isotopic analyses for sulfur, sulfate, carbon, and oxygen were performed at the Nevada Stable Isotope Lab by Dr. Simon Poulson.

The underground mapping was digitized into CAD and blended with Newmont's cartography. Extraction of structural data from cartography was done using SpheriStat 2.2, with the help of Mike Robinson, to define possible structural

domains and fold geometry, and to record the strike and dip of bedding planes, faults, joints, and veins (Appendix A).

PREVIOUS WORK

Since the combined works of Rota (1991), Heitt (1992), Williams (1992), Sha (1993), Cole (1995), Sagar (2000a,2000b), Harlan et al. (2002), and Johnston and Arehart (2003) for Gold Quarry-Chukar Footwall orebodies, the geological framework of both deposits has been well defined. In general terms, all the data suggest a protracted period of tectonism and hydrothermal activity since Eocene times responsible for the formation of the Quarry Main, Chukar Footwall, Deep West, and Deep Sulfide Feeder gold systems. Mainly on the basis of drillhole data from Chukar Footwall, Sagar (2000a) described the Popovich Formation as consisting of silty limestone, massive calcarenite, and micrite, from top to bottom. The underlying silty limestone of the Roberts Mountains Formation hosts the economic orebodies at structural intersections. The micron-size gold is hosted in the sooty sulfides, although visible gold is also found along fractures and bedding planes in unoxidized silty limestones of the Roberts Mountains Formation.

Similarly, Johnston and Arehart (2003) made available wallrock alteration data in conjunction with $\delta^{18}O$ and $\delta^{13}C$ isotopic analyses and carbonate staining from core samples from the upper levels of the Chukar Footwall deposit. The body of data has led to the author's conclusions that (1) the Chukar Footwall deposit is similar in many aspects to other Carlin-type orebodies, (2) carbonate

staining along with another techniques (e.g., oxygen stable isotopes) could be used as exploration tools due to the observed correlation between the intensity of purple stain and gold grades, and (3) $\delta^{18}O$ data suggest a widespread hydrothermal alteration of the host rocks due to interaction with meteoric-hydrothermal solutions, which also led to the formation of the Chukar orebodies.

2. PHANEROZOIC GEOLOGICAL EVOLUTION OF NORTH-CENTRAL NEVADA

This chapter outlines the complex geological evolution of north-central Nevada since the Paleozoic, with special emphasis on tectonic history, magmatism, and metallogeny. Figures 2, 3 and 4 provide a general view of the major geological elements and the stress regime that characterize the tectonic realm in the region since middle Paleozoic.

The first general synthesis on the geology of the region was provided by Roberts et al. (1958) and Roberts (1960), who produced important sedimentological and structural interpretations of certain key sections in north-central Nevada. One of the conditioning factors for such a synthesis was the recognition of the Antler orogeny and the nature of the Roberts Mountain allochthon since this ensures that coeval sediments are being compared and fitted into the overall paleogeographical settings for the region. Modern contributions on the geology and metallogeny of north-central

FIGURE 2. Generalized tectonic setting and depositional environments of north-central Nevada, which shows the extent of the Roberts Mountains, Golconda, and Fencemaker-Luning thrusts. Also, major tectonic windows are shown, whereby the Carlin trend lies in the Lynn-Maggie Creek window. The miogeoclinal strata, mostly silty carbonates, were deposited on the continental shelf. Coeval sedimentation in the continental slope, however, deposited deep-water siliciclastic sediment interbedded with volcanic rocks. When both facies interfinger, the term transitional facies is used (after Stewart, 1980; Ettner, 1989)

Nevada have been discussed by Stewart (1980), Madrid (1987), Hofstra and Cline (2000), Lewis (2001), Teal and Jackson (2002), Cook and Corboy (2002), and Dickinson (2006) among others. The geological history of north-central Nevada began with passive margin sedimentation during most of the lower Paleozoic along the western margins of Laurentia shortly after a margin rifting event took place between 800 and 500 Ma (Burchfiel et al., 1992). In general, lower Paleozoic miogeoclinal rocks (eastern facies) consist of carbonates, siltstone, quartzite, chert, and shale deposited in trangressive conditions in both deep and shallow marine environments. During the Ordovician and Silurian periods, shallow to deep carbonate sedimentation formed a continuous sequence of silty carbonates with interbedded shales and cherts, as opposed to the dominant siliciclastic Cambrian sequences (Stewart, 1980; 1991).

The coeval lower Paleozoic eugeoclinal rocks (the western facies), exposed within the Roberts Mountains allochthon (RMA) in north-central Nevada, were deposited outboard of the passive margin of Laurentia in outer shelf areas. These time-equivalent eugeoclinal rocks clearly differ from those of the miogeoclinal sequences in (1) chert and argillite lithologies predominate over clastic, carbonate, and mafic ones and (2) these rocks are highly deformed (Madrid, 1987). Clearly, these differences indicate that both eastern and western facies formed two separate parts of the Laurentian continental margin and have been juxtaposed into the present geographical configuration

along the RMA (Roberts et al., 1958; Ketner, 1991). Further, the isotopic boundary of the Precambrian continental margin, as defined by the $Sr_{initial}$ ratio of 0.706, suggest that the eastern facies was deposited on continental crust whereas the western package was deposited on oceanic crust (Madrid, 1987; Graugh et al., 2003). In north-central Nevada, the allochthon stratigraphy is represented by thick sequences of strongly deformed Cambrian through Devonian rocks, structurally emplacing older- over-younger formations (Roberts et al., 1958; Stewart, 1980). In the Independence Range, a significant occurrence of eugeoclinal rocks (seamount facies in association with turbidites) during the Ordovician reflects a continental slope environment during the deposition of the Valmy Group (Watkins and Browne, 1989).

It is generally agreed that the Antler collisional event during the late Devonian to late Mississippian resulted from the collision and complex interaction between the western passive margin of Laurentia and an island-arc system wherein the eugeoclinal strata were obducted eastward onto the Cordilleran margin about 145 km (Stewart, 1980). This short lived orogeny has been recognized in northern California, Nevada, Kootenay Arc, and in other several sectors of the Canadian Cordilleran (Gehrels and Smith, 1987; Turner et al., 1989). Its evolution may had been similar to the actual plate tectonic configuration in southeast Asia whereby the Indian-Australian plate is being overriden by the Eurasian plate (Carpenter et al., 1994).

Metamorphism in both the allochthon and autochthon is essentially synkinematic with greenschist grades, whereas the thermal metamorphism is related to plutonic intrusions (Madrid, 1987; Speed et al., 1988; Boskie, 2001). Structural features related to the Antler event are NNE- trending folds and thrusts formed by the E-WNW directed shortening of the RMA. In the Tuscarora Mountains, D_1 deformation produced NNE-trending concentric folds in the allochthon (Evans and Theodore, 1978). Deformation of the autochthon package, however, has undergone a polyphasic deformational history, with three deformational phases having been recognized in the Osgood Mountains (Evans, 1980; Madrid, 1987, Boskie, 2001). Finally, crustal thickening due to thrust stacking has been estimated by Madrid (1987) to be around 4,500 m.

Shortly after the emplacement of the RMT, by late Mississippian time, the Antler overlap siliciclastic assemblage, an autochthonous sedimentary sequence, disconformably overlies the autochthonous package. Sedimentary basin analyses in the Osgood Mountains and Battle Mountain by Saller and Dickinson (1982) allowed characterization of the Pennsylvanian to early Permian depositional evolution of north-central Nevada. Regional stratigraphy exhibits a local marine transgression during the late Paleozoic characterized by the development of a continental siliciclastic package (Battle Formation) conformably overlain by shallow marine carbonates (Etchart Formation). The temporal and spatial relationships between these lithological

units documented a progressive marine transgression recording a transition between deltaic to shallow marine environments in a quiescent tectonic period (Saller and Dickinson, 1982) until it ended in response to a major tectonic event, the Sonoma orogeny. In addition, the data of Gehrels and Dickinson (2000) demonstrate that U-Pb ages of detrital zircons from the overlap sequences are similar to these of the eugeoclinal rocks, thus identifying the RMA as the source area for detritus.

The post-Antler geodynamic evolution of north-central Nevada can be divided into the following four main stages: (1) Late Paleozoic deformation, (2) the Sonoma Orogeny, (3) Mesozoic back-arc magmatism and deformation, and (4) Cenozoic magmatism and extensional regimes. In addition to these major geological divisions, the occurrence of at least two distinctive mineral trends (e.g., the Battle Mountain-Cortez and Carlin trends) provide insights into the relationships among the inherent regional fabric and the mechanical and thermal state of the lithosphere during gold mineralization.

Recent reinterpretation of the geodynamic evolution of central Nevada has stemmed from the recognition of several deformation events during the late Paleozoic (Trexler et al., 2004). These authors documented three early Mississippian through early Permian deformation phases at Carlin Canyon, near Elko. The principal structures are north-east trending mesoscopic folds, imbricate thrusts, and normal faults. This has led Trexler et al. (2004) to

propose that some Antler structures might be ascribed to late Paleozoic deformation, which requires a new understanding of the the timing for the Antler orogeny as well as the geodynamic evolution of Western North America during late Paleozoic times.

A late Paleozoic to early Triassic deformational event, the Sonoma orogeny, seems to have started during the Permian, related to obduction processes similar to the mid-Paleozoic Antler orogeny (Speed et al., 1988; Dickinson, 2006). The effects of this orogeny are recognizable in a number of areas of the Western Cordillera, notably in California, Nevada, and Oregon. In Nevada, this deformation is characterized by eastward thrusting of Pennsylvanian-Permian deep marine sediments along the Golconda thrust onto the parautochthonous Antler overlap sequence and RMA (Speed, 1971; Stewart, 1980). The Golconda allochthon has been divided into two structural-lithostratigraphic assemblages, the Schoonover and Havallah sequences, that are highly deformed and disrupted by east verging folds, shearing, and thrust faults as a result of a polyphase deformation (Gabrielse et al., 1983). According to Riley et al. (2000), the Golconda allochthon was deposited in a backarc basin near its present location, receiving detritus from both a Sierra terrane to the west and the RMA to the east based on systematic studies on detrital zircon geochronology from sandstones (Figures 2 and 3).

Post-Sonoma geology is reflected by a magmatic arc and backarc environments related to changes of the angle of subduction of the Mezcalera

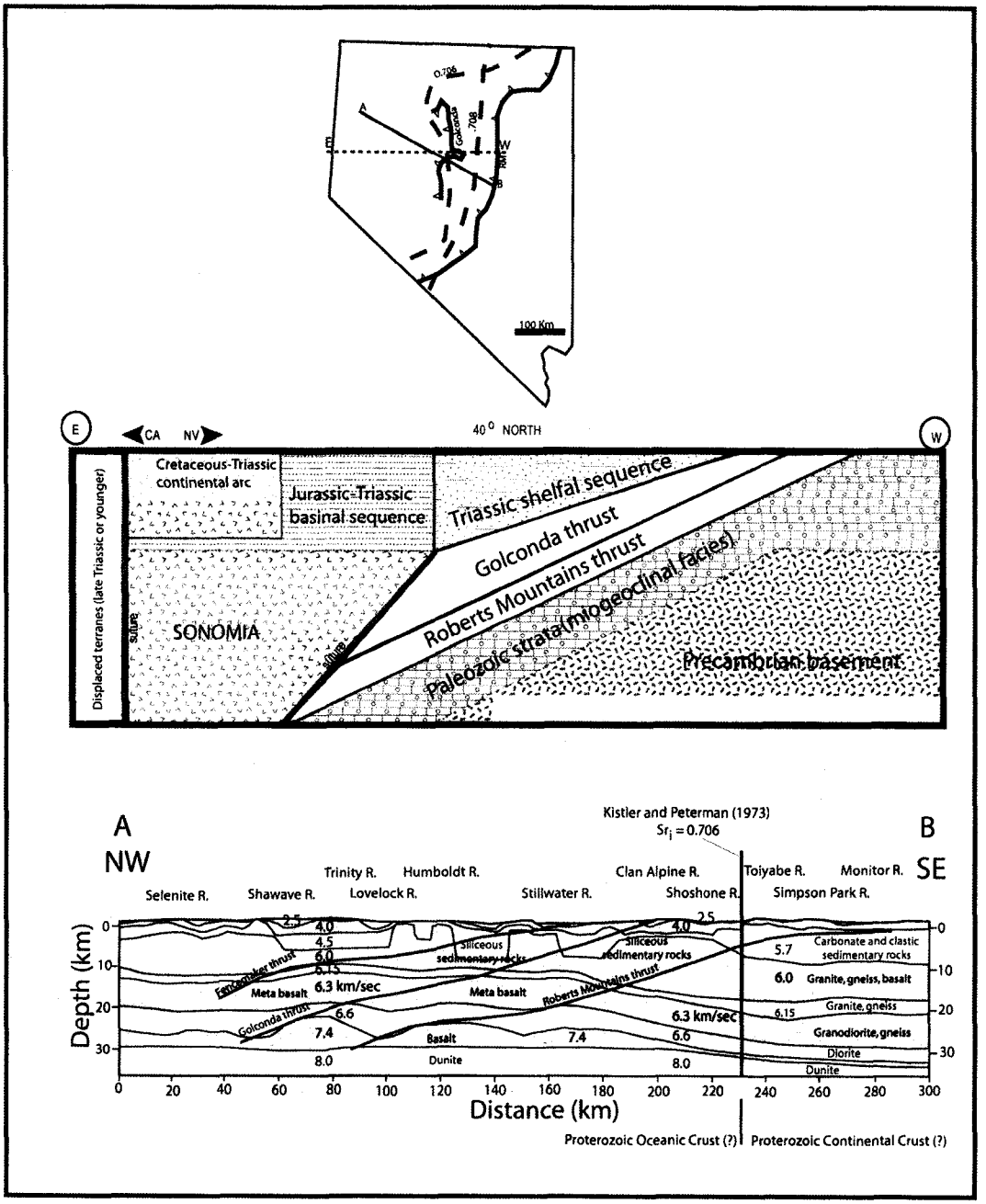

Figure 3. Map and crustal section showing the different Sr isopleths that define the continental crust (western edge of the basement). The Sr= 0.706 and Sr=0.708 lines are from Carpenter et al. (1994) and Farmer (1983), respectively. The NW-SE crustal and upper mantle section is based on Catchings and Mooney (1991) model (from Campbell et al., 2005). The E-W section is along the 40th parallel between Sierra Nevada and north-central Nevada (from Speed et al., 1988)

plate along the western margin of North America (c.f. Dickinson, 2006; Fig.6). In north-central Nevada, intrusive rocks associated with Jurassic backarc magmatism are predominantly granodiorites to monzogranites formed by crustal melts in contrast to the mantle-derived Mesozoic quartz-diorites and tonalites in the Klamath Mountains, suggesting a relationship between the petrological and geochemical signatures of the plutons and that of the nature of the basement (Farmer, 1983). Examples include the Jurassic Goldstrike stock, the late Cretaceous Richmond Mountain stock, and Jurassic-Cretaceous two-mica granites and monzogranites in the Ruby Mountains. A metamorphic aureole surrounds the plutonic intrusions and gives rise to marbles and calc-silicate hornfels (Walck, 1989; Heitt et al., 2003; Mariño, 2003).

Middle to late Jurassic strata in northeastern Nevada and northwestern Utah were deformed in the Elko or Nevadan orogeny (Schweickert et al., 1984; Thorman et al., 1992; Dickinson, 2006). The WSW-ENE stresses transmitted during this deformation produced regional NNW and WNW-trending folds (Post , Betze, Tuscarora, Alta, and Rain anticlines) and faults (Good Hope and Dillon deformation zone) (Lewis, 2001) and the intrusion of several granitic stocks. Schweickert et al. (1984) , in the Sierra Nevada region, constrained this short lived deformation at ~155 Ma as a result of another collisional episode between an island arc and the western margin of the North America Cordillera. Finally, evidence of late Jurassic-early Cretaceous folding and thrusting were reported by

Ketner and Smith (1974) in the Adobe and Piñon Ranges producing mesoscopic NNE-trending structures such the Adobe syncline.

Additional deformation events in north-central Nevada are represented by both the Luning-Fencemaker and Willow Creek allochthons (Oldow, 1984; Speed et al., 1988). A number of allochthonous assemblages structurally overlying the Golconda allochthon occur in the so-called Winnemucca deformation belt. These lithotectonic units contain basinal sediments and magmatic rocks deposited in a back-arc basin environment that were folded and thrust during late Jurassic through early Cretaceous. Major structures associated with thrusts include NE-trending folds and synkinematic intrusions (Oldow, 1984). In central Nevada, structures related to the Luning-Fencemaker fold-thrust belt have been described by Wyld et al. (2003). In this domain, D1 macrostructures are represented by tight to isoclinal fold related to Early Jurassic shortening. Crustal thickening during D1 induced a regional metamorphism under temperatures of 400 ^{o}C . By contrast, D2 structures are localized in the eastern portion of the belt, and metamorphism was absent during D2 shortening.

The geodynamic evolution of north-central Nevada during the Sevier orogeny is manifested by a thin-skinned tectonic style, characterized by crustal thickening, thrust faulting, regional metamorphism, and plutonism (Thorman et al., 1991). The structural patterns of the Sevier deformation are dominated by similar Elko phase structures of NNW and WNW-trending folds and NNW and WNW-striking faults (Mariño, 2003). On the basic of their orientation with respect

to the SE-directed Sevier shortening, Hofstra (1994) described N-to-NE-trending folds and E-to-NW-striking faults in the Independence Mountains, NNW of Elko. Pulses of regional metamorphism and plutonism occurred at ~ 110 Ma, 75 Ma, and 50 Ma (Thorman et al., 1991).

Late Mesozoic to Early Cenozoic tectonics in north-central Nevada was controlled by the kinematic interactions among the North America, Pacific, and Farallon plates. The tectonic regime within the region switched from contractional to extensional by the beginning of Tertiary times (Lewis, 2001; Dickinson, 2006). Dickinson (2006) recognized two successive phases of extension in the Great Basin related to different geodynamic settings: (1) pre-middle Miocene extension and formation of metamorphic core complexes due to back-arc deformation, and (2) post-middle Miocene extension linked to the development of the San Andreas transform zone. Similarly, Muntean et al. (2001) and Henry et al. (2001) discussed and presented data on the Tertiary extensional regimes in north-central Nevada. According to these authors, by late Eocene times there was a west-northwest extensional regime operating in eastern and north-central Nevada, with a peak of ~ 50 % extension during the Eocene-Oligocene that declined to about 10 % in the Miocene. Subsequently, shortly after the formation of Carlin-type deposits during late Oligocene, high to moderate extensional rates may have obliterated or displaced the original geological configuration of these deposits. However, the overall extensional patterns in north-central Nevada during Basin and Range extension are dissimilar to those elsewhere in Nevada.

They are distinguished by more extreme extension from 100 % near Las Vegas to about 75 % in central Nevada (Leeman and Harry, 1993). In more detail, Bogen and Schweickert (1985) estimated the E-W extension along the 40th parallel to be 178±33 km (Fig. 4).

Extension in the Basin and Range was accompanied by extensive volcanism, minor plutonism, and the contemporaneous formation of Carlin-type deposits, porphyry Cu-Au, and skarns (Silberman et al, 1976; Henry et al., 2001; Johnston, 2005). Widespread volcanic activity developed in Nevada from 43 to 6 Ma characterized by a definable temporal and spatial distribution of volcanic rocks thought to be related to the relative motions of the Pacific, Farallon, and North America plates and the development of the San Andreas transform system (Silberman et al., 1976; Dickinson, 2006).

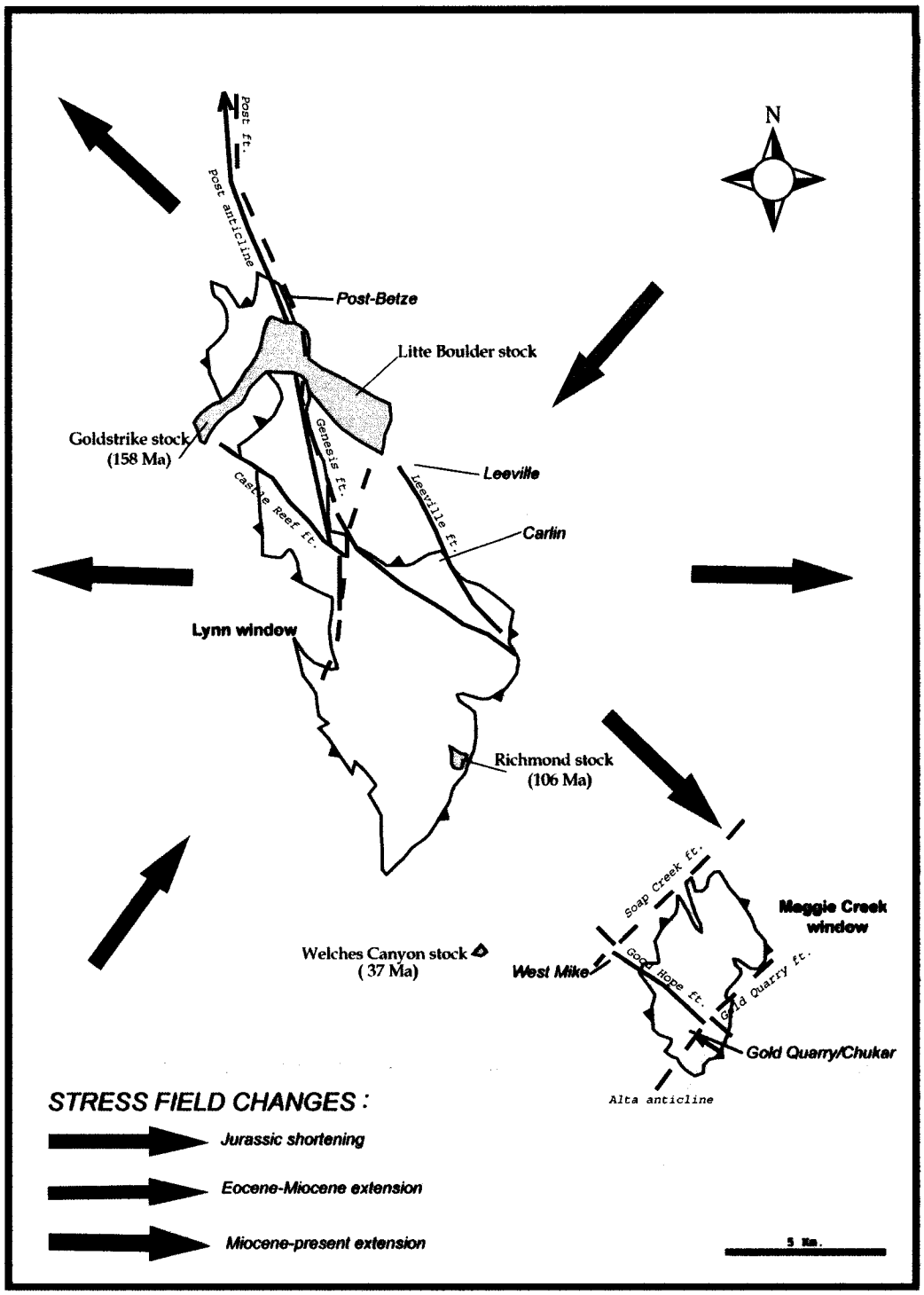

FIGURE 4. Geological framework of the north and south areas of the Carlin trend showing the Lynn and Maggie Creek-Carlin windows, which host gold mineralization of Eocene age. Main strain fields,denoted by color arrows, record significant Jurassic shortenning, and Tertiary polyphasic extensional regime with probable fault reactivations (Modified after Moore, 2001; Lewis, 2001).

In the context of Tertiary volcanism in north-central Nevada, the works of Henry and Ressel (2000), Ressel et al. (2000), Henry et al. (2001), and Ressel and Henry (2006) are important. According to these authors, most of the Carlin-type orebodies are spatially and temporally linked to Eocene magmatism, ranging from dikes to lavas of silicic to intermediate composition. Thus, the presence of widespread Eocene igneous rocks and the possible genetic linkage with Carlin-type deposits suggest that deep-seated plutonic complexes were emplaced along the Carlin trend (cf. Ressel and Henry, 2006).

After the onset of Eocene silicic volcanic activity, a rifting event took place about 16.5 and 14.7 Ma with abundant episodes of bimodal basalt-rhyolite volcanism hosting epithermal Au-Ag deposits (e.g., Midas, Mule Canyon). The northern Nevada rift trends north-northwest and is part of a regional middle Miocene rift zone, the Nevada-Oregon lineament, that may have been controlled by an ancient, deep fracture zone. This rifting episode was the result of a WSW-ENE extension during the middle Miocene (Stewart et al., 1975).

In summary, the geological evolution of north-central Nevada, part of the Great Basin region, is complex and broadly related to the following sequence of events (Fig. 5):

I. Rifting of Laurentia c. 800-500 Ma. Development of passive margin sedimentation of clastic and carbonate strata onto the Precambrian basement during the lower Paleozoic.

II. Short-lived Paleozoic orogenies (Antler, Sonoma) were produced as island-arcs accreted to the western margin of North America. Regional thrust sheets were emplaced eastward, placing eugeoclinal strata onto miogeoclinal rocks.

III. End of passive margin settings by Triassic time. Widespread back-arc plutonism resulting from the development of a Cordilleran magmatism arc due to the subduction of the Farallon plate. Two major orogenic events are recognizable in north-central Nevada: Nevadan-Elko and Sevier phases.

IV. By early Tertiary extension began within the Basin and Range realm. Coevally, extension-related magmatism swept southward through Nevada. Intensive Eocene magmatism is spatially and temporally associated with some of the Carlin-type deposits. Finally, Oligocene metamorphic core complexes developed in areas of high extension rates.

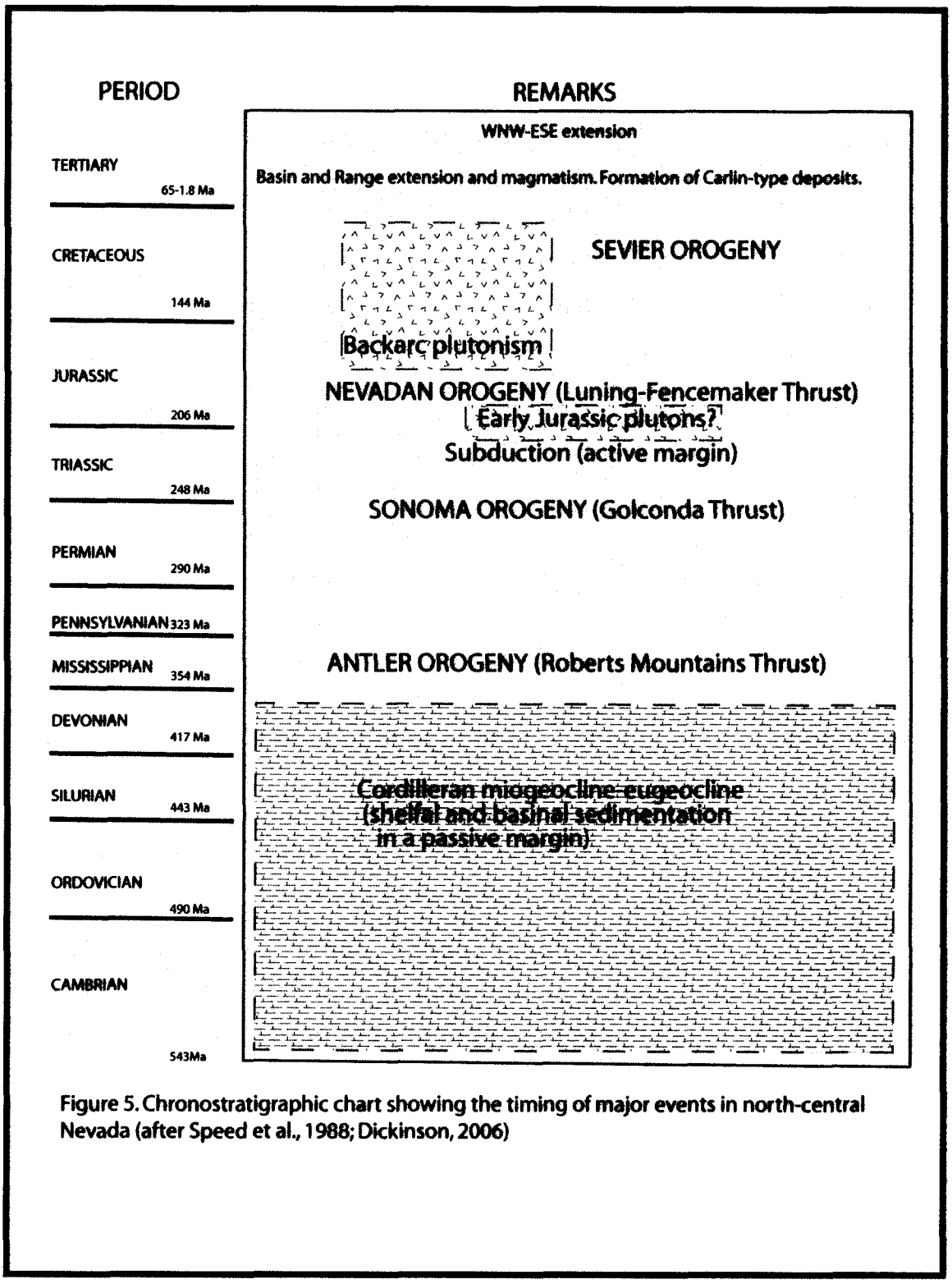

Figure 5. Chronostratigraphic chart showing the timing of major events in north-central Nevada (after Speed et al., 1988; Dickinson, 2006)

3. LITHOSTRATIGRAPHIC SETTING OF THE CHUKAR FOOTWALL DEPOSIT

The Chukar Footwall deposit lies beneath the southwest highwall of the Gold Quarry mine in the footwall of the Chukar Gulch fault (Fig. 6), a NE striking fault dipping 60° SE that may be interpreted as a structural domain boundary for the deposit (Sagar, 2000b). The Gold Quarry deposit have mainly been described by Rota and Hausen (1991), Williams (1992), Sha (1993), Cole (1995), and Harlan et al. (2002). The stratigraphic sequence at Chukar Footwall is comprised of silty carbonates of the miogeoclinal facies wherein the economic orebodies, outlined by a 0.20opt Au cutoff, are hosted in the Silurian-Devonian Roberts Mountains Formation.

The presence of NNW-trending magnetic anomalies in the northern and central parts of the Carlin belt has been interpreted as plutonic intrusions of various ages, sizes, shapes, and depths of emplacement (Ressel and Henry, 2006). Regarding the prominent positive magnetic anomalies and the extensive contact metamorphic aureole southwest of the Gold Quarry / Chukar Footwall deposits, they are thought to be related to large multiple-intrusive plutonic masses emplaced at relatively deep crustal levels (Chakurian, 2001; Ressel and Henry, 2006). In addition, there are several small lamprophyre dikes in the Gold Quarry and Chukar Footwall, emplaced along high angle NW-striking faults that may be related in space and time with these igneous rocks.

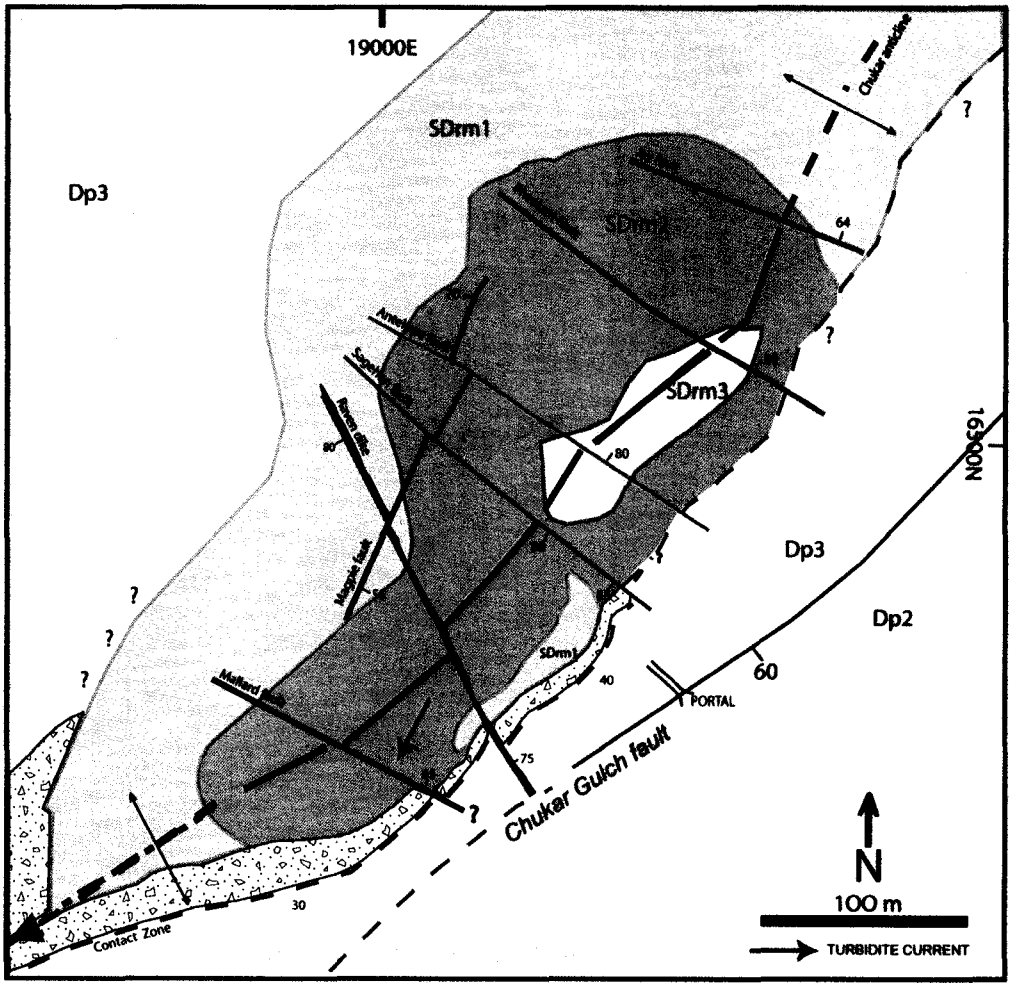

FIGURE 6. Simplified geologic map of the Chukar Footwall mine at the 4650 level.The Silurian-Devonian Roberts Mountains Formation (SDrm) is the main host rock for disseminated gold mineralization. The geometry of the Contact Zone, interpreted in this study as a mixed zone of dissolution-collapse breccias and low to high fault density, is still poorly constrained along the crest and west limb of the Chukar anticline.The Devonian Popovich Formation (Dp2,Dp3) is a monotonous package of massive, dark to grey micrites. Toward the deeper mine levels (not shown), these units were afected by a metasomatic metamorphism characterized by diopside hornfels (Modified from Newmont, 2003).

Metasomatic metamorphism gave rise to gray-green diopside hornfels (exoskarn), locally generating coarse mottled textures along former bedding planes. Drill hole data from Chukar Footwall suggest an intrusive body toward the WNW, because the metamorphic thermal effects increase with the appearance of new mineral phases. This setting is similar to the one observed in rocks of the nearby Mike (Soap Creek) deposit described by Norby and Orobona (2002), wherein the Cretaceous Richmond stock was responsible for the thermal event and associated base metal-Bi-W-Mo mineralization. Likewise, the exoskarn observed at Chukar Footwall deposit may be the result of Jurassic metamorphism correlative with a deep-seated plutonic body to the west of Gold Quarry.

SILURIAN-DEVONIAN ROBERTS MOUNTAINS FORMATION

The Roberts Mountains Formation (SDrm) consists of thin to relatively thick-bedded to laminated silty limestone of middle Silurian-early Devonian age (Evans, 1980; Mullens, 1980). Regionally, the SDrm has been interpreted as basinal to slope sediments sharing many of the characteristics of carbonate turbidites as well as deep water environments (Cook and Corboy, 2004; Wilson, 1969). Ettner (1989) described several ichnofossils in the Tuscarora Mountains, which interpret bathymetry and paleoecological conditions during the sedimentation of the SDrm. Mullens (1980), based on the presence of pyrite,

carbonaceous material, and absence of fossils, hypothesized that during the deposition of the silty limestone that the pH was about 7.9-8.2 and the Eh was close to -0.3. Conodont data from the Carlin mine indicates an episodic temperature spike between 350-450°C (Armstrong et al., 1987) that may be related to Jurassic intrusions.

At Chukar Footwall (Fig. 7), as elsewhere in the Carlin trend, the SDrm has been divided in four informal gradational units (Sagar, 2000a, 2002b; Harlan et al., 2002). The basal unit, $SDrm_4$, is approximately 220 m of monotonous, planar, silty limestone similar to the upper unit $SDrm_1$. Samples from this unit only come from deep cores that did not intercept the underlying Ordovician Hanson Creek Formation, the ore host of the Murray mine in the Jerritt Canyon district (Hutcherson, 2002).

The $SDrm_3$, with an approximate thickness of about 66 m, is a silty limestone unit easily recognizable due to the presence of quasi-rhythmic centimetric calcarenite beds.

The next 52 m, $SDrm_2$, consists of a silty limestone with erratic, thin calcarenite beds with laminae to locally wispy textures. Brassy or sooty pyrite is commonly found along or around the wisps and/or zones of carbonaceous matter. The wispy textures have generally been thought of as a product of bioturbation (Armstrong et al., 1998).

The upper unit, $DSrm_1$, is a minimum of 27 m of monotonous silty limestone with some erratic calcarenite beds toward the base.

The medium-dark gray to light gray colors of these units appear to be the result of the degree of hydrothermal alteration, content of carbon, and bleaching by ground waters. Several sedimentary structures have been recognized during underground mapping and from core logging. Load cast structures are somewhat common on the calcarenite beds and can be followed for a few meters until they pinch out with the silty limestone. Also, small sedimentary boudinage, diagenetic structures formed due to the degree of sediment competence during compaction, were noted in a calcarenite bed near the hinge line of the Chukar anticline. The presence of minute flute marks on the sole of the SDrm2 unit (4680 level) records turbidity current movements to the SW/SSW; however, a paleocurrent analysis was not undertaken due to the scarcity of these types of structures in mine exposures. From cores, soft-sediment deformation is common, with a range in thicknesses between a few centimeters up to tens of centimeters.

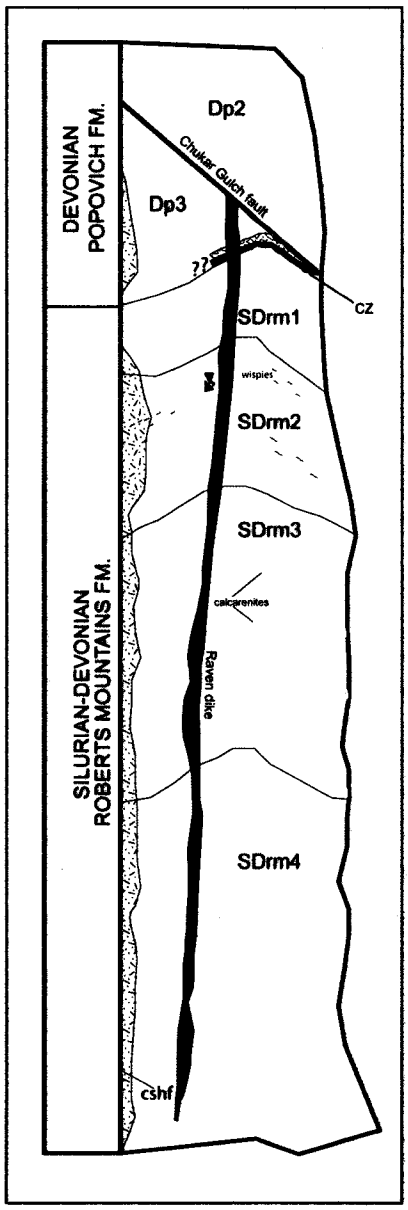

FIGURE 7. Generalized tectono-stratigraphic section of the Chukar Footwall mine. The contact between the Silurian-Devonian Roberts Mountains Fm. and Devonian Popovich Fm. (Dp3) is along a complex zone of dissolution-collapse breccia and fault(s). The Early Jurassic Raven dike was emplaced along NNW-trending structures, and it has been locally brecciated due to later fault reactivation. Metasomatic metamorphism, which increases to the SW, is characterized by calc-silicate lithologies (cshf) that overprint the original carbonate mineralogy.

DEVONIAN POPOVICH FORMATION

Structurally overlying the SDrm Formation is the Devonian Popovich Formation (Dp), where only the lower section (Dp_3) can be characterized in 3 mine levels. Along the Carlin trend, this formation exhibits different facies attributes and thicknesses as a result of the environments of deposition and later diagenetic processes. Furthermore, the boundary between SDrm and Dp units is in dispute (Evans, 1980; Radtke, 1985; Ettner, 1989; Armstrong et al., 1998; Harlan et al., 2002; Mariño, 2003). Regarding the age of the Popovich Formation, an Early Devonian-Late Devonian interval has been assumed by Evans (1980), Ettner (1989), and Armstrong et al. (1998), whereas Cook and Corboy (2004, Fig. 2) place this formation in the Middle Devonian.

Ettner (1989) reported sections between 210 m thick at Tuscarora Spur (4 kms NW of the Carlin West pit) and 70 m thick in the Carlin mine. Harlan and others (2002) divided this formation into three informal gradational units at Gold Quarry mine, with a thickness of 360 m. The basal unit, Dp_3, consists of micrite with beds of silty limestone, calcarenite and bioclastic limestone. The overlying Devonian units consist of a thin succession of calcarenite, bioclastite, silty limestone (Dp_2) and brecciated silty limestone (Dp_1).

As mentioned above, at Chukar Footwall the contact between SDrm unit and the Dp_3, where it has been mapped during this study, is along a variable width zone of dissolution-collapse breccias referred in this study as the Contact Zone (Contact Fault Zone; Newmont, 2003). As identified from cores and mine exposures, the Dp_3 is a monotonous package of massive, dark to grey micrites

with abundant carbonaceous material, pyrite and calcite veins. Also, the unit is further characterized by zones of crackle -to matrix- supported breccias and local shearing obliterating the rock fabric.

The Dp_3 does not host economic grade mineralization at Chukar Footwall mine (Joe Sagar, personal communication, 2004).

STYLOLITES

In zones of decarbonatization, stylolites developed sub-parallel to and at high angles across bedding at both microscopic and macroscopic scales. Four stylolite forms have been observed in hand samples (rectangular, wave-like, smooth-type, and sharp-peak; Guzzetta,1984), with a thickness of about 1mm filled with both carbonaceous matter and calcite. At leas two phases of stylolitization have been observed in thin sections, whose time of formation has been established on the basis of crosscutting relationships: (a) an early, pre-ore event associated either with diagenesis or D1 deformation, and (b) a syn- or post-ore stylolitization (pyrite stylolites). In general, the stylolites are deflected by quartz grains and rarely they crosscut or truncate carbonate veinlets and grains. In strongly decarbonatized intervals the high density of stylolites imposed two distinctive fabrics upon the SDrm and Dp_3 lithologies, stylolaminated and stylobreccia (Evans, 2000). From thin section observations, the former fabric is characterized by parallel trends of very thin carbonaceous stylolites. On the other hand, the latter fabric occurs where breccia clasts are bounded by stylolites or where an intensive stylolitization produced and bounded fragments.

METASOMATISM: DIOPSIDE HORNFELS

Both the SDrm and Dp units at Chukar Footwall are partially affected by a progressive metasomatism of possible Early-Middle Jurassic age connected with a plutonic intrusion. Locally, the Raven dike produces a zone of about 6 m wide of weak thermal alteration on the host lithologies. In general, samples from different depths are composed of carbonates± Mg silicates- K-feldspar that may have formed within the hornblende hornfels in the SDrm/Dp units.

Although the lack of systematic sampling due to mine exposures makes it impracticable to define isograds, some generalization can be made from the available samples. In the SDrm/Dp units affected by the thermal aureole, the exoskarn mineralogy indicates a spatial zoning due to its proximity to the intrusive body. The mineralogical zonation may suggest that an underlying intrusion lies to the WNW-to-SSW of the deposit. This inference is drawn from the occurrence of vesuvianite at deeper depths (e.g., hole CFU-137), wherein visible vesuvianite porphyroblasts define a weak preferred orientation (S_1). The pyroxene hornfels in the SDrm units are characterized by prograde assemblages of : **(AI)** calcite± dolomite± quartz± biotite/phlogopite± K-feldspar± tremolite, and **(AII)** calcite± quartz± diopside± vesuvianite± K-feldspar± tremolite. The appearance of diopside from assemblage AII, the most proximal to the intrusion, suggests a temperature range between 400-600 C^{o} (Walck, 1989; Bucher and Frey, 2002). Formation of phlogopite in assemblage AI could represent an early

K-metasomatism episode. Finally, retrograde exoskarn alteration, controlled by structures and mineralogy, occurs as fibrous phyllosilicate front (talc?) and fine grained carbonates, preferentially replacing vesuvianite.

BRECCIA BODIES: THE CONTACT ZONE

Breccia bodies are ubiquitous features in the Carlin trend, but their nature and interpretation within the deposit stratigraphy and their relationship with gold deposition have not been conceptualized until recent years, even though such bodies host the main mineralization at the Meikle, Deep Star, Post, and Rain deposits (Emsbo et al., 2003; Heitt et al., 2003; Evans, 2000; Williams, 1992). At the Gold Quarry mine, Williams (1992) described collapse and fault breccias. Texturally, the collapse breccias consist of angular monolithic clasts of SDrm in a matrix of calcite, barite, and quartz. Breccia geometries range from funnel to tabular to irregular shapes, and are spatially related to strongly decalcified rocks. Geochemically, these bodies are enriched in Au, As, Hg, and Sb relative to the surrounding SDrm units. With respect to fault breccias, Williams (1992) characterized both NNE and NNW trending structures displaying fragment zoning and tabular geometries. These structures record several episodes of brecciation, mineral deposition, and element enrichment which indicate they were feeder structures (Williams, 1992).

The contact between SDrm and the Dp (the Contact Zone, CZ) along the Tracker Decline and in the 4610 level is characterized by zone with high fracture and fault density with little or no gouge, dissolution-collapse breccias, and calcite

veins and calcite flooding. During a pre-ore event, intense fracturing in the SDrm limestone resulted in the formation of multistage white calcite veins and localized calcite flooding (stage 1). Stage 2 is characterized by the development of dissolution-collpase breccias due to strong decarbonatization that resulted in the collapse of the section by carbonate removal. In general, the breccias (Fig. 8) consist of angular-to- subrounded, poorly sorted and decarbonatized SDrm-Dp clasts exhibiting a range of sizes (mm to cm in the same hand sample) and a crude coarsening-upward fabric. The breccias are matrix-supported, mostly composed of fine, anhedral nonferroan vuggy, wavy-banded calcite as indicated by their pinkish-reddish staining. Contacts between clasts and the matrix are sharp, and commonly the clasts are crosscut by late calcite±quartz veinlets.

Moderate to high rotation of breccia clasts suggests minor to large movements within the collapse breccia body. Lastly, pyrite grains may be abundant along the edges of clasts. Usually, the breccias display cockade and minor crackle textures.

Isotopic and fluid inclusion data from calcite veins (ST-1 and ST-2 stages) suggest that much of the fluid responsible for this stage was meteoric. Through time, fluid changes produced a silicification event that is characterized by the patchy introduction of silica and kaolinite±sericite as a flooding and veinlets. Abundant multistage veins (< 1mm) of quartz±barite±saddle dolomite cut across the breccia. The lack of carbonaceous debris and the presence of residual materials in the matrix further characterize this body. Late-stage calcite veins cut both stages 1 and 2. The next recognizable stage (stage 3) is characterized by

low angle normal NE-striking faults due to volume loss of the limestone. The fault breccias , volumetrically small, contain angular to subangular fragments of strongly decarbonatized and silicified SDrm, whose structural fabric has been somewhat obliterated by later hydrothermal events and fault reactivation (s).

Geochemically, the CZ dissolution-collapse breccias are characterized, relative to mineralized rocks by (1) ~ zero Au values, (2) irregular low Al, Fe, Sb, Se, Tl values, and (3) variable, high Ba, Ca,,Mg, and Zn values. The geometry and stratigraphic location of these tabular bodies of dissolution-breccias were strongly constrained by rheological factors between SDrm and Dp rocks. The thin to medium-bedded silty limestone of the upper SDrm units, in contrast of the massive Dp_3 micrites, were the main locus of decalcification and silicification during an early hydrothermal event thus creating a semi-impermeable barrier for subsequent ore fluids. Tentatively, the formation of these dissolution-collapse breccias is interpreted to have been a pre-ore event. Silicification eliminated the pore space and prevented the introduction of later hydrothermal, gold-enriched fluids (Joe Sagar, personal communication, 2004).

In the SDrm, breccias are a common feature, especially in the $SDrm_{1-2}$ units. In the Dp_3 unit, however, breccia is much less pervasive than in the underlying units due to the massive fabric of the micrites and/or lower

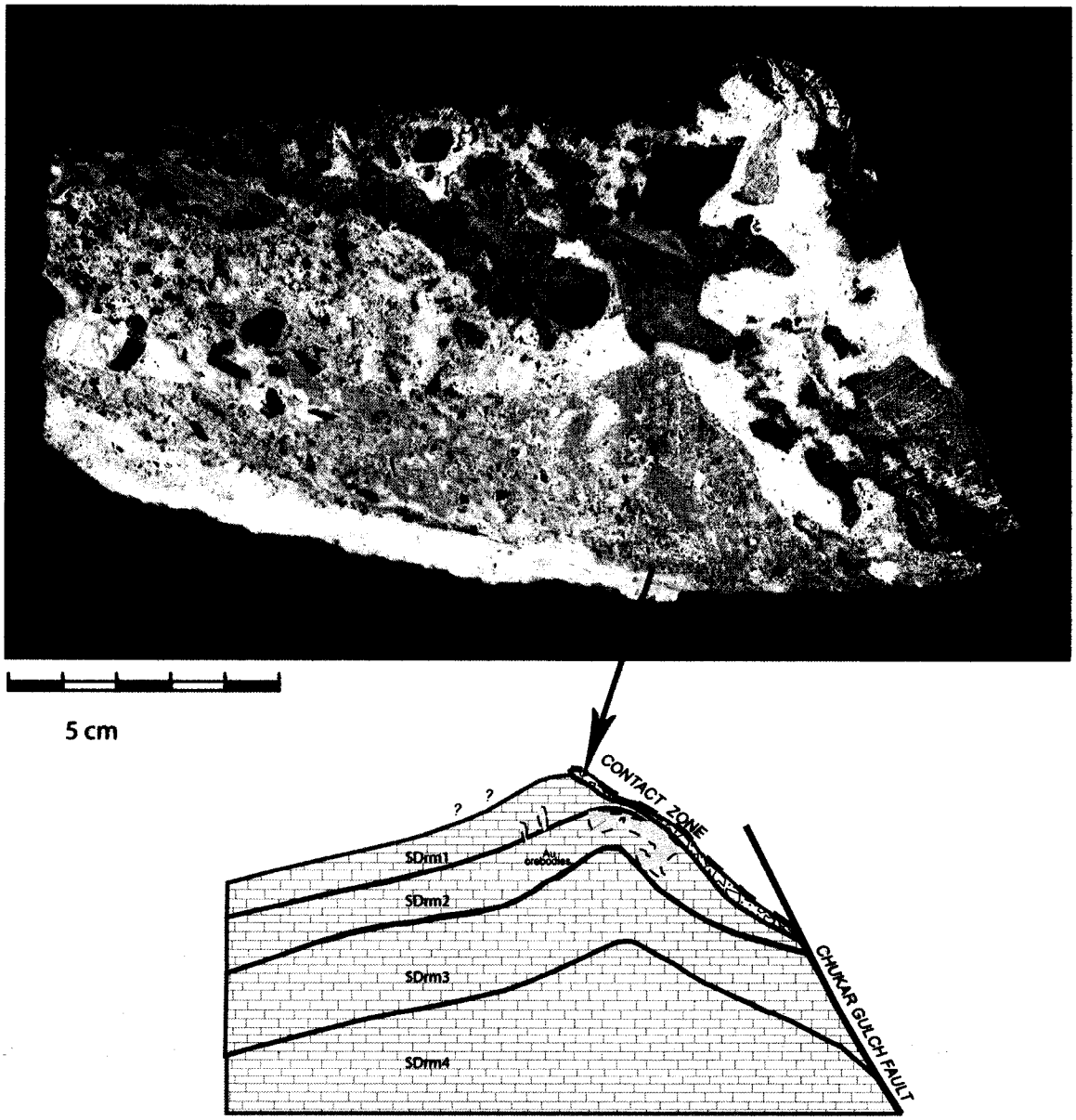

FIGURE 8. Weakly silicified dissolution-collapse breccia from the Contact Zone, along the Tracker Decline. This matrix-supported monolithic breccia contains decalcified clasts with earlier thin calcite veins. Minor to moderate rotation of breccia clasts indicates small movements. The breccia body acted as a cap for later hydrothermal fluids. Schematic cross-section, not to scale.

concentration of fractures and joints, which channeled the fluids responsible for the chemical dissolution of the rocks.

Additional dissolution-collapse breccia bodies have been recognized in the 4610 and Tracker Exploration Drift mine levels. One such body has a vertical, funnel shape (Fig. 9) about 4 m high and 2 m wide, and is composed of poorly sorted, angular monolithic clasts ranging from millimeters to several centimeters in size and consisting of decarbonatized and silicified SDrm1 embedded in a calcite matrix. Internal sedimentary fabrics are absent; however, there is a crude preferred orientation of the clasts' long axes that may be interpreted as being parallel to former bedding planes. The fragment orientation appears to be the result of in-situ brecciation. The spatial position of this breccia body relative to a NNW-trending fault zone supports the interpretation that the latter structure served as a pathway for hydrothermal fluids. Briefly, the breccia sample shows enrichment in Au, Ag, As, Sb, and Ti; and depletion in Ba, Cr, and Mg relative to adjacent SDrm host rocks.

Finally, centimetric to millimetric bodies of bedding-parallel collapse breccias occur in decarbonatized SDrm rocks. These breccias are monolithic, matrix supported, and fragments are mostly angular. In thin section, the density of stylolites within fragments is greater than the surrounding rock.

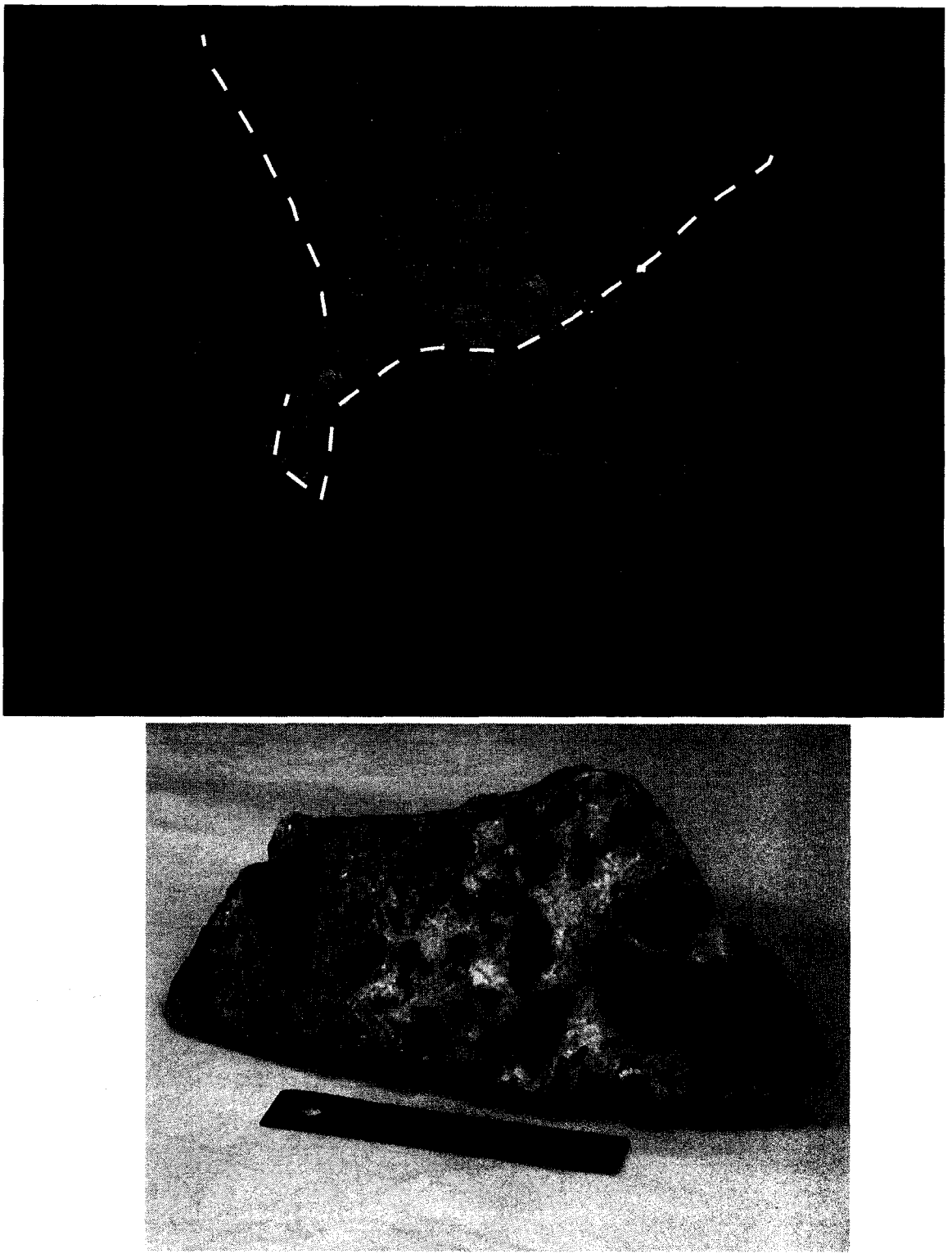

FIGURE 9. Funnel-shaped dissolution-collapse breccia in the 4610 level (hammer for scale at the upper right). The breccia is monolithic and matrix-supported with angular to sub-angular clasts of the Roberts Mountains Fm. Sample 131 yielded 0.0951 opt Au.

INTRUSIVE ROCKS: THE RAVEN DIKE

A wide variety of dikes have been reported in the Carlin trend, including lamprophyre, monzonite porphyry, latite, dacite, rhyolite, and granodiorite to diorite (Radtke, 1985; McComb, 1993; Altamirano, 1999; Tretbar , 2000; Chakurian, 2001; Jackson et al., 2002; Heitt et al., 2003; Mariño, 2003) . Available radiometric data suggest at least two main peaks of intrusive activity related with both the emplacement of the Goldstrike stock at about 159 Ma, and the Richmond stock at 106 Ma (Evans, 1980; Moore, 2001; Norby and Orobona, 2002). Similarly, Evans (1980) reported a radiometric age of 37 Ma for a small quartz monzonite intrusion, the Welches Canyon stock, and related dikes in the Lynn window. Dikes are characterized by (1) facts that they were emplaced along high angle faults with sharp contacts, (2) host economic gold mineralization (e.g. the Beast dike, Ressel et al., 2000), and (3) show extensive hydrothermal alteration that makes it difficult or impossible to determine the original fabric and geochemistry in most cases.

Several NNW- trending lamprophyre dikes showing a high degree of alteration have been exposed in the Gold Quarry pit showing a high degree of alteration (McComb, 1993; Ressel and Henry, 2006). Although no age constraints exist yet, these dikes have been tentatively assigned Jurassic-Cretaceous ages in Newmont's cartography, and they pre-date the main gold mineralization period (Harlan et al., 2002). In addition to these dikes, a prominent intrusion known as the Raven dike is exposed in several underground levels in Chukar Footwall. Dike emplacement was along NW-to-NNW trending faults, with

steep SW to NE dips. The Raven dike has been slightly offset and rotated by some NE-trending faults (e.g., Magpie fault). It shows local intense brecciation toward its borders due to later fault reactivation.

The Raven dike shows sharp contacts with the SDrm and Dp units, producing a visible, metric scale thermal effect on either side characterized by intense bleaching and recrystallization of carbonates. The dike ranges from a few centimeters up to a meter in width, and is up to 220 m in length at the 4650 level (Newmont, 2003). The Raven dike was emplaced along NNW-trending faults (e.g. Raven Dike fault at the 4580 and 4590 levels). In the 4580 level, the dike has been brecciated to angular to subangular centimetric fragments embedded in a matrix of calcite and clay gouge. Furthermore, the dike may locally be mineralized (Joe Sagar, personal communication, 2004).

At outcrop scale, the dike is easily recognizable by its greenish, gummy clay that produces a perceptive, irregular alteration halo. Although the dike is completely altered, it shows a homogeneous texture. In thin-sections (Fig. 10), the dike is characterized by inequigranular, glomeroporphyritic textures of relic phenocrysts of feldspars, hornblende, and biotite in a fine groundmass totally altered to sericite, kaolinite, anhydrite, quartz, and unidentified opaques. Plagioclase is altered to microcrystalline masses of sericite, quartz, and kaolinite. Similarly, biotite is replaced by iridescent sericite and chlorite. Sulfide minerals, pyrite and marcasite, comprise up to 10 vol. % of the rock and they partially or completely pseudomorph mafic phenocrysts. Pyrite, the main sulfide mineral,

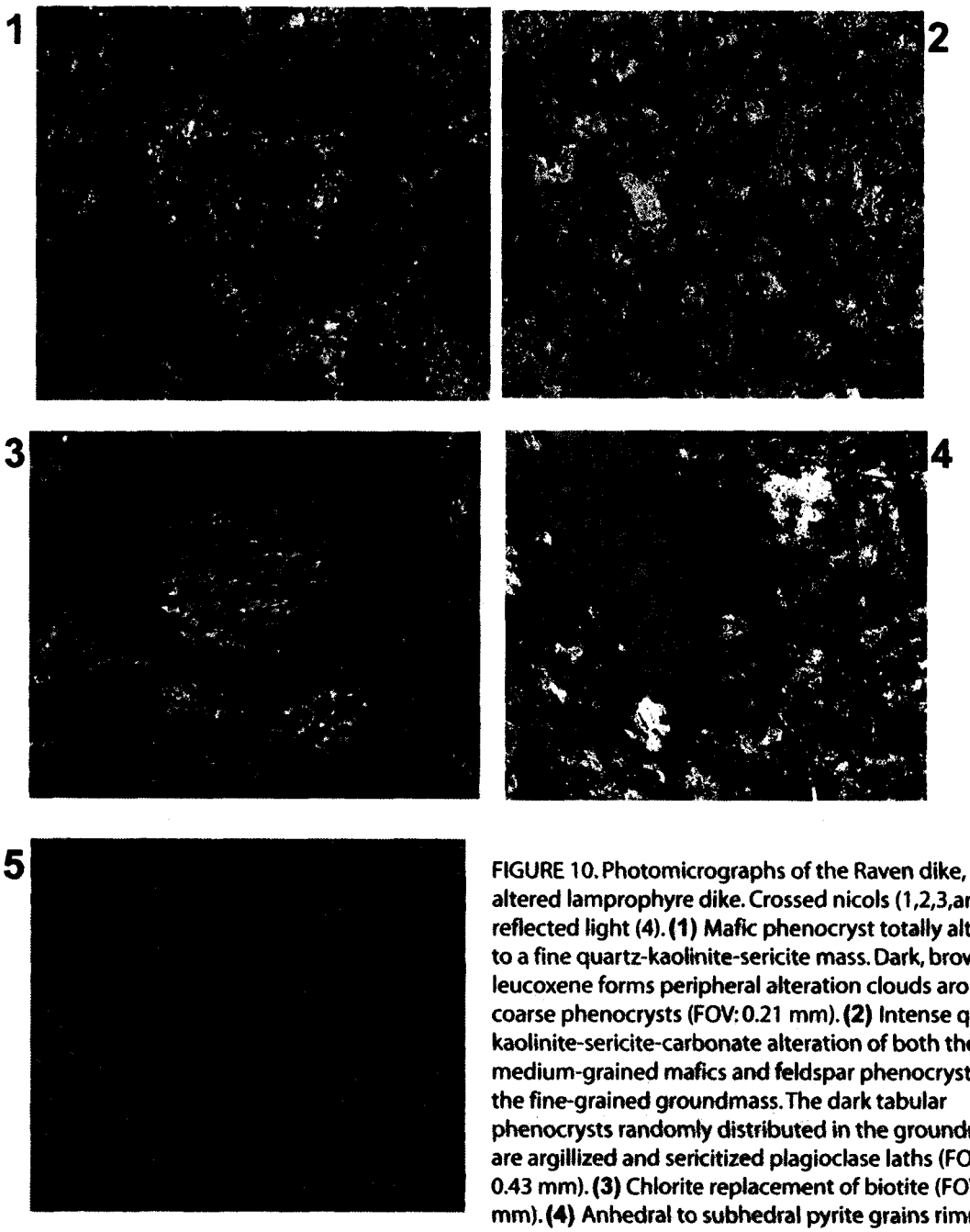

FIGURE 10. Photomicrographs of the Raven dike, an altered lamprophyre dike. Crossed nicols (1,2,3,and 5) and reflected light (4). **(1)** Mafic phenocryst totally altered to a fine quartz-kaolinite-sericite mass. Dark, brownish leucoxene forms peripheral alteration clouds around coarse phenocrysts (FOV: 0.21 mm). **(2)** Intense quartz-kaolinite-sericite-carbonate alteration of both the medium-grained mafics and feldspar phenocrysts and the fine-grained groundmass. The dark tabular phenocrysts randomly distributed in the groundmass are argillized and sericitized plagioclase laths (FOV: 0.43 mm). **(3)** Chlorite replacement of biotite (FOV: 0.21 mm). **(4)** Anhedral to subhedral pyrite grains rimming and sulfidizing mafic phenocryst (FOV: 0.21 mm). **(5)** Late barite-fluorite vein. Triangular pits of fluorite along cracks or cleavages of earlier barite. Fluorite contains fluid inclusions. (FOV: 0.21 mm).

occurs as anhedral to subhedral grains locally replacing mafic phases, forming late veinlets, and in discrete grains overgrown by marcasite. From deep hole samples (QRC1489@1040'), there is an greater abundance of pyrite veinlets, altered to malachite, relative to samples from mine exposures. Late barite and fluorite veins crosscut the dike. Anhedral to euhedral discrete purple fluorite grains are distributed along barite cleavages and fractures, and fluid inclusions are abundant. Finally, prismatic hydrothermal apatite phenocrysts (~ 40 to 60μm in size) were observed within the dike groundmass, forming part of the alteration assemblage.

The above petrographic description, coupled with data by McComb (1993) and Ressel and henry (2006), indicates the Raven dike appears to be a lamprophyre showing an advance degree of hydrothermal alteration (quartz-kaolinite-sericite-pyrite).

4. U-Pb ZIRCON GEOCHRONOLOGY AND APATITE FISSION- TRACK DATING OF THE RAVEN DIKE: RESULTS AND INTERPRETATION

One dike sample (215) from the 4580 level was selected for both zircon U-Pb geochronology and apatite fission-track dating. These measurements were performed at Apatite to Zircon, Inc. using 23 LA-ICPMS spot analyses on 9 zircon grains (Appendix 2). The zircon grains were isolated from pyrite crystals

and their morphology suggests that they are magmatic (Ray Donelick, personal communication, 2005). The concordia diagram for the Raven dike is shown in Fig. 11.

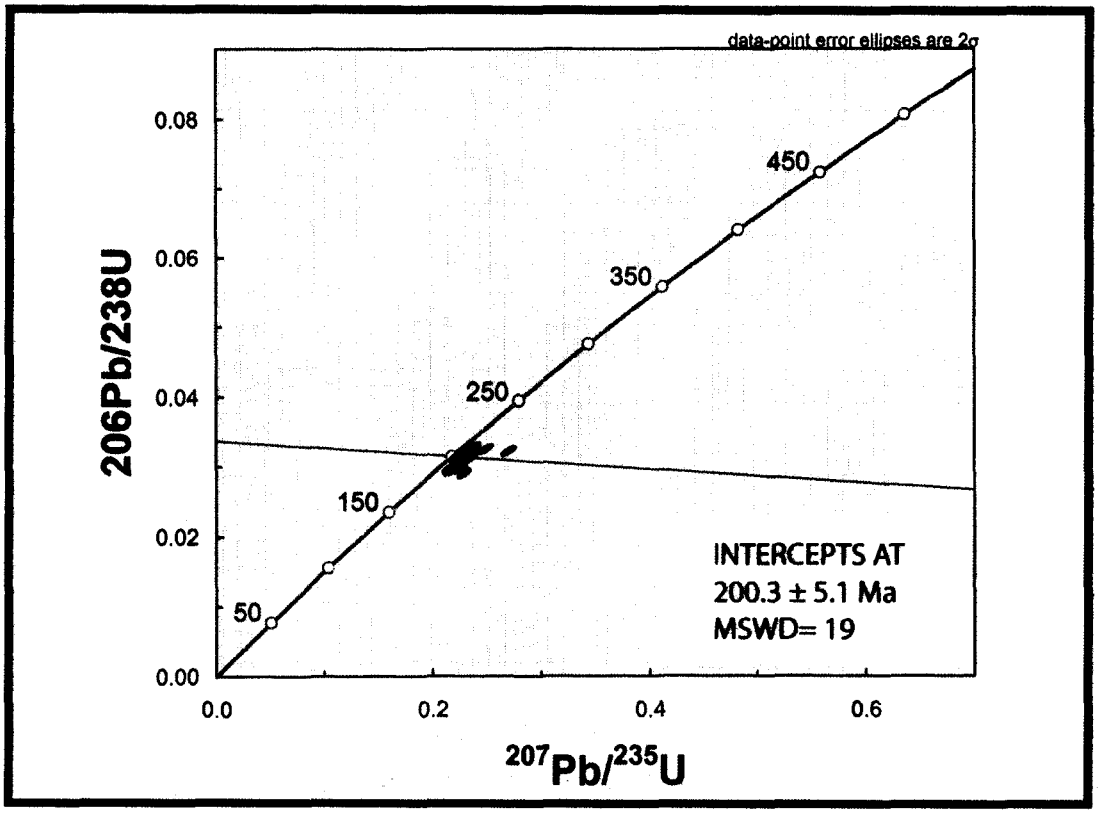

FIGURE 11. LA-ICPMS zircon analyses from the Raven dike (4580 level, sample 215) on the concordia diagram. The U-Pb zircon data yield an Early Jurassic age for the emplacement of the Raven dike at Chukar Footwall.

The concordia plot of the U-Pb zircon data yields an age of 200.3±5.1 Ma (Early Jurassic) for the emplacement of the Raven dike at Chukar Footwall.

Apatite crystals from the same sample were isolated for apatite fission track dating (AFT). These yielded a pooled fission-track age of 17.7±3.7 Ma, representing the cooling through ~135 to 110° C (Green et al., 1989)

In the region, radiometric ages range from ~ 186 Ma for the Bald Mountain area, ~ 158 Ma for the Goldstrike intrusion, to ~35.4 Ma for the Target Hill rhyolite, near Eureka (Mortensen et al., 2000). In addition to these magmatic bodies (Fig. 12), abundant rhyolitic to dacitic dikes of Eocene age (42 to 36 Ma) occur, and are thought to be temporally and spatially associated with Carlin-type deposits (Henry and Ressel, 2000; Henry et al., 2001; Ressel and Henry, 2006). Regarding ages for gold mineralization, Arehart (1996) summarized all reported radiometric data for Carlin-type deposits in the Great Basin ranging from 152 Ma to 8 Ma. However, some radiometric ages remain poorly constrained given the fact that they are from minerals unrelated to gold mineralization (Arehart, 1996; Teal and Jackson, 2002; Tommy Thompson, personal communication, 2005).

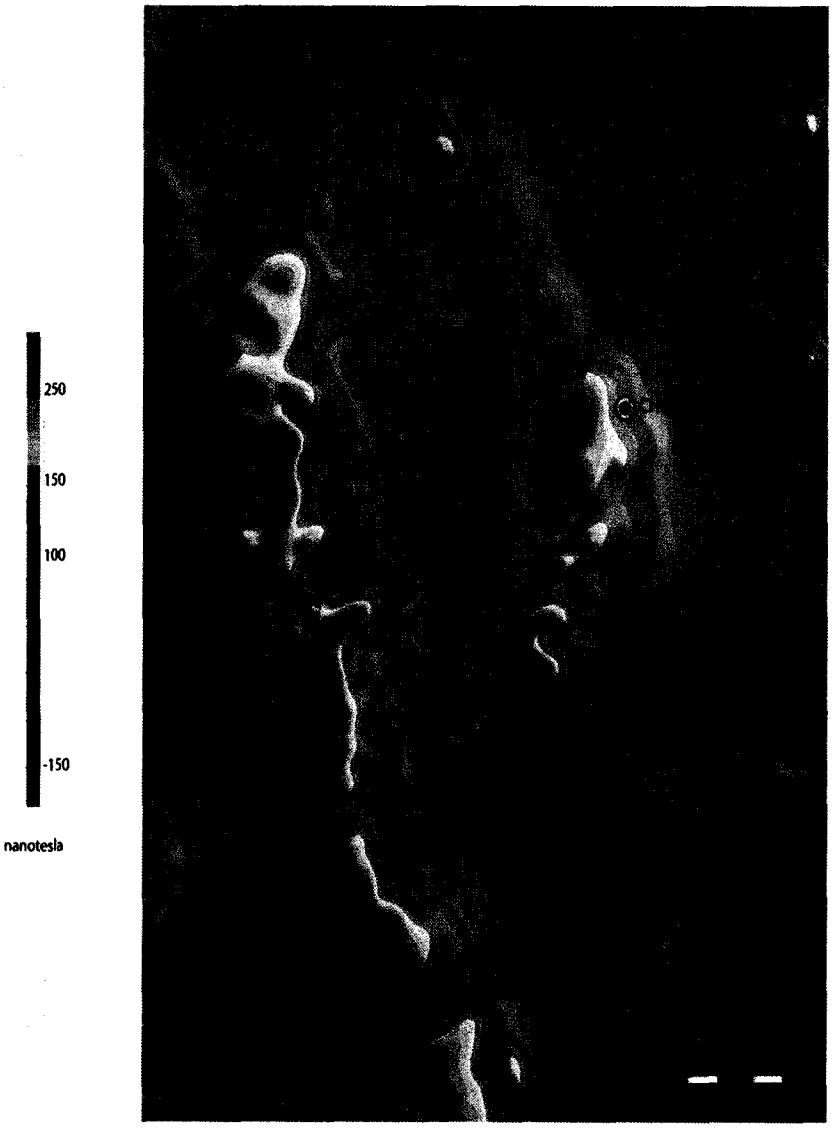

FIGURE12. Inferred igneous bodies from aeromagnetic contour data. A large, concealed Jurassic plutonic body is inferred from the extensive exoskarn in the deeper levels of the Chukar Footwall mine (Aeromagnetic data from Wright, 1993).

AFT pooled age data (Fig. 13) indicate the time of a thermal event at 17.7±3.7 Ma that could possibly be linked to a local scale reset of apatite fission-track ages associated with Tertiary volcanism and extension (Chakurian et al., 2003; Tommy Thompson, personal communication, 2006). This suggestion can be tentatively supported by the combined observations by Rota (1989), who reported stibnite in the Carlin Formation (14.4 to 15.1 Ma, Fleck et al., 1998), and an AFT age of 18.6± 4.5 Ma from the East Carlin deposit ,interpreted as a result of Miocene extension and volcanism in the Tuscarora Mountains (Chakurian et al., 2003).

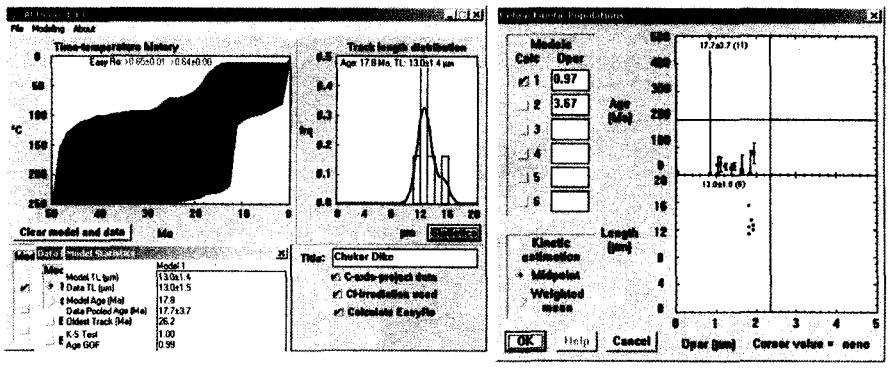

KNOWN PARAMETERS AND ASSUMPTIONS

Client Sample Number	Chukar Dike
DAI Sample Number	672-01
Kinetic Parameter Modeled	Dpar (μm)
Stratigraphic Age (Ma)	not provided
Present-day Temperature (°C)	10°C assumed
Timing of Uplift/Cooling (Ma)	cooling-only assumed

IMPLICATIONS OF THE FISSION TRACK DATA

Age of Oldest Fission Track (Ma)	Dpar=1.40 μm: 26.2±5,5 Ma
Timing of Initiation of Uplift/Cooling (Ma)	Dpar=1.40 μm: 26.2±5.5 Ma

Client Sample Name	AZZ Sample Number	Grains (dmnls)	Dpar (μm)	Dper (μm)	N_s (tracks)	Area Analyzed (cm^2)	$\Sigma(P\Omega)$ (cm^2)	$1\sigma\ \Sigma(P\Omega)$ (cm^2)	ζ_{NIS}	$1\sigma\ \zeta_{NIS}$	^{43}Ca (apatite) / ^{29}Si (zircon) bkg:sig (dmnls)	^{238}U bkg:sig (dmnls)	Q (dmnls)	Pooled Fission-Track Age (Ma)
Apatite														
Age Standards														
Durango	DR06	492	1.86	0.42	3512	2.88E-02	9.0328E-04	1.7093E-06	16.2121	0.2753	2.5655E-02	2.1668E-03	0.6239	31.4+/- 0.8
Durango	DR01E	40	1.80	0.41	288	2.44E-03	8.0065E-05	6.1208E-07	16.3888	0.4091	1.9723E-02	5.5396E-03	0.1212	29.4+/- 1.9
Fish Canyon Tuff	FC01E	40	2.32	0.60	233	1.24E-03	6.8115E-05	5.5964E-07	16.3975	0.4060	2.5514E-02	1.1584E-02	0.2763	28.0+/- 2.0
672-Series														
Chukar Dike	672-01	11	1.42	0.62	23	1.13E-04	9.6300E-06	1.8275E-07	14.8794	0.3716	1.4591E-02	1.6066E-03	0.1037	17.7+/- 3.7

Analyst: apatite=RAD

FIGURE 13. Apatite Fission-track data from the Raven dike, sample 215 (672--1). The apatite cooling modeling suggest a thermal event/uplift that began at 26.2±5.5 Ma, with a pooled age of apatite grains producing an age of 17.7±3.7 Ma. Regional AFT data from Chakurian et al. (2001) may suggest a short-lived thermal episose during Miocene times.

5. STRUCTURAL GEOLOGY OF THE CHUKAR FOOTWALL DEPOSIT

The structural settings of the Gold Quarry-Chukar Footwall deposits are a direct consequence of tectonic events since the Antler orogeny. Cress (1972) recognized four tectonic phases in the Carlin-Maggie Creek window, from earliest to latest: (1) NNE- trending folds related to the Antler orogeny; (2) NNW-trending open folds, and NW- trending tight folds, possibly correlated to Antler deformation; (3) pre-mineralization NW- striking reverse faults (Good Hope fault) and ENE- striking normal faults, and (4) Basin and Range normal faults.

Similarly, Cole (1995) established four generations of structures at Gold Quarry deposit: (1) folds related to the Roberts Mountains thrust, (2) wrench, reverse, and normal faults, (3) normal faults due to collapse during decarbonatization, and (4) normal faults that moved during the Tertiary extensional regime.

Gold mineralization and wallrock alteration were strongly controlled by major and minor structures. The most important ore-controlling feature is the structural intersection of the Chukar anticline with northeast-striking faults (Joe Sagar and Kevin Creel, personal communication, 2005). On the other hand, minor structures (fractures and joints) are also of great importance in controlling and localizing gold pods by increasing the amount of open space in the host rocks whereby the ore fluids were able to move farther, both vertically and horizontally from major fluid conduits.

FOLDS

The Chukar anticline is the main macroscopic feature observable underground (Fig. 6 and Plate 11). This fold, at outcrop scale, does not exhibit any penetrative fabrics within the thin-to-massive bedded silty SDrm units nor in the Dp_3 lithologies. Adjacent and subparallel to the NE-striking Chukar Gulch fault, the Chukar anticline (Fig. 14A) is a northeast-trending open fold that plunges at shallow angles to the southwest. Small scale parasitic folds are present in the northwest and southeast limbs of the anticline, with hingelines trending WNW and NE and plunging 10° and 14°, respectively. The hingeline of the Chukar anticline has been offset up to 22 m by the NW-striking Sagehen fault (Joe Sagar, personal communication, 2005), and bedding attitudes in both limbs indicate an asymmetric, non-cylindrical structure because all the poles are not homogenously distributed along a great circle. The anticline is a fairly simple structure, showing greater bed thickness (~1 m) at the anticline hinge relative to the limbs (~ 14 cms) , typical of similar folds (Ramsay and Huber, 1987). On the basis of its orientation, the Chukar anticline could be related either to the Antler, late Paleozoic, or Sonoma orogenies (Evans and Theodore, 1978; Trexler et al., 2004).

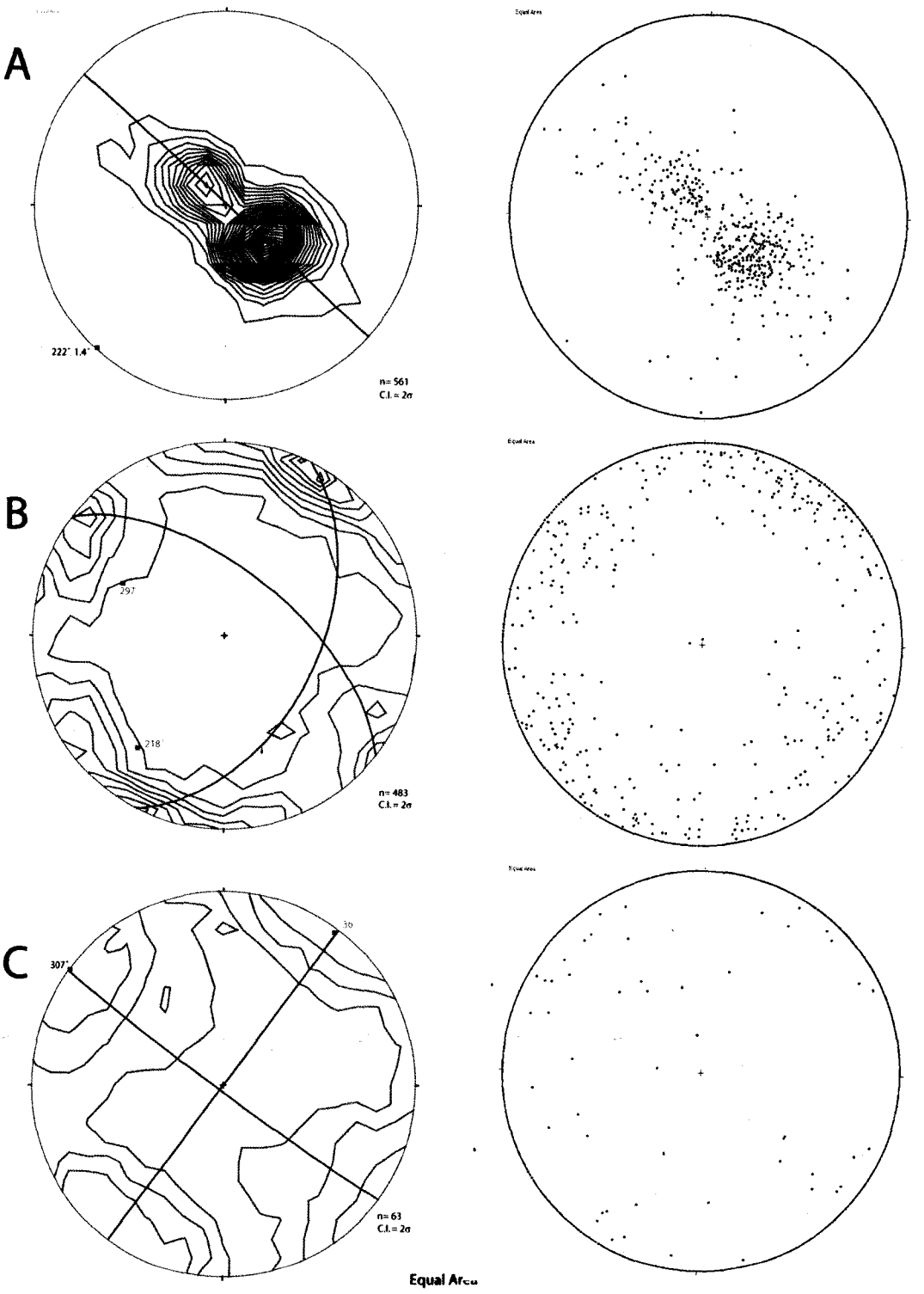

FIGURE 14. Poles to bedding (A), to joints (B), and poles to calcite veins (C) from all mine levels. Contoured by the method of Kamb using Stereonet 6.3.2x (Data from Newmont and this study).

FAULTS

Brittle deformation is represented by two dominant fault trends throughout the deposit (Fig. 15): (1) a WNW / NNW-trending system represented by major structures such as the Jay, Pheasant, Antelope, Sagehen, Raven Dike, Mallard, and Crow faults, and (2) NNE-NE striking faults represented by the Contact Zone (CZ), Magpie, and Chukar Gulch faults. Both fault systems record multiple sets of slip indicators due to later fault reactivation thus producing incoherent cross-cutting relationships.

Faults of the **WNW/NNW**-striking fault system commonly have both moderate and steep dips to the NE and to the SW. In general, they are unhealed structures up to 2 meters wide, with clay, breccia, and friable gouge. Kinematic indicators such as calcite crystal fibers, grain striations, and fault mullions point out multiple senses of displacement in both fault systems due to later reactivation(s). Sub-horizontal to sub-vertical rakes were recorded on fault planes discerning a general trend of (1) an oblique dextral normal slip, which rakes between 10 to 70 degrees to the northwest, and (2) strike-slip faults with sub-horizontal slickenlines. The intrusion of the Raven dike along NNW-striking faults may suggest that these structures formed prior to about 200 Ma.

The **Crown fault** (320°, 69° SW; Plate 10) , only exposed along the Main Decline near the Trucker Exploration Drift, cuts the SDrm pyroxene hornfels and is defined by several curvilinear slip surfaces in a 90-100 cms wide damage zone. The fault breccia is composed of angular to subangular fragments cemented with calcite, which also forms small veinlets parallel to the fault. Iron

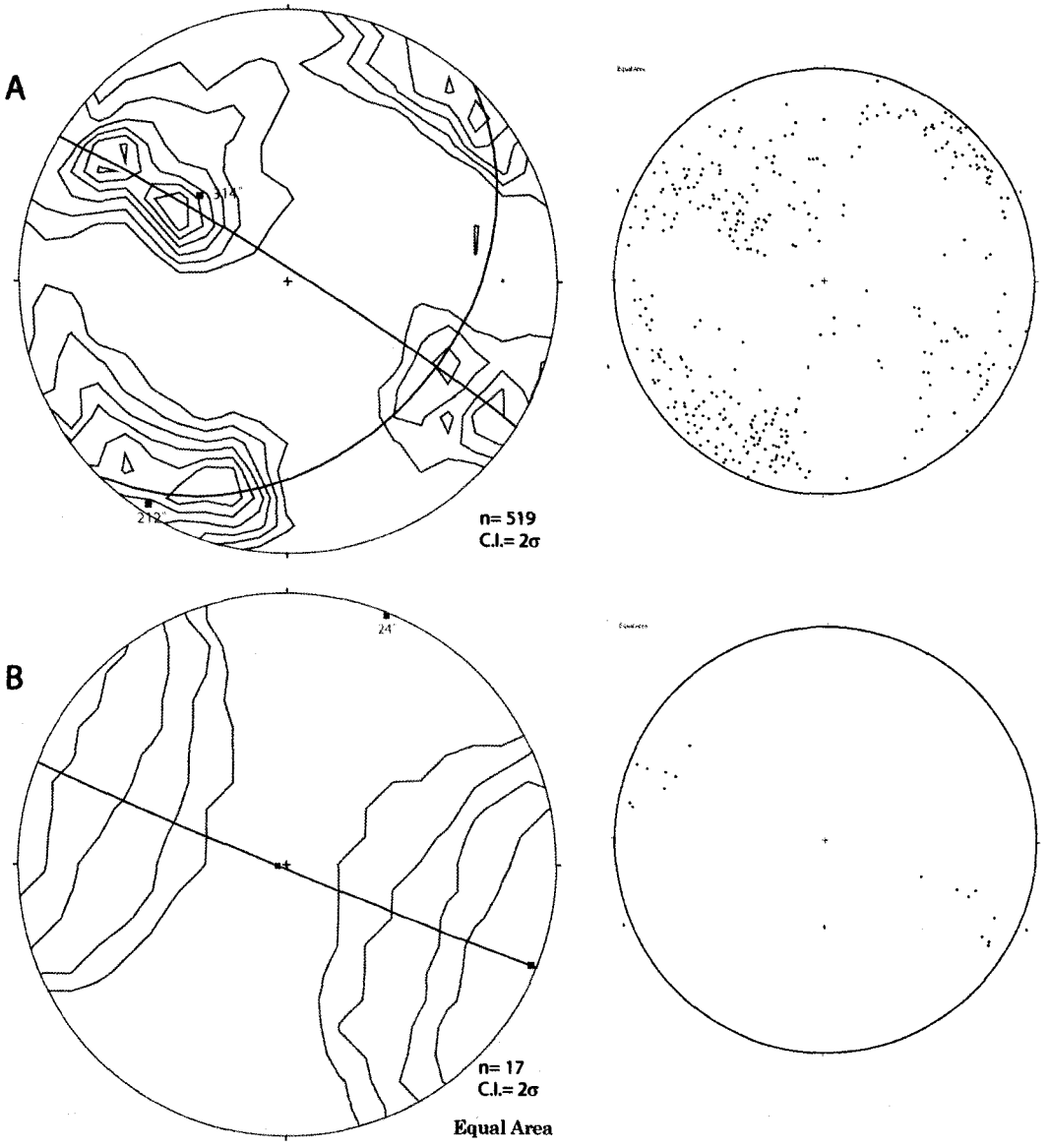

FIGURE 15. Kamb contours of poles to (A) faults at Chukar Footwall, and (B) Magpie fault. Ore controlling (NNE, ESE) and post-ore (WNW, NE) structures form a conjugate set with an angular separation of 85 degrees (Data from Newmont and this study).

sulfide grains (pyrite and marcasite) are present rimming breccia clasts and filling open spaces. Fracture density (up to 3 fractures per meter) increases toward the fault in an asymmetric fashion. This fault cuts a 55°, 74° SE small fault delineating a structural intersection zone that may have served as an important ore fluid pathway. Kinematic indicators were not found along the fault.

The **Sagehen** and **Antelope** faults (Fig. 6) are well exposed in the 4720, 4740, 4770, 4580, 4600, and 4650 mine levels. The average attitudes of the Sagehen fault are: 300°,74° SW at the 4720 level; 300°, 78° SW at the 4740 level; 305°, 70° SW at the Chukar North Decline; 303°, 80° SW at the 4580-4600 level; and ~310°, 68° SW at the 4770 level. Similarly, the Antelope fault has the following average attitudes: 285°, 73° NE at the 4740 level; 303°, 70° NE at the Chukar North Decline; and 295°, 80° NE at the 4770 level.

Observations from the 4720 mine level characterize the Sagehen fault as a damage zone of about 2 m width with multiple subparallel slip planes producing a weak to intense breccia along the contact with the $SDrm_1$ unit. The decarbonatized breccia clasts (up to 10 cm long) are supported by a friable calcite± clay (kaolinite) matrix. Subparallel to the master fault, in the hangingwall section, a high density fracture zone of about 5 m defines the Sagehen fault zone, characterized by an strongly-developed breccia. Close to the Sagehen fault, the Antelope fault is defined by a 1 m wide zone of decarbonatized breccia clasts from the $SDrm_1$ units. The gouge, less than 10 cms thick, consists of dark, gray clay, and calcite veins are absent along the fault. Kinematic indicators were observed only along the Sagehen fault at the 4770 level where fault grooves rake

70° NW indicating a dextral-oblique slip component. Locally, in the central portion of the 4740 level, normal displacement of both the Sagehen and Antelope faults produced a small horst with an up-throw of about 25 m in the $SDrm_2$ units (Joe Sagar, personal communication 2004). This structure could be linked to the last episode of extension that has been documented for Late Miocene times during Basin and Range normal faulting, when older structures were reactivated as a normal faults in the study area (Cole, 1995).

The northwest striking faults were reactivated sometime during the Eocene to Miocene extensional regime, thus serving as pathways for meteoric fluids that scavenged metals and possibly interacted with contrasting ore solutions leading to the formation of late stage barite and sulfide veins with visible gold mineralization.

The conjugate of the WNW-NNW faults is a system of high to low angle NNE/NE-striking faults, which are normally cut and offset by the former structures. These faults are characterized by breccia, variably silicified and decalcified gouge with abundant crosscutting calcite± barite veins.

The **Magpie fault** (Fig. 6 and 15B), a major feeder structure at Chukar Footwall, hosts a discontinuous calcite±barite± stibnite breccia zone along dilational jogs. Stibnite deposition postdates movements on the structure due to lack of crystal deformation. Further, late stage fractures through the fault zone controlled mineral deposition that includes orpiment, realgar, and barite. The Magpie fault at the 4720 level has average attitudes from 30°, 64° NW to 12°, 50° W. This change in attitudes may have triggered dilatation thus explaining the

drop in gold grades where the fault changes in direction. Slickensides show variable rakes of 30°WNW and 65°NW, with the steeper rake measured in the shallower dipping portion of the fault. This fault also is well exposed at the 4590 level, where it strikes 35° and dips about 70° SE. The fault is marked by a ≤ 20 cms wide, clay-poor gouge, and both weak silicification and decarbonatization around the host $SDrm_2$ units. Open spaces around the $SDrm_2$ clasts are filled with calcite± barite± stibnite. Moreover, thin sections from these faults at the 4720 level show cockade textures (reflecting dilatational, low temperature fault environments), wherein fragments of altered limestone are surrounded by fine grained quartz, calcite, and barite.

The **Contact Zone** (CZ) (Fig. 6 and 16) is a somewhat complex zone of dissolution-collapse breccias and high density of faults and veins. In the Tracker Decline, where well exposed, the CZ separates the Popovich Fm. in the hangingwall from the Roberts Mountains Fm. in the footwall. The CZ is characterized here by a ~ 26 m wide zone with several sigmoidal, subparallel splays with patchy silicification and decarbonatization in the diopside hornfels packages although some slivers of $SDrm_1$ and Dp_3 rocks are also present. It is regarded as an ore-controlling feature that caps gold mineralization at Chukar Footwall (Joe Sagar, personal communication, 2004). The main characteristic of the CZ is the continuous

TRACKER DECLINE: detail of the CZ showing brecciation stages (ST-1 and ST-2) and normal faulting (ST-3)

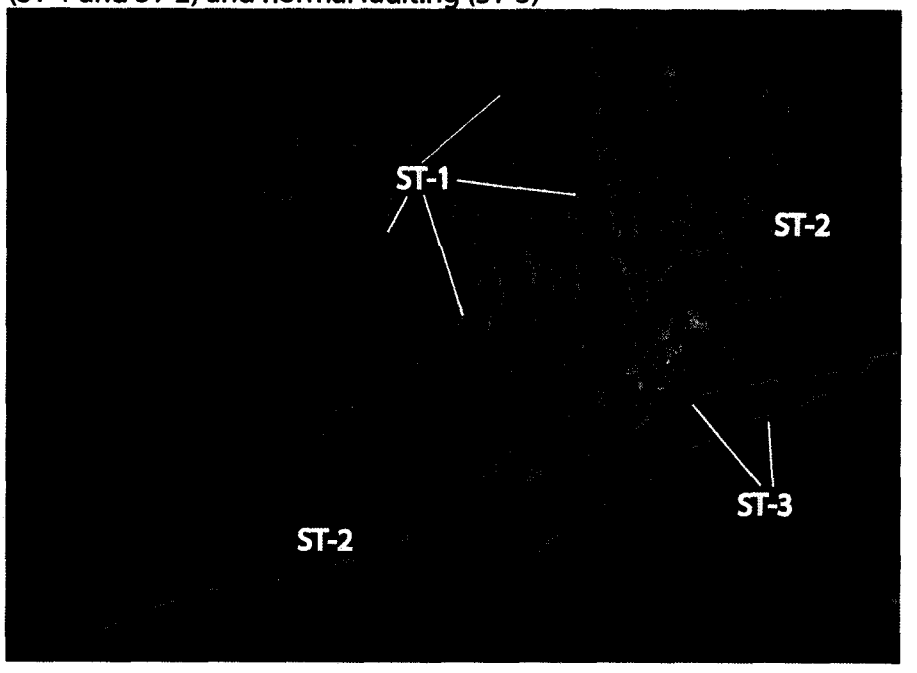

4610 LEVEL: dissolution collapse-breccia formed between the Roberts Mountains Fm. and the Popovich Fm.

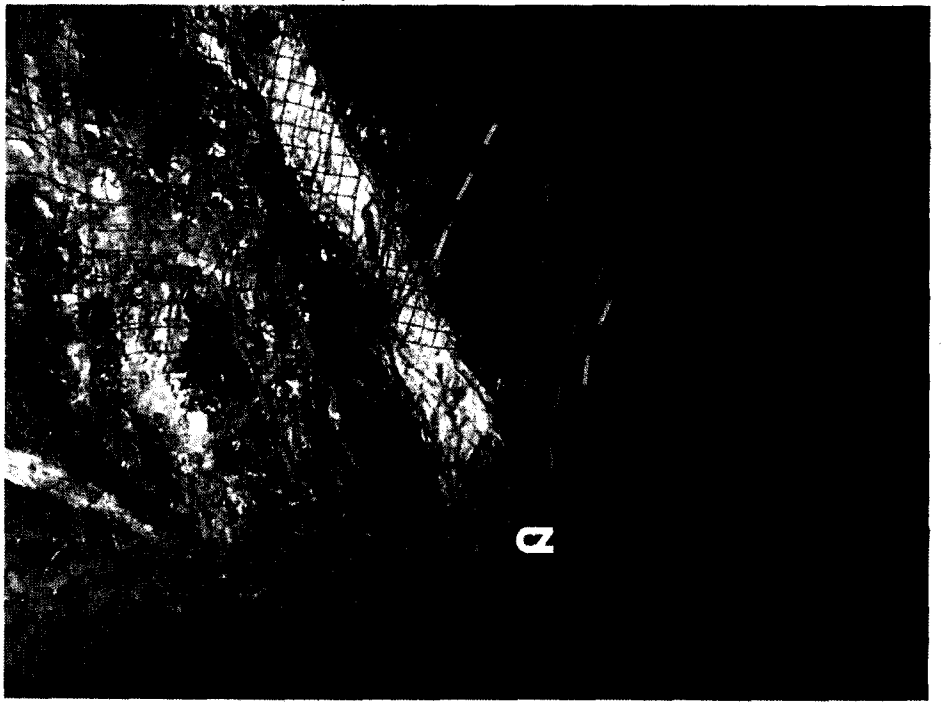

FIGURE 16. Contact Zone (CZ) at Tracker Main Decline and 4610 level. Note the attitudes of the calcite veins (yellow) in both the footwall and hangingwall sections of the CZ.

presence in the hangingwall section of a thick apron of collapse breccias with a minor component of fault breccias, and a high density of calcite veins; however, some of these attributes may be absent in some exposures thus characterizing the CZ as a small, faint structure. The CZ fault, in the Tracker Decline, contains little gouge and is locally silicified and coated with later carbonate veins and red clays. The extent of the CZ is still unknown as is illustrated in Figures 2 and 6. Several sets of orientations for the CZ faults were measured at the Tracker Decline (80°, 39° SW), 4650 level (32°, 30° SE), and the 4610 level (70°, 45° SE). The genesis of these structures seems to be linked spatially to carbonate dissolution and collapse processes during an early hydrothermal event within the the Roberts Mountains Formation (cf. Bakken, 1990; Williams, 1992; Cole 1995; Mariño, 2003).

In general, underground observations suggest that displacement along faults is rather small, a few meters at most. Faults similar to these at Chukar Footwall have been described along the Carlin trend (cf. Evans, 1980; Lewis, 2001); thus, the relative timing of folding and faulting can be constrained. The NE-trending Chukar anticline is difficult to interpret because it differs from the general NW-trending anticlinal folds along the Carlin trend. Evans (1980) described similar NE-trending folds in the Lynn Window as a result of eastward to southeastward emplacement of the Roberts Mountains allochthon during the Antler orogeny. According to Mariño (2003) and Lewis (2001) WSW-ENE shortening during the Sonoma orogeny developed multiscale regional NNW-trending anticlines such as the Post and Tuscarora anticlines. Finally, 2 main

sets of faults have been distinguished within the Chukar Footwall deposit based on cross-cutting relationships, from older to younger (Fig. 17): (1) NE-striking faults, and (2) NW-striking faults. During the Tertiary extensional regime (cf. Lewis, 2001) reactivation of these fault sets produced contradictory crosscutting relationships and oblique slip, particularly on the NW-striking structures.

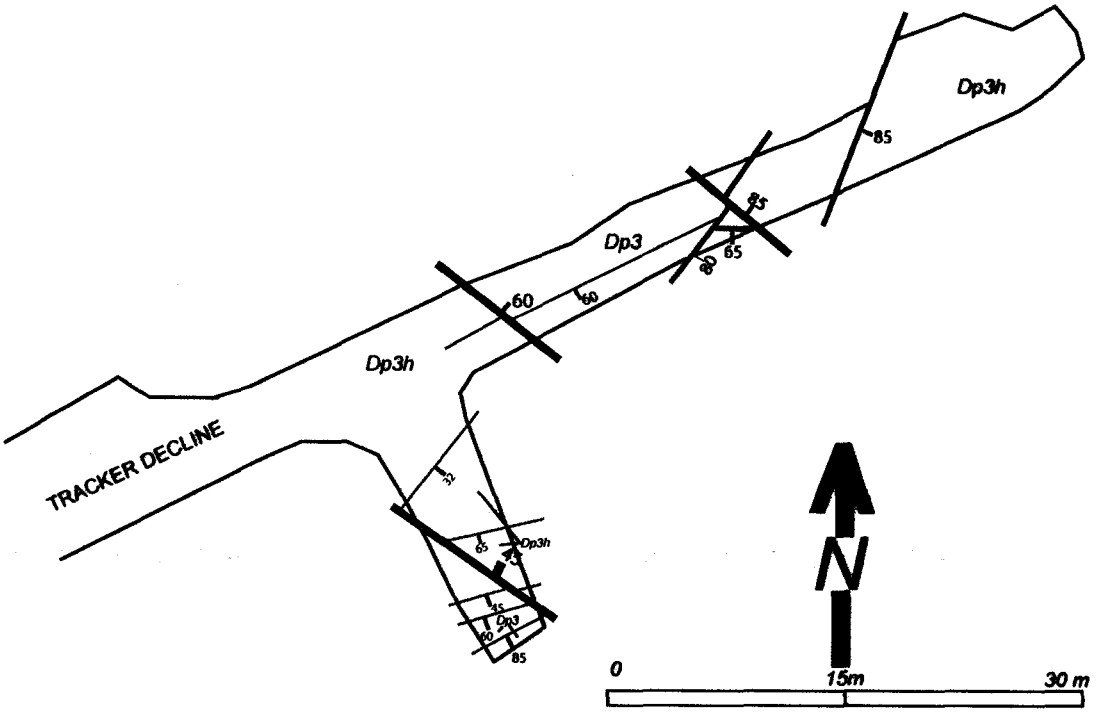

FIGURE 17. Crosscutting relationships among sets of faults at the Tracker Decline. Most of the NW-striking faults cut and offset older NE -striking faults. However, during Cenozoic extension, fault reactivation was widespread thus producing contradictory crosscutting relationships and extensive breccia. Dp3h: calc-silicate rocks.

STRUCTURAL SYNOPSIS

Stereonet data were plotted to visualize possible structural domains through mine levels (Appendix A). From these data sets, all mine levels are practically homogeneous with respect to each other, and thus the deposit statistically behaves as a single tectonic domain. From data in Appendix A several fundamental observations can be drawn: (1) The dominant fault attitudes are about 306°, 87° SW and 41°, 43° ESE-SE forming a conjugate set intersecting at 85°, and (2) It appears that faults, joints, and veins are kinematically related to a common period of stress conditions due to their spatial relationships. Firstly, during underground mapping, density in fractures and veins with similar attitudes increases toward the primary fault. And secondly, joint and vein pattern analyses revealed two dominant attitudes, which are coplanar with the major fault systems: NNE and NW-trending joints and veins with almost vertical dips.

6. GEOCHEMICAL SIGNATURES OF THE CHUKAR FOOTWALL DEPOSIT

Geochemical data were obtained from 53 samples collected during underground mapping and from a data set of mineralized intervals provided by Newmont (holes QRC 1636, QRC 1657, and QRC 1664; Apendix 6). Samples were analyzed for 31 multi-elements by ICPMS at the Newmont lab. The

selected samples were taken perpendicular to and at measured intervals from structures such as faults, joints, and veins to determine possible ore fluid pathways and to make geochemical comparisons between mine levels. Also, the geochemical data have been utilized in identifying hydrothermal alteration signatures.

Four correlation matrices of elements (Table 1,2,3, and 4) were produced using Microsoft Excel™ to contrast the geochemical signatures between the entire deposit and selected mineralized intervals within the deposit. The symbol "±" indicates that the preceding element shows variable r^2 values in the correlation matrices generated during this study. Finally, silver was deleted from the geochemical database as most of the samples have virtually nil Ag values.

As outlined by Craig and Wakefield (1991) and Rota (1991), the geochemical signatures of the Carlin trend and the Gold Quarry mine are generally depicted by a gold suite of elements (Au-As-Sb-Hg-Tl) and a base metal suite (Ag-Cd-Cu-Pb-Zn), which have been interpreted to represent several synkinematic deposit-scale mobilizations of metals from the host rock lithologies into structures (Sha, 1993).

Geochemical data from the Chukar Footwall deposit show some differences compared to those described for the Carlin trend. At the deposit scale (n= 86), Au correlates weakly (r^2 = ≤0.700) with As, Co, Cu, Fe, Hg, and Te. Ba and Sb, reflected in the ore mineralogy as barite and stibnite, show no correlation with Au. This observation, may tentatively be explained by the post-ore nature of Ba and Sb in Carlin-type deposits (Harris and Radtke, 1976; Radtke, 1985; Sha,

1993; Arehart, 1996; Heitt et al., 2003; Mariño, 2003). On the basis of their strong correlation ($r \geq 0.700$), four element suites are represented at the deposit scale by the association of (i) As-Hg, (ii) Bi-Sn-Te,(iii) Ca-Zn, and (iv) Sn-Te. However, the geochemical signature of relatively high gold grade intervals from QRC 1636, QRC 1657, and QRC 1664 holes shows that (1) Au correlates well ($r \geq 0.700$) with Cu-Hg-Tl± As± Zn, and As and Te correlate weakly with gold, (2) another elemental association is depicted by the suite of As±Sb-Te-Tl. The good correlation between As and Tl (hole QRC 1657) could be attributed to the presence of arsenic-thallium sulfosalts in the ore.

The high grade samples show a general enrichment in Al, As, Cr, Cu, Fe, Sb, Hg, Pb, Ti, and Tl and a depletion in Ba, Ca, Sr, Mo, and Zn relative to low grade/unmineralized samples. Finally, a systematic incompatible behavior pattern between Al and Ba has been noticed: as Al increases/decreases, Ba decreases/increases.

Averages for selected elements, from non-mineralized to weakly mineralized (<0.1 opt Au) wallrock samples collected during this study, are as follows: Ag (1.3 ppm), Al (2025 ppm), As (428 ppm), Ba (1385 ppm), Cu (6.3 ppm), Hg (0.8 ppm), Pb (52.2 ppm), Sb (41.9 ppm), Se (13.7 ppm), Tl (64 ppm), and Zn (265.9 ppm). Similarly, element averages (analyzed by Chemex Labs) of high grade intervals from QRC cores are: Al (2927 ppm), As (1103 ppm), Ba (294 ppm), Cu (18.2 ppm), Hg (4.9 ppm), Pb (5.8 ppm), Sb (31.5 ppm), Se (0.42 ppm), Tl (20.6 ppm), and Zn (49.1 ppm). The average As, Cu and Hg contents from cores are higher relative to the entire deposit average. However, the low

average values of the rest of the elements contrasts with the relatively higher average values obtained from the entire deposit. From an exploration standpoint, a spike in As, Cu and Hg relative to the elemental averages of the surrounding host rocks could be used as a pathfinders for targeting blind mineralized shoots.

The results of the geochemical distribution of some selected elements (As, Ba, Fe, Sb, and Tl) within the entire deposit show an overall random behavior; however, the spatial distribution of elements appears to form a continuum reflecting the influence of host rock lithology, the degree of wallrock alteration, and the relative proximity to faults. First, the SDrm rocks have heterogeneous geochemical features as is reflected by their gradational lithologies, diagenetic histories, and effects from thermal events thus introducing random or unclear geochemical distribution patterns. Second, the results of hydrothermal alteration across faults show a tabular zonation of elements. For example, transect data perpendicular to the Magpie fault on the 4720 level indicate a strong concentration of Au, As, Fe, and Sb close to the fault; away from the fault there is a sharp decrease in these elements, accompanied by an increase in Zn, and erratic behavior of Ba.

In summary, the geochemical signatures of the Chukar Footwall deposit are characterized by (1) two correlative elemental suites of Au-Cu-Hg-Tl± As± Zn and As±Sb-Te-Tl, and (2) wallrock alteration and faults are significant factors controlling tabular, metric-scale element zonations.

	Ag	Al	As	Au	Ba	Be	Bi	Ca	Cd	Co	Cr	Cu	Fe	Hg	Li	Mg	Mn	Mo	Na	Ni	Pb	P	Sb	Se	Sn	Sr	Ti	Tl	Va	Zn
Ag	1																													
Al	-0.13286	1																												
As	0.07131	0.18249	1																											
Au	-0.059209	0.113029	0.52543	1																										
Ba	0.182142	-0.419359	-0.145869	-0.180501	1																									
Be	0.330475	0.306363	0.109361	-0.159949	-0.279533	1																								
Bi	-0.032784	-0.349245	-0.14587	-0.06572	-0.078996	-0.199258	1																							
Ca	0.044096	-0.309282	-0.25634	-0.243893	-0.16644	0.266105	0.196367	1																						
Cd	-0.014746	-0.225971	-0.095625	-0.115355	-0.144268	-0.211069	**0.748989**	-0.020651	1																					
Co	-0.114406	0.111679	0.087886	0.392617	0.018465	-0.237112	-0.161959	-0.263689	-0.095872	1																				
Cr	0.145687	-0.234706	-0.116672	-0.200303	0.605614	-0.261187	-0.008221	-0.497596	0.215706	-0.002832	1																			
Cu	0.24255	-0.085182	-0.050237	0.254083	-0.091632	0.180816	0.25043	-0.166439	0.372704	0.13025	0.125026	1																		
Fe	-0.015223	0.571116	0.541862	0.340255	-0.294018	0.110185	-0.177597	-0.467452	-0.039578	0.04661	-0.080902	0.128226	1																	
Hg	-0.04601	0.180347	**0.886194**	0.443096	-0.114537	-0.034377	-0.092252	-0.23773	-0.065624	-0.029795	-0.058592	-0.05817	0.53086	1																
Li	-0.078453	0.590219	-0.100112	-0.049616	-0.137577	0.190995	-0.155069	0.087271	-0.138937	-0.035534	-0.133559	-0.013584	0.053547	-0.064436	1															
Mg	0.110951	-0.26936	-0.173348	-0.157791	-0.170202	0.282013	0.338856	0.515632	0.081542	-0.340164	-0.356816	-0.066086	-0.340162	-0.220832	-0.074731	1														
Mn	0.299947	-0.383107	-0.158556	-0.216005	-0.010602	0.288495	0.648657	0.413862	0.327879	-0.234703	-0.04829	0.154878	-0.302113	-0.185878	-0.112215	0.502326	1													
Mo	0.301342	-0.197952	0.029541	-0.104649	-0.086512	0.126839	0.526927	0.100371	0.680919	-0.140016	0.045298	0.309111	-0.013732	0.004891	-0.137557	0.324025	0.446599	1												
Na	-0.03938	0.078318	-0.030631	-0.027918	-0.07532	-0.140113	-0.06661	-0.185163	-0.05968	0.052827	0.113254	0.045532	0.025298	0.156536	0.016215	-0.195139	-0.158749	-0.04267	1											
Ni	0.327241	0.216752	0.053892	-0.047716	-0.078235	0.447189	0.022706	-0.123479	0.097783	-0.023849	0.093921	0.523433	0.5346	0.018638	-0.068574	0.033426	0.16191	0.318716	-0.008622	1										
Pb	0.016948	0.186474	0.070044	-0.015934	-0.311535	0.207247	-0.105408	0.341888	-0.177194	-0.143815	-0.350754	-0.186421	0.089635	0.019658	0.148607	0.173279	0.15277	-0.112039	-0.240846	-0.024798	1									
P	-0.035252	0.245687	-0.069995	0.019065	-0.19139	0.096987	0.204815	-0.156323	0.282685	0.066353	-0.119411	0.408757	0.476624	-0.088542	0.090158	-0.070115	0.099487	0.188343	-0.068513	0.582906	-0.049069	1								
Sb	-0.000451	0.217201	**0.732397**	0.437002	-0.051359	-0.015468	-0.151558	-0.324113	-0.105033	-0.014521	-0.001463	0.03339	0.585128	**0.772541**	-0.081148	-0.26482	-0.213044	-0.015665	-0.024525	0.138158	0.099954	-0.019255	1							
Se	0.15974	0.437507	0.46396	0.202678	-0.092649	0.423293	-0.528437	-0.146608	-0.50384	-0.049862	-0.076088	-0.020157	0.686112	0.416789	0.097845	-0.099537	-0.176111	-0.142895	-0.078265	0.527765	0.288359	0.144828	0.49595	1						
Sn	-0.07015	-0.329921	-0.141376	-0.04941	-0.123071	-0.29008	**0.828526**	0.152554	**0.734946**	-0.144365	-0.055565	0.261768	-0.156001	-0.103098	-0.184501	0.230744	0.307149	0.34891	-0.079252	-0.029084	-0.188115	0.232973	-0.175296	-0.66405	1					
Sr	0.133455	-0.019152	-0.288956	-0.353014	0.333439	0.117477	-0.127773	0.5099	-0.198434	-0.080503	-0.00738	-0.171522	-0.318411	-0.243303	0.385648	0.117212	0.13433	-0.017397	-0.155809	-0.056159	0.370283	-0.162571	-0.277526	0.052531	-0.208552	1				
Ti	-0.009619	**0.753016**	-0.043246	-0.131934	-0.202164	0.361952	-0.133099	0.016652	-0.07274	-0.093597	-0.109679	-0.083254	0.188154	-0.03291	**0.807396**	-0.016609	-0.099553	-0.001186	-0.00157	0.126568	0.096439	0.083698	-0.045231	0.217015	-0.166895	0.285139	1			
Tl	-0.032695	0.201528	**0.703346**	0.269502	0.023233	0.053559	-0.360756	-0.03275	-0.316109	0.019018	-0.042946	-0.359894	0.278757	0.69848	0.043733	-0.134499	-0.190696	-0.083698	-0.116112	-0.135709	0.173046	-0.368939	0.542176	0.511513	-0.419343	0.065115	0.173281	1		
Va	0.364184	-0.135242	0.008992	-0.176499	-0.100111	0.573152	0.421737	0.162111	0.393453	-0.222098	-0.024611	0.560324	-0.047866	-0.070439	-0.07403	0.375229	0.509572	0.637802	-0.075956	0.518091	-0.117224	0.222033	-0.073274	-0.019698	0.317918	-0.003256	0.082611	-0.234877	1	
Zn	0.104663	0.018371	-0.128853	-0.256089	-0.214205	0.44855	-0.211916	**0.770199**	-0.155041	-0.195271	-0.35083	-0.175634	-0.206318	-0.130996	0.226398	0.262958	0.206067	0.068903	-0.18121	0.015952	0.443973	-0.159165	-0.175597	0.25104	-0.32441	0.5238	0.226178	0.191882	0.064785	1

TABLE 1. Correlation matrix produced for this study. Strong correlations are in yellow.

	Au	Al	As	Ba	Be	Bi	Ca	Cd	Co	Cr	Cu	Fe	Hg	Li	Mg	Mn	Mo	Ni	Pb	Sb	Se	Sn	Sr	Te	Ti	Tl	Zn
Au	1																										
Al	-0.109669	1																									
As	0.190024	-0.741109	1																								
Ba	-0.043473	-0.287965	-0.19428	1																							
Be	-0.265314	**0.958296**	-0.818881	-0.031068	1																						
Bi	-0.112668	-0.367806	-0.297775	0.341753	-0.285714	1																					
Ca	-0.698353	-0.26667	0.532596	-0.230202	-0.220156	-0.320757	1																				
Cd	0.266734	-0.449467	**0.926947**	-0.332205	-0.565383	-0.624897	0.500897	1																			
Co	-0.487746	**0.784561**	-0.462745	-0.640355	**0.701057**	-0.280423	0.232296	-0.269343	1																		
Cr	**0.701989**	-0.546574	0.139518	0.534859	-0.52362	0.464387	-0.641717	-0.03356	-0.879792	1																	
Cu	**0.951497**	-0.394323	0.45429	0.008468	-0.532153	-0.084366	-0.504431	0.460511	-0.666673	**0.762687**	1																
Fe	-0.335695	-0.663178	**0.853198**	-0.237189	-0.677633	-0.160386	0.859776	0.724404	-0.155055	-0.234084	-0.059745	1															
Hg	-0.048273	0.015051	-0.095407	-0.662678	-0.15954	0.476183	-0.065366	-0.218502	0.398833	-0.138905	-0.087358	0.055205	1														
Li	0.407585	0.338798	-0.668582	-0.028618	0.263181	0.559259	-0.868248	-0.703526	0.086102	0.39066	0.197269	-0.788547	0.499486	1													
Mg	-0.232952	0.477874	-0.93588	0.490157	0.632458	0.508574	-0.523016	-0.970471	0.184161	0.074508	-0.430078	-0.779667	-0.020437	0.617612	1												
Mn	-0.730937	0.321114	0.100585	-0.329368	0.356348	-0.579066	0.82193	0.253609	0.641206	-0.926413	-0.704182	0.445082	-0.155311	-0.697518	-0.234475	1											
Mo	0.410596	0.038925	-0.393919	**0.821995**	0.188962	0.188982	-0.690487	-0.393648	-0.556447	0.670744	0.326231	-0.657731	-0.602543	0.348155	0.56065	-0.589256	1										
Ni	0.176263	-0.447811	**0.931544**	-0.441309	-0.579771	-0.579771	0.578987	0.986253	-0.17071	-0.127407	0.375312	**0.791671**	-0.081552	-0.700935	-0.992306	0.316357	-0.536875	1									
Pb	-0.226555	0.577897	-0.953527	0.477536	**0.731925**	0.365963	-0.508953	-0.931695	0.239457	0.004046	-0.443329	-0.813519	-0.119594	0.561833	0.987333	-0.152145	0.580948	-0.965394	1								
Sb	0.359187	-0.771706	0.98137	-0.1589	-0.866575	-0.229388	0.361883	**0.897814**	-0.568129	0.306329	0.609796	**0.752192**	-0.072789	-0.532154	-0.90736	-0.084769	-0.283221	**0.887847**	-0.934406	1							
Se	0.550738	0.375649	-0.112945	0.269023	0.380617	-0.618502	-0.426652	0.160766	-0.186784	0.215155	0.429382	-0.484297	-0.728315	-0.014608	0.039087	-0.118678	0.629386	0.016091	0.162507	-0.052816	1						
Sn	-0.697813	-0.183903	0.477681	-0.124274	-0.107143	-0.428571	**0.979767**	0.49099	0.222001	-0.655118	-0.522419	**0.783889**	-0.246921	-0.921132	-0.466736	**0.866599**	-0.566947	0.543535	-0.426956	0.301602	-0.261674	1					
Sr	-0.63721	-0.387337	0.620641	-0.243767	-0.355626	-0.249497	**0.999156**	0.550209	0.143149	-0.550659	-0.415639	**0.822068**	-0.00027	-0.850676	-0.590415	0.734982	-0.714294	0.632848	-0.594628	0.463958	-0.492353	**0.946785**	1				
Te	-0.285506	-0.544752	**0.848551**	-0.424061	-0.611933	-0.269665	**0.851482**	**0.773432**	-0.016966	-0.333371	-0.04052	0.978713	0.145627	-0.754746	-0.846877	0.49803	-0.76835	**0.852377**	-0.867943	**0.746348**	-0.458258	**0.767509**	**0.909675**	1			
Ti	-0.150841	0.439394	0.229999	-0.447946	0.367806	-0.956296	0.500005	0.541403	0.495766	-0.700298	-0.180453	0.246111	-0.341148	-0.609837	-0.462206	0.779849	-0.389249	0.537373	-0.326637	0.117243	0.408314	0.58849	0.416099	0.363168	1		
Tl	0.324643	-0.741514	**0.988679**	-0.14173	-0.825128	-0.304824	0.409688	**0.927605**	-0.548495	0.255917	0.575864	**0.767062**	-0.148705	-0.602717	-0.919589	-0.01311	-0.2781	0.911827	-0.933466	**0.995174**	-0.002334	0.365264	0.501134	**0.780846**	0.19485	1	
Zn	**0.916709**	-0.475106	0.438068	0.17725	-0.566413	0.002563	-0.515979	0.405023	-0.780641	**0.890081**	**0.984526**	-0.066757	-0.177241	0.180603	-0.354946	-0.75439	0.440762	0.306844	-0.376429	0.596272	0.429059	-0.522843	-0.425635	-0.083362	-0.277145	0.563471	1

TABLE 2. Correlation matrix for hole QRC 1636. Strong correlations are in yellow.

	Au	Al	As	Ba	Be	Bi	Ca	Cd	Co	Cr	Cu	Fe	Hg	Li	Mg	Mn	Mo	Ni	Pb	Sb	Se	Sn	Sr	Te	Ti	Tl	Zn
Au	1																										
Al	0.028945	1																									
As	0.413752	0.6973	1																								
Ba	-0.25265	-0.409567	-0.212406	1																							
Be	-0.241715	0.816889	0.508482	-0.414644	1																						
Bi	-0.519697	0.083844	0.020243	-0.043369	0.526637	1																					
Ca	-0.627343	0.176732	0.169218	0.158138	0.581877	0.914296	1																				
Cd	0.297869	0.807788	0.474031	-0.517571	0.493441	-0.435005	-0.360933	1																			
Co	0.44513	0.813876	0.631151	-0.300866	0.601103	-0.191267	-0.133555	0.838858	1																		
Cr	0.222196	-0.608913	-0.262125	0.267089	-0.889191	-0.63949	-0.612395	-0.300135	-0.5628	1																	
Cu	0.840402	0.188169	0.7394	-0.219264	-0.014255	-0.177429	-0.195644	0.188198	0.41176	0.076011	1																
Fe	0.405025	0.692625	0.622754	-0.392239	0.713492	0.061615	0.102999	0.665251	0.899141	-0.718692	0.457107	1															
Hg	0.881434	0.21384	0.403008	-0.430905	0.099486	-0.362723	-0.459491	0.486258	0.658024	-0.164981	0.712833	0.725259	1														
Li	-0.585927	0.408863	0.30706	0.104049	0.715271	0.78019	0.937876	-0.069825	0.12873	-0.71691	-0.154194	0.316619	-0.341978	1													
Mg	-0.02648	-0.306627	-0.125817	0.02505	0.021086	0.567353	0.340959	-0.609205	-0.363621	-0.120029	0.009994	-0.201468	-0.12088	0.031678	1												
Mn	-0.343396	0.203212	0.178267	-0.33445	0.673172	0.883607	0.791093	-0.226272	-0.056288	-0.66071	-0.054206	0.256128	-0.126099	0.661035	0.618963	1											
Mo	-0.053976	0.162816	0.543404	0.140363	0.263744	0.007485	0.301324	0.029339	0.028198	0.039591	0.217627	0.172054	-0.044619	0.314713	-0.00471	0.248072	1										
Ni	0.215622	0.107155	0.118961	0.533186	-0.086246	-0.352335	-0.153852	0.243224	0.476733	-0.104184	0.147268	0.358577	0.285885	0.069681	-0.573257	-0.55091	-0.074727	1									
Pb	0.582135	-0.117655	0.244535	0.045844	-0.364998	-0.752217	-0.569684	0.310385	0.225141	0.446156	0.483312	0.217798	0.545904	-0.404929	-0.621479	-0.616849	0.321365	0.491206	1								
Sb	0.416451	0.512256	0.660955	0.311204	0.281027	-0.204102	-0.004262	0.438583	0.767033	-0.301218	0.508967	0.654957	0.457119	0.207534	-0.330644	-0.24228	0.237933	0.781836	0.375694	1							
Se	0.05982	-0.407391	-0.017494	0.498741	-0.413796	0.023635	0.004735	-0.587905	-0.455921	0.485008	0.078692	-0.523314	-0.301067	-0.256393	0.665179	0.00913	0.255479	-0.279136	-0.21709	-0.083259	1						
Sn	-0.610139	0.107295	0.077049	0.004812	0.568662	0.967305	0.973358	-0.406585	-0.212018	-0.612202	-0.216556	0.065988	-0.429323	0.868858	0.458362	0.885335	0.217747	-0.329302	-0.645744	-0.182364	-0.003576	1					
Sr	-0.660011	0.296491	0.197851	0.065422	0.665108	0.843275	0.968309	-0.183127	-0.025563	-0.667412	-0.229573	0.200248	-0.423947	0.983078	0.119286	0.731806	0.299644	-0.074548	-0.471875	0.031308	-0.219804	0.92908	1				
Te	0.274879	0.587228	0.786022	-0.331534	0.614401	0.499133	0.474692	0.210957	0.512256	-0.579636	0.6588	0.632795	0.360122	0.539224	0.144149	0.520787	0.150068	0.001799	-0.142677	0.457518	-0.170355	0.456048	0.473427	1			
Ti	-0.222116	0.817778	0.405102	-0.298043	0.956497	0.463024	0.491935	0.519751	0.679947	-0.922019	-0.099359	0.716977	0.11383	0.633562	0.034488	0.556261	0.094682	0.054358	-0.430079	0.371368	-0.376852	0.464209	0.560837	0.523649	1		
Tl	0.816237	0.490301	0.762224	-0.437476	0.191594	-0.42083	-0.384627	0.653066	0.717087	-0.049786	0.853994	0.688672	0.833381	-0.197466	-0.355287	-0.197057	0.210876	0.260034	0.626986	0.586909	-0.2837	-0.419661	-0.307296	0.54279	0.128151	1	
Zn	0.167737	-0.216207	-0.123973	0.715446	-0.527092	-0.664201	-0.450758	0.052318	0.091475	0.437241	-0.021745	-0.142812	0.022594	-0.32239	-0.524741	-0.847483	-0.014238	0.808193	0.563053	0.503838	0.101407	-0.617339	-0.4222	-0.456796	-0.381272	0.047116	1

TABLE 3. Correlation matrix for hole QRC 1657. Strong correlations are in yellow.

	SiO2	Al203	Fe	MgO	CaO	K2O	TiO2	P2O5	QTZ	DOL	CAL	ILL	PYR	RUTL
SiO2	1													
Al203	0.049054	1												
Fe	0.218172	0.975554	1											
MgO	-0.547055			1										
CaO	-0.60843			0.959171	1									
K2O	-0.187834	0.969443	0.914998	-0.703627	-0.657196	1								
TiO2	-0.161061	0.975792	0.907419	-0.736454	-0.655282	0.990925	1							
P2O5	-0.425258	0.882971	0.779097	-0.520514	-0.440443	0.965428	0.960784	1						
QTZ	0.937794	-0.20698	-0.007161	-0.277518	-0.413907	-0.408158	-0.415657	-0.631933	1					
DOL	-0.698476	-0.744164		0.981128	0.962332	-0.559547	-0.592835	-0.347524	-0.455196	1				
CAL	0.343542	0.945042	0.953892			0.836813	0.868575	0.697097	0.05461	-0.91177	1			
ILL		0.364771	0.159312	0.082695	0.255756	0.530945	0.558462	0.730297	-0.975441	0.266485	0.138842	1		
PYR	0.483298	0.885049	0.917617			0.743945	0.781121	0.57735	0.199007	-0.963087	0.987878	0	1	
RUTL	-0.425258	0.882971	0.779097	-0.520514	-0.440443	0.965428	0.960784	1	-0.631933	-0.347524	0.697097	0.730297	0.57735	1

TABLE 4. Semiquantitative X-Ray Fluorescence Analysis correlation matrix for hole QRC-1664 (high grade intervals). Strong positive and negative correlation in yellow and blue, respectively.

7. HYDROTHERMAL ALTERATION

The Chukar Footwall mine exhibits hydrothermal alteration assemblages typical of Carlin-type gold deposits: (a) decarbonatization, (b) silicification, (c) dolomitization, (d) argillization, and possibly (e) baritization. Arehart (1996) evaluated the hydrothermal alteration in the Carlin trend and concluded that there is a general spatial pattern of wallrock alteration that can be characterized by distal, volumetrically extensive decarbonatization that envelopes silicified and argillized zones adjacent to the gold mineralization. With regard to temporal relationships between these alteration types, recent work by Harlan et al. (2002) summarized wallrock alteration paragenesis in the Maggie Creek district typified, from oldest to youngest, by decalcification →dolomitization- sericitization→ argillization→ sulfidation→ supergene weathering.

At Chukar Footwall, the hydrothermal alteration was initiated by a **decarbonatization** event(s) along faults, faults zones, joints, and bedding planes. Such structures fully control the extent of decalcification producing sharp boundaries between altered and fresh rocks, a distinctive trademark of this deposit relative to the Carlin mine and other deposits (Mike Robinson, personal communication, 2004). The degree of decarbonatization is accompanied by variations in the amount of calcite veins and stockworks, stylolites, and brecciation. Multistage white calcite veins range from a

millimeter up to a meter wide, and they are usually concentrated within the hangingwall of structures and along bedding planes.

Following decarbonatization, a selective, fracture controlled **hydrothermal dolomitization** and silicification took place within the SDrm and Dp units (Fig. 18). The spatial extent of this alteration event is unknown; however, stained carbonate samples document a volumetrically small dolomitization stage on the deposit scale. Transitions from calcite to ferroan calcite to ferroan dolomite are either fracture controlled or selective; typically, the dolomitized rocks are cut by calcite or barite veinlets. District wide dolomitization has been ascribed to form as hydrothermal fluids were focused along major and minor structures diffusing throughout the rocks and producing a dolomitization front of limited extent (e.g. Stenger et al., 1998). **Silicification**, much easier to detect than dolomitization, represents the second main hydrothermal alteration stage characterized by microcrystalline silica flooding replacing the silty limestones units (jasperoids) and breccia bodies with variable degrees of silica content. Quartz veinlets are common, and they crosscut at a high angle the stratigraphy and earlier calcite veins. Silicification processes are volumetrically important toward the deeper levels of the mine, associated with the CZ and NE-striking structures. Similar precipitation mechanisms responsible for silica precipitation in Gold Quarry were also operating in Chukar Footwall as determined by analogous mineralogical patterns at Gold Quarry characterized by an early

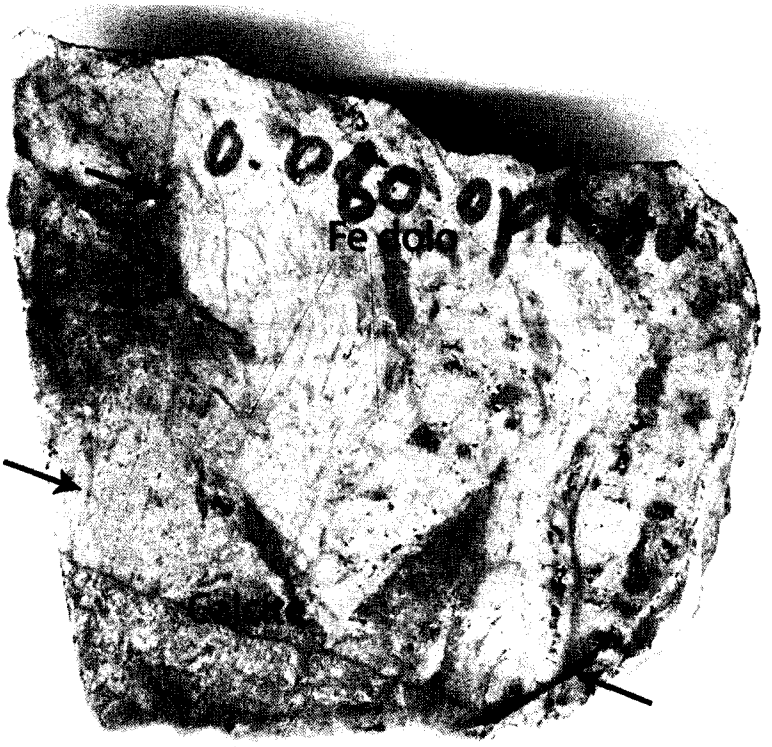

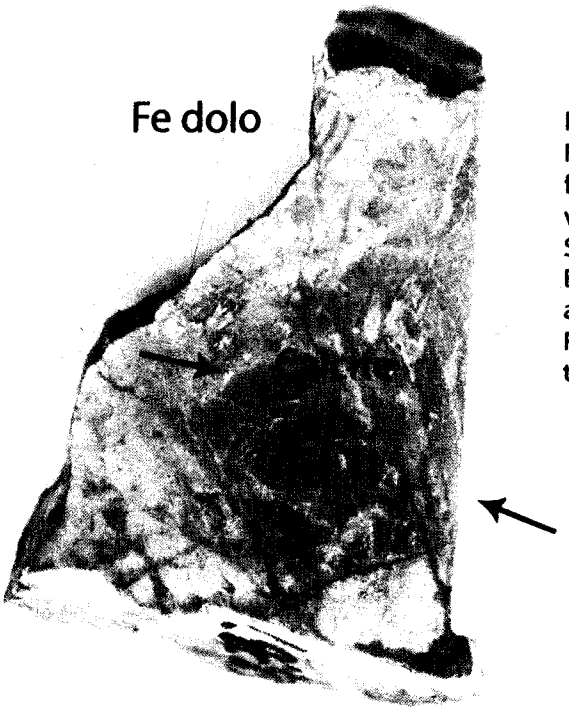

FIGURE 18.
Fracture-controlled hydrothermal ferroan dolomite (light color) exhibiting veinlets cutting calcite (dark pink). Stained samples from the Tracker Exploration drift (18583E,15638N), near a high-angle NE-striking fault. Pyrite grains are abundant along and near the fractures (arrows).

microcrystalline silica replacement, followed by barite precipitation in small veinlets (Harlan et al., 2002). Similarly, silicification is structure-controlled, and there is evidence for multistage events of hydrothermal quartz. For example, sample 169 from the 4680 level was taken in the hangingwall section of a 50°, 70° SE structure producing strong decalcification and patchy silicification in the $SDrm_2$ host rocks. In thin section, cockade textures with clasts of $SDrm_2$ are common in a matrix of dolomite±fine sericite±barite. Two silicification events surround the clasts: qtz_1 presents granular texture, while qtz_2 occurs in jigsaw texture.

Argillization has only been observed in the 4720 level, in the vicinity of the Sagehen fault zone, and in the Raven dike in both the 4590 and 4710 levels. It is a localized type of alteration due to its structural control, and is difficult to identify during underground mapping in the SDrm units. In thin section, kaolinite±dickite± sericite overprint the SDrm matrix. In some intervals, the dike presents strong argillization occurring as a pale-green gummy oxidized mass. In less altered samples, phenocrysts are replaced by kaolinite and sericite.

The final main stage of alteration is represented by a widespread barite flooding and veining, apparently associated with subparallel NNW marcasite-pyrite and calcite veinlets. What is striking about this late stage is the presence of abundant, visible gold flecks associated with late barite veinlets on the 4730 level. Associated with this late stage, hydrothermal **dedolomitization,** the replacement of dolomite by calcite, has been reported

by Williams (2002) in samples from the 4730 level as calcite incipiently replaces diagenetic or hydrothermal dolomite.

8. PETROGRAPHY AND PARAGENESIS

All the mine levels and specific core intervals were sampled to obtain material for petrography, geochemistry, stable isotopes analyses, and fluid inclusion microthermometry. Petrographic studies of 50 thin sections and several hand-sample specimens were conducted to (1) identify and quantify the major ore phases, (2) document the spatial and temporal relationships among mineral phases, and (3) describe the alteration paragenesis. Finally, petrography was augmented through XRD and SEM analyses of selected samples, and thin section billets were stained with a solution of alizarin red S stain and potassium ferricyanide stain for rapid carbonate identification.

In general, the paragenetic sequence at Chukar Footwall involves three main paragenetic stages (Fig. 19), where ore textures reflect crystallization in open spaces mainly consisting of comb, cockade, and vug filling textures. Also, decarbonatization and brittle movements produced extensive breccia textures (Appendix 6)

The first stage is characterized by both diagenetic sulfides (pyrite) and a metasomatic suite as a result of the emplacement of a hitherto unknown blind plutonic body and the Raven dike producing an aureole of diopside hornfels (exoskarn) in the SDrm

GENERAL PARAGENETIC SEQUENCES OF MINERAL DEPOSITION FOR CHUKAR FOOTWALL MINE

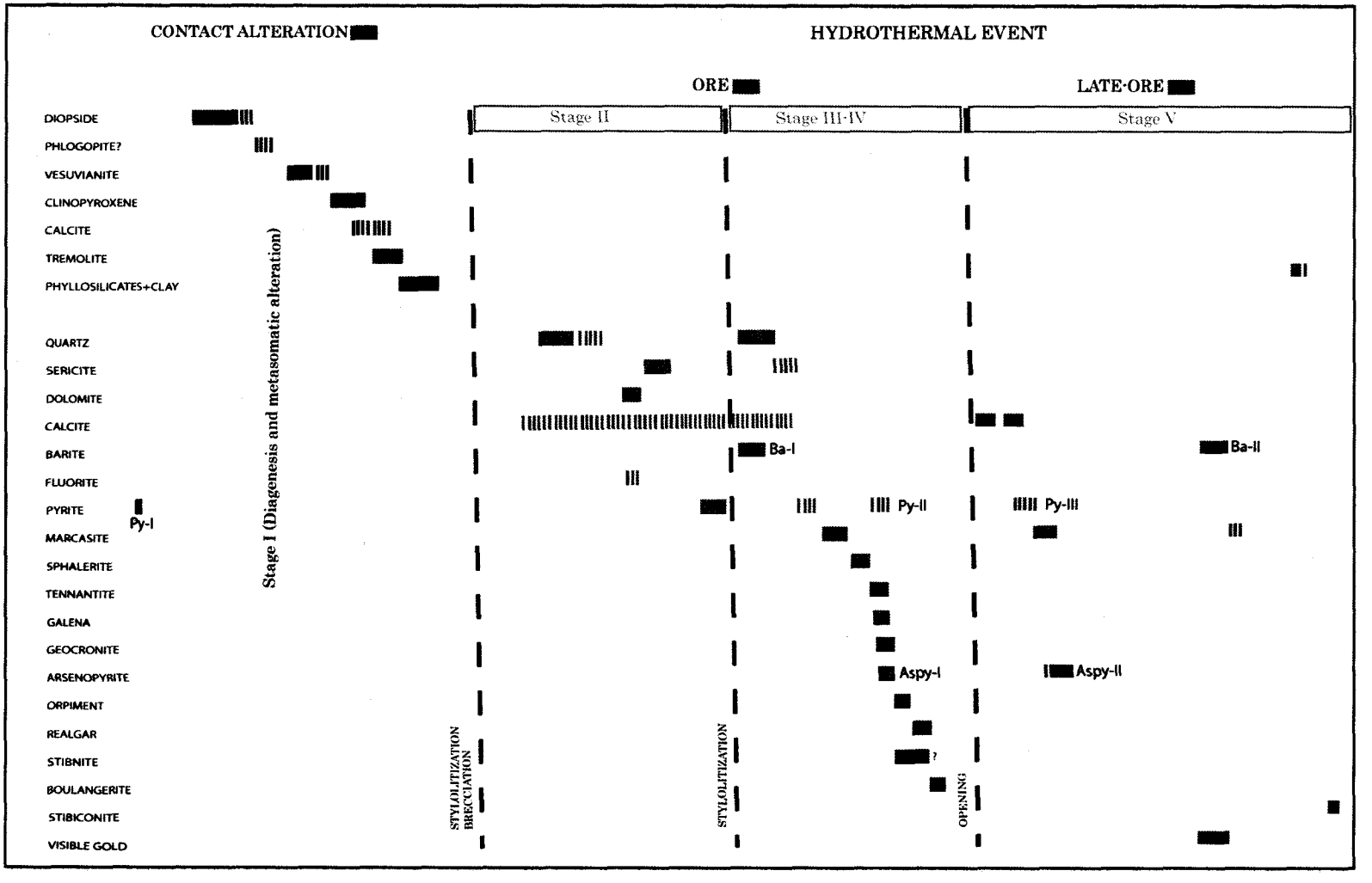

FIGURE 19. Paragenetic sequence of mineral deposition for Chukar Footwall Mine. Note that micron gold was not identified during petrographic studies and therefore not included in the paragenetic sequence.

and Dp units. This exoskarn assemblage is composed of biotite/phlogopite ± clinopyroxene± vesuvianite (idocrase) ± tremolite±quartz±calcite±K-feldspar. These minerals are in most of the samples replaced by fine phyllosilicates and clays.

The second, third, and fourth stages represent ore hydrothermal events dominated by ore stage quartz±carbonates±sericite/clay±barite±pyrite±Sb and As minerals. A late-ore stage (stage V) is characterized by sulfides±calcite±barite ±visible gold±quartz and small oxidation products.

PETROGRAPHY OF METASOMATIC METAMORPHIC ROCKS

The exoskarn assemblage (diopside hornfels, Figs. 20 and 21) is characterized by both a fine to medium grained granoblastic texture and porphyroblastic texture. In hand samples, these rocks are gray to greenish in color. In same cases, a weak fabric is produced by vesuvianite porphyroblasts, and later hydrothermal events produced a moderate overprinting alteration on the exoskarn mineralogy.

Diopside (5-25 %) occurs as an anhedral, interlocking grains in a granoblastic texture making up the matrix with granoblastic calcite, phlogopite (?), K-feldspar, and opaques. In most of the cases, **vesuvianite** (1-15 %) is present as (1) euhedral laths, (2) radiating aggregates,(3) and subhedral-euhedral porphyroblasts producing a visible fabric of light green millimetric porphyroblasts. Vesuvianite is altered pervasively to grid texture phyllosilicates and carbonates. **Tremolite** (3-10 %), locally abundant, occurs as individual laths and bow-tie

textures. In the same way as vesuvianite, tremolite is also altered to either phyllosilicates or clays. **Calcite** (20 %) forms fine to medium grained anhedral grains that make up the matrix of the pyroxene hornfels. Also making up the matrix mineralogy, anhedral **K-feldspar** grains (≤ 1 %) with ragged boundaries occur as interstitial grains, showing normal to undulose extinction.

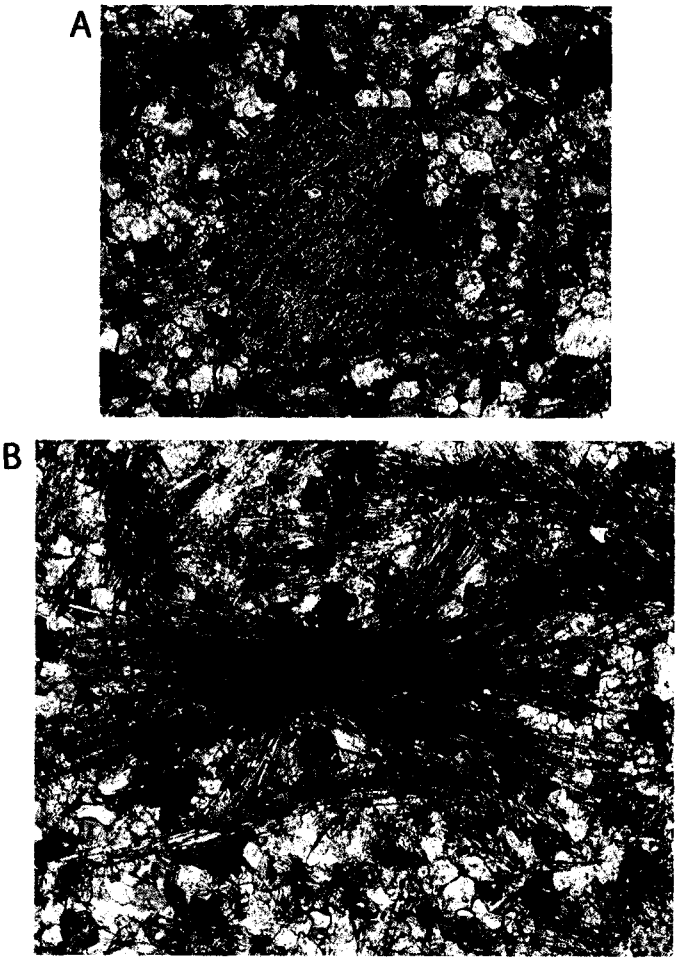

FIGURE 20. Photomicrographs of the diopside hornfels exoskarn. (A) Porphyroblast of vesuvianite, a calcium magnesium aluminosilicate hydroxide, altered to talc and chlorite, (B) Radiating aggregates of vesuvianite. Crossed nicols. FOV: 0.21 mm.

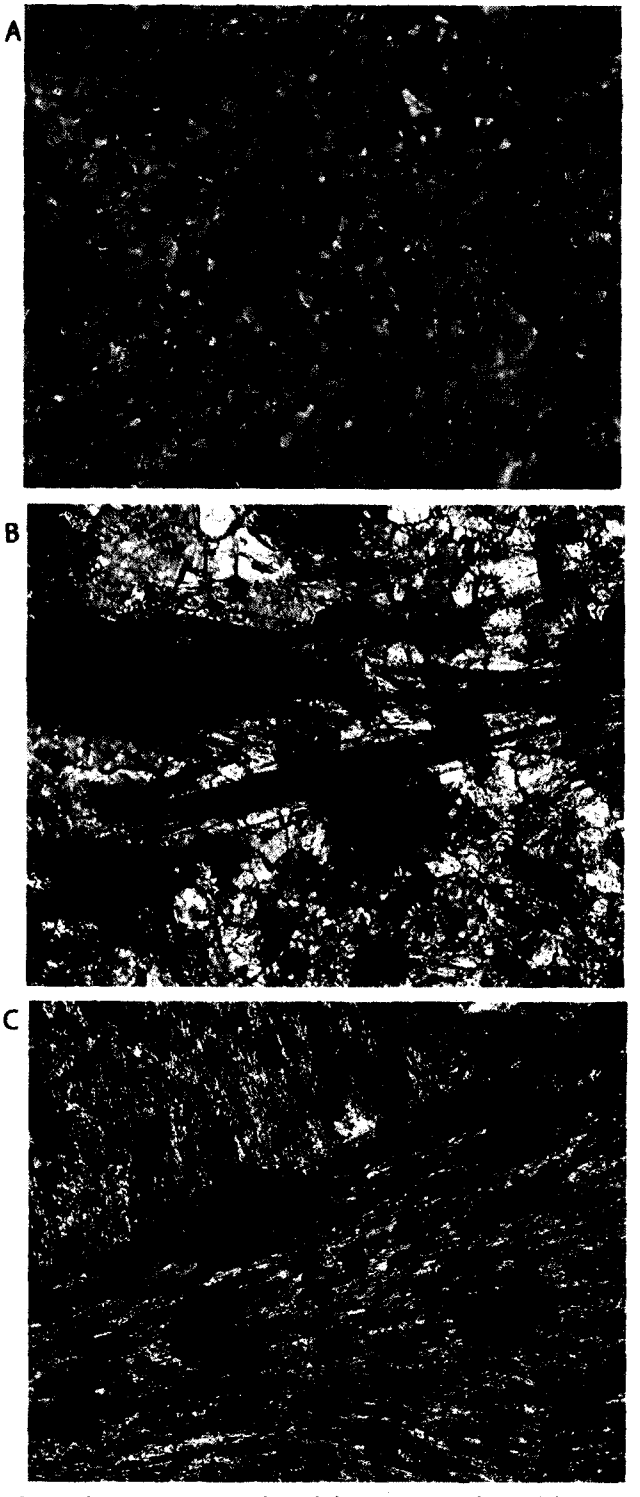

FIGURE 21. Photomicrographs of the diopside hornfels exoskarn.
(A) Diopside hornfels containing equant anhedral grains disseminated in calcite and K-feldspar, (B) Radiating crystals of tremolite postdating the skarn matrix mineralogy, (C) Fibrous phyllosilicates and chlorite overprinting the pyroxene hornfels as a result of a low temperature hydrothermal episode (retrograde metamorphism). Crossed nicols. Field of view: 0.21 mm.

CARLIN-STYLE ORE FABRICS

Pyrite (Figs. 22 and 23) is the most common sulfide in the deposit, making up to ~ 4 volume percent of the rock. It occurs as (1) aggregates of euhedral to subhedral grains, (2) poikiloblastic, ragged, ratty grains, and (3) disseminated grains within stylolites (pyrite stylolites) and wispy textures on the SDrm. Framboidal pyrite, however, was not identified petrographically. SEM analyses of several pyrite grains indicate that this sulfide is rather homogenous in composition regardless of morphology and paragenetic stage; no zonation was recognized within crystals. Also, SEM examination failed to detect any submicron arsenian-rich rims and gold particles in pyrites. On the other hand, most pyrite grains contain minute inclusions of quartz±zircon± opaque minerals producing distinctive growth patterns.

At least three generations of pyrite may be distinguished on the basis of occurrence and optical properties. Py-I occurs as euhedral (Fig. 23A) to subhedral cubic aggregates disseminated in carbonaceous stylolites or along the margins of stylolites (Fig. 23C) and wispy-textured silty limestone. Commonly euhedral, brassy pyrite cubes define bedding-controlled sulfide laminae in the SDrm lithologies. These observations indicate that Py-I could be a product of an early (diagenetic) sulfidation event. Py-II, in contrast, exhibits large inequigranular, disseminated euhedral to anhedral grains (Fig. 23B). Two subtypes of pyrite may be observed: relatively older, high reflectivity pyritohedron grains, and relatively younger subhedral to anhedral, low reflectivity, and porous pyrite grains. In addition, euhedral to

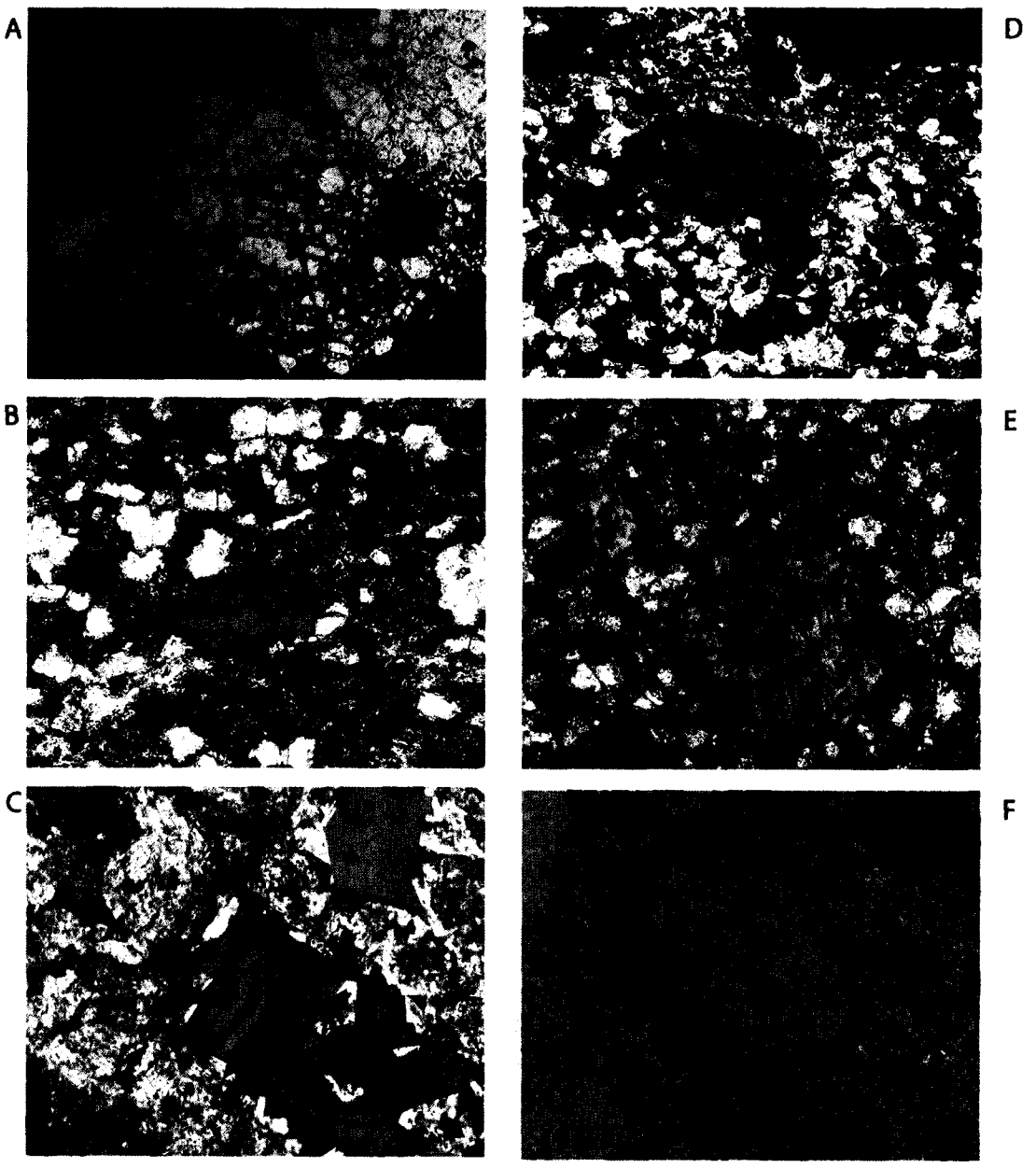

FIGURE 22. Reflected light polished sections of pyrite. (A) anhedral pyrite grains in an atoll structure;(B) Pyrite grain displaying a ratty-texture in strongly altered SDrm; (C) Anhedral pyrite grains from high ore grade sample displaying arsenopyrite lamellae ; (D) Pyrite grain partially enclosing realgar; (E) Ratty-texture of pyrite. Note the sulfide association with carbonaceous matter (dark); and (F) Euhedral pyrite grain partially fragmented due to its proximity to a later calcite vein. FOV:0.21 mm. Reflected light.

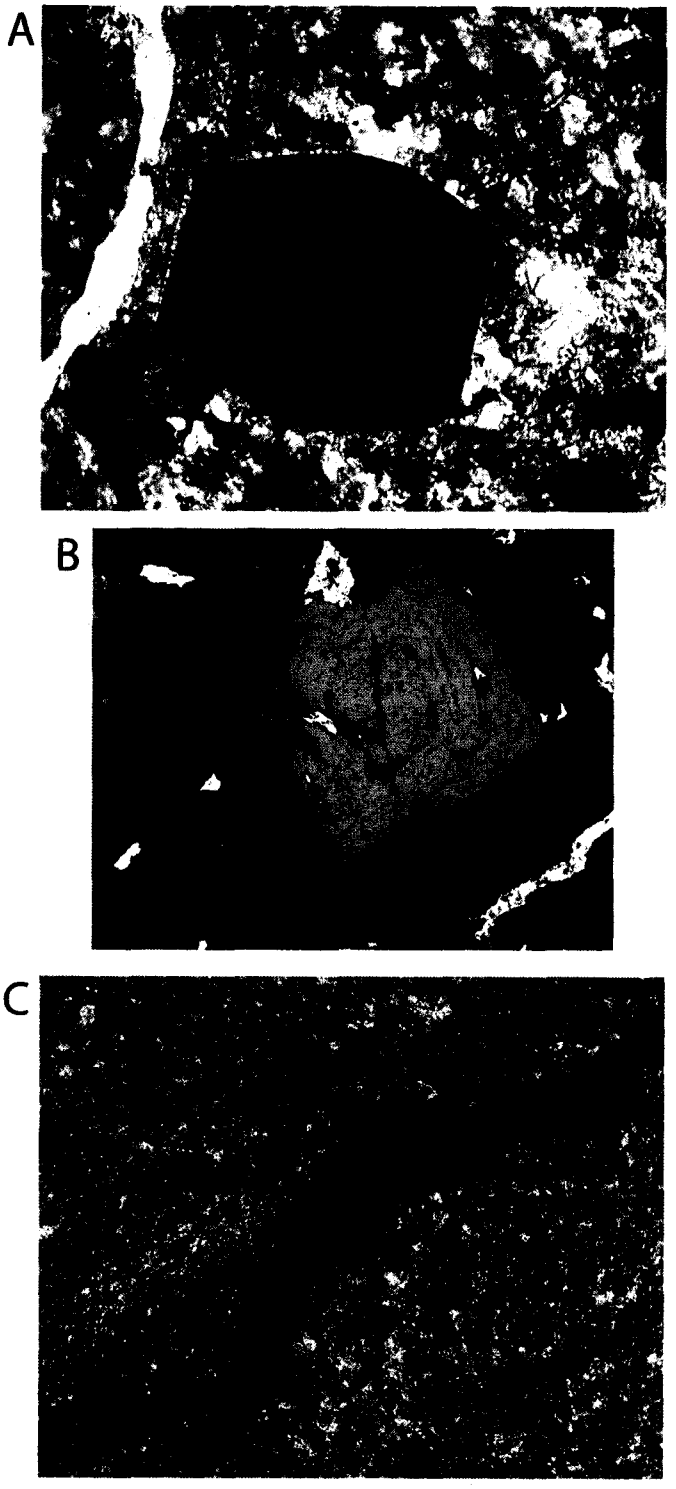

FIGURE 23. Common modes of pyrite occurrence : (A) Isolated diagenetic pyritohedron with abundant inclusions (Py-I), (B) Late subhedral cube replacing iron-poor sphalerite (Py-II), and (C) Pyrite stylolites consists of anhedral, pitted grains of pyrite associated with carbonaceous matter along the stylolite. Reflected light. FOV: 0.67 mm.

subhedral Py-II grains replace sphalerite. This stage may represent the ore stage on the basis of (1) the spatial relationship with quartz+sericite+pyrite alteration (i.e., Sha, 1993; Leach, 1999); and (2) some Py-II idioblasts are fractured and filled with late carbonate veinlets. Finally, Py-III is relatively coarse, euhedral to anhedral, and present in veinlets cross-cutting earlier minerals and bedding. This late-ore stage is also observed associated with marcasite along some WNW-striking structures and veinlets suggesting mild oxidizing conditions during Py-III deposition.

Marcasite (Fig. 24) occurs as ≤3 mm botryoidal aggregates in open spaces on WNW-striking structures (i.e., Crown fault and the Sulfide vein at the 4730 level). This sulfide is rare at deposit scale (< 1 %), but it may be abundant locally in the exoskarn as bladed idioblasts replacing sphalerite.

Arsenopyrite (Fig. 24) was observed as idioblasts associated with veinlets of sphalerite, marcasite, and pyrite in the exoskarn. It appears as pseudo-rhombic crystals disseminated in the veins and host rock, making up ≤1 volume percent of the rock. Relatively late to pyrite or cogenetic with it, arsenopyrite also occurs as replacement lamellae in Py-I grains. Also, this sulfide occurs as corroded star-like shapes associated with the base metals mineralization (Aspy-I) and late-ore mineral (Aspy-II) with barite+calcite+visible gold at the 4730 level.

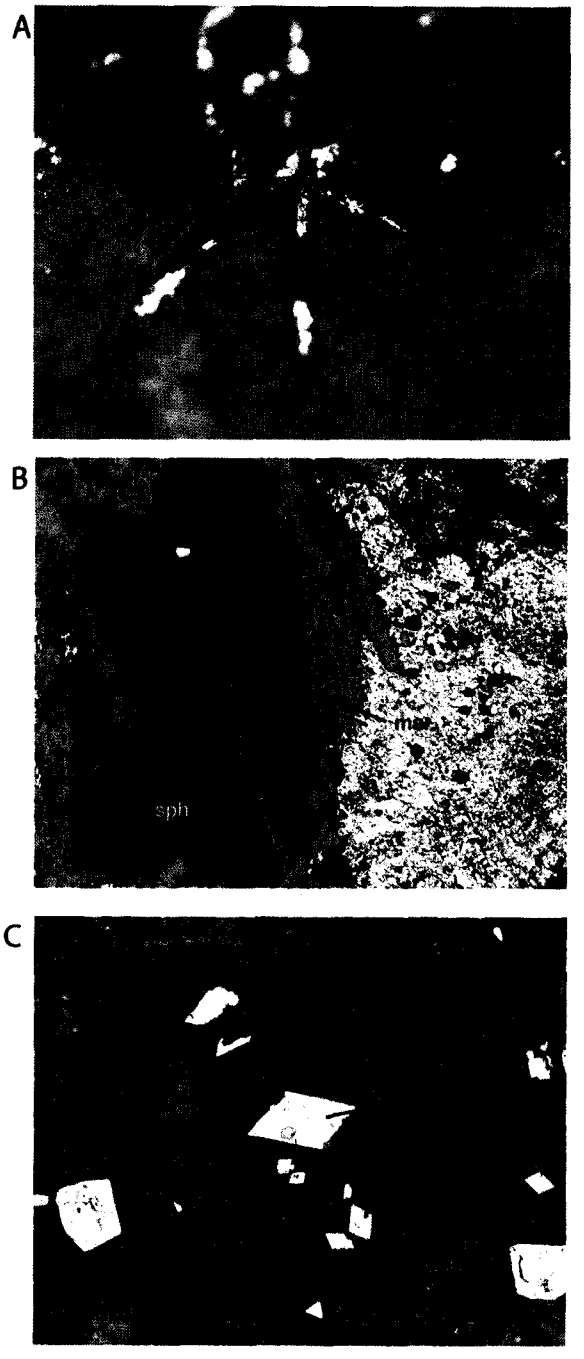

FIGURE 24. Sulfide occurrences at Chukar Footwall: (A) Late-stage star-like arsenopyrite crystals from the 4730 level, (B) Marcasite blades partially replacing sphalerite (base metal suite), and (C) Pseudo-rhombic disseminated arsenopyrite crystals from the ore-stage base metal suite. B and C from the 4400 level. Reflected light, FOV: (A) 2.5 mm, (B) and (C) 0.67 mm.

Orpiment and Realgar (Fig. 25) are rare minerals at Chukar Footwall. Limited material from a NE-striking structure with Sb and As sulfides at the 4600 level was donated by Joe Sagar for examination. Both orpiment and realgar occurs macroscopically as fine grains in veinlets in decarbonatized SDrm. Orpiment is cut and partially replaced by a later realgar veinlet. Away from the veinlets, interstices between the grains are filled with very fine realgar. Due to the inaccessibility of this level, no crosscutting relationships between these sulfides and stibnite can be made.

Sphalerite (Fig. 25) is a major ore mineral observed in the exoskarn (~ 25 volume percent of the total sulfide), where it occurs as isolated tetrahedrons and small fine-grained veinlets within other sulfides. Sphalerite is replaced by minute inclusions of **tennantite, galena,** and **geocronite-guettardite** (Pb_{14} $(Sb,As)_6$ S_{23}, Pb $(Sb,As)_2$ S_4) as observed in SEM photomicrographs (Fig. 26). Sphalerite exhibits a zonal distribution of Fe poor and rich layers. It's rimmed and partially replaced by euhedral-subhedral pyrite (e.g., some pyrite idioblasts contains relics of sphalerite).

Stibnite (Fig. 26) is relatively abundant (up to 25 % of the ore) in the 4590 and 4740 mine levels, spatially associated with NE-striking structures. Under the microscope, stibnite occurs as anhedral, highly anisotropic grains filling voids in brecciated zones commonly showing lamellae extinctions and undulose extinction.

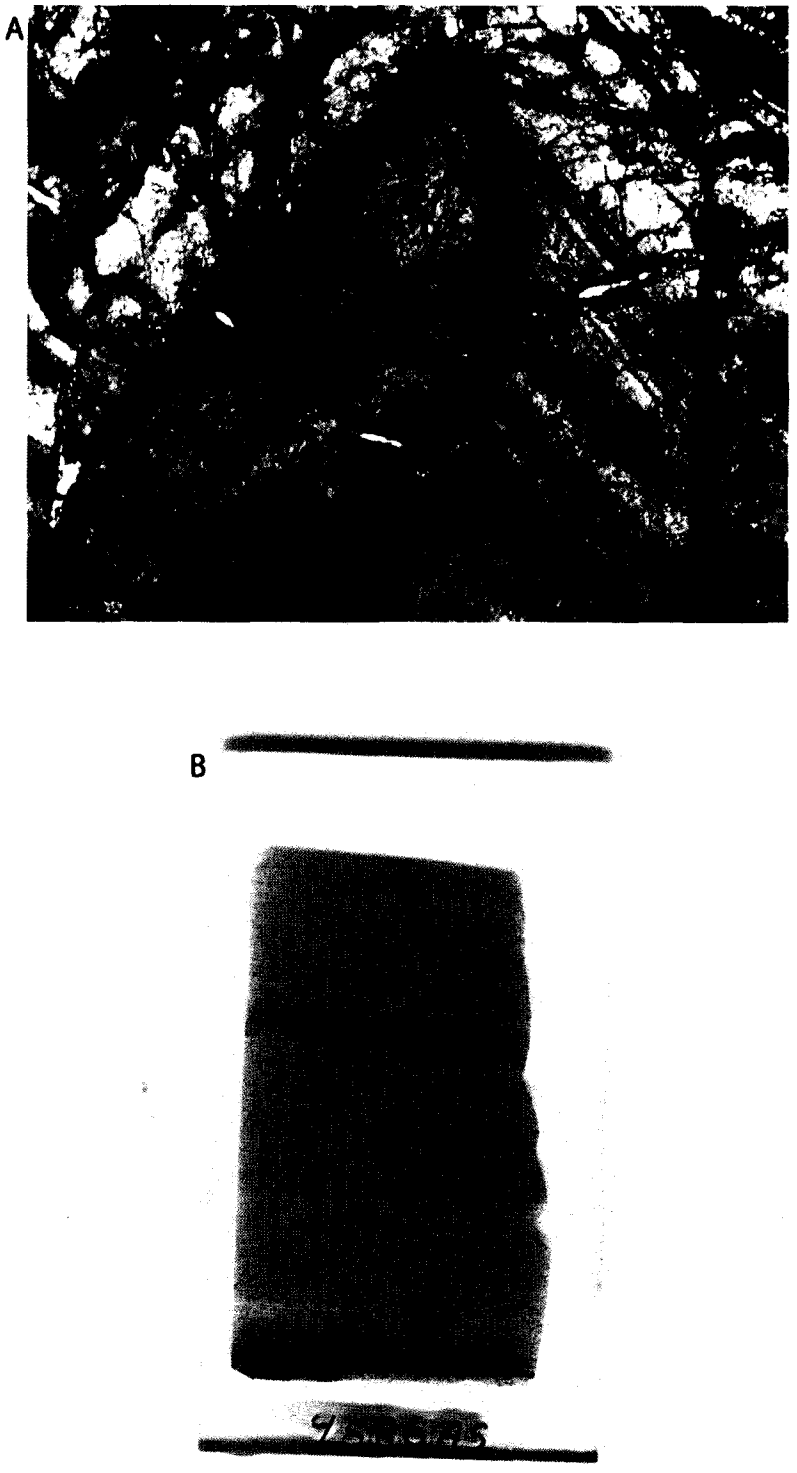

FIGURE 25. Sulfide ocurrences at Chukar Footwall: (A) Sphalerite dislaying iron poor and rich growth layers. Note extensive late fractures filled with quartz (base metal suite, 4400 level) Crossed nicols, FOV: 0.67 mm
(B) Stratiform orpiment in SDrm rocks. Late realgar veins cut and partially replace orpiment.

Boulangerite, $Pb_5Sb_4S_{11}$, was noted during SEM examination partially replacing a stibnite grain (sample 23, 4590 level). Also, stibnite is locally abundant in the 4590 level, forming thin veinlets in decarbonatized SDrm. It is partially oxidized to a yellowish coating of **stibiconite**, $Sb^{+3}\ Sb_2^{+5}(OH)$.

Barite can occur as prismatic, rhombohedral crystals associated with silica stages within fractures and veins (Ba-I stage). The other barite stage (Ba-II) is associated with Fe sulfides, carbonates, and visible gold. It may be locally abundant (up to 5 %) as subhedral to anhedral crystals filling veins and vugs. On the 4730 level, barite appears as massive to millimetric tabular crystals containing visible **gold**, suggesting that both minerals are cogenetic. Cross-cutting relationships suggest that Ba-I precipitated earlier than stibnite in the Magpie fault (sample 203, 4740 level).

Carbonates, in general, consist of **calcite** and **dolomite** (Fig. 27), which are locally abundant (up to 20 %). Calcite occurs as a major constituent in the exoskarn mineralogy, wherein it has been recrystallized producing equigranular coarse-grained calcite grains showing typical triple junctions between grains. On the scale of the deposit, calcite occurs as multistage veins and veinlets cross-cutting decarbonatized SDrm and Dp units. Calcite grains range from fine to coarse sizes that exhibit intense and colorful twin lamellae. Rarely, some calcite grains from the exoskarn have kinked twin lamellae as a result of local shearing phenomena. Calcite rhombs are generally observed as clusters of coarse aggregates with inclusion zoning. Macrocrystals of calcite are typically honey to

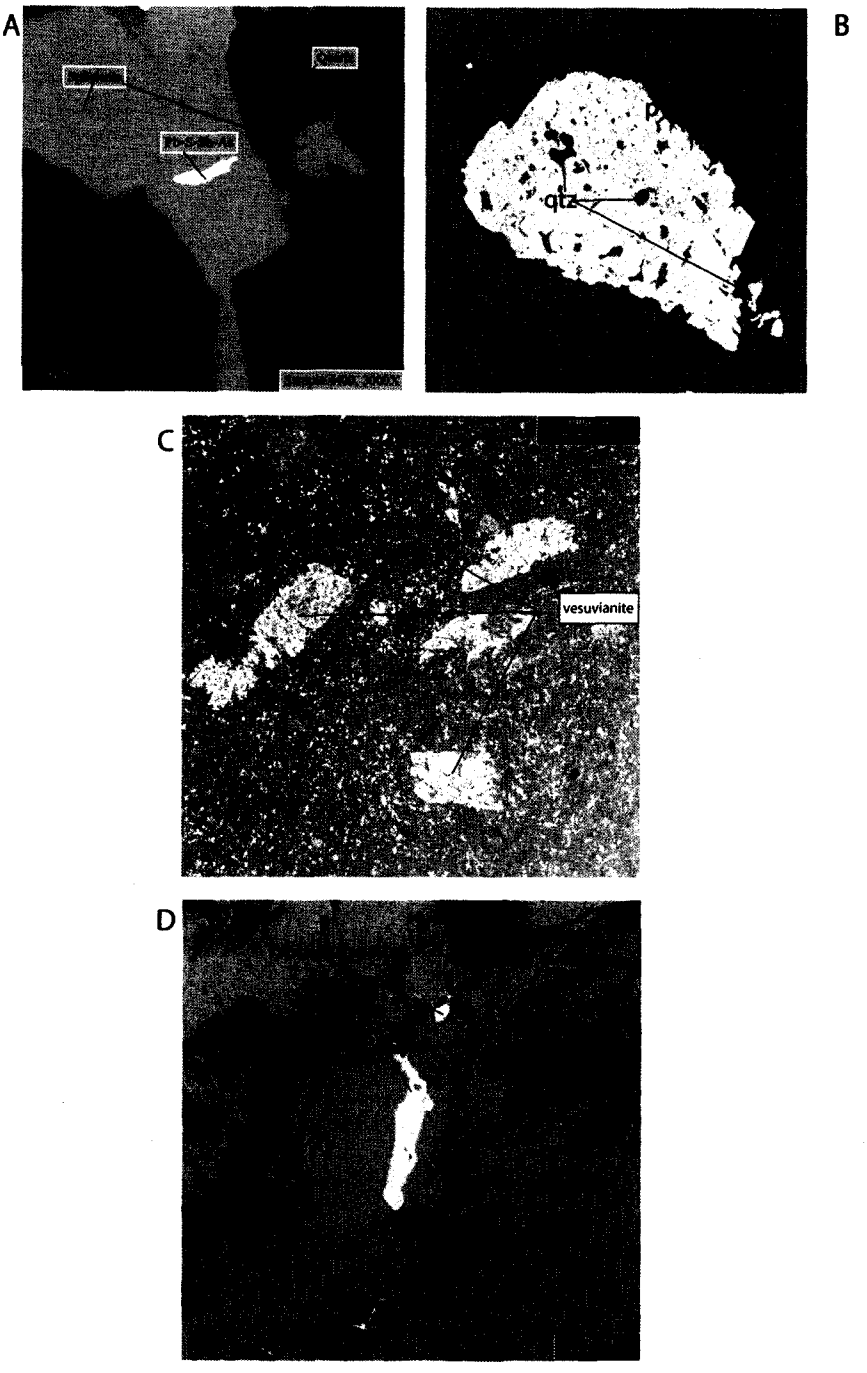

FIGURE 26. High resolution photomicrographs of ore asemblages from Chukar Footwall: (A) Base metal suite with sphalerite, quartz, and a grain of geocronite-guettardite partially replacing sphalerite (4400 level), (B) Pyrite-II grain with abundant quartz inclusions (4590 level), (C) Vesuvianite porphyroblasts (Hole CFU-137), and (D) Boulangerite, a lead antimony sulfide, replacing stibnite along fractures (4590 level)

greenish in color, filling open fractures and vugs, exhibiting distinct form types such as the obtuse rhombohedron crystals. From several samples (e.g. 4610 level and CZ-Tracker Decline), it seems that Ba-II stage and calcite are cogenetic wherein the former occurs as small (≤2 mm) subhedral inclusions that, under short wave UV, produced an intense yellowish fluorescent light. Calcite peaks from XRD analyses reveal a low Mg content (up to 5 mole percent). Finally, dedolomitization has been reported from some samples from the 4730 level (Williams, 2002).

Dolomite commonly occurs as fine to coarse crystalline grains in veinlets and coarse, individual rhombs in veinlets associated with quartz±sericite±Py-II and carbonate flooding. Two major types have been observed: (a) medium to coarse equigranular, interlocking saddle (baroque) dolomite that is very distinct under the microscope due to their curved faces, strong undulose extinction, mottling, and hypidiotopic textures of Friedman (1965); and (b) sparsely distributed inequigranular rhombic crystals that lack zoning under the microscope. This dolomite type could be classified as having idiotopic textures (i.e., inequigranular fabric wherein the carbonate grains are mostly euhedral; Friedman, 1965).

Staining and XRD analyses from Chukar Footwall reveal that most of the carbonate mineralogy could be the result of partial solid solutions between ferroan dolomite (ferrodolomite) and zincian dolomites (minrecordite, $CaZn(CO_3)_2$) in the system $CaCO_3$-$MgCO_3$-$MnCO_3$-$FeCO_3$-$ZnCO_3$ (Rosenberg and Champness, 1989). Numerous authors have mentioned and described

dolomitization along the Carlin Trend. For example, Arehart (2001) examined several lines of interpretation which call into question the distribution and origin of dolomites in Carlin-type deposits. Leach (1999) observed a spatial zonation of carbonates composition through depth at the Deep Post mine with Mn-Mg carbonates at shallow depths and Mg-Ca carbonates at deeper levels. Dewitt (1999) drew attention to the presence of hypogene zinc carbonates at the SSX mine (Jerritt Canyon district) and their spatial relationships with NE-trending structures.

At Chukar Footwall, carbonate peaks shown an overall presence of both dolomite and minrecordite in the analyzed samples. These carbonates are hydrothermal in origin due to their spatial occurrence in veins and carbonate flooding suggesting an Mg and a relatively later Zn metasomatism on the carbonate lithologies on the basis of petrographic observations, SEM analyses, geochemical evidence, and the data presented by Zabinski (1980) and Rosenberg and Champness (1989). Furthermore, geological mapping showed that the overall distribution of samples with the above mineralogical characteristics are spatially related to both northeasterly and northwesterly trending faults which have an extended history of reactivation thus allowing circulation of hydrothermal and meteoric fluids.

Quartz (≤ 65 %) exhibits a variety of textures such as xenomorphic, granular, cockscomb, jigsaw, comb, and replacement (jasperoids). Quartz in multistage veins is mottled and anhedral with abundant submicron fluid inclusions. When specifically replacing dissolution breccias or the whole rock

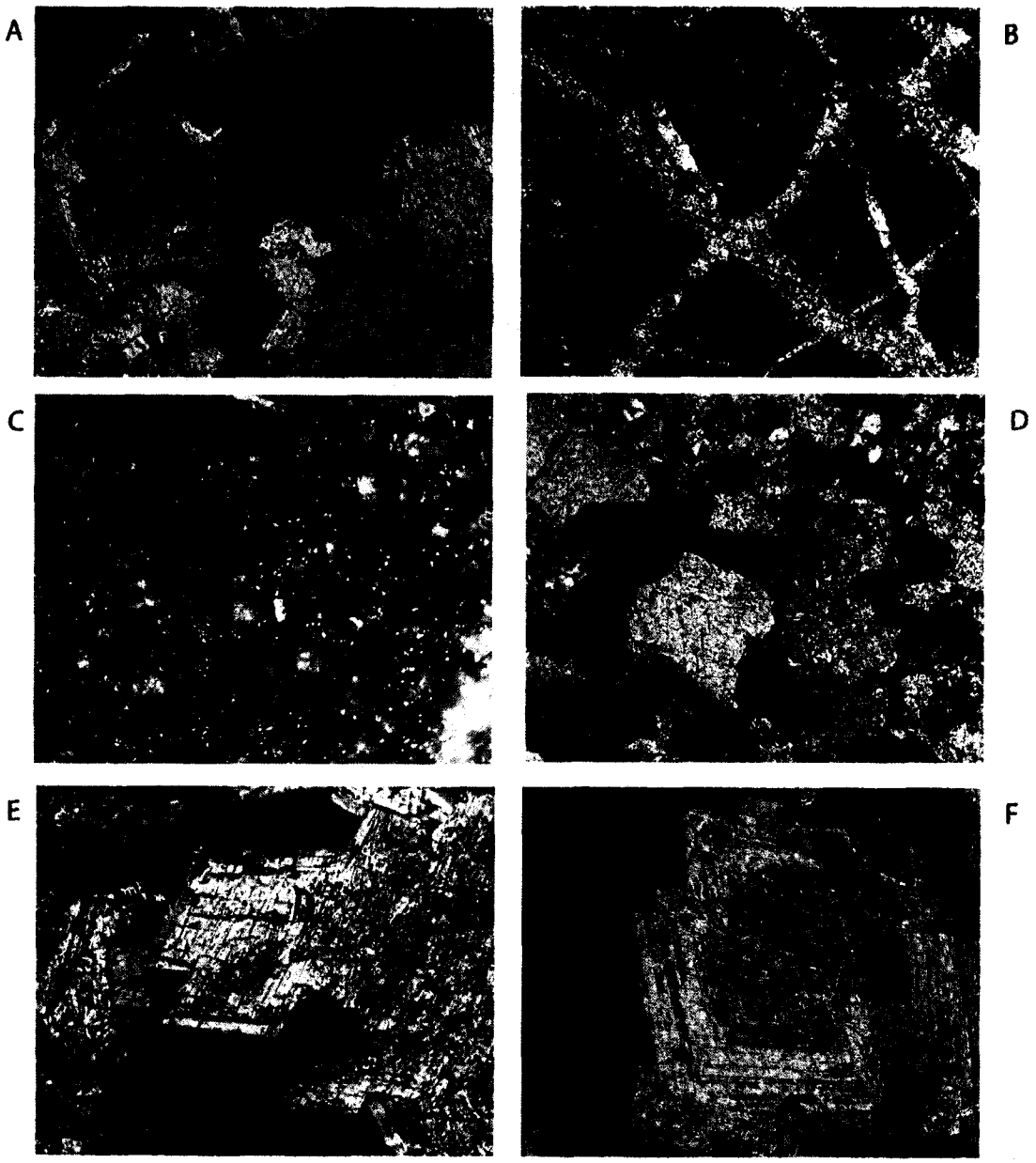

FIGURE 27. Photomicrographs showing carbonates at Chukar Footwall. Rhombohedral and prismatic forms of calcite with abundant inclusion zoning (A and E). Multistage calcite veins on micrite host rock (B). Dolomite commonly occurs as saddle (baroque) aggregates (D and F) and rhombic grains associated with brassy pyrite in the Magpie fault (C). Crossed nicols, FOV: 0.67 mm.

matrix, quartz occurs as a medium to fine grained jigsaw or xenomorphic textures. Quartz also formed during the late-ore stage as millimetric doubly terminated crystals ("herkimer diamond") in open spaces in a calcite vug on the 4730 level. Chalcedony was observed as botryoidal bands in sample 203 from the Magpie fault at the 4740 mine level.

SEM analyses and XRD data indicate that the dominant **clays** from healed and unhealed structures and hydrothermally altered samples are represented by muscovite-illite (detritical?), illite-1M, and kaolinite-dickite. The latter phase occurs as very fined, light to dark brown grains typically associated with quartz, sericite and Py-I in veins and also as late flooding(s). Regarding the **sericite** (~ 5 to 15 %), its cross-cutting relationships observed in thin-sections suggest three sericite alteration stages, the youngest one possibly related to the contact metamorphism event, and two later sericite stages possibly linked to hydrothermal events. In general, sericite occurs as a fine grained material in veinlets, groundmass, and carbonate-sericite flooding. Coarse sericite has been observed only locally associated with dolomite rhombs and stibnite in samples from the Magpie fault at the 4740 level, and it has been replaced locally by chlorite.

Although micron-size **gold** was not observed from SEM analyses, visible gold (Fig. 28) is somewhat abundant in the shallower mine levels (the 4730 and 4770 levels are the only areas where visible gold has been found). Geological mapping from these mine levels show that the occurrence of visible gold is along fractures of all orientations near major NW-trending structures (Sagehen fault,

4770 level; Pheasant fault, 4730 level). The majority of the visible gold occurs as (1) millimetric flakes, masses, or grains intergrown with Ba-II in calcite±sulfides veinlets, (2) along fractures, or (3) commonly found along bedding planes in decarbonatized, gritty $SDrm_1$ rocks. Finally, SEM analyses of gold flakes showed that gold contains silver.

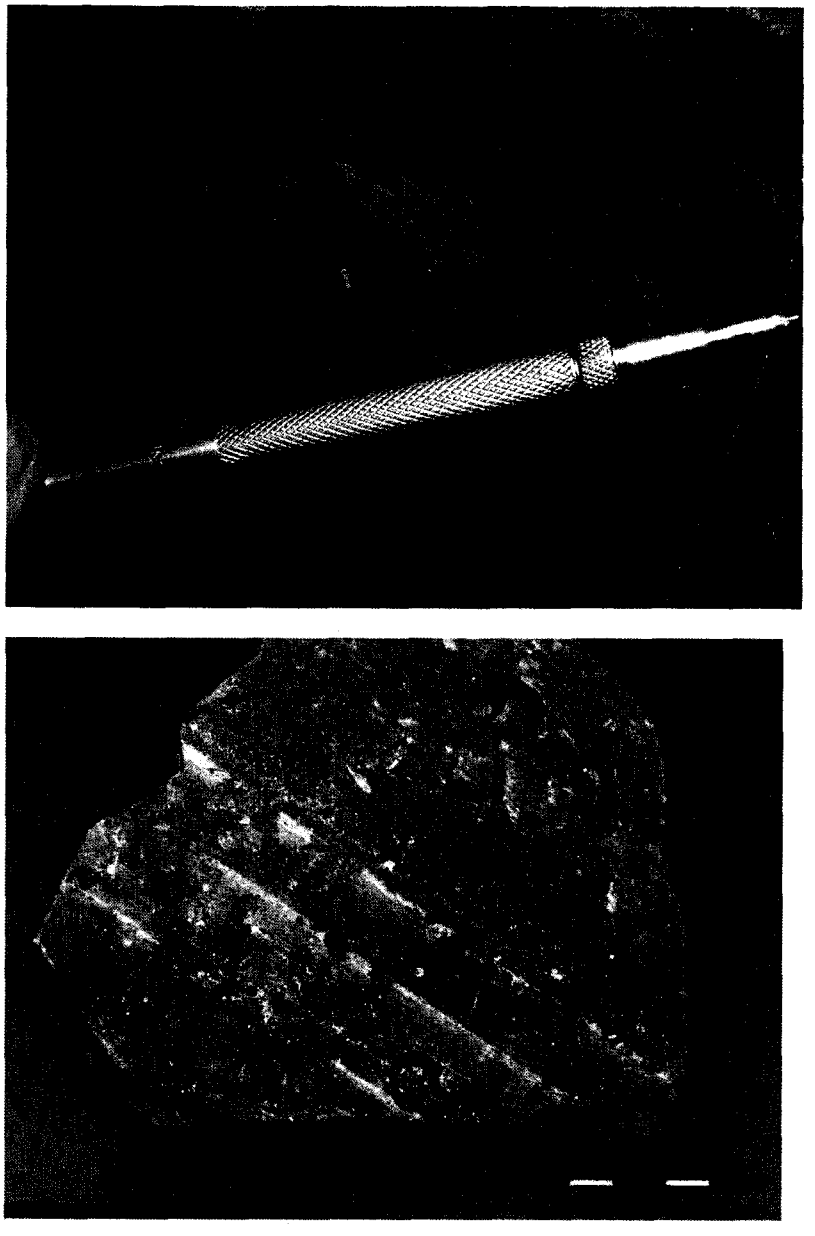

FIGURE 28. Late-stage visible gold from the 4730 mine level. Gold occurs in fractures of all orientations near major NW faults in strongly decalcified (gritty texture) SDrm rocks.

PARAGENETIC STAGES

Based on crosscutting relationships observed in thin-sections and hand samples, five general paragenetic stages are observed (Fig. 19): (I) diagenetic sulfides, (II) quartz± dolomite± sericite± pyrite± barite± fluorite (III) quartz±barite± calcite±base metals → (IV) quartz±carbonates±sericite±barite±As-minerals± stibnite→ (V) pyrite+marcasite±arsenopyrite±calcite±barite+visible gold± quartz.

Associated with the ore stage, stages II through IV are characterized by quartz± sericite and quartz± dolomite± sericite± barite ±pyrite veinlets and flooding. As and Sb sulfides are ubiquitous during the waning ore stage, occurring as discrete veinlets, sealing interstitial voids around the matrix quartz grains, and vug fillings. Stage III is volumetrically small relative to the others. It began with quartz, barite, and calcite precipitation in veinlets and open spaces followed with a minor deposition of low iron sphalerite, arsenopyrite, pyrite, and Sb sulfosalts. This stage cuts the ore stage II and it may have been genetically related to the latest stages of the main mineralization. Finally, stage V marks the late-ore stage at Chukar Footwall characterized by calcite±barite±visible gold± sulfides±quartz veins in zones of strong hydrothermal alteration. Quartz represents the last phase that may have precipitated in the deposit.

9. STABLE ISOTOPE STUDIES OF THE CHUKAR FOOTWALL MINE

Systematic studies of stable isotopes of $\delta^{18}O$, $\delta^{13}C$, and $\delta^{34}S$ in the Carlin trend and elsewhere have shown consistent isotopic changes recorded in both fresh rocks and mineralized host-rocks thus demonstrating that there have been significant ore fluid-rock interactions. For example, Stenger et al. (1998) documented haloes of low $\delta^{18}O$ values on rocks surrounding the orebodies relative to unmineralized, more distal rocks in Twin Creeks, Nevada. Similarly, Pinckney and Rye (1972) carried out a study of the relationships among $\delta^{18}O$, $\delta^{13}C$, and limestone textures in the Hill Mine, in the fluorite district of southern Illinois. They reported variations in the isotopic ratios of $\delta^{18}O$ and $\delta^{13}C$ as the Mississippian limestone was repetitively altered, suggesting a textural and mineralogical control on the $\delta^{18}O$ and $\delta^{13}C$ values. With regard to the potential of stable isotopes studies for mineral exploration for blind, deep orebodies, this methodology have been used as a rapid and preliminary step to delineated areas of former hydrothermal activity that may host mineralization (cf. Schmauder et al., 2005).

This chapter addresses several fundamental questions regarding the isotopic signature at Chukar Footwall: (1) Is there any relationship among structures, degree of hydrothermal alteration, and isotopic values? (2) Is there any isotopic zonation? (3) What is the isotopic signature, if any, of the late-stage barite+gold veins relative to the other veins? and (4) Does the Chukar Footwall deposit exhibit unique isotopic features? In order to answer these questions,

several isotopic transects were made perpendicular to major structures and a total of 64 hand-specimens were selected for whole-rock and vein carbonate isotope analyses. Additionally, 14 powder samples were obtained from sulfides and sulfates for sulfur and oxygen analyses to evaluate the possible sources of the sulfur.

The $\delta^{13}C$ –$\delta^{18}O$ relationships of whole-rocks and carbonates are shown on Figure 29, and the $\delta^{34}S$ and $\delta^{18}O$ data for sulfides-sulfates are shown in Figure 30. The $\delta^{18}O$ and $\delta^{13}C$ values are reported relative to V-SMOW and V-PDB, respectively (Table 5).

CARBON AND OXYGEN STABLE ISOTOPE DATA

$\delta^{18}O$ and $\delta^{13}C$ ISOTOPIC TRANSECTS

Carbon and oxygen isotope analyses were performed on samples of late-stage calcite veins and wallrocks of the Roberts Mountains Fm. along perpendicular transects to the Magpie fault, Sagehen fault zone, Antelope fault, Pheasant fault, and several structures in the 4610 level (Figs. 31, 32, and 33) to determine whether the wallrocks around structures exhibit isotopic shifts due to the degree of hydrothermal alteration and/or the proximity to faults or joints.

The Magpie fault, a major NNE-striking feeder structure at Chukar Footwall, at the 4720 level shows a lack of relationships between $\delta^{18}O$ and $\delta^{13}C$ along the transect (Fig. 34; samples 210,211,212, and 213 on Figure 32) that could be interpreted as different competing processes dominate both the

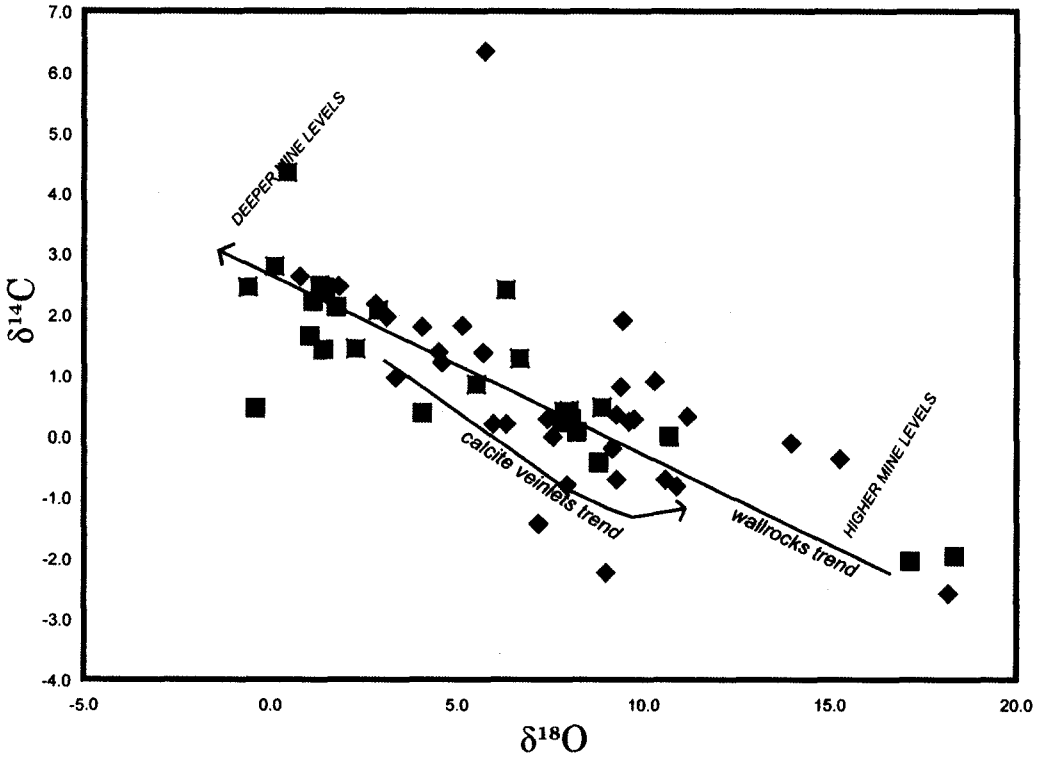

FIGURE 29. Carbon and oxygen isotope values of host rocks and calcite veins at Chukar Footwall. The trend from fresh to altered limestone is towards lighter oxygen and heavier carbon values at deeper mine levels. In contrast, the calcite veinlets trend toward lighter carbon and heavier oxygen values at higher mine levels. Red rhombs= limestone, green squares= calcite veins.

carbon and oxygen isotope signature. The $\delta^{13}C$ values show little variation between the footwall and hangingwall section; in the footwall the $\delta^{13}C$ values increase toward the structure, then decrease in the hangingwall. The $\delta^{18}O$ values, however, show somewhat greater variations but with an opposite behavior. $\delta^{18}O$ values decrease toward the hangingwall. It is noteworthy that the respective maximum and minimum values of carbon and oxygen coincide with the Magpie fault. Finally, this behavior is complemented by a small transect perpendicular to the structure (samples 63 and 70 on Figure 32) whereby the maximum and minimum ratios, respectively, for $\delta^{13}C$ and $\delta^{18}O$ values also coincide with the fault.

Concerning the $\delta^{18}O$ and $\delta^{13}C$ isotopic patterns along the Sahegen fault zone, a WNW- striking fault, at the 4720 level (samples 53, 57,58, and 111 on Figure 32), they exhibit somewhat similar ratios to these adjacent of the Magpie fault. The overall $\delta^{13}C$ pattern is characterized by a decrease in the footwall, then increasing toward the hangingwall. However, $\delta^{18}O$ values increase in the footwall and then decrease toward the hangingwall portion of the structure (Fig. 35). Another WNW-striking structure, the Antelope fault, at the 4740 level shows minimal isotopic variations along the hangingwall section (samples 21,25,26,27, and 28 , Fig. 31) and it displays similar $\delta^{13}C$ and $\delta^{18}O$ patterns to those of the Magpie and Sagehen faults, with a tendency to higher $\delta^{13}C$ and lower $\delta^{18}O$ values toward the fault (Fig. 36).

Isotopic transects on the 4730 and 4610 levels (Fig. 33) display very different $\delta^{13}C$ and $\delta^{18}O$ patterns from to those described above. The spikes in

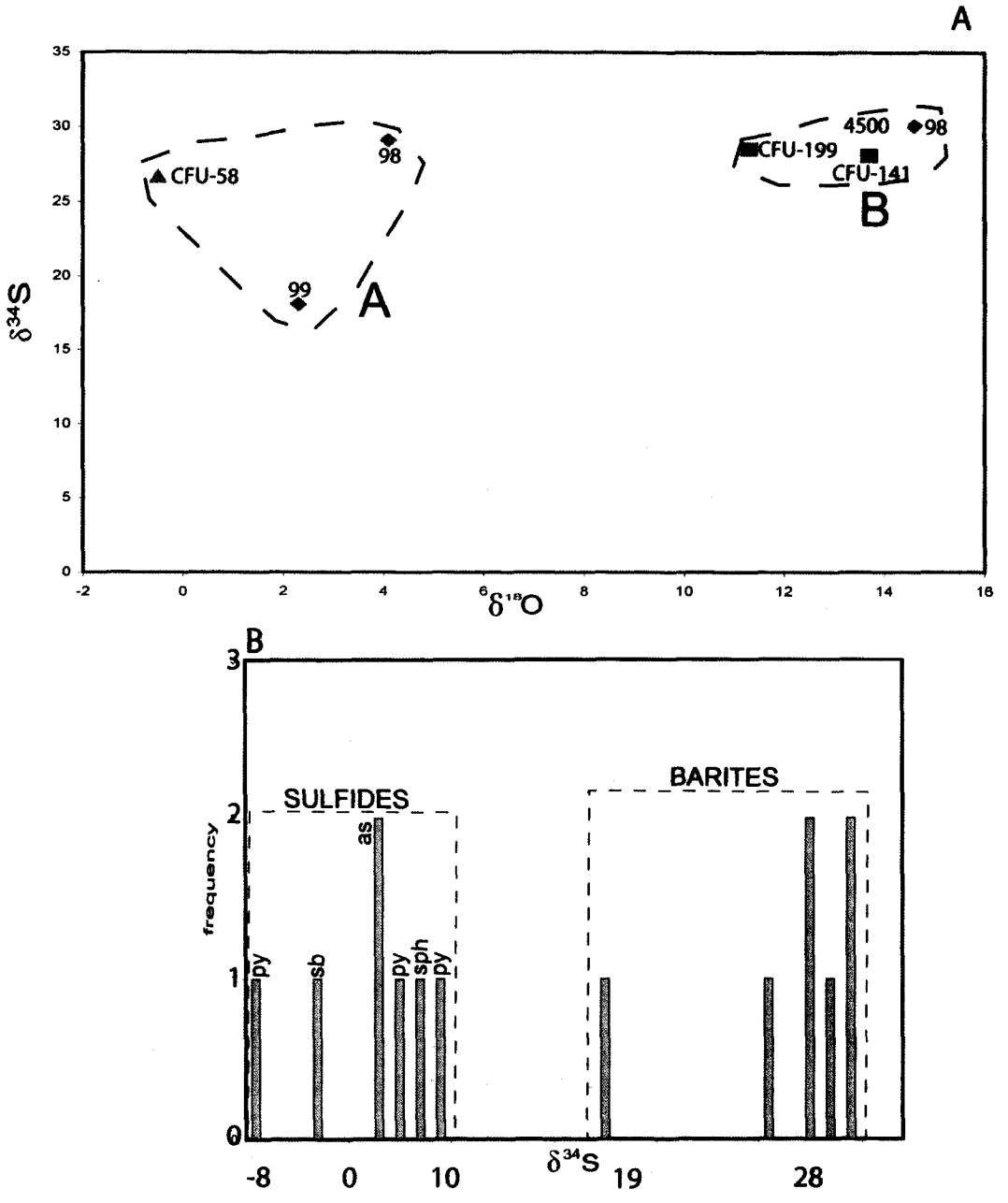

FIGURE 30.(A) Oxygen and sulfur isotope data from barites. Two populations are defined on the basis of their isotopic signatures. Note the enrichment in both sulfur and oxygen from samples from deeper mine levels (population B). Numbers denote samples.(B) Histogram of sulfur values in sulfides and sulfates in Chukar Footwall. Py=pyrite, sb= stibnite, sph= sphalerite,as=realgar and orpiment.

both $\delta^{13}C$ and $\delta^{18}O$ values in Figures 37 and 38 might be controlled by the intense fracture density that served as pathways for late-ore hydrothermal fluids, which significantly change the original isotopic wallrock signature. This observation is supported by petrographic, geochemical, and fluid inclusion data that suggest a late-ore stage hydrothermal event associated with NW-striking structures with mobilization of metals into these structures and the formation of barite+gold+sulfides veinlets.

In summary, the carbon and oxygen patterns of the Roberts Mountains Fm. from several perpendicular transects to major structures record (1) isotopic haloes around structures are spatially associated with a specific degree of hydrothermal alteration, and (2) although the $\delta^{13}C$ and $\delta^{18}O$ patterns in structures from the 4730 and 4610 levels are difficult to explain by isotopic systematics, petrographic and fluid inclusion data reveal interaction of late-ore hydrothermal fluids with already isotopically altered wallrock.

$\delta^{13}C$ and $\delta^{18}O$ SYSTEMATICS OF CARBONATE ROCKS AND CALCITE VEINS

The $\delta^{18}O$ values of the Roberts Mountains Fm. range from 0.8 to 18.2 ‰. Samples from the 4730 level (7.4 to 18.2 ‰) are the least altered among samples from different mine levels. Thus, these limestones clearly do not represent unaltered rocks when compared to the $\delta^{18}O$ values for unmineralized Roberts Mountains Fm. limestone near the Carlin mine, which range from 21.2 to 23.0 ‰ (Radtke et al., 1980). The $\delta^{13}C$ values of the same samples range from -

2.6 to 6.3 ‰. The range of these values overlaps those from the Carlin mine (-1.9 to 0.8 ‰, Radtke et al., 1980).

In a plot $\delta^{13}C$ vs. $\delta^{18}O$ (Fig.29) the data display a trend with a slope that reflects a negative correlation between carbon and oxygen isotopes. This may suggest that both isotopic signatures were governed by different processes (e.g., fluid/rock ratios, pH, oxygen fugacity), which shifted the carbon and oxygen isotopic values independently during decarbonatization.

When cross-cutting relationships are present (Fig. 39), temporal oxygen and calcite isotopic variations exist. For example, a late multistage calcite vein parallel to Sahegen fault (sample 19 on Figure 31, 4740 level) has $\delta^{18}O$ and $\delta^{13}C$ values ranging from 5.5 to 8.9 ‰ and 0.4 to 0.9 ‰, respectively. The fluids shifted toward heavier $\delta^{18}O$ values while the $\delta^{13}C$ values become progressively lighter. The calcite $\delta^{13}C$ values are close to those of the nearest limestone analyzed (samples 14 and 16, 4740 level) and the local SDrm limestones, which suggest that the carbon may have been derived from dissolution of carbonate minerals and organic carbon from the wallrocks. With regard to the oxygen isotopic signature, the earlier $\delta^{18}O$ value is substantially lower than the surrounding wallrocks, but becomes heavier later. A meteoric fluid could have produced this trend toward heavier $\delta^{18}O$ values as the degree of water-rock exchange fluctuated through time. Furthermore, fluid inclusion data from similar late stage calcite veins shown low homogenization temperatures ($\leq 115^{\circ}$ C) and very low salinities indicating and supporting the oxygen isotopic data that much of the late fluid was meteoric in origin.

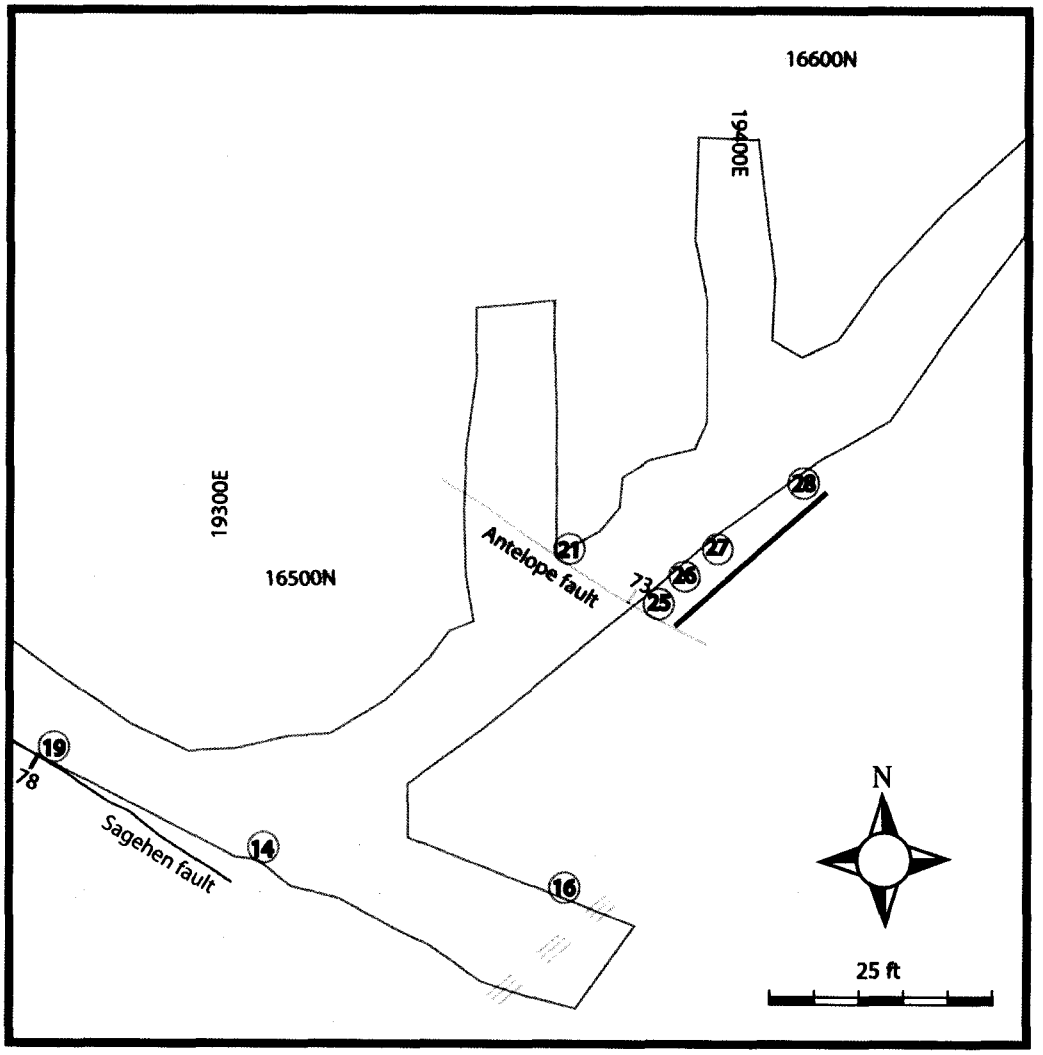

Figure 31. Location map (4740 level) showing location of samples taken for stable isotope analyses (Chukar Footwall coordinates). Green line represents the isotopic transect (see Fig. 36).

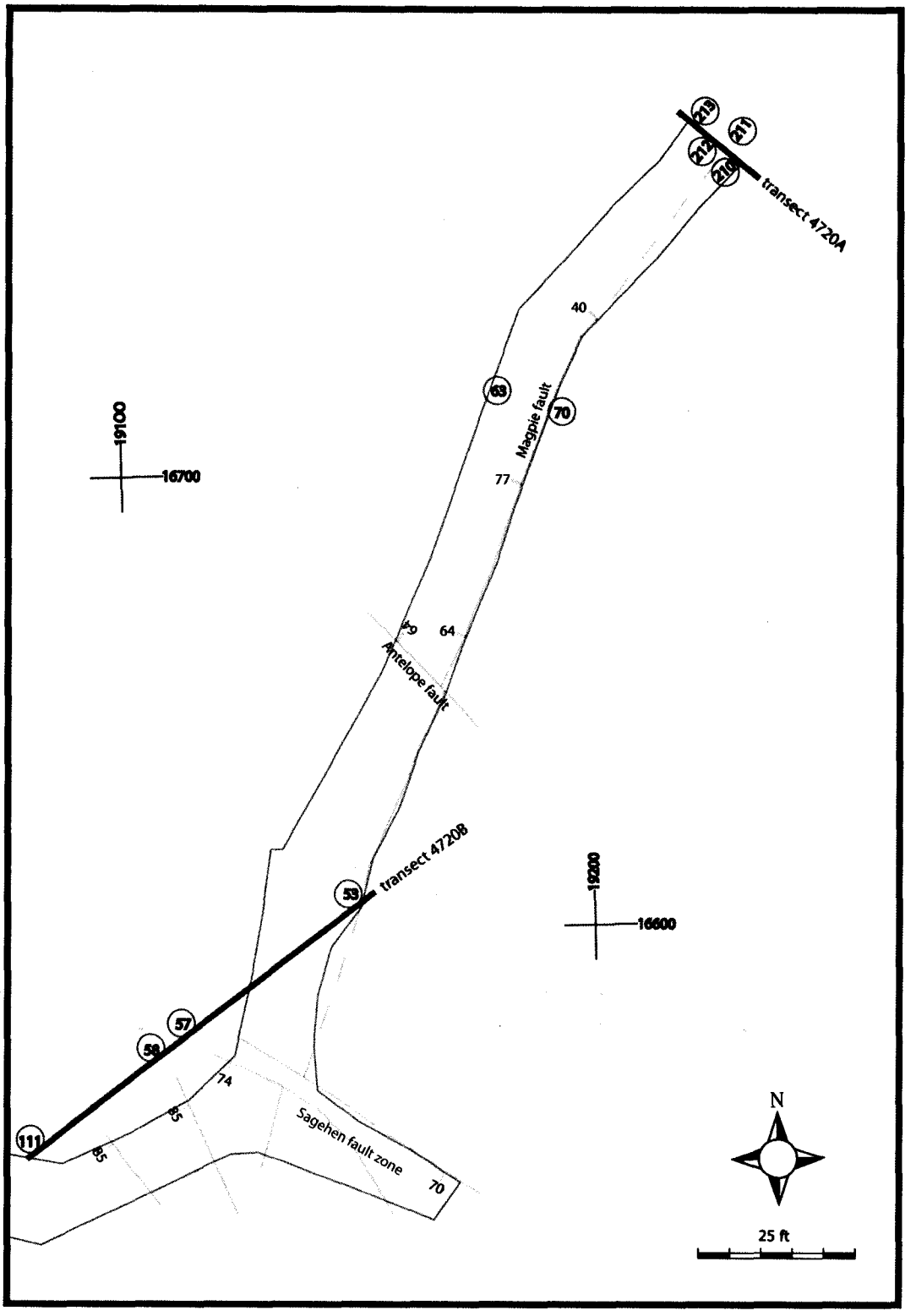

FIGURE 32. Location map (4720 level) showing location of samples taken for stable isotope analyses. Green lines represent transects (see Figures 34 and 35). Chukar Footwall coordinates.

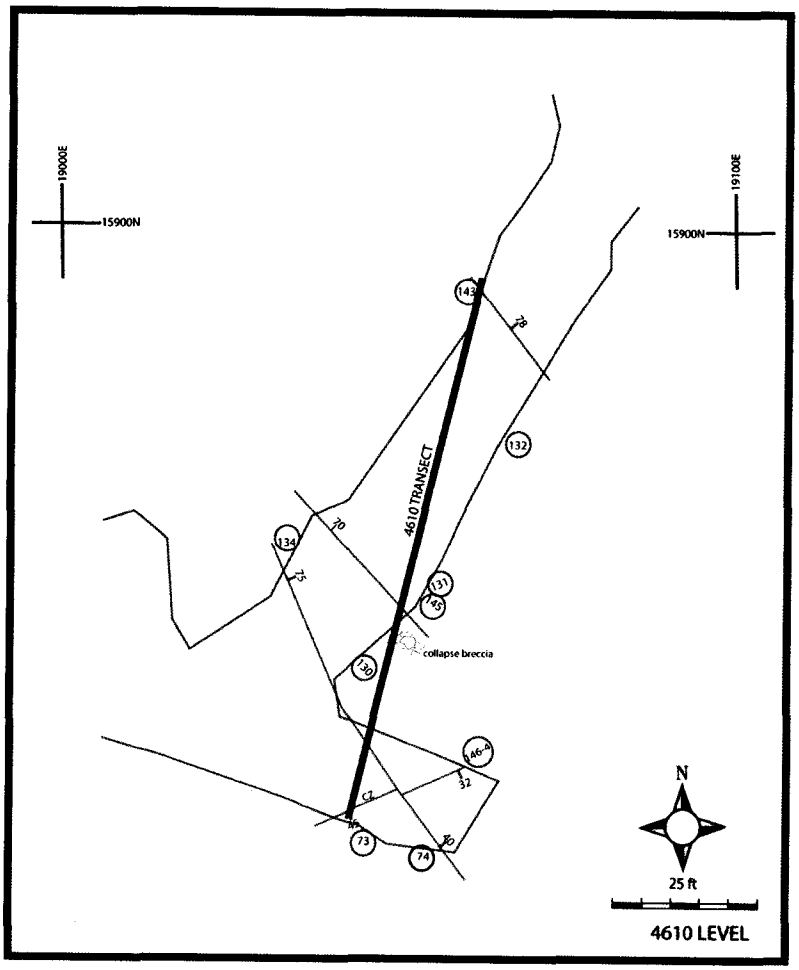

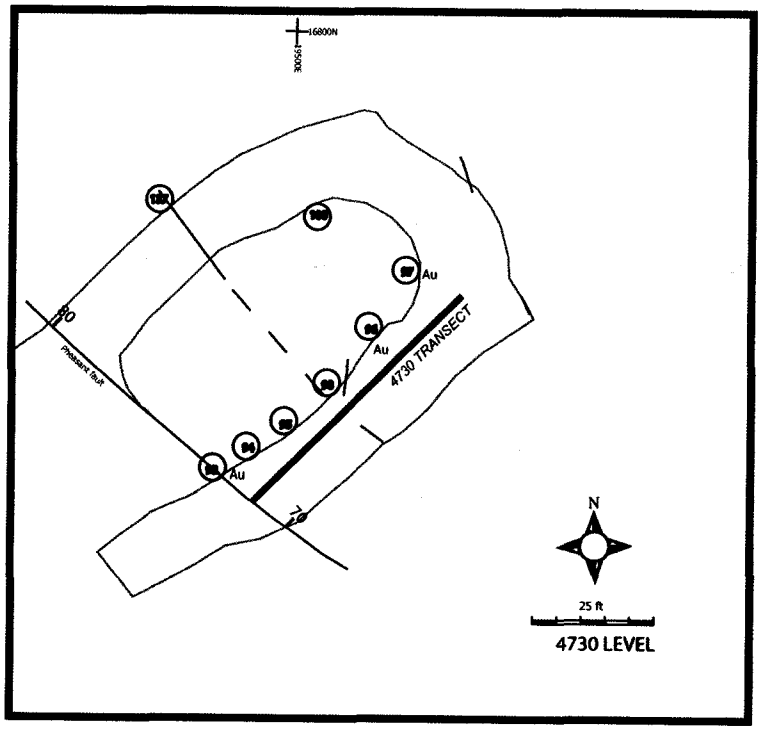

FIGURE 33. Location maps (4610 and 4730 levels) showing location of samples taken for both stable isotope and fluid inclusion analyses. Green lines on the 4730 map are late calcite+sulfides+ barite veins. Au= visible gold. Chukar Footwall coordinates. CZ= Central Zone.

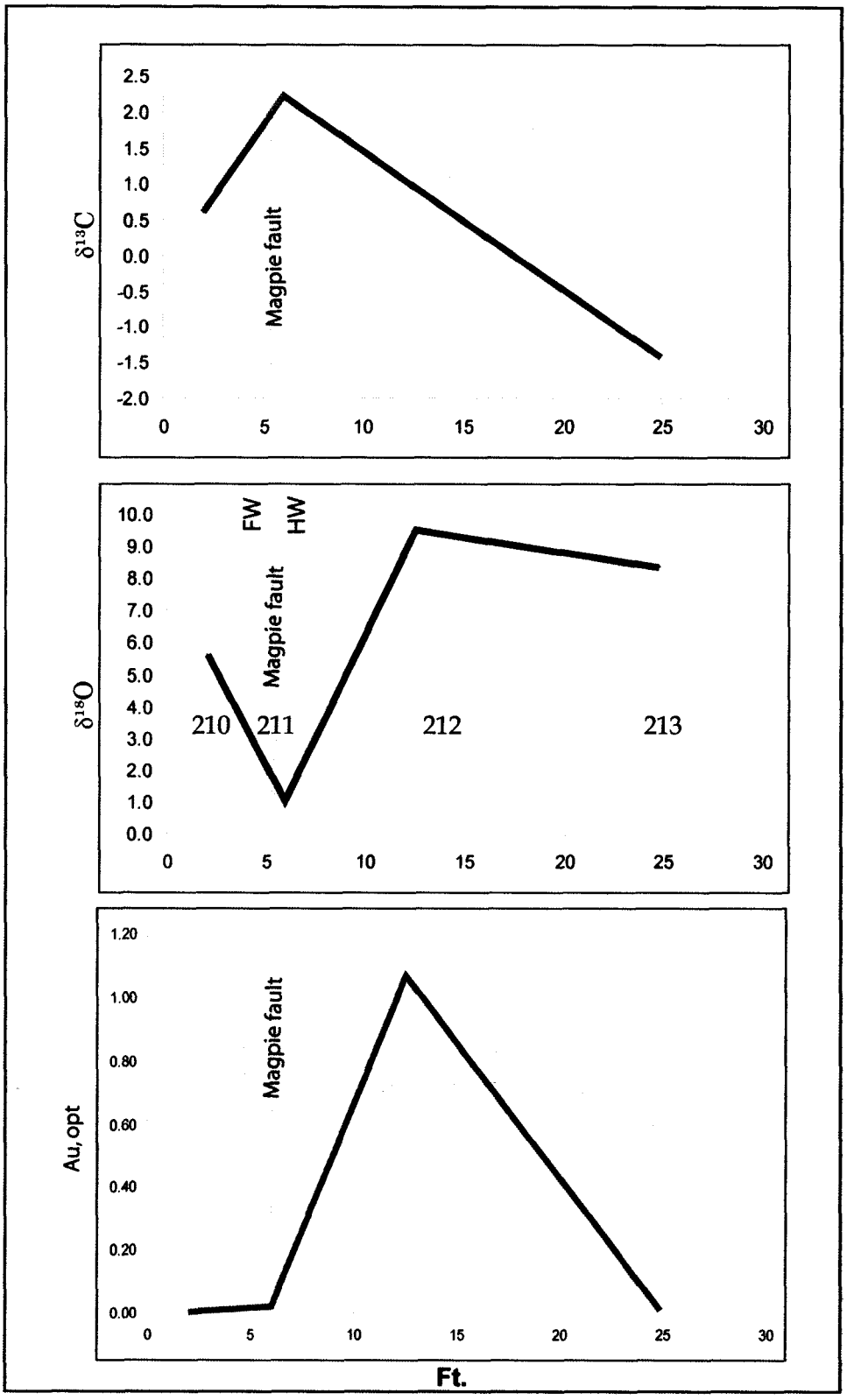

FIGURE 34. Spatial variation of stable isotopes and gold along transect 4720A, perpendicular to the Magpie fault (see Figure 5). FW= footwall, HW= hanging wall. Blue numbers denote wallrocks samples.

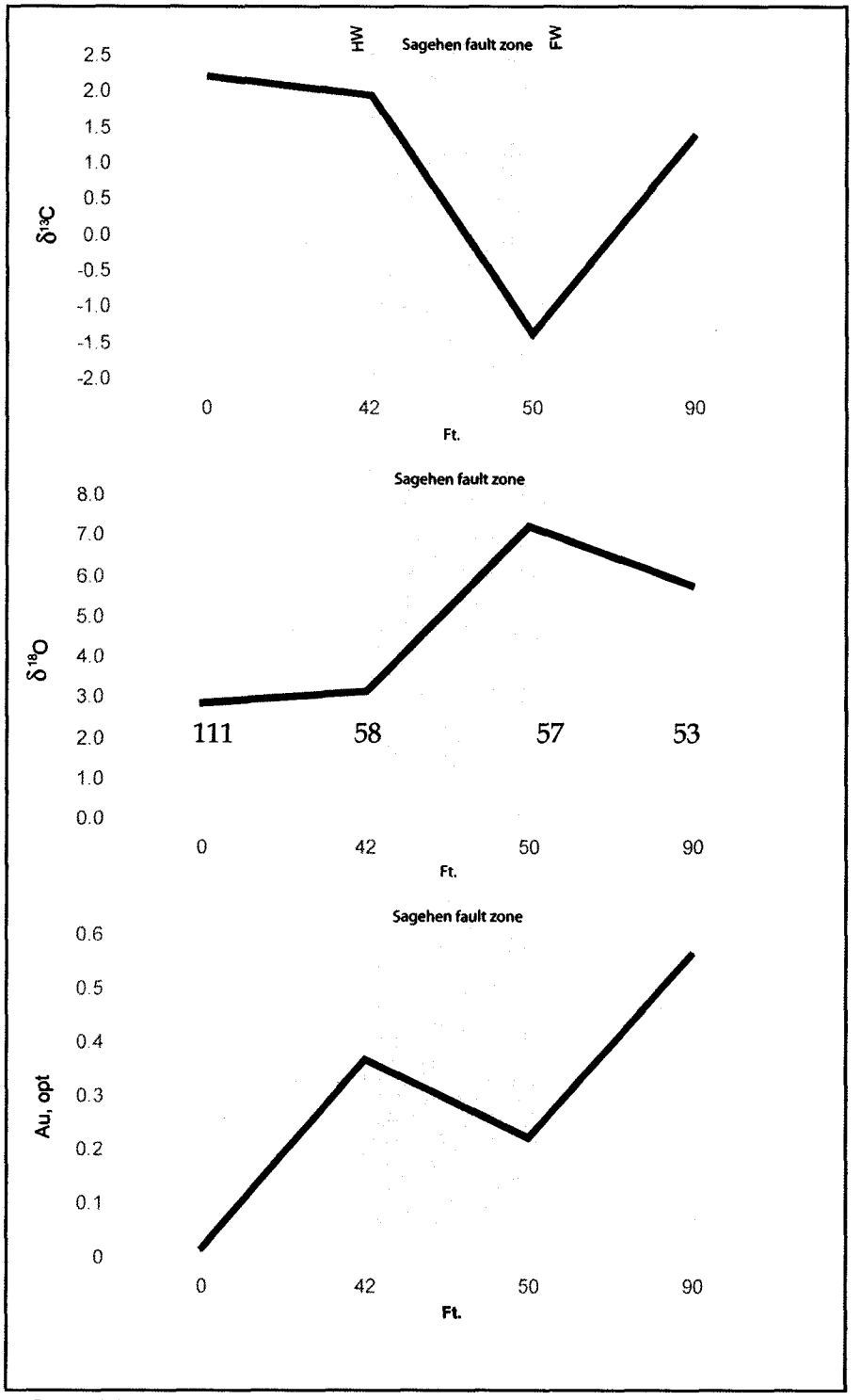

FIGURE 35. Spatial variation of stable isotopes and gold values along transect 4720B perpendicular to the Sagehen fault zone. HW= hangingwall, FW= footwall. Blue numbers denote wallrocks samples.

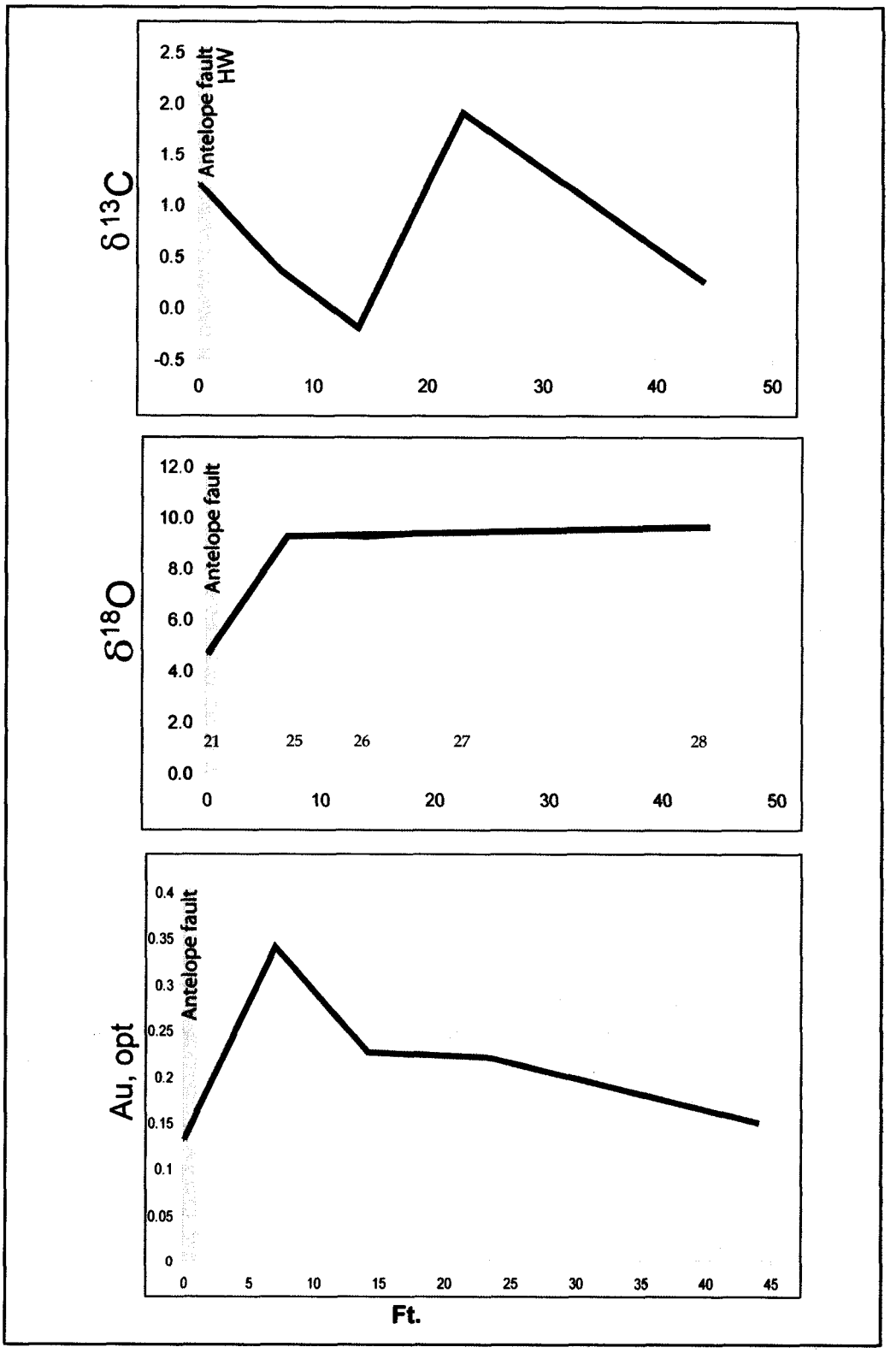

FIGURE 36. Spatial variation of stable isotopes and gold values perpendicular to the Antelope fault (4740 level). HW= hangingwall. Blue numbers denote wallrock samples.

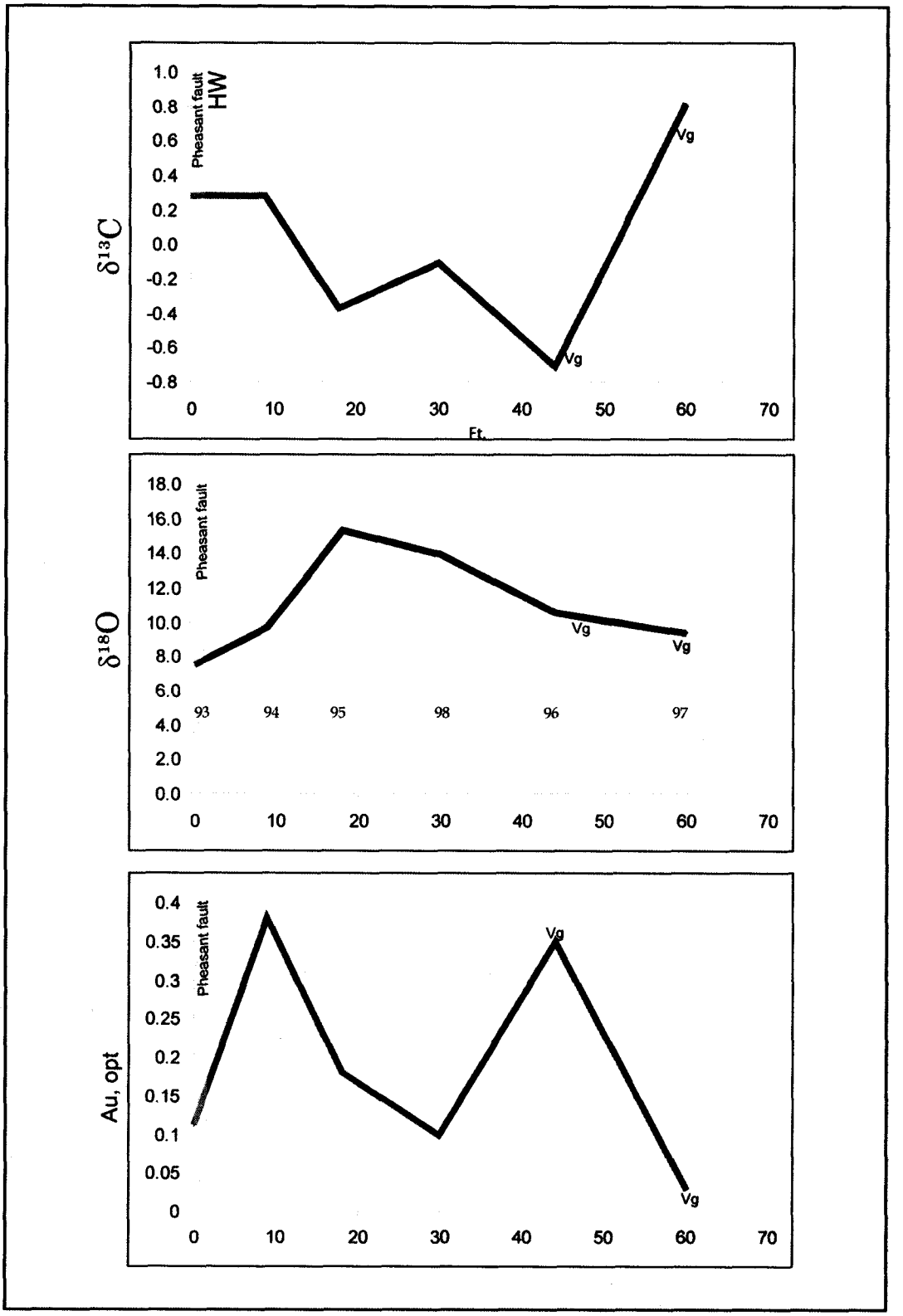

FIGURE 37. Spatial variation of stable isotopes and gold values perpendicular to the Pheasant fault (4730 level). Blue numbers denote wallrock samples. HW: hangingwall, Vg: visible gold.

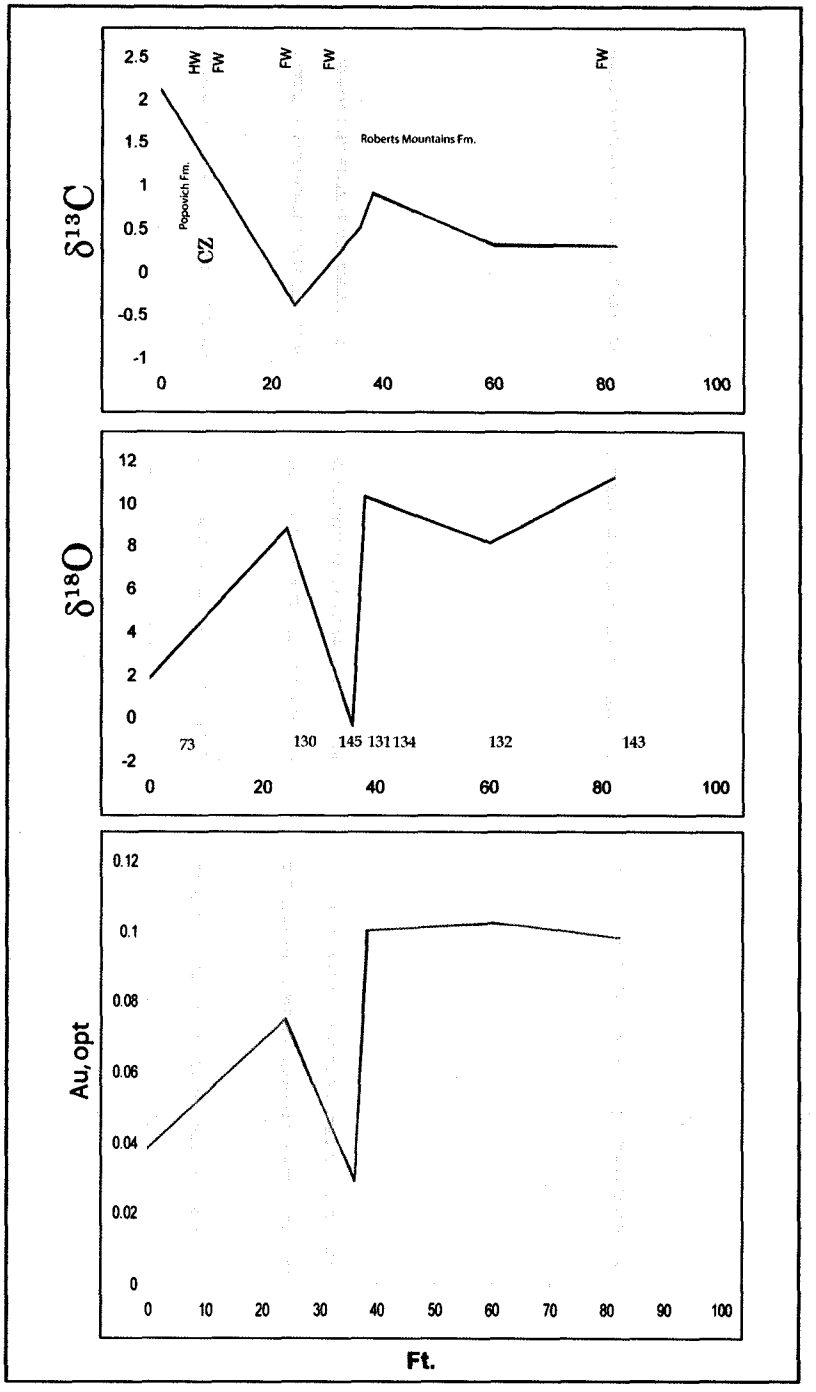

FIGURE 38. Spatial variation of stable isotopes and gold values along a transect in the 4610 level (see Figure 33). Vertical lines are faults. Blue numbers denote wallrock samples. CZ= Contact Zone.

Similar temporal variations in $\delta^{18}O$ and $\delta^{13}C$ values are recorded in sample 86 (4650 level, Fig. 39C). This sample is a typical dissolution-collapse breccia produced by decarbonatization reactions (cf. Williams, 1992). The earliest wavy calcite possibly precipitated from meteoric waters interacting with wallrocks, which is supported by the oxygen and carbon isotope data ($\delta^{18}O$: 2.9 ‰, $\delta^{13}C$: 2.1‰). In contrast, a late calcite vein crosscuts the massive, wavy earlier calcite. It was deposited from a fluid with heavier $\delta^{18}O$ and lighter $\delta^{13}C$ signature ($\delta^{18}O$: 7.9 ‰, $\delta^{13}C$: 0.4‰) relative to the earliest calcite.

Using the fractionation factors compiled by Friedman and O'Neil (1977) for the $CaCO_3$-H_2O pair at a temperature of 100° C, the $\delta^{18}O$ range for the water in isotopic equilibrium with late-stage calcite veins is 1.3 to -17.6 ‰. This range in $\delta^{18}O$ values is typical of meteoric water (Taylor, 1997).

In summary, I interpret the oxygen and carbon isotopic data from wall rocks and calcite veins as follows: (1) both $\delta^{18}O$ and $\delta^{13}C$ values in the wallrocks correlate fairly well with the degree of decarbonatization thus suggesting that this mechanism was responsible for these spatial isotopic shifts during decarbonatization, (2) the overall shift toward lighter $\delta^{18}O$ values in the wallrocks is a result of interaction with hydrothermal fluids responsible for gold deposition, (3) the $\delta^{13}C$ signature of calcite veins suggests that the carbon was derived from the carbonate mineral and organic carbon in the SDrm limestone. The relatively $\delta^{13}C$ low values in calcite may suggest (a) a strong organic carbon component through time and (b) CO_2 degassing (Zheng, 1990) , and (4) the temporal

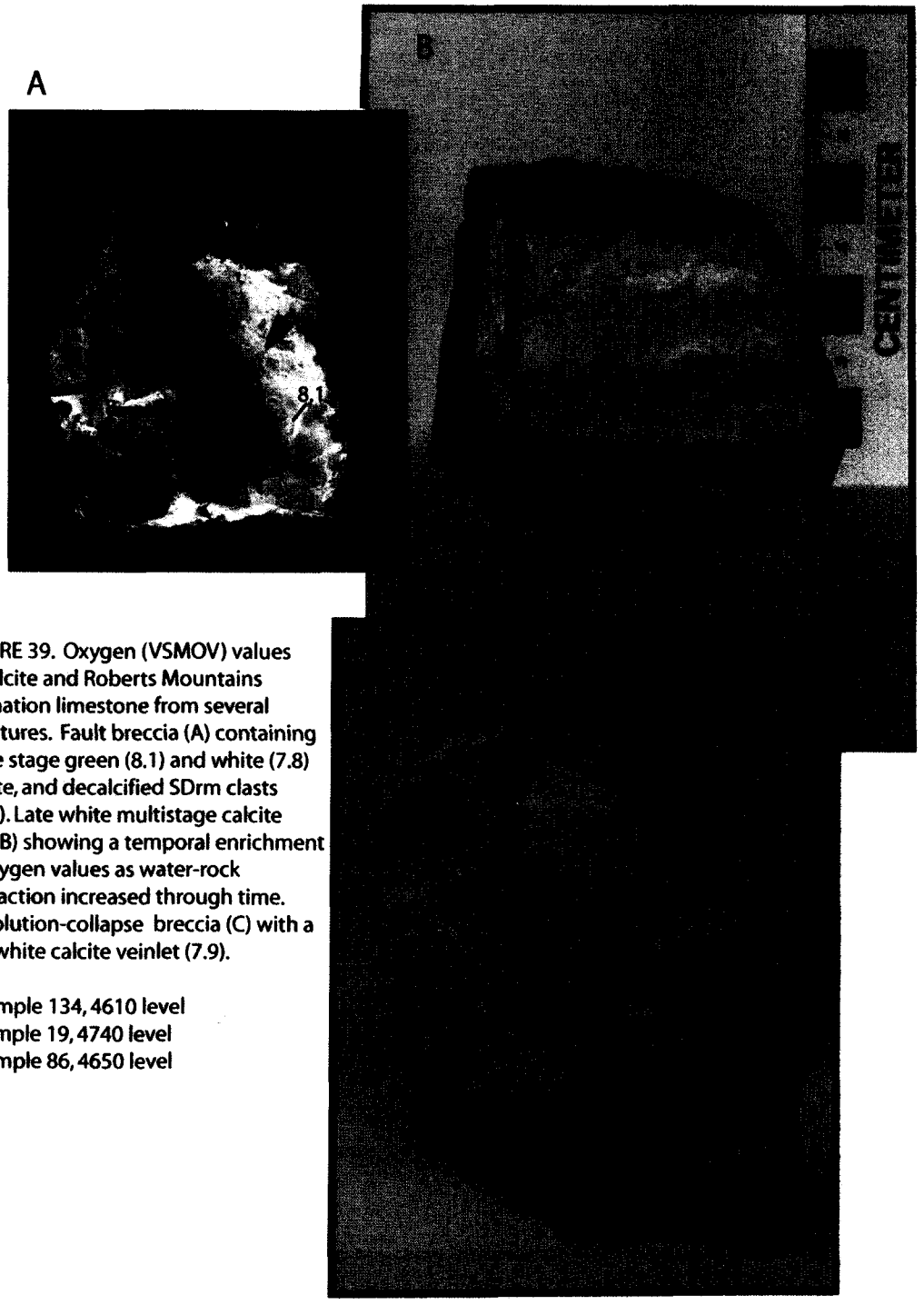

FIGURE 39. Oxygen (VSMOV) values of calcite and Roberts Mountains Formation limestone from several structures. Fault breccia (A) containing same stage green (8.1) and white (7.8) calcite, and decalcified SDrm clasts (10.7). Late white multistage calcite vein(B) showing a temporal enrichment in oxygen values as water-rock interaction increased through time. Dissolution-collapse breccia (C) with a late white calcite veinlet (7.9).

A: sample 134, 4610 level
B: sample 19, 4740 level
C: sample 86, 4650 level

isotopic values coupled with fluid inclusion studies suggest a shifting interaction between meteoric waters and the host rocks. Thus, meteoric fluids underwent an isotopic exchange with the wallrock decreasing the $\delta^{18}O$ values for the earlier precipitates. At time progressed, lower water-rock ratios and temperatures took place producing carbonate veins with progressively heavier $\delta^{18}O$ signatures and lower $\delta^{13}C$ signatures. Consequently, the temporal shifts in isotopic values of the calcite veins may reflect differences in temperature, fluid composition, and loss of CO_2 (Rye and Ohmoto, 1974; Zheng, 1990).

CARBON-OXYGEN ISOTOPIC MODELING

Quantitative modeling of the carbon-oxygen isotopic data of late-stage calcite veins has been carried out to identify the dominant carbon species involved in their precipitation. For the purpose of comparison, both CO_2 and HCO^-_3 fractionation curves were calculated using the best fitting initial water values ($\delta^{18}O$: 2 ‰, $\delta^{13}C$: -4 ‰), and then compared to the calcite vein array at Chukar Footwall (Fig. 40), which shows decreasing $\delta^{13}C$ and increasing $\delta^{18}O$ values along the calcite array and a decrease in temperature through time.

In this case, the theoretical $CaCO_3$ - HCO^-_3 fractionation curve approximates the some slope as the calcite vein array, a likely indication that HCO^-_3 was the dominant carbon species in the hydrothermal fluid.

TABLE 5. $\delta^{13}C$ and $\delta^{18}O$ VALUES FOR CARBONATE WALLROCKS AND VEINS FROM CHUKAR FOOTWALL MINE

(See Fig. 29 for plot of data)

SAMPLE	LEVEL	$\delta^{13}C$	$\delta^{18}O$	Au, opt	REMARKS
14L	4740	-0.8	10.9	0.67	D
16L	4740	0.2	6.3	0.073	D
25L	4740	0.4	9.3	0.342	D
26L	4740	-0.2	9.2	0.226	D
27L	4740	1.9	9.4	0.221	D
28L	4740	0.2	9.6	0.15	D
19-1C	4740	0.9	5.5	0.066	
19-2C	4740	0.5	8.9	0.066	
19-3C	4740	0.4	8	0.066	
21BL	4740	1.2	4.6	0.129	D
93L	4730	0.3	7.4	0.11	D
94L	4730	0.3	9.8	0.38	D
95L	4730	-0.4	15.3	0.18	D
96L	4730	-0.7	10.6	0.35	D
97L	4730	0.8	9.4	0.029	D+VG
98L	4730	-0.1	14	0.1	D
100-1L	4730	-0.7	9.3	0	D
100-2C	4730	-2.1	17.2	0	
100-3C	4730	-2	18.3	0	
137L	4730	-2.6	18.2	0.064	UNALTERED
53L	4720	1.4	5.7	0.567	D
57L	4720	-1.4	7.2	0.221	UNALTERED
58L	4720	2	3.1	0.267	D
60C	4720	2.5	-0.6	0.016	D
63L	4720	1.4	4.5	0.264	D
64C	4720	4.4	0.5	0.363	D
64L	4720	6.3	5.7	0.363	D
69C	4720	1.3	6.7	0.363	D
69L	4720	1.8	4.1	0.363	D
70L	4720	2.5	1.8	0.264	D
71C	4720	0.1	0.1	0.249	D
71L	4720	0.2	6	0.249	D
111-1L	4720	2.2	2.8	0.008	D+ARG
111-3C	4720	1.4	2.3	0.008	D
210L	4720	0.6	5.6	0.005	D
211L	4720	2.2	1	0.021	D
212L	4720	1	9.5	1.069	D
213L	4720	-1.4	8.4	0.007	D
29	4710	-2.2	9	0.02	UNALTERED
30-1L	4710	1.8	5.1	0.022	D
30-2C	4710	0.1	8.2	0.203	D
48L	4710	0	7.6	0.203	D
48AL	4710	-0.8	7.9	0.203	D
86-1C	4650	2.1	2.9	0.058	CZ BX
86-2C	4650	0.4	7.9	0.058	CUTS 86-1C
86-3L	4650	2.4	6.3	0.058	D+BX
73-1C	4610	2.1	1.8	0.038	Dp3
73-2C	4610	2.5	1.3	0.038	Dp3
74C	4610	0.4	4.1	0.029	
130C	4610	-0.4	8.8	0.075	
131-1C	4610	1.4	1.4	0.075	
131-2L	4610	0.9	10.3	0.1	D
131-3L	4610	2.6	0.8	0.1	
131-4C	4610	1.7	1.1	0.075	
132-1C	4610	0.3	8.1	0.102	
132-2C	4610	1	3.4	0.102	
134-1C	4610	0.3	8.1	0.075	
134-2C	4610	0.2	7.8	0.029	
134-3L	4610	0	10.7	0.029	D
143L	4610	0.3	11.2	0.098	
145C	4610	0.5	-0.4	0.029	
146-4-1C	4610	2.2	1.1	n/a	CZ BX
146-4-2C	4610	2.4	1.4	n/a	CZ
146-4-3C	4610	2.4	1.5	n/a	CZ

D= altered limestone
ARG= argillized sample
L= limestone
C= calcite vein
CZ BX= Contact Zone (dissolution-collapse breccia)
BX= dissolution-collapse breccia
VG= visible gold

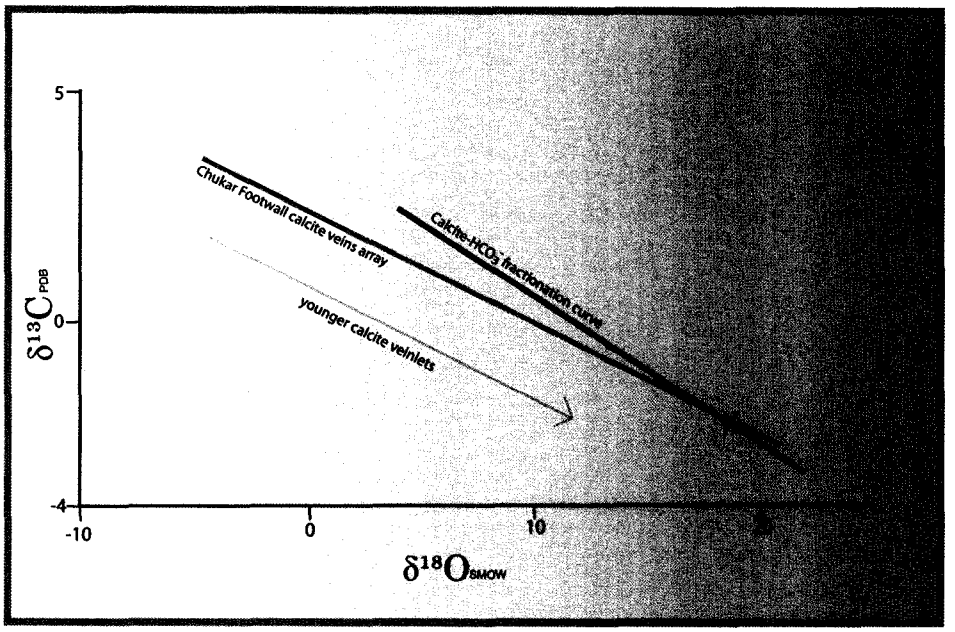

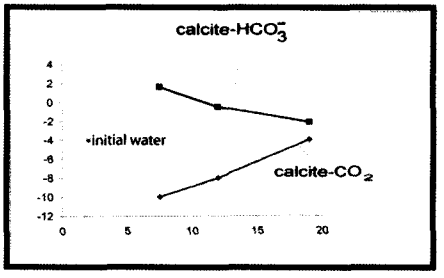

FIGURE 40. Calcite-HCO_3^- theorical fractionation curve and the stable isotopic array of calcite veins at Chukar Footwall illustrate that HCO_3^- was the dominant dissolved carbon species during the precipitation of late stage calcite veinlets. The small diagram shows both calcite-HCO_3^- and calcite-CO_2 curves calculated from initial water values (see text). X= 100° C (temperature from fluid inclusion microthermometry).

Zheng (1990) pointed out that the calcite veins at the Kushikino gold mines (Kyushu, Japan) precipitated under equilibrium conditions with a hydrothermal fluid in which the dominant carbon species was HCO^-_3 under low temperatures ($\leq 180^\circ C$) and increasing pH. In this respect, the calcite array at Chukar Footwall may suggest similar characteristics of calcite precipitation. First, CO_2–bearing fluid inclusions were not detected in late-stage calcite veins because either they are absent or the CO_2 content of the inclusions is very low. Probably, decalcification was nonexistent during the late-stage thus significant amounts of CO_2 were not being released into the system.

SULFUR ISOTOPE DATA

Sulfur isotope data were obtained on sulfide and sulfate samples from different mine levels. The data are shown in Figure 30B and Table 6. The $\delta^{34}S$ values from sulfides (pyrite, sphalerite, orpiment+realgar, and stibnite) range from – 8.5 ‰ (pyrite) to 10.1 ‰ (pyrite), whereas the $\delta^{34}S$ values from barite range from 18.1 ‰ to 30.2 ‰.

SULFIDES

The $\delta^{34}S$ clustering for sulfides observed in Figure 30B may suggest a common origin for the sulfur in these samples. For example, one sample of late-ore orpiment and realgar (sample 4580As) has similar $\delta^{34}S$ values for both minerals. Similarly, the values $\delta^{34}S$ (1.2 ‰for syn-ore sphalerite and pyrite from

sample CFU 199-118 are 9.2‰ and 8.0 ‰, respectively. Another observation that can be made regarding this narrow range of $\delta^{34}S$ values in these sulfide minerals is that H_2S in the fluid was highly fractionated by sulfide precipitation. Thus, according to Ohmoto (1986) during isotopic equilibrium the amount of H_2S must exceed the amount of metals (Pb, Zn, Cu, Fe) in the fluid, and the precipitation of these phases was controlled by the original metal content of the ore fluid.

The textural relationships between sphalerite and pyrite from sample CFU-199, suggest they were precipitated under equilibrium conditions; however the calculated isotopic equilibrium temperature using the pyrite-sphalerite fractionation factors ($\Delta\ ^{34}S_{py\text{-}sph}$ values (1.2 ‰) of Ohmoto and Rye (1979) yielded a temperature of 360° C. This temperature greatly exceeds microthermometric data obtained in this study and those of other Carlin-type deposits (Hofstra and Cline, 2000).

Low positive to negative $\delta^{34}S$ values are also present in post-ore stibnite (4.5 ‰, sample 203) and pyrite (-8.5 ‰, sample 111-2). Thus, sulfide mineral precipitation proceeded under non-equilibrium conditions.

SULFATES

The $\delta\ ^{34}S$ values of late-stage barite range from 18.1 ‰ to 30.2 ‰. The heavier and the lighter samples come from veins of the 4500 and 4730 level, respectively. There is a spatial correlation among isotopic values, depth, and

presence of visible gold; gold has only been found in the upper mine levels (Population A, Fig. 30A).

On the basis of their $\delta^{34}S$ and $\delta^{18}O$ values, two populations of late-stage barite are recognized. Population A represents samples from the shallower mine levels, and visible gold is present in all the analyzed barites. The $\delta^{34}S$ and $\delta^{18}O$ values range from 18.1 to 29.1 ‰ and from -0.5 to 4.1 ‰, respectively. In contrast, barites from population B were collected from deeper levels and visible gold was not detected. Relative to population A, B samples show heavier $\delta^{34}S$ and $\delta^{18}O$ signatures with $\delta^{34}S$ values that range from 28.1 to 30.2 ‰ and $\delta^{18}O$ values ranging from 11.3 to 14.6 ‰. Anomalously, one sample from the shallow levels with visible gold plots within this population. These isotopic differences in both populations may have been derived by either fluctuations during fluid mixing of two or more fluids or the involvement of several sulfate sources.

Using the fractionation factors compiled by Friedman and O'Neil (1977) for the $BaSO_4$-H_2O pair at a temperature of 200^{O} C, the $\delta^{18}O$ range for the water in isotopic equilibrium with late-stage barite veins is 8 to -7.1 ‰. This range in $\delta^{18}O$ values is indicative of formation waters (Taylor, 1997) , suggesting mixing conditions either between meteoric waters and the wallrocks, or between two contrasting fluids.

TABLE 6. $\delta^{34}S$ and $\delta^{18}O$ VALUES FOR SULFIDES AND SULFATES FROM CHUKAR FOOTWALL DEPOSIT (See Fig. 30 for plot of data)

SAMPLE	LEVEL	$\delta^{34}S$	$\delta^{18}O$	REMARKS
4580As	4600	7.3		Realgar
4580As	4600	7		Orpiment
111-2	4720	-8.8		Pyrite-III
203	4720	4.5		Stibnite from Magpie fault
99	4730	10.1		Sulfide vein on Fig. 48
CFU-199@118'		8		Brassy pyrite
CFU-199@118'		9.2		Sphalerite
98	4730	29.2	4.1	Barite-II
98	4730	30.1	14.6	Barite-II with visible gold
99	4730	18.1	2.3	Barite-II with visible gold
CFU-199@118'		28.5	11.3	Barite-I
CFU-58@146'		26.7	-0.5	Barite-II with visible gold
CFU-141@142'		28.1	13.7	Barite-II veinlet
4500	4500	30.2	14.3	Barite-II veinlet

SOURCE OF SULFUR

Sulfur from sulfides and sulfates can basically be derived from several sources: (1) a magmatic source, (2) an organic source, (3) a sedimentary source/sulfate reservoir, and (4) any combination of the above (cf. Ohmoto, 1986). Due to the low number of sulfur analyses for this study (n= 7), the following suggestions are primarily based on published data on Carlin-type deposits in Nevada.

The $\delta^{34}S$ mean from sulfides from Chukar Footwall is about 5.4 ‰, which may suggest a significant contribution from a sedimentary source. Thus, the hydrothermal fluid may have obtained the H_2S from the host rocks or by the dissolution of early magmatic sulfides. Finally, the strong negative $\delta^{34}S$ value of a pyrite vein (sample 111-2), interpreted as a late-stage product, could be explained by the generation of some sulfur species during the final stages of mineralization (Hofstra and Cline, 2000).

The high $\delta^{34}S$ values from barites, with a mean around 27.3 ‰, argue that the sulfate was not derived from the oxidation of sulfides (Ohmoto, 1986). Regional data from sulfates by Arehart (1998) and from this study point toward a sulfate reservoir (sedex barite) as a main source for the H_2S in the sulfate. In the surrounding area, beds and veins of barite are hosted in several formations from both the upper and lower plates (Papke, 1984) that appear to be the most likely source. Hence, barites from Chukar Footwall deposit show $\delta^{34}S$ values similar to Paleozoic barites in north-central Nevada (Rye et al., 1978; Radtke et al, 1980; Arehart, 1998).

GOLD GRADES VERSUS ISOTOPIC COMPOSITIONS

Plots of Au vs. $\delta^{13}C$ and $\delta^{18}O$ (Fig. 41) show no spatial correlation between the metal and the stable isotopic signature of the host rocks. Previous work on Carlin-type deposits has suggested that the lack of correlation may be due to the intrinsic characteristics of the fluids (Hutcherson, 2002), and Au precipitation and C isotopic fractionation are governed by different and independent mechanisms (Hofstra and Cline, 2000).

Assuming that gold precipitation and isotopic fractionation are, indeed, contemporaneous processes, the above characteristics may suggest that during gold deposition, possibly due to mixing or involvement of two or more isotopically unique fluids, the non-equilibrium precipitation of sulfides and lack of gold correlation with wallrock and calcite veinlet isotopic ratios suggests they operated independently at slightly different times. Furthermore, the final isotopic signature generated by the combination of multiple ore fluids can also be influenced by later hydrothermal fluids or any other geological mechanisms able to produce an isotopic resetting. Obviously, if the host rocks underwent later events (i.e., late-stage argillization, interaction with ground waters), there would be a lack of linear correlation between gold and stable isotope ratios.

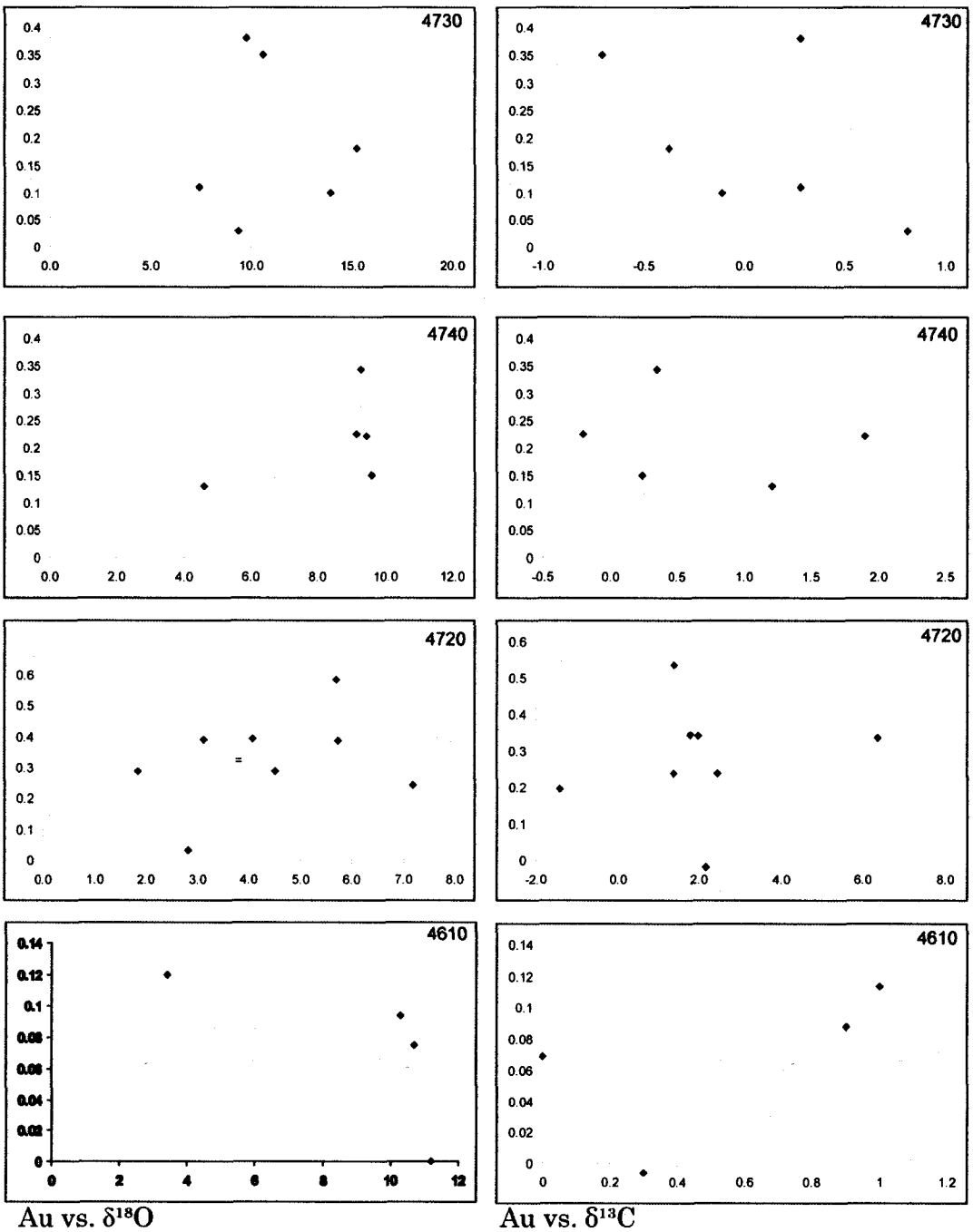

FIGURE 41. Plots of gold grades vs.$\delta^{18}O$ and $\delta^{13}C$ of selected mine levels at Chukar Footwall. The number next to the plot indicates the mine level. Au values in opt.

10. FLUID INCLUSION MICROTHERMOMETRY

Microthermometric data from both late-stage calcite and barite veins at Chukar Footwall are summarized in Table 7 and Figure 43. Although numerous fluid inclusions were observed both in quartz and carbonates of earlier stage(s), their sizes were too small for microthermometric analyses. Therefore, only primary or pseudo-secondary fluid inclusions observed in late-stage veins (barite, calcite, and barite±gold) were used to obtain the minimum homogenization temperatures (T_h) and final melting temperature of ice (T_m). Simultaneously, salinities were calculated from T_m as wt % NaCl equiv. Raman spectrographic analyses have not been carried out during this study.

Most of the fluid inclusions from these late-stage veins at room temperature are liquid+vapor types with varied L:V ratios due to the numerous sizes and geometrical shapes of the inclusions (Fig. 42). A small proportion of one phase (H_2O?), empty looking fluid inclusions were also observed in barite, probably the result of necking. The sizes of the fluid inclusions were in the range of 5 to 20μ. In general, fluid inclusions from late-stage barite veins are elongate to oval-shape defining planar trends and clusters in contrast to the equant to tabular shape, isolated inclusions of the late-stage calcite veinlets. In all fluid inclusions no daughter minerals were observed nor was CO_2 detected.

FIGURE 42. Fluid inclusions are found in both late-stage barite and calcite. Primary inclusions contain liquid and vapor. (A) Mean homogenization temperatures and salinities of fluid inclusions from Ba-II are 180.2°C and <1.1 wt % NaCl equiv, respectively. Visible gold coprecipitated with Ba-II (4730 level). (B) Fluid inclusions from Ba-II (4400 level). They homogenized to a liquid phase at an average temperature of 190°C, with salinities up to 3.2 wt % NaCl equiv. (C) Fluid inclusions from a late-stage calcite vein (CZ). This sample (CZ-3) yielded a homogenization temperature of 92.3°C and salinities around 0.7 wt % NaCl equiv. FOV: 0.500 mm.

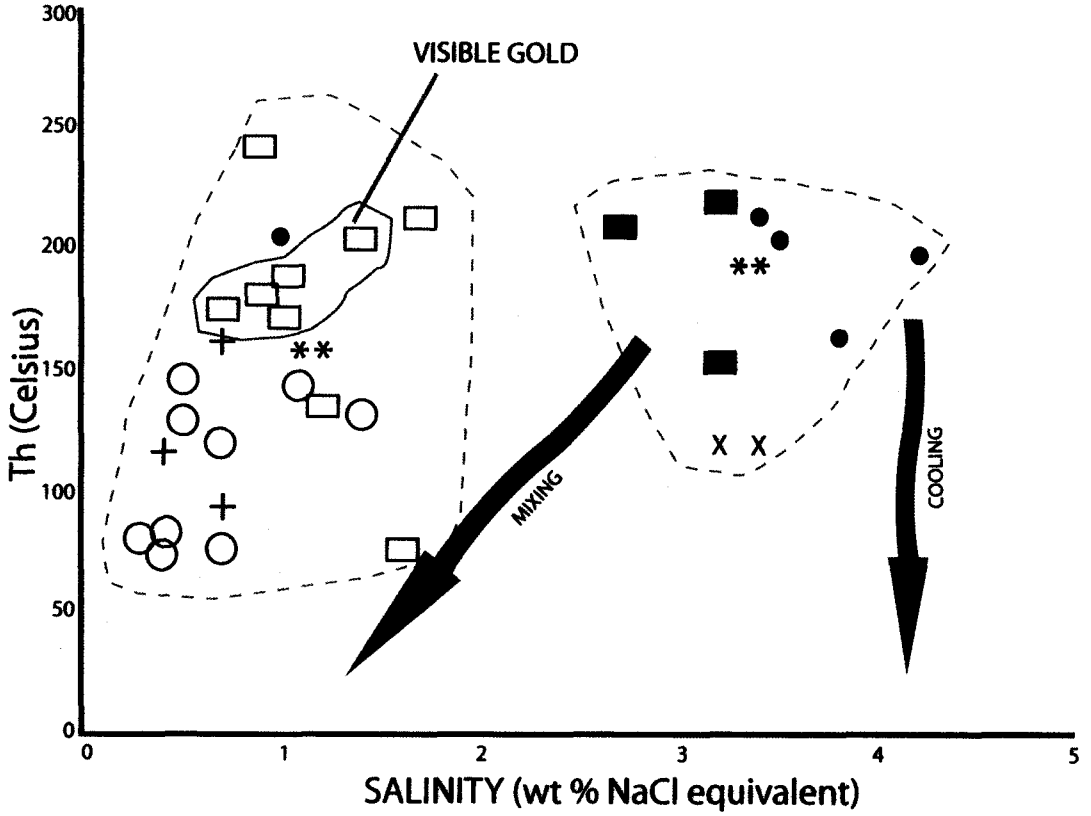

FIGURE 43. Salinity-Th diagram for fluid inclusions data in late-stage barite and calcite from Chukar Footwall. □= 4730-BARITE, ■= 4500-BARITE, ●= 4400-BARITE, * =CFU141-BARITE, X= CFU143-BARITE, += CZ-CALCITE, ○= 4730CALCITE.

FLUID INCLUSION DATA FROM LATE-STAGE BARITE±GOLD VEINS

Fluid inclusion microthermometric data from late-stage barite veinlets were obtained from cleaved barite crystals from samples collected in the 4730, 4400, and 4500 levels. Additionally, fluid inclusion analyses from selected core intervals, CFU-141 and CFU-143, were conducted to document if significant differences of T_h and salinities are present in the deposit (Fig. 43).

Two fluid inclusion types have been recognized (Kuehn, 1989; Kuehn and Rose, 1995): type 1C are one-phase (H_2O?), empty looking, high relief fluid inclusions. This unusual type occurs as isolated fluid inclusions, far from cleavages or fracture planes suggesting that they are primary. During freezing runs, type 1C inclusions usually nucleated a bubble allowing us to interpret with confidence that the entrapped phase is liquid H_2O (Roedder, 1984; Kuehn, 1989). In contrast, type 2D fluid inclusions are two-phases generally distributed along trails on cleavage planes, fractures, and in isolated clusters. Thus, 2D inclusions are considered here both primary and pseudosecondary. During microthermometric runs, neither CO_2 nor clathrates were observed in type 2D inclusions.

From Figure 43, it appears that significant variations among fluid inclusions exist in terms of their salinities and T_h. Mean salinities and mean T_h from the deeper levels (4400 and 4500 levels) range from 3.03 to 3.18 wt % NaCl equiv and between 183.1° and 179.3° C, respectively. However, mean salinities and T_h from the 4730 level is around 1.16 wt % NaCl equiv and 177.3° C,

respectively. Additional microthermometric data from cores (CFU-141@142' and CFU 143@447') exhibit mixed mean salinities and mean T_h values that range from 3.0 to 2.3 18 wt % NaCl equiv and between 142.2° and 172.3° C, respectively.

FLUID INCLUSION DATA FROM LATE-STAGE CALCITE VEINS

Fluid inclusion microthermometric data from late-stage calcite veins were obtained from the CZ along the Tracker decline, and from both 4400 and 4730 levels. The paucity of data is due to the scarcity of inclusions and problems with decrepitation during the heating runs.

Only isolated 2D type fluid inclusions were observed. Inclusions are oval to trapezoidal. Mean salinities and mean T_h values range from 0.55 to 0.70 wt percent NaCl equiv and between 87.6° to 117.0° C, respectively. Finally, no CO_2 or CH_4 were observed during the analyses.

DISCUSSION OF THE MICROTHERMOMETRIC DATA

Abundant fluid inclusion microthermometric data from the Carlin trend are now available to present a brief synthesis: Kuehn and Rose (1995) modeled the evolution of the hydrothermal system based on fluid characteristics from the Carlin mine during the main and late gold stage from quartz, calcite, and barite veins. During the main gold stage, the hydrothermal fluids were gas rich (CO_2 and H_2S), with salinities around 3 % NaCl equiv. Throttling conditions were

TABLE 7. FLUID INCLUSION DATA FROM LATE-STAGE BARITE AND CALCITE VEINS FROM CHUKAR FOOTWALL DEPOSIT
(See Fig. 43 for plot of data)

Sample	T_h (°C)	wt % NaCl equiv.		
4730-1	74.8	1.6		
4730-2	134.6	1.2		
4730-3	170.6	1		
4730-4	173.5	0.7		
4730-5	181.6	0.9		
4730-6	186.6	1		
4730-7	203.3	1.4		
4730-8	211.5	1.7		
4730-9	241.6	0.9		
4730-10	125.2	n/a		
4730-11	137.2	n/a		
4730-12	161.3	n/a		
4730-13	241.6	n/a		
4730-14	223	n/a		
4730-15	191.6	n/a		
4730-16	178.6	n/a		
4400-1	164.3	3.8		
4400-2	198.8	4.2		
4400-3	204	3.5		
4400-4	205.2	1		
4400-5	212.9	3.4		
4400-6	154.4	n/a		
4400-7	168.6	n/a		
4400-8	181.7	n/a		
4400-9	208.5	n/a		
4400-10	166.1	n/a		
4400-11	176.9	n/a		
4400-12	140.4	n/a		
4400-13	198.8	n/a		
4400-14	164.3	n/a		
4400-15	196.9	n/a		
4400-16	158.3	n/a		
4400-17	170.5	n/a		
4400-18	204	n/a		
4400-19	140.4	n/a		
4500-1	152	3.2		
4500-2	207.9	2.7		
4500-3	218	3.2		
4500-4	170.7	n/a		
4500-5	167.1	n/a		
CFU 143	118.2	3.2		
CFU 143	118.5	3.2		
CFU 143	118.3	3.4		
CFU 143	118	3.4		
CFU 143	157.8	1.2		
CFU 143	192	3.4		
CFU 143	197.7	n/a		
CFU 143	130.1	n/a		
CFU 143	129.3	n/a		
CFU-141	157.8	1.2		
CFU-141	157.8	1.1		
CFU-141	192.3	3.3		
CFU-141	192	3.4		
CFU-141	119.5	n/a		
CFU-141	215	n/a		
CFU-141	128.7	n/a		
CFU-141	215	n/a		
4730-1	74.8	0.7		
4730-2	77.6	0.4		
4730-3	77.6	0.3		
4730-4	94	n/a		
4730-5	117.8	0.7		
4730-6	127.7	0.5		
4730-7	130.9	1.4		
4730-8	141.5	1.1		
4730-9	145.5	0.5		
CZ-164-1	74.2	0.4	Cuts the CZ	(Fig. 16)
CZ-164-2	74.2	0.4	Cuts the CZ	(Fig. 16)
CZ-164-3	92.3	0.7	Cuts the CZ	(Fig. 16)
CZ-164-4	92.3	0.7	Cuts the CZ	(Fig. 16)
CZ-164-5	115.4	0.4	Cuts the CZ	(Fig. 16)
CZ-164-6	154.2	n/a	Cuts the CZ	(Fig. 16)
CZ-164-7	161.6	0.7	Cuts the CZ	(Fig. 16)
CZ-164-8	172	n/a		
CZ-164-9	116.6	n/a		
4400-1	80.7	n/a		
4400-2	84.1	n/a		
4400-3	90.1	n/a		
4400-4	95.6	n/a		

responsible for gold mineralization. On the contrary, the hydrothermal fluids during the late stage were gas poor, and with low salinities (~1.5 % NaCl equiv). The P-T conditions were estimated by the authors assuming lithostatic conditions at 215°±30° C and 800±400 bars for the main gold stage, and a temperature range between 175° and 250° C during the late gold stage.

In a similar study, fluid inclusions from multistage barite, calcite, and quartz veins at Gold Quarry were studied by Sha (1993), who recognized and modeled four distinct fluids during the hydrothermal event responsible for the gold and base metal mineralization. The fluid evolution at Gold Quarry began with a low salinity and moderate temperature fluid rich in CO_2. Through the main stage, CO_2 is still the main component during the mixing of meteoric fluids with connate fluids. Finally, a fluid with low salinity, low temperature, and CO_2 deficient represents the last episode of a collapsing hydrothermal system. Gold and base metals mineralization, according to Sha (1993), are associated with decalcification and fluid mixing during the early and main stages, respectively. Fluid mixing during the late stage produced a further cooling and oxidation of the fluid. The P-T conditions during the later hydrothermal stages were modeled by Sha (1993) at 230±20° C and 870±220 bars (early stage), 200±50° C and 850±300 bars (main stage), and 160±20° C and 100±50 bars (last stage).

In the same way, Lamb (1995) documented and compared fluid characteristics from the Meikle and Post/Betze deposits. Major features of this study are as follow: three hydrothermal stages are defined in both orebodies, starting with an early stage with salinities up to 20 wt % NaCl equiv. This was

followed with a gold stage with lower salinities, ≤10 wt % NaCl equiv, and T_h modes between 200° to 225 °C (Meikle, Purple Vein) and 150° to 210° C (Post/Betze). A late ore stage is represented by low P-T phases typical of supergene oxidation. Both deposits formed from H_2O-CO_2 fluids, causing gold precipitation at interpreted depths of about 3 kilometers.

In contrast, Groff et al. (2002) conducted fluid inclusions analyses from late-stage phases at the Betze and Carlin mines. Homogenization data from paragenetically late orpiment±calcite range from 108° to 182° C, with relatively moderate salinities in the range from 1.7 to 5.4 wt % NaCl equiv. This suite is followed paragenetically by a realgar±barite association with significant differences in both T_h and salinities relative to the latter suite. Low salinity fluids, 1.1 to 2.9 wt % NaCl equiv, are characterized with a T_h between 110° to 300° C implying mixing conditions. In addition, one of the more important results from this work is the evidence that reequilibration of fluid inclusions in the realgar±barite veins is due to geological and analytical factors that lead to overestimated the T_h temperatures (Groff et al., 2002).

As stated earlier, fluid inclusion microthermometric studies have been undertaken on late-stage barite and calcite veins to contrast both the hydrothermal fluid temperatures and salinities throughout mine levels and to provide further information on the late-stage barite±gold mineralization. Thus, the P-T-X conditions during late-stage veining at Chukar Footwall can be constrained through the data generated during this study and by comparison of this deposit

to the deposits briefly described above, revealing some similarities in terms of fluid evolution during the late-stage veining.

Most of the primary and pseudosecondary fluid inclusion data in barite and calcite yield two main field ranges of salinities and temperatures (Fig. 43): a relatively moderate temperature, low salinity group represented by barite veins from the deeper levels (e.g., 4400, 4500, and core holes CFU-141@ 142' and CFU-143@447') in contrast of a lower temperature, lower salinity group of both barite and calcite veins from shallower levels (e.g., 4730 and CZ). Such representation in the salinity-T_h diagram could be interpreted in terms of cooling and mixing conditions. Hence cooling in both groups is interpreted as a decrease in temperature of the hydrothermal fluid through time or with decreasing depth, triggering the precipitation of paragenetically late sulfides (pyrite± marcasite±bournonite?) and quartz as observed petrographically in the late-stage veins. Conversely, the differences between both groups' salinities could be explained by mixing phenomena whereupon cold, oxidizing meteoric waters migrated downward along active NW-trending structure networks during Tertiary times interacting with the host rocks and/or with hotter, more saline fluids. Therefore, mixing could explain these salinity and temperature differences between groups and the late-stage barite±gold±sulfides mineralization in the upper levels of the Chukar Footwall deposit. Barite and gold solubilities could have been affected by a decrease in salinity and increasing oxidizing conditions, respectively, due to the mixing conditions that were operating in the shallower mine levels (Sha,

1993; Arehart, 1996; Rimstidt, 1997). In addition, the presence of marcasite in the veins argues for a fairly acidic environment with the later barite+gold precipitation.

Compared with some other Carlin-type orebodies, such as the nearest Carlin or Gold Quarry deposits, the Chukar Footwall deposits shows a relatively similar fluid evolution during the late-stage hydrothermal event. Fluid composition seems to be H_2O-dominant with low salinities (0.4 to 4.2 wt % NaCl equiv). This coupled with the absence of CO_2 in the fluid inclusions and petrography suggest (1) the involvement of meteoric waters, (2) the lack of both decalcification and supergene weathering, and (3) the formation of contemporaneous calcite veins by fluid mixing. With regard to the depth of formation, given the brecciated and open-space fillings nature of the veins, the absence of gas-rich inclusions, and the lack of a supergene mineralogy (e.g., jarosite, goethite, or alunite) a shallow depth of about 1 km is suggested when constrained with data from Sha (1993), Groff et al. (2002) and Cline et al. (2005). Finally, the age of these veins may be constrained between the disemminated gold mineralization and the deposition of the Carlin Formation due to the presence of abundant stibnite in the Tertiary sediments (Rota, 1989).

In summary, the late-stage calcite and barite+gold veins record relatively low temperatures, and low salinities due to cooling and mixing of at least two different fluids. The H_2O rich-fluid was controlled by active NW-trending structures during late Tertiary extension. Likewise, extension may also have allowed the upward migration of hotter, more saline fluids from the deeper structural levels which may have produced a continuous and gradual record of

P-T-X conditions during mixing.

11. OREBODY FEATURES

The Chukar Footwall mine is currently mined by longhole-stope and cut-and-fill methods. It has produced about 146,000 ounces of gold with an average grade of 0.288 opt Au from unoxidized ore since underground operations began in 1996 (Joe Sagar, written communication, 2005).

The deposit consists of irregular stratabound orebodies within the SDrm units with a strong structural control. Figure 44 shows trace element concentrations with gold grades along a geochemical transect across the NNE-striking Magpie fault at the 4740 level, and the geochemical dispersion of elements near the Pheasant fault (4730 level) . Decreases in Au, As, Fe, and Sb away from the fault clearly reinforce that the Magpie fault acted as a feeder structure, channeling the hydrothermal fluids toward the anticline east limb. However, data from a geochemical transect from the CZ, a zone with dissolution-collapse breccias and low angle ENE- striking structures, revealed erratic, low gold values compared to those adjacent to the Magpie fault; thus, this structure, and possibly all ENE-striking ones, may be considered as barren structures. In addition to this structural control, a grade-thickness map generated by Newmont (2004) (Fig. 45) demonstrates that (1) gold orebodies form two main sub-parallel trends running approximately NNE, one along the southeast limb of the Chukar anticline and one parallel to the

Magpie fault; and (2) brittle deformation (e.g., NNE-striking structures and joints and shear fractures) played an important role in focusing ore fluids toward the Chukar anticline hinge and limbs, resulting in the formation of economic orebodies. A regional comparison on structural control of the Chukar Footwall with other deposits in the Carlin trend suggests late Eocene to Oligocene wrench tectonics, which accommodated extension at both local and regional scales, produced large-scale fractures with dilatant zones that led to the channeling and ultimately the deposition of gold and other metals (Cole, 1995; Tosdal and Nutt, 1999).

High grade gold mineralization at Chukar Footwall mine correlates well with strong decarbonatization and relatively high sulfide content (up to 3 vol. percent sulfides; Joe Sagar, personal communication, 2004). Silicification and dolomitization do not appear to be controls on gold grades. Another metallogenic characteristic of Chukar Footwall is that gold mineralization is hosted in both limestone and calc-silicate hornfels (exoskarn), reinforcing the concept pointed out by Thompson (2000) that carbonate lithologies are not the exclusive hosts for gold mineralization on the Carlin trend (Fig. 46). Geochemically, the economic gold orebody at Chukar Footwall exhibits anomalous concentrations, relative to unmineralized fresh rocks, of As, Fe, and Sb, with As and Fe as excellent pathfinders.

4720 LEVEL

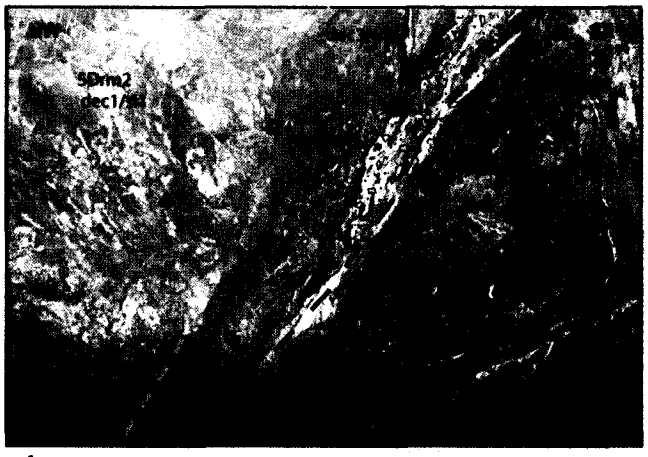

1. Au: 0.005 opt, As: 66.47 ppm, Fe: 15401 ppm, Sb: 23.38 ppm, Ba: 785.8 ppm, Zn: 255.4 ppm

2. Au: 0.021 opt, As: 141.0 ppm, Fe: 3901 ppm, Sb: 12.46 ppm, Ba: 2018 ppm, Zn: 258.1 ppm

3. Au: 1.069 opt, As: 5527 ppm, Fe: 35692 ppm, Sb: 431 ppm, Ba: 379.5 ppm, Zn: 177.5 ppm

4. Au: 0.007 opt, As: 80.29 ppm, Fe: 12487 ppm, Sb: 16.05 ppm, Ba: 92.58 ppm, Zn: 519.0 ppm

4730 LEVEL

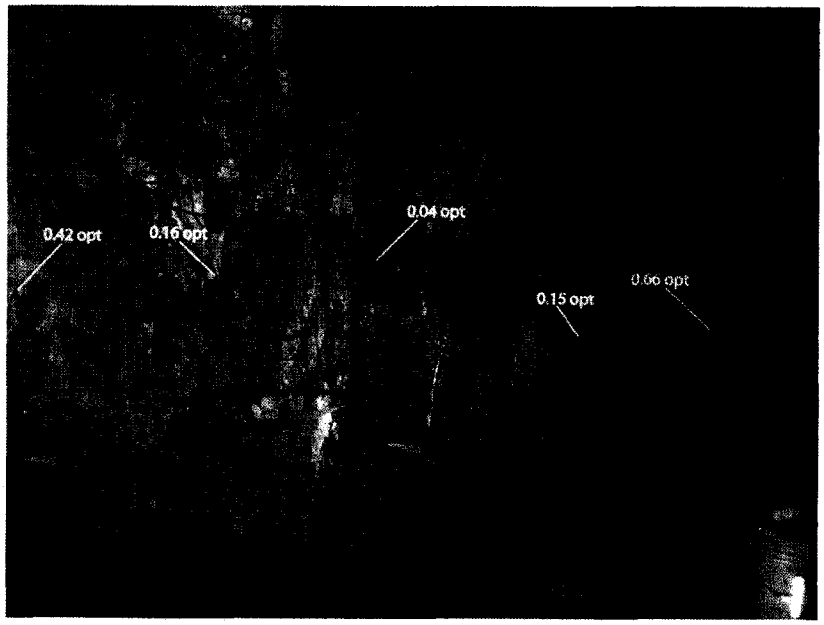

FIGURE 44. The Magpie fault-vein (4720 level), a NNE-striking fault, served as a pathway for ore fluids with As, Au, Fe, and Sb values decreasing away from the structure. Late, euhedral to subhedral stibnite and barite were deposite in open spaces within the fault breccia (4720 level). Decarbonatization and silicification are code as weak (dec1, si1) or strong (dec3,si3). Geochemical dispersion of elements near the Pheasant fault (4730 level), a NW-striking structure. Descending fluids circulated into the fault and fractures produced a lateral zonation of elements due to small scale remobilization, and allowing coprecipitation of abundant, visible gold with barite.

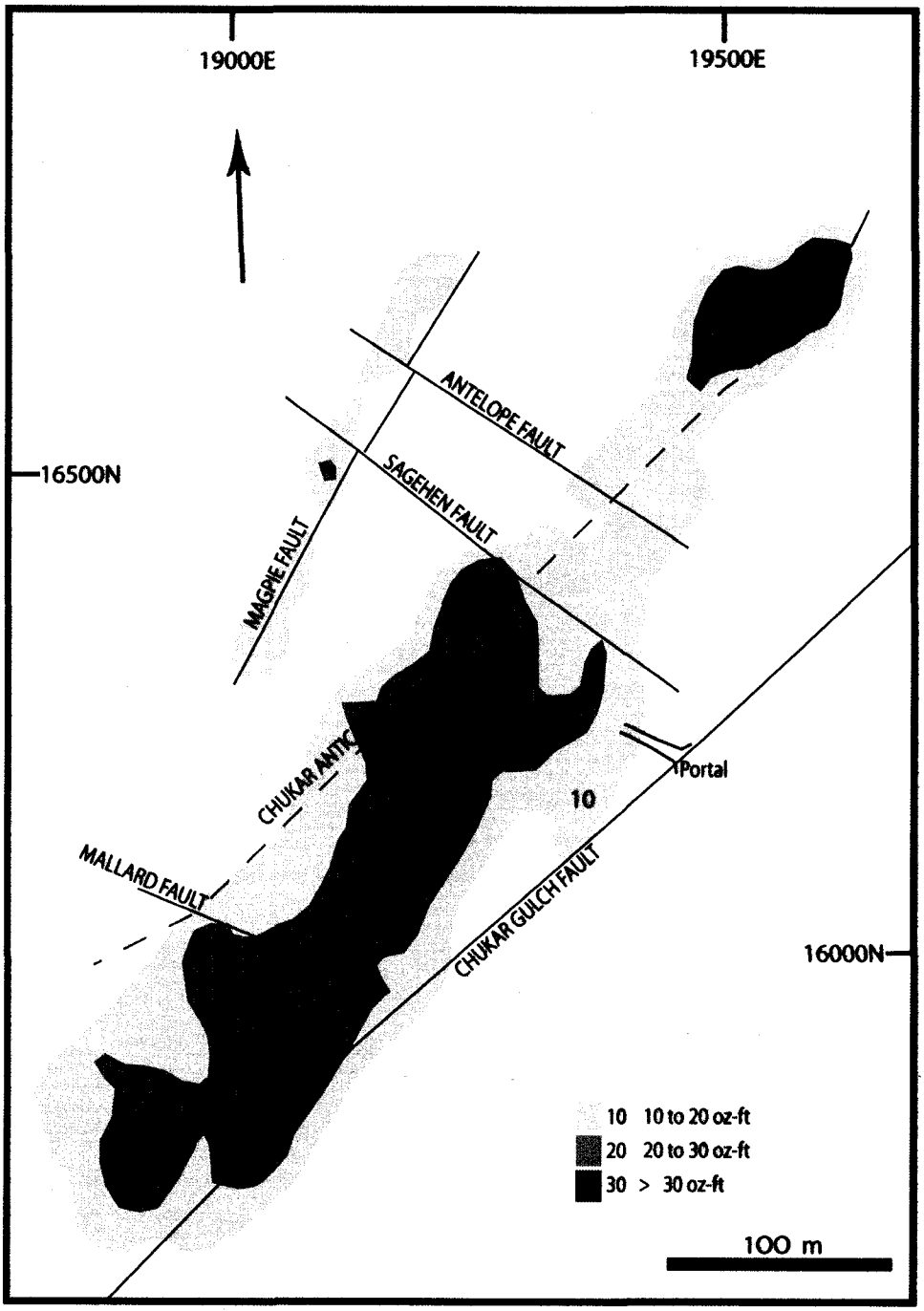

FIGURE 45. Grade thickness map of the Chukar Footwall mine. Approximate trace of the structures at the 4650 ft. elevation. Gold orebodies form two main sub-parallel linear trends: (1) the Chukar anticline trend and (2) the Magpie trend. The spatial distribution of gold orebodies relative to NE-striking faults and the east limb of the anticline shows a strong structural control on the Chukar Footwall deposit (Contour map from Newmont, 2004).

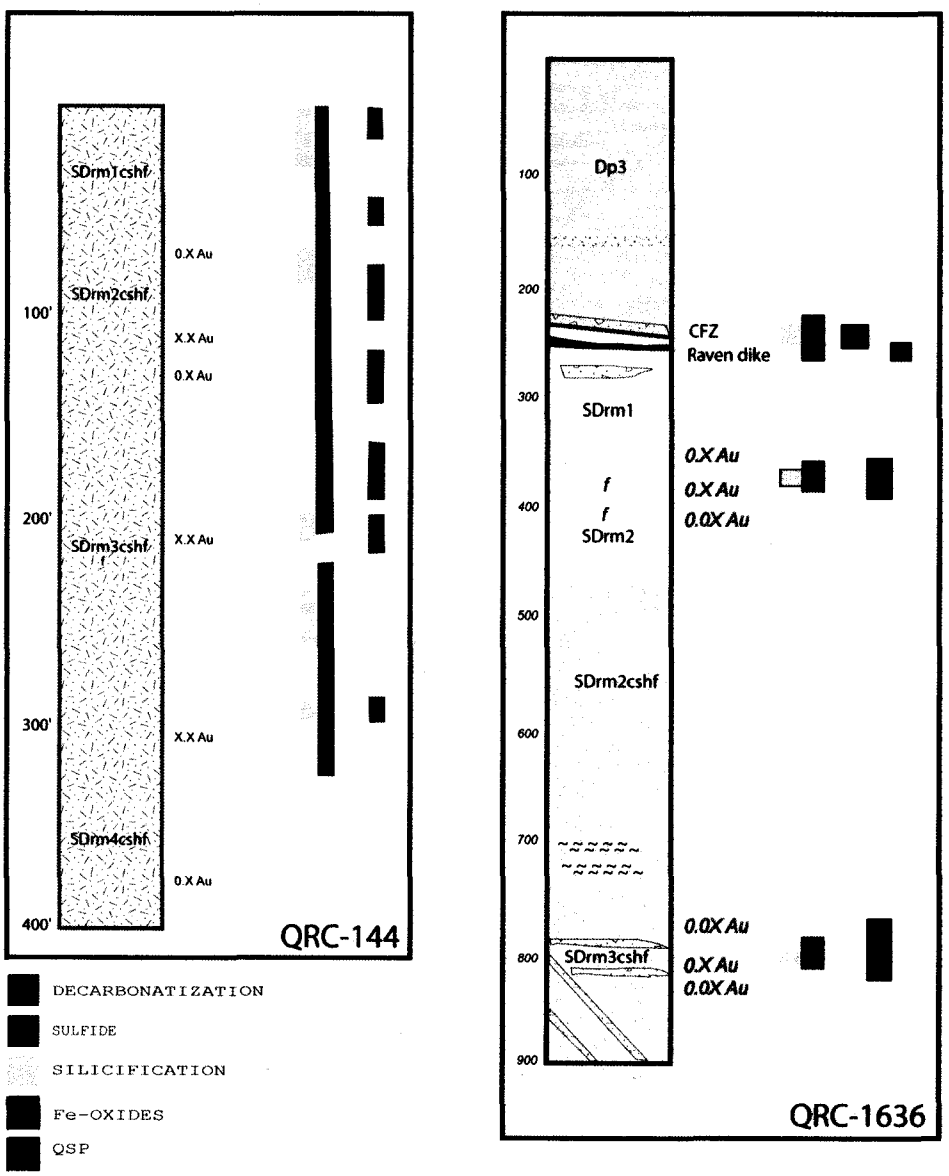

FIGURE 46. Core logs from drill-holes QRC-144 (west limb) and QRC-1636 (east limb) showing ore grades and associated hydrothermal alteration. Note high grade mineralization hosted in calc-silicate hornfels in hole QRC-144 , a good example that carbonate rocks are not the exclusive host-rocks for hosting Carlin-type orebodies (Core log data from Newmont, 2004).

12. THE METALLOGENIC EVOLUTION OF THE CHUKAR FOOTWALL DEPOSIT

Notwithstanding uncertainties reflected by both the lack of isotopic and fluid inclusion data from ore stage minerals and the geological data from the new, deeper mine levels, the body of data presented in this work allows some interpretations on the deposit's geological (Table 8) and metallogenic evolution as a proposal for a genetic model for the Chukar Footwall deposit. Figure 47 is a conceptual sketch showing the metallogenic model of the Chukar Footwall deposit.

Thick Paleozoic packages of shallow-to-deep water carbonates and siliciclastic rocks in the Tuscarora Mountains area were deformed during the Antler orogeny and intruded by several stocks and myriad of mafic dikes since Early Jurassic (cf. Evans, 1980). At Chukar Footwall, the host units (SDrm and Dp_3 packages (although the Dp_3 does not host economic mineralization) were folded into a northeast-trending anticline (D_1) during the Antler event or late Paleozoic orogenesis. Metasomatic metamorphism developed in the deeper mine levels and gave rise to diopside hornfels. This aureole could be linked to a blind Early Jurassic plutonic intrusion, which may lie buried toward the southwest of the Chukar Footwall deposit. At about 200 Ma lamprophyre dikes were emplaced along NNW-trending structures. Although the Raven dike is not a feeder structure, it is mineralized on some mine levels.

TABLE 8. TEMPORAL DIAGRAM OF THE TIMING OF GEOLOGICAL EVENTS AT CHUKAR FOOTWALL MINE AND SURROUNDINGS

TIME	EVENT	REMARKS
Antler/late Paleozoic /Sonoma orogenies	Chukar anticline (D1)	Trexler et al. (2004)
	NE-striking faults	Carbonates+clay+qtz+ barite±Sb
	NW-striking faults	Unhealed structures Intruded by Jurassic dikes Barite± visible gold
~200 Ma Early Jurassic	Plutonic intrusion Metamorphic aureole Raven dike	Blind, deep seated pluton(s) Pyroxene hornfels. QSP altered.
	Contact Zone	Dissolution-collapse breccias
40.9±4.0 Ma	Mineralization at Carlin East mine	Chakurian et al. (2003)
~ 37 Ma	Welches Canyon stock	Emplaced at shallow depths. Weak metamorphic aureole
~27 Ma	Alunite (late ore event) at Gold Quarry	Heitt (1992)
26.2±5.5 Ma	Initial cooling began at Chukar Footwall	AFT modeling data from the Raven dike (Fig. 13)
~20 Ma	Reactivation of structures due to Basin and Range extension	Muntean et al. (2001)
17.7±3.7 Ma	Latest thermal event at Chukar Footwall	AFT pooled age data from Raven dike
~15-14 Ma	Stibnite occurrence in the Carlin Fm. at Gold Quarry	Rota (1989)

Sometime between the intrusion of the Raven dike and the gold mineralization, a noteworthy pre-ore collapse breccia body formed during an early decarbonatization episode from metals-barren hydrothermal fluids as inferred from their geochemical signature. Combined $\delta^{16}O$ and $\delta^{13}C$ data and fluid inclusion microthermometric studies from these breccias suggest a significant component of meteoric waters. Further, the development of this breccia mass led to the formation of a structural and stratigraphic cap that may have prevented further upward migration of ore fluids into the overlaying Dp_3 unit.

Ore and late-ore forming events are spatially and temporally related to Eocene-Miocene hydrothermal systems that led to the formation of the Chukar Footwall orebodies, among other Carlin-type deposits, suggesting a relatively protracted period of hydrothermal activity and ore forming processes. However, it is not known if the micron-size gold, during the ore stage, was introduced in a single or multistage event. In such a scenario, the presence of visible, late-ore gold in the highest mine levels may imply that the ore-stage gold could have been remobilized by oxidized, circulating meteoric fluids along open NNW-trending structures and subsequent precipitation probably controlled by temperature, of visible gold with sulfates, carbonates, and sulfides at a redox boundary. The age of this mineralization event may possibly be loosely constrained as being Miocene, based on paragenetic similarities with other Carlin-type deposits (e.g., Chakurian et al., 2003; Emsbo and Hofstra, 2003), and in terms of the reactivation effects of older structures during the Miocene extension, although this extensional regime seems to be minor at Chukar

Footwall relatively to other areas of higher extensional rates in north-central Nevada.

The Chukar Footwall orebodies show many similarities to those along the Carlin trend and Jerritt Canyon district. These features include host-rock, mineral assemblages, and structural controls of the (a) hydrothermal alteration, (b) geochemical and isotopic signatures, and (c) mineralization. Significant differences at Chukar Footwall are (a) the paucity of As-bearing minerals, and (b) presence of abundant, visible gold.

Major and minor high angle northeast-trending structures were responsible for the upward migration of hydrothermal fluids during the ore stage that, together with other factors such as degree of hydrothermal alteration and fracture density of the SDrm units, control the location of the orebodies. Furthermore, the structural intersection between the later system and the Chukar anticline produced small-sized structural traps for upwelling ore fluids that defined a sub-parallel trend along the anticline axial surface. Finally, AFT age data from the altered Raven dike could suggest the age of the latest thermal event at about Early-Middle Miocene.

With regard to the youngest fault system, the high angle northwest-trending structures, a complex reactivation history is recorded by localized fault breccias and superimposed slickensides. Apparently, during Miocene extension,

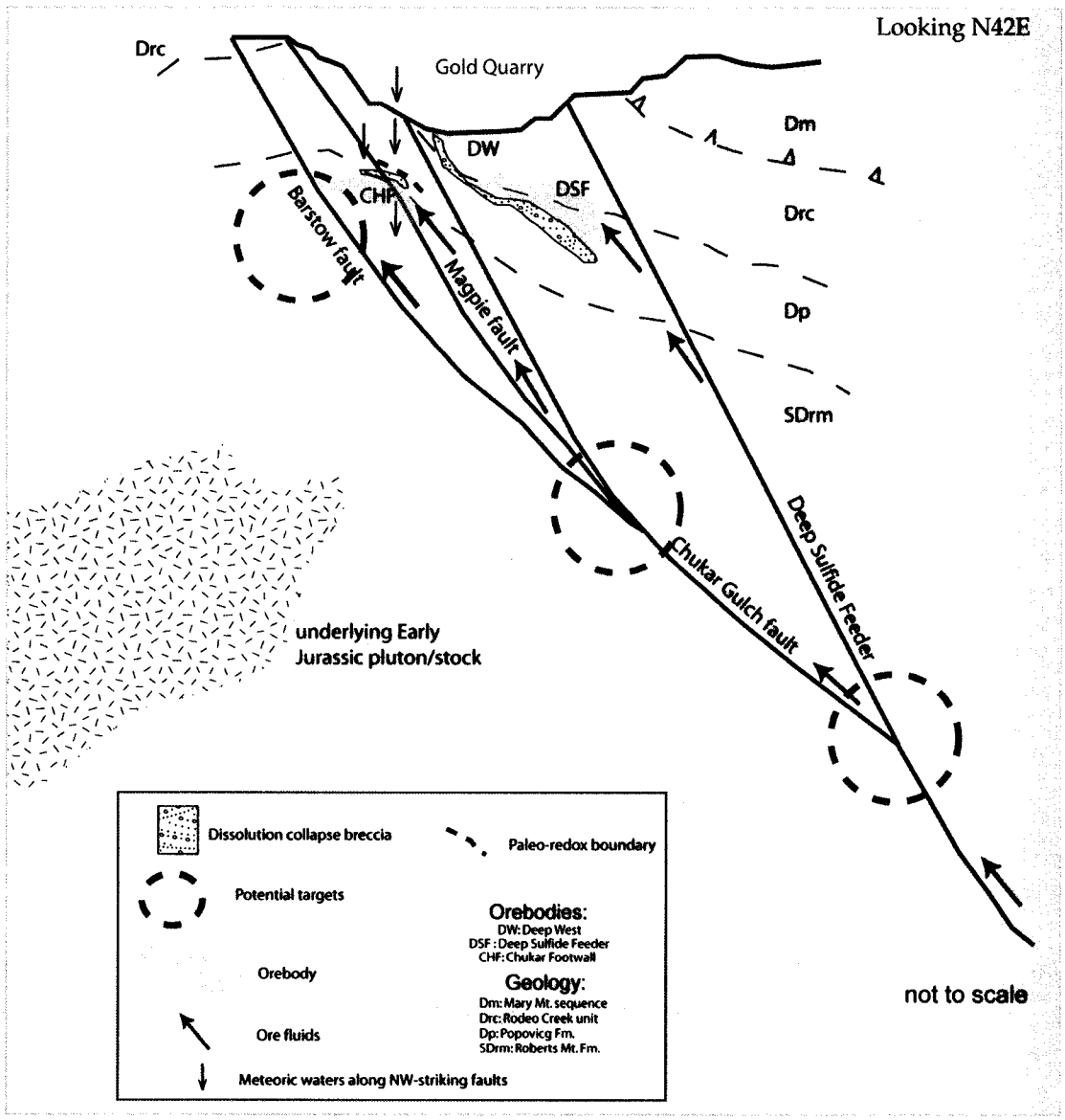

FIGURE 47. Schematic geologic cross section showing the metallogenic evolution of the Chukar Footwall orebody. It is possible to visualize a continuous evolution of the Gold Quarry hydrothermal system during Tertiary times. The common link among the gold systems at Gold Quarry are their relation to NE-striking structures and decarbonatization events. As a whole, the different mineralization styles present in Gold Quarry might be indicative of a continuum in ore forming processes related in space to the Deep Sulfide Feeder and Chukar Footwall faults. Tentatively, the Magpie fault is interpreted to be a splay off the nearby Chukar Gulch fault with its apparent structural control on orebodies at Chukar Footwall. The presence of late barite and visible gold in Chukar Footwall suggest precipitation under cool, low salinity, oxidizing conditions near the surface (Section from Bulletin 111, Gold Deposits in the Carlin Trend, Plate 3).

these structures were open to allow downward penetration of meteoric fluids that interacted with the SDrm units, allowing small scale metal remobilization (Fig 47). Thus, mineral precipitation along northwestern systems took place via cooling or fluid mixing processes at relatively low temperatures (< 200° C). Although this structural system may be regarded as a secondary ore-grade/control at mine scale, geological data reveals that these structures were also responsible for chanelizing ore-fluids due to the spatial relationship among structures, wall-rock alteration, and ore-grade distribution as observed, for example, in the 4770 level (Sagehen and Antelope faults) and the structural intersection between the Crown fault and northeast-trending structures near the Trucker Exploration drift. In this context, it is worth noting that (a) The possibility to envisage either a syn-mineralization event during Miocene extensional regime or (2) Most likely the Chukar Footwall mineralization could be linked to a huge, long-lived hydrothermal system(s) developed during the Eocene-Miocene throughout north-central Nevada wherein ore fluids upwelled along NE and NW-striking faults and interacted with meteoric fluids, and (3) These structures should be evaluated during mine exploration.

Finally, the metallogenetic evolution of the Chukar Footwall deposit has to be understood in terms of both local and regional geological settings. Ore (main stage) and post-ore paragenesis were modeled for the Betze deposits by Woitsekhowskaya and Peters (1998). According to this model-derived mineral assemblage, the paragenetic sequence of Carlin-type deposits in Nevada could be explained in terms of cooling, mixing, pH fluctuations and mineral solubilities

when hydrothermal fluids interact with the carbonate host rocks. Briefly, changes from acid to more alkaline fluid conditions due to decarbonatization reactions would trigger both silica and gold precipitation. Gold deposition is envisaged as a sulfidation process thus consuming the available Fe to form As-pyrite and -marcasite followed by As (orpiment and realgar) and Sb (stibnite) sulfides. The observed mineral assemblage and hydrothermal alteration patterns at Chukar Footwall are comparable and allow extension of the geochemical model for the Betze deposit. Furthermore, mineralogical and geochemical studies could suggest that iron for sulfidation was ultimately derived from hydrothermal ferroan dolomite, although other sources for iron from nearby igneous and skarn bodies could be expected. One final point worthy of note is the significant paucity of As minerals relative to other deposits suggesting that the H_2S was almost used up by earlier sulfides.

A key factor in the formation and localization of the Chukar Footwall deposit is its spatial association, regardless of age or type of mineralization, within the Gold Quarry gold systems (Main Quarry, Deep West, and Deep Sulfide Feeder, Fig. 47). The distribution of these gold systems shows a clear pattern consisting of successive NE-trending mineralized zones mainly between the Chukar Gulch fault and the Deep Sulfide Feeder fault. Early fluids were focused along these NE-striking structures and reactive rock packages, producing major collapse breccia bodies due to decarbonatization and gold and base metals deposition (Williams, 1992; Sha, 1993; Cole, 1995). As the Gold Quarry hydrothermal system evolved through time, later ore fluids encountered

the Deep Sulfide Feeder breccia zone that acted as a cap thus deflecting the upwelling fluids toward the footwall section of the Chukar Gulch fault and the hangingwall portions of the Magpie, Les, and Barstow faults. Later extension resulted in the activation of NW-striking structures and the downward movement of meteoric fluids that probably scavenged metals from the surrounding rocks. Fluid inclusion data suggest fluid mixing between two contrasting fluids that shifted the redox boundary producing the deposition of late-stage visible gold that is intergrown with sulfates and carbonates during the waning stages of the Gold Quarry hydrothermal system.

13. CONCLUSIONS

The major conclusions and results drawn from this study are:

1. The main host rocks at Chukar Footwall mine are the variable hydrothermally altered silty limestone of the Roberts Mountains Formation and calc-silicates (pyroxene hornfels). However, the micrites of the Popovich Formation and the Raven dike may host economic gold mineralization.
2. The dominant fault sets are NE and NNW-striking high angle structures forming a conjugate system with an angular separation of 85°. A small number of kinematic indicators from these systems reveal predominant right oblique normal slip and minor normal and strike-slip movements developed in a homogenous kinematic domain for the entire deposit. Fault reactivation, linked with late Tertiary extension, is relatively common in both systems producing openings and brecciation along the NNW structures that channalized fluids responsible for a late-ore mineralization event characterized by sulfides, barite, and visible gold.
3. Steeply dipping dikes intruded along NNW-striking structures, produced a weak thermal alteration within the surrounding rocks. Their age is constrained at 200±5.1 Ma by U-Pb dating on zircon.
4. In the deeper mine levels, calc-silicate rocks are represented by hornblende hornfels affecting both the SDrm and Dp units. The presence of diopside suggests a peak temperature range between 400-600 °C.

5. The geochemical signatures are characterized by typical Carlin-type deposits pathfinders. Gold correlates well with Cu, Hg, Tl, As, and Zn. Another elemental suite of elements is represented by the association of As, Sb, Te, and Tl.
6. Decalcification reactions in the host rocks, which are spatially related and controlled with major and minor structures, was the leading mechanism for both the $\delta^{13}C$ and $\delta^{18}O$ isotopic shifts observed along perpendicular transects on major structures. Hence, depleted $\delta^{18}O$ values occur near the structure where decalcification is stronger while relatively enriched $\delta^{18}O$ values are generally observed further from it.
7. The clustering of $\delta^{34}S$ values from several sulfides suggests a common source for sulfur. This observation may explain the paucity of late phases such as realgar and orpiment at Chukar Footwall due to depleted H_2S by precipitation of earlier sulfides phases. $\delta^{34}S$ isotopic differences between sulfides and sulfates can be attributed to different sources and temperatures. Sulfur isotope data of sulfides may indicate leaching from the host rocks. However, sulfate isotope data from barites probably represent derivation from Paleozoic sedex barite and sulfide deposits.
8. Apatite fission-track data indicate a thermal event at 17.7±3.7 Ma interpreted as a regional age reset of apatite ages due to (1) volcanism and extension or (2) local scale hydrothermal event in the vicinity of Gold Quarry. Furthermore, initial cooling of the Chukar Footwall system began at 26.2±5.5 Ma with cooling below 125°C at 17.7±3.7 Ma (Fig. 13).

9. Microthermometric data from late stage mineralization barite± calcite± sulfide± visible gold veins revealed evidence of fluid mixing during this late event. Additionally, the $\delta^{18}O$ data on carbonate rocks indicate ore fluid mixing with high level oxidized meteoric fluids. During Late Tertiary extension meteoric fluids flowed into open NW-trending structures, producing gold and sulfate coprecipitation along a paleo-redox boundary. Also, extension allowed the ascension of hotter, more saline fluids thus producing the observed continuum in salinities and temperatures through the deposit. Tentatively, in the absence of absolute ages, the age of this latest hydrothermal event is no younger than 17 Ma.
10. The Chukar Footwall orebody forms part of the Gold Quarry gold system to which the same basic genetic ideas may apply. The metallogenic evolution of the Chukar Footwall deposit began with a significant pre-ore episode of dissolution-collapse breccia between the Roberts Mountains Formation and the Popovich Formation that formed a semi-impermeable cap to later hydrothermal fluids. During ore-stage, ore fluids were channelized along major active NE-striking structures, and probably micron-size Au and base metals precipitation took place as a result of sulfidation and a shift toward higher pH values. During Late Miocene extension, NW-striking faults were open for descending cool, weakly saline meteoric fluids and ascending relatively hotter, more saline hydrothermal fluids producing metal remobilization along and visible gold

precipitation along structures. It seems that the common link among the Gold Quarry gold systems is its structural relation to the Deep Sulfide Feeder and Chukar Gulch faults, which served as major conduits for hydrothermal fluids.

14. REFERENCES

Altamirano-Morales, C., 1999, Structural control and alteration at the Deep Star deposit, Eureka County, Nevada, [M.S. Thesis]: University of Nevada, Reno, 78 p., 1 plate.

Arehart, G., Chryssoulis, S., and Kesler, S. 1993, Gold and arsenic in iron sulfides from sediment-hosted disseminated gold deposits: implications for depositional processes: Economic Geology, v. 88, p. 171-185.

Arehart, G., Foland, K., Naeser, C., and Kesler, S., 1993, $^{40}Ar/^{39}Ar$, K-Ar, and fission-track geochronology of sediment-hosted disseminated gold deposits at Potz/Betze, Carlin Trend, northeastern Nevada: Economic Geology, v. 88, p.622-646.

Arehart, G., 1996, Characteristics and origin of sediment-hosted disseminated gold deposits: a review: Ore Geology Reviews, v. 11, p.383-403.

Arehart, G., 1998, Isotopic signature of hydrothermal sulfates from Carlin-type ore deposits, *in* Arehart,G. and Hulston, J.R., ed, Proceedings of the 9th International Symposium on Water-Rocks Interaction, Balkema, p.517-520.

Arehart, G., 2001, Geochemistry of wallrock carbonates in Carlin-type deposits: 2001 CREG Proposal: Geochemistry of wallrock carbonates in CTDs, 5 p.

Armstrong, A.K., Theodore, T.G., Oscarson, R.L., Kotlyar, B.B., Harris, A.G., Bettles, K.H., Lauha, E.A., Hipsley, R.A., Griffin, G.L., Abbot, E.A., and Cluer, J.K., 1998, Preliminary facies analysis of the Silurian and Devonian autochthonous rocks that host gold along the Carlin Trend, Nevada: U.S. Geological Survey Open-File Report 98-338, p.38-68

Armstrong, A.K., Bagby, W.C., Ekburg, C., and Repetski, J., 1987, Petrographic and scanning electron microscope studies of samples from the Roberts Mountains and Popovich formations, Carlin Mine area, Eureka Country,

Nevada: U.S. Geological Survey Bulletin 1684, 23 p.

Bogen, N. and Schweickert, R., 1985, Magnitude of crustal extension across the northern Basin and Range province: Contraints from paleomagnetism: Earth and Planetary Science Letters, v. 75, p.93-100.

Bucher, K. and Frey, M, 2002, Petrogenesis of Metamorphic Rocks, 7th edition: Springer, Berlin, 341p.

Burchfield, B., Cowan, D., and Davis, G., 1992, Tectonic overview of the Cordilleran orogen in the western United States, *in* Burchfield, B., Lipman, P., and Zoback, M., eds, The Cordilleran Orogen: The Conterminous U.S., The Geology of North America, Volume G3: Geological Society of America, p. 407-480.

Campbell, K., Delwiche, B., Heath, K., Heimgartner, M., Koehler, R., Lopez, C., Mach, C., Ruiz-Parraga. J., Turner, R., and Sturmer, D., 2005, Cenozoic Tectonic Elements of the Western United States: Geology 702b Poster (unpublished), UNR.

Carpenter, J., Carpenter, D., and Dobbs, S., 1994, Antler orogeny: Paleostructural analysis and constraints on plate tectonic models with a global analogue in southeast Asia, *in* S.W. Dobbs and W.J. Taylor,eds, 1994, Structural and Stratigraphic Investigations and Petroleum Potential in Nevada, with Special Emphasis South of the Railroad Valley Producing Trend: Nevada Petroleum Society Conference Volume II, p. 187-240.

Chakurian, A.M., 2001, Age of mineralization at the Carlin East Mine, Eureka County, Nevada [M.S. Thesis]: University of Nevada, Reno, 186 p.

Chakurian, A., Arehart, G., Donelick, R., Zhang, X., and Reiners, P., 2003, Timing Constraints of Gold Mineralization along the Carlin Trend Utilizing Apatite Fission-Track, $^{40}Ar/^{39}Ar$, and Apatite (U-Th)/He Methods: Economic Geology, v. 98, p. 1159-1171.

Cline, J., Hofstra, A., Muntean, J., Tosdal, R., and Hickey, K., 2005, Carlin-Type Gold Deposits in Nevada: Critical Geologic Characteristics and Viable Models, *in* Hedenquist, J., Thompson, J., Goldfarb, R., and Richard, J., eds, Economic Geology 100th Anniversary Volume,p.451-484.

Cole, D.M., 1995, Structural evolution of the Gold Quarry deposit and implication for development, Eureka County, Nevada, [M.S. Thesis]: Colorado State University, Fort Collins, 78 p.

Cook, H.E., and Corboy, J.J., 2004, Great Basin Paleozoic carbonate platform:

facies, facies transitions, depositional models, platform architecture, sequence stratigraphy, and predictive mineral host models: U.S. Geological Survey Open-File Report 2004-1078, 129 p.

Craig, R.R., and Wakefield, T.W., 1991, Geochemistry of the Carlin Trend, in Craig, R., ed., Geology and Geochemistry of the Carlin Trend: Association of Exploration Geochemists, Field Trip 4, p. 1-7.

Cress, L.D., 1972, Geology of the Carlin window area, Eureka County, Nevada [M.S. Thesis]: California State University, San Jose, 103 p.

Dewitt, A., 1999, Alteration, Geochemical dispersion, and Ore Controls at the SSX Mine, Jerritt CanyonDistrict, Elko County, Nevada [M.S. Thesis]: University of Nevada, Reno, 95 p.

Dickinson, W. and Gehrels, G., 2000, Sandstone petrofacies of detrital zircon samples from Paleozoic and Triassic strata in suspect terranes of northern Nevada and California, *in* Soreghan, M. and Gehrels, G., eds, Paleozoic and Triassic paleogeography and tectonic of western Nevada and northern California: Geologica Society of America Special Papers 347, p.151-171.

Dickinson, W., 2006, Geotectonic evolution of the Great Basin: Geosphere, v.2, no.7, p. 353-368.

Emsbo, P., Hofstra, A., Zimmerman, J.M., and Snee, L., 1996, A Mid-Tertiary age constraint on alteration and mineralization in igneous dikes on the Gold Strike property, Carlin Trend, Nevada: GSA Abstracts with Programs, v. 28, n. 7, p. A476.

Emsbo, P., Hofstra, A., Lauha, E., Griffin, G., and Hutchinson, R., 2003, Origin of high-grade gold ore and source of ore fluid components in the Meikle gold deposit, northern Carlin trend, Nevada: Economic Geology, v.98, p. 1069-1105.

Emsbo, P. and Hofstra, A., 2003, Origin and Significance of Postore Dissolution Collapse Breccias Cemented with Calcite and Barite at the Meikle Gold Deposit, Northern Carlin Trend, Nevada: Economic Geology, v. 98, p.1243-1252.

Erickson, R., Silberman, M., and Marsh, S., 1978, Age and composition of igneous rocks,Edna Mountain Quadrangle, Humboldt County, Nevada: Journal of Research USGS, v. 6, p. 727-743.

Ettner, D.C., 1989, Stratigraphy and structure of the Devonian auochthonous rocks, North-Central Carlin Trend of the Southern Tuscarora Mountains, Northern Eureka County, Nevada, [M.S. Thesis]: Idaho State University, Pocatello, 177 p.

Evans, J. and Theodore, T., 1978, Deformation of the Roberts Mountains Allochthon in North-Central Nevada: U.S. Geological Survey Professional Papers 1060,18 p.

Evans, J.G., 1980, Geology of the Rodeo Creek and Welches Canyon quadrangles, Eureka County, Nevada : U.S. Geological Survey Bulletin 1473, 81 p.

Evans, D.C., 2000, Carbonated-hosted breccias in the Meikle mine, Nevada, and their relationships with gold mineralization: [M.S. Thesis]: Golden, Colorado, Colorado School of Mines, 266 p.

Farmer, G., 1983, Origin of Mesozoic and Tertiary granite in the western U.S. and implications for pre-Mesozoic crustal structure, [Ph.D. Dissertation]: University of California, Los Angeles, 263 p.

Fleck, R., Theodore, T., Wojcicki, A., and Meyer, C., 1998, Age and Possible Sources of Air-Fall Tuffs of the Miocene Carlin Formation, Northern Nevada, *in* Tosdal, R., ed., Contributions to the gold metallogeny of northern Nevada: U.S. Geological Survey Open-File Report 98-338, p. 176-192.

Friedman, G., 1965, Terminology of crystallization textures and fabrics in sedimentary rocks: Journal of Sedimentary Petrology, v.35, p. 643-655.

Friedman, I., and O'Neil, J., 1977, Compilation of Stable Isotope Fractionation Factors of Geochemical Interest: USGS Professional Paper 440-KK, 12 p., 49 figures.

Gabrielse, H., Snyder, W., and Stewart, J., 1983, Sonoma orogeny and Permian to Triassic tectonism in western North America: Geology, p.484-486.

Grauch, V., Rodriguez, B., and Wooden, J., 2003, Geophysical and Isotopic Constraints on Crustal Structure Related to Mineral Trends in North-Central Nevada and Implications for Tectonic History: Economic Geology, v. 98, p. 269-286.

Green, P., Duddy, I., Laslett, G., Hegarty, K., Gleadow, A., and Lovering, J., 1989, Thermal annealing of fission tracks in apatite: Quantitative modeling

techniques and extension to geological time scales: Chemical Geology, v. 79, p.155-182.

Groff, J., Campbell, A., and Norman, D., 2002, An Evaluation of Fluid Inclusion Microthermometric Data for Orpiment-Realgar-Calcite-Barite-Gold Mineralization at the Betze and Carlin MInes, Nevada: Economic Geology, v. 97, p.1341-1346.

Guzzetta, G., 1984, Kinematics of stylolite formation and physics of the Pressure-solution process: Tectonophysics, v. 101, p.383-394.

Harlan, J.B., Harris, D.A., Mallette, P.M., Norby, J.W., Rota, J.C., and Sagar, J.J., 2002, Geology and Mineralization of the Maggie Creek District, in Thompson, T.B., Teal, L., and Meeuwig, R.O., eds, Gold deposits of the Carlin Trend: Nevada Bureau of Mines and Geology, Bulletin 111, p.115-142.

Harris, M. and Radtke, A., 1976, Statistical study of selected trace elements with reference to geology and genesis of the Carlin gold deposit, Nevada: U.S. Geological Survey Professional Paper 960, 21 p.

Heitt, D., 1992, Characterization and Genesis of Alunite from the Gold Quarry Mine, Eureka County, Nevada , [M.S. Thesis]: Eastern Washington University, Cheney, 98 p., 1 plates.

Heitt, D., Dunbar, W., Thompson, T., and Jackson, R., 2003, Geology and geochemistry of the Deep Star gold deposit, Carlin Trend, Nevada: Economic Geology, v. 98, no. 6, p. 1107-1135.

Henry, C.D. and Ressel, M.W., 2000, Eocene magmatism of northeastern Nevada: the smoking gun for Carlin-type gold deposits, *in* Cluer, J.K., Price, J.G., Struchsacker, E.M., Hardyman, R.F., and Morris, C., eds., Geology and Ore deposits 2000: The Great Basin and Beyond, Proceedings, p.365-388.

Henry, C., Faulds, J., Boden, D., and Ressel, M., 2001, Timing and Styles of Cenozoic Extension Near the Carlin Trend, Northeastern Nevada: Implications for the formation of Carlin-Type Gold Deposits, *in* Shaddrick, D., Zbinden, E., Mathewson, D., and Prenn, C.,eds., Regional Tectonics and Structural Control of Ore: The Major Gold Trends of Northern Nevada, Geological Society of Nevada, Special Publication 33, p. 115-128.

Hofstra, A.H., 1994, Geology and Genesis of the Carlin-Type Gold Deposits in the Jerrit Canyon District, Nevada, [Ph.D. Dissertation]: University

of Colorado, Boulder, 719 p.

Hofstra, A.H., and Cline, J.S., 2000, Characteristics and models for Carlin-Type gold deposits, in Thompson, T.B., ed., Reviews in Economic Geology: Society Economic Geologists, v. 13, p. 163-220.

Howard, K., Kistler, R., Snoke, A., and Willden, R.,1979, Geologic map of the Ruby Mountains, Nevada: USGS Map I-1136 (1/125,000).

Hutcherson, S., 2002, Geology, Geochemistry and Alteration of Zone 5 of the Murray Mine, Jerritt Canyon District, Elko County, Nevada, [M.S. Thesis]: University of Nevada, Reno, 114 p., 4 plates.

Ilchik, R.P., and Barton, M.D., 1997, An amagmatic origin of Carlin-Type gold deposits: Economic Geology, v. 92, p. 269-288.

Jackson, M., Lane, M., and Leach, B., 2002, Geology of the West Leeville deposit, in Thompson, T.B., Teal, L., and Meeuwig, R.O., eds, Gold deposits of the Carlin Trend: Nevada Bureau of Mines and Geology, Bulletin 111, p.106,-114

Johnston, M. and Arehart, G., 2003, Composition, Extent, and Zonation of Wallrock Alteration Associated with the Chukar Footwall Carlin-type Deposit, Eureka County, Nevada. Newmont internal report, 50 p.

Johnston, M.K. and Ressel, M.W., 2004, Carlin-Type and distal disseminated Au-Ag deposits: Related distal expressions of Eocene intrusive centers in north-central Nevada: SEG Newsletter, no. 59, p.12-14.

Johnston, M., 2005, Late Eocene tectonism and magmatism in the Great Basin, USA, and the development of porphyry-related, pollymetallic vein, distal disseminated, and Carlin-type deposits: Geological Society of America Abstracts with Program, v. 37, p. 418.

Ketner, K. and Smith, J., 1974, Folds and overthrusts of late Jurassic or early Cretaceous age in northern Nevada: Journal Research US Geological Survey, v. 2, p. 417-419.

Ketner, K., 1991, Stratigraphy, Sedimentology, and Depositional Conditions of Lower Paleozoic Western-Facies rocks in Northeastern Nevada, *in* Cooper, J. and Stevens, C., eds, Paleozoic Paleogeography of the Western United States-II: Pacific Section SEPM, v. 67, p.735-746.

Kuehn, C., 1989, Studies of disseminated gold deposits near Carlin, Nevada: Evidence for a deep geologic setting of ore formation [Ph.D dissertation]:

Pennsylvania State University, University Park, 396 p.

Kuehn, C., and Rose, A., 1992, Geology and geochemistry of wall-rock alteration at the Carlin gold deposit, Nevada: Economic Geology, v.87, p.1697-1721.

Leach, T., 1999, Petrological evaluation of the alteration and mineralization at Deep Star, Deep Post, and LBB. Newmont internal report, 55 p.

Lamb, J., 1995, A Petrography and Fluid Inclusion Study of the Purple Vein and Post/Betze Orebodies, Carlin, Nevada [M.S. Thesis]: University of Nevada, Las Vegas, 161 p.

Lewis, P., 2001, Structural analysis of gold deposits of the Carlin Trend, Elko and Eureka Counties, Nevada. Newmont Mining Corp. and Barrick Goldstrike Mines Inc. Internal Report, 166 p.

Madrid, R., 1987, Stratigraphy of the Roberts Mountains Allochthon in north-central Nevada [Ph.D dissertation]: Stanford University, 341 p.

Mariño, F.A., 2003, Geology of the Deep Post mine, Northern Carlin Trend, Nevada, [M.S. Thesis]: University of Nevada, Reno, 118 p.

McComb, M., 1993, Petrographic examination and semiquantitative XRD-XRF analysis of Gold Quarry dike rocks: Newmont Exploration Ltd., Memorandum to D. Pietz, November 23, 1993, 19 p.

McCrossan, R.G., 1958, Sedimentary "boudinage" structures in the Upper Devonian Ireton Formation of Alberta: Journal of Sedimentary Petrology, v. 28, p. 316-320.

Mortensen, J., Thompson, J., and Tosdal, R., 2000, U-Pb Age Constraint on Magmatism and Mineralization in the Northern Great Basin, Nevada, *in* Cluer, J., Price, J., Struhsacker, E., Hardyman, R., and Morris, C., eds, Geology and Ore Deposits 2000: The Great Basin and Beyond: Geological Society of Nevada Symposium Proceedings, p. 416-438.

Mullens, T.E., 1980, Stratigraphy, Petrology, and Some Fossil Data of the Roberts Mountains Formation, North-Central Nevada: U.S. Geological Survey Professional Paper 1063, 67 p.

Muntean, J., Tarnocai, C., Coward, M., Rouby, D., and Jackson, A., 2001, Styles and Restoration of Tertiary Extension in North-Central Nevada, *in* Shaddrick, D., Zbinden, E.,Mathewson, D., and Prenn, C.,eds., Regional Tectonics and Structural Control of Ore: The Major Gold Trends

of Northern Nevada, Geological Society of Nevada, Special Publication 33, p. 55-69.

Moore, S., 2001, Ages of fault movement and stepwise development of structural fabrics on the Carlin Trend: Regional tectonics and structural controls of ore: The major gold trends of Northern Nevada: Geological Society of Nevada Special Publication 33, p. 71-89.

Newmont, 2003, Chukar Footwall, Geologic map at 4650 elevation, 1/1,200

Newmont, 2004, Chukar Footwall. Grade Thickness Map, 1/1,200

Norby, J.W. and Orobona, M.J., 2002, Geology and mineral systems of the Mike deposit, in Thompson, T.B., Teal, L., and Meeuwig, R.O., eds, Gold deposits of the Carlin Trend: Nevada Bureau of Mines and Geology, Bulletin 111, p.143,-167.

Ohmoto, H., and Rye, R., 1979, Isotopes of sulfur and carbon, *in* Barnes, H.L., ed., Geochemistry of Hydrothermal Ore Deposits, 2nd ed.: New York, Wiley, p. 509-567.

Ohmoto, H., 1986, Stable isotope geochemistry of ore deposits: Reviews in Mineralogy, v.16, p. 491-559.

Oldow, J.,1984, Evolution of a late Mesozoic back-arc fold and thrust belt, northwestern Great Basin, U.S.A.: Tectonophysics, v. 102, p. 245-274.

Papke, K.G., 1984, Barite in Nevada: Nevada Bureau of Mines and Geology, Bulletin 98, 125 p.

Pinckney, D., and Rye, R., 1972, Variation of O^{18}/O^{16}, C^{13}/C^{12}, Texture, and Mineralogy in Altered Limestone in the Hill Mine, Cave-in-District, Illinois: Economic Geology, v. 67, p. 1-18.

Radtke, A., Rye, R., and Dickson, F., 1980, Geology and Stable Isotope Studies of the Carlin Gold Deposit, Nevada: Economic Geology, v. 75, p. 641-672.

Radtke, A. S., 1985, Geology of the Carlin gold deposit, Nevada: U.S. Geological Survey Professional Paper, 1267, 124 p.

Riley, B., Snyder, W., and Gehrels, G., 2000, U-Pb detrital zircon geochronology of the Golconda allochthon, Nevada , *in* Soreghan, M. and Gehrels, G., eds, Paleozoic and Triassic paleogeography and tectonic of western Nevada and northern California: Geologica Society of America Special Papers 347, p.65-75.

Rimstidt, J., 1997, Gange Mineral Transport and Deposition, *in* Barnes, H.L., ed., Geochemistry of Hydrothermal Ore Deposits, 3 rd ed.: New York, Wiley, p. 487-515.

Ramsay, J. and Huber, M., 1987, The Techniques of Modern Structural Geology, Volume II: Folds and Fractures: Academic Press, 700 p.

Ressel, M., Noble, D., Henry, C, Trudel, W., 2000, Dike-hosted ores of the Beast deposit and the importance of Eocene magmatism in gold mineralization of the Carlin trend, Nevada: Economic Geology, v. 95, no.7, p. 1417-1444.

Ressel, M. and Henry, C., 2006, Igneous Geology of the Carlin Trend, Nevada: Development of the Eocene Plutonic Complex and Significance for Carlin-Type Gold Deposits: Economic Geology, v. 101, pp. 347-383.

Roberts, R.J., Hotz, P.E., Gilluly, J., and Ferguson, H.G., 1958, Paleozoic rocks of North-Cental Nevada: American Assoc. Petroleum Geologist Bulletin, v. 42, no. 12, p. 2813-2857.

Roberts, R.J., 1960, Alignment of mining districts in North-Central Nevada: Geological Survey Professional Papers 400-B, p. B17-B19.

Roedder, E., 1984, Fluid Inclusions: Reviews in Mineralogy, v. 12, 644 p.

Rosenberg, P. and Champness, P., 1989, Zincian dolomites and associated carbonates from the Warynski mine, Poland: An AEM investigation: American Mineralogist, v. 74, p. 461-465.

Rota, J., 1989, Stibnite Occurrence in Tertiary Sediments: Newmont Mining Corporation Memorandum, 3p.

Rota, J.C., 1991, A review of Gold Quarry geology, in Craig, R., ed., Geology and Geochemistry of the Carlin Trend: Association of Exploration Geochemists, Field Trip 4, p. 1-24.

Rye, R., and Ohmoto, H., 1974, Sulfur and Carbon Isotopes and Ore Genesis: A Review: Economic Geology, v. 69, p. 826-842.

Rye, R., Shawe, D., and Poole, F., 1978, Stable Isotopes Studies of Bedded Barite At East Northumberland Canyon in Toquima Range, Central Nevada: Journal of Research USGS, v.6, no.2, p. 221-229

Sagar, J.J, 2000a, The Chukar Footwall model. Newmont Internal Report, 7p.

Sagar, J.J., 2000b, Gold Quarry mine tour: Geological Society of Nevada Symposium Geology and Ore deposits 2000, p. 81-83.

Saller, A. and Dickinson, W., 1982, Alluvial to marine facies transition in the Antler overlap sequence, Pennsylvanian and Permian of north-central Nevada: Journal of Sedimentary Petrology, v. 52, p.925-940.

Schmauder, G., Arehart, G., and Donelick, R., 2005, Thermal and Chemical Profiling of the Bald Mountain District, White Pine County, Nevada: 2004 Year-End Research Meeting, CREG-University of Nevada, Reno, 29 p.

Schweickert, R., Bogen, N., Girty, G., Hanson, R., and Merguerian, C., 1984, Timing and structural expression of the Nevadan orogeny, Sierra Nevada, California: Geological Society of America Bulletin, v. 95, p.967-979.

Seedorff, E., 1991, Magmatism, extension, and ore deposits of Eocene to Holocene age in the Great Basin- Mutual effects and preliminary genetic relationships: Geology and ore deposits of the Great Basin Symposium, Geological Society of Nevada, Reno, Proceedings, p. 133-178.

Sha, P., 1993, Geochemistry and genesis of sediment-hosted disseminated gold mineralization at the Gold Quarry mine, Nevada, [Ph.D. Dissertation]: University of Alabama, Tuscaloosa, 229 p.

Stewart, J., Walker, G., and Kleinhampl, F., 1975, Oregon-Nevada lineament: Geology, v.3, p.265-268.

Stewart, J., 1980, Geology of Nevada: A discussion to accompany the geological map of Nevada: Nevada Bureau of Mines and Geology Special Report 4, 136 p.

Speed, R., Elison, M., and Heck, F., 1988, Phanerozoic Tectonic Evolution of the Great Basin,*in* Ernst, W.,editor, Metamorphism and Crustal Evolution of the Western United States: Rubey Volume VII, Prentice Hall, New Jersey, p.572-605.

Stenger, D., Kesler, S., Peltonen, D., and Tapper, C., 1998, Deposition of gold in Carlin-type deposits: The role of sulfidation and decarbonation at Twin Creeks, Nevada: Economic Geology, vo. 93, p. 201-215.

Stenger, D., Kesler, S., and Vennemann, T., 1998, Carbon and oxygen isotope zoning around Carlin-type gold deposits: a reconnaissance survey at Twin Creeks, Nevada: Journal of Geochemical Exploration, v. 63, p. 105-121.

Taylor, H.P., 1997, Oxygen and Hydrogen Isotope Relationships in Hydrothermal Mineral Deposits, *in* Barnes, H.L., ed., Geochemistry of Hydrothermal Ore Deposits, 3 rd ed.: New York, Wiley, p. 229-302.

Teal, L. and Jackson, M., 2002, Geologic overview of the Carlin Trend gold deposits, in Thompson, T.B., Teal, L., and Meeuwig, R.O., eds, Gold deposits of the Carlin Trend: Nevada Bureau of Mines and Geology, Bulletin 111, p.9,-19.

Thompson, T.B., 2000, What are "Carlin-Type" gold deposits?: GSA Abstracts with Programs, v. 32, n. 7, p. A250.

Thorman, C., Ketner, K., W. Brooks, L. Snee, and R. Zimmermann, 1991, Late Mesozoic-Cenozoic Tectonics in Northeastern Nevada, *in* G. Raines, R. Lisle, R. Schafer, and W. Wilkinson, eds, Geology and Ore Deposits of the Great Basin, Symposium Proceedings, Geological Society of Nevada, p. 25-45.

Thorman, C. Ketner, K., and Peterson, F., 1992, The Middle to Late Jurassic Elko Orogeny in Eastern Nevada and Western Utah: GSA Abstracts with Programs, p. 66.

Tosdal, R.M. and Nutt, C.J., 1999, Late Eocene and Oligocene tectonic setting of Carlin-type Au deposits, Carlin trend, Nevada, USA, *in* Stanley and others, eds., Mineral Deposits: Processes and Processing, p.905-908.

Tretbar, D., 2000, Controls on Gold Deposition in the 194 Orebody, a Collapse Breccia in the Getchell Mine, Humboldt County, Nevada: Ralph J. Roberts CREG Annual Research Meeting, Program and Reports, 49 p.

Trexler, J., Cashman, P., Snyder, W. and Davydov, V., 2004, Late Paleozoic tectonism in Nevada: Timing, kinematics, and tectonic significance: GSA Bulletin, v. 116, p.525-538.

Turner, R., Madrid, R., and Miller, E., 1989, Roberts Mountains allochthon: Stratigraphic comparison with lower Paleozoic outer continental margin strata of the northern Canadian Cordillera: Geology, v. 17, p.341-344.

Walck, C., 1989, Petrology and petrography of the metamorphic aureole associated with the Deep Post orebody, Eureka County, Nevada, [M.S. Thesis]: University of Missouri-Rolla, Rolla, 58 p.

Watkins, R. and Browne, Q., 1989, An Ordovician continental-margin sequence of turbidite and seamount deposits in the Roberts Mountains allochthon,

Independence Range, Nevada: Geological Society of American Bulletin, v.101, p.731-741.

Williams, C.L., 1992, Breccia bodies in the Carlin Trend, Elko and Eureka Counties, Nevada, [M.S. Thesis]: Colorado State University, Fort Collins, 213 p.

Williams, S.A, 2002, Petrographic report to Newmont, 4 p.

Wilson, J.L., 1969, Microfacies and sedimentary structures in "deeper water" lime mudstones, *in* Friedman, G.M., ed, Depositional environments in carbonate rocks: Society Economic Paleontologists and Mineralogists Special Publication 14, p. 4-19.

Woitsekhowskaya, M. and Peters, S., 1998, Geochemical modeling of alteration and gold deposition at the Betze deposit, Eureka County, Nevada: : U.S. Geological Survey Open-File Report 98-338, p.211-222.

Wright, J., 1993, Carlin Trend Geophysical Review, *in* Christensen, O., ed, Gold Deposits of the Carlin Trend, Nevada: Society of Economic Geologic, Guidebook Series, v. 18, p.93-110.

Wyld, S., Rogers, J., and Copeland, P., 2003, Metamorphic evolution of the Luning-Fencemaker fold-thrust belt, Nevada; illite crystallinity, metamorphic petrology, and $^{40}Ar/^{39}Ar$ geochronology: Journal of Geology, v. 111, no. 1, p. 17-38.

Zabinski, W., 1980, Zincian dolomite: the present state of knowledge: Mineralogia Polonica, vol. 11, p. 19-31.

Zheng, Y.F., 1990, Carbon-oxygen isotopic covariation in hydrothermal calcite during degassing of CO_2. A quantitative evaluation and application to the Kushikino gold mining area in Japan: Mineralia Deposita, v. 25, p. 246-250.

APPENDIX 1

STRUCTURAL DATA
FOR
THE CHUKAR FOOTWALL DEPOSIT

AZIMUTH	DIP	STRUCTURE	EASTING	NORTHING	ELEVATION	REMARK
328	13	bedding	19552	16679	4773	
328	13	bedding	19552	16679	4773	
51	71	joint	19539	16713	4772	
51	71	joint	19539	16713	4772	
96	76	shear fracture	19556	16685	4772	
96	76	shear fracture	19556	16685	4772	
282	47	fault	19565	16696	4771	
330	83	fault	19561	16692	4771	
171	69	fault	19548	16715	4771	
282	47	fault	19565	16696	4771	
330	83	fault	19561	16692	4771	
171	69	fault	19548	16715	4771	
171	76	shear fracture	19547	16724	4770	
171	76	shear fracture	19547	16724	4770	
347	73	fault	19533	16673	4769	
286	77	fault	19554	16653	4769	
286	77	fault	19554	16653	4769	
345	14	bedding	19548	16670	4769	
215	9	bedding	19558	16734	4769	
345	14	bedding	19548	16670	4769	
215	9	bedding	19558	16734	4769	
244	70	joint	19520	16685	4769	
12	56	joint	19574	16704	4769	
12	56	joint	19574	16704	4769	
341	15	bedding	19583	16710	4768	
341	15	bedding	19583	16710	4768	
207	38	joint	19590	16716	4768	
207	38	joint	19590	16716	4768	
110	77	fault	19493	16642	4767	
265	16	bedding	19578	16753	4766	
265	16	bedding	19578	16753	4766	
9	54	joint	19476	16641	4765	
285	82	joint	19481	16651	4765	
137	84	fault	19502	16650	4764	
103	70	fault	19470	16647	4764	
226	28	bedding	19480	16662	4764	
9	13	bedding	19516	16656	4764	
319	19	bedding	19611	16747	4764	
319	19	bedding	19611	16747	4764	
318	90	vein	19474	16627	4764	
48	87	shear fracture	19616	16743	4764	
48	87	shear fracture	19616	16743	4764	
297	61	fault	19503	16674	4763	
155	82	fault	19483	16676	4763	
218	7	bedding	19497	16668	4763	
233	15	bedding	19515	16675	4763	
2	23	bedding	19617	16758	4763	
255	18	bedding	19464	16640	4763	
2	23	bedding	19617	16758	4763	
126	88	joint	19621	16753	4763	
126	88	joint	19621	16753	4763	
119	65	shear fracture	19492	16673	4763	
86	53	shear fracture	19510	16660	4763	
305	77	fault	19485	16689	4762	
231	28	bedding	19413	16640	4757	
255	17	bedding	19213	16535	4750	
115	60	joint	19327	16679	4750	
110	60	joint	19328	16683	4750	
43	90	joint	19312	16678	4750	
45	65	joint	19312	16665	4750	
90	90	vein	19313	16654	4750	
296	78	fault	19460	16701	4749	
117	73	fault	19468	16679	4749	
276	80	fault	19370	16627	4749	
210	29	bedding	19488	16686	4749	
270	5	bedding	19332	16653	4749	
200	20	bedding	19341	16647	4749	
225	35	bedding	19358	16645	4749	
145	35	bedding	19366	16643	4749	
215	32	bedding	19372	16627	4749	
295	50	bedding	19315	16629	4749	
300	35	bedding	19307	16592	4749	
300	50	bedding	19313	16582	4749	
298	36	bedding	19318	16571	4749	
224	40	bedding	19329	16584	4749	
218	35	bedding	19327	16591	4749	
245	82	joint	19475	16659	4749	
210	60	joint	19343	16630	4749	
210	60	joint	19339	16630	4749	
105	90	joint	19379	16644	4749	
105	90	joint	19385	16644	4749	
110	70	joint	19391	16644	4749	
120	90	joint	19433	16644	4749	
115	90	joint	19418	16629	4749	
270	85	joint	19398	16630	4749	
260	85	joint	19390	16630	4749	
250	80	joint	19378	16628	4749	
115	90	joint	19413	16645	4749	
35	90	joint	19413	16646	4749	
90	78	joint	19331	16578	4749	
125	90	joint	19321	16565	4749	
125	90	joint	19320	16567	4749	
349	80	joint	19307	16590	4749	

AZIMUTH	DIP	STRUCTURE	EASTING	NORTHING	ELEVATION	REMARK
150	90	joint	19327	16599	4749	
120	85	vein	19370	16643	4749	
124	76	fault	19495	16627	4748	
335	5	fault	19517	16607	4748	
142	77	fault	19502	16642	4748	
193	17	fault	19481	16639	4748	
136	76	fault	19471	16645	4748	
115	75	fault	19468	16646	4748	
200	6	bedding	19488	16609	4748	
261	19	bedding	19490	16632	4748	
260	30	bedding	19326	16551	4748	
260	30	bedding	19331	16544	4748	
250	28	bedding	19339	16527	4748	
242	20	bedding	19348	16506	4748	
247	23	bedding	19362	16513	4748	
220	50	bedding	19353	16533	4748	
220	25	bedding	19348	16543	4748	
90	90	bedding	19307	16469	4748	
211	25	bedding	19300	16473	4748	
212	40	bedding	19295	16475	4748	
214	25	bedding	19274	16485	4748	
250	35	bedding	19269	16470	4748	
210	30	bedding	19295	16456	4748	
232	70	joint	19501	16602	4748	
37	88	joint	19489	16629	4748	
123	87	joint	19499	16631	4748	
105	90	joint	19470	16647	4748	
45	90	joint	19477	16652	4748	
90	90	joint	19461	16628	4748	
115	85	joint	19338	16562	4748	
115	90	joint	19345	16548	4748	
115	90	joint	19347	16545	4748	
110	80	joint	19356	16525	4748	
110	80	joint	19359	16519	4748	
115	78	joint	19364	16510	4748	
5	85	joint	19342	16520	4748	
5	5	joint	19341	16522	4748	
5	80	joint	19335	16535	4748	
175	75	joint	19292	16479	4748	
160	70	joint	19288	16482	4748	
68	72	joint	19285	16484	4748	
340	90	joint	19289	16459	4748	
300	80	fault	19387	16496	4747	ANT
295	70	fault	19349	16508	4747	ANT
125	68	fault	19340	16414	4747	SAG
127	80	fault	19288	16460	4747	
129	80	fault	19266	16474	4747	
245	55	joint	19357	16469	4747	
245	55	joint	19356	16466	4747	
270	90	joint	19353	16447	4747	
225	85	joint	19347	16433	4747	
145	85	joint	19325	16460	4747	
70	75	joint	19312	16457	4747	
213	15	bedding	19199	16742	4738	
236	24	bedding	19180	16738	4738	
213	15	bedding	19199	16742	4738	
236	24	bedding	19180	16738	4738	
211	89	joint	19196	16724	4738	
98	2	joint	19189	16720	4738	
119	87	joint	19186	16742	4738	
211	89	joint	19196	16724	4738	
98	2	joint	19189	16720	4738	
119	87	joint	19186	16742	4738	
207	82	joint	19180	16713	4737	
207	82	joint	19180	16713	4737	
212	70	fault	19241	16740	4736	
212	70	fault	19241	16740	4736	
214	24	bedding	19166	16711	4736	
214	24	bedding	19166	16711	4736	
118	75	fault	19286	16453	4735	SAG
217	64	fault	19248	16752	4735	
217	64	fault	19248	16752	4735	
135	35	bedding	19288	16452	4735	
40	14	syncline	19297	16468	4735	
215	60	bedding	19318	16440	4734	
145	90	joint	19277	16477	4734	
145	85	joint	19275	16478	4734	
95	90	joint	19269	16482	4734	
135	90	joint	19367	16417	4734	
20	75	joint	19357	16420	4734	
330	75	joint	19328	16436	4734	
140	90	joint	19325	16438	4734	
306	80	joint	19313	16444	4734	
120	90	joint	19288	16470	4734	
46	61	fault	19408	16535	4733	
126	78	fault	19404	16531	4733	
125	78	fault	19415	16523	4733	
259	21	fault	19404	16558	4733	
232	22	fault	19394	16552	4733	
258	20	bedding	19403	16560	4733	
244	20	bedding	19395	16535	4733	
197	13	bedding	19425	16548	4733	
250	20	contact	19414	16562	4733	

AZIMUTH	DIP	STRUCTURE	EASTING	NORTHING	ELEVATION	REMARK
115	85	joint	19343	16447	4733	
130	80	joint	19366	16438	4733	
35	90	joint	19306	16467	4733	
48	78	joint	19410	16550	4733	
31	78	joint	19423	16543	4733	
313	72	joint	19405	16552	4733	
120	82	joint	19396	16543	4733	
109	75	fault	19413	16595	4732	
254	25	fault	19378	16542	4732	
25	50	bedding	19339	16463	4732	
235	23	bedding	19402	16581	4732	
228	30	bedding	19376	16555	4732	
240	22	contact	19386	16546	4732	
336	88	joint	19400	16585	4732	
42	90	joint	19334	16479	4731	
308	81	fault	19465	16722	4730	PHE
293	61	fault	19531	16678	4730	PHE
282	90	fault	19473	16699	4730	
257	21	bedding	19443	16731	4730	
223	29	bedding	19494	16711	4730	
255	31	bedding	19474	16692	4730	
235	18	bedding	19514	16696	4730	
242	20	contact	19516	16674	4730	
90	90	joint	19344	16489	4730	
5	90	joint	19345	16490	4730	
308	87	joint	19429	16734	4730	
40	82	joint	19451	16716	4730	
222	90	vein	19446	16727	4730	
222	90	vein	19436	16715	4730	
210	90	vein	19479	16728	4730	
211	90	vein	19462	16710	4730	
143	73	fault	19349	16535	4729	
207	81	fault	19336	16740	4729	
135	63	fault	19388	16740	4729	
134	75	fault	19410	16718	4729	
207	81	fault	19336	16740	4729	
135	63	fault	19388	16740	4729	
134	75	fault	19410	16718	4729	
236	20	bedding	19346	16525	4729	
236	10	bedding	19373	16511	4729	
232	20	bedding	19311	16745	4729	
228	22	bedding	19329	16744	4729	
231	33	bedding	19342	16743	4729	
248	18	bedding	19308	16691	4729	
248	20	bedding	19374	16734	4729	
209	25	bedding	19396	16718	4729	
209	41	bedding	19225	16757	4729	
224	20	bedding	19240	16754	4729	
232	20	bedding	19311	16745	4729	
228	22	bedding	19329	16744	4729	
231	33	bedding	19342	16743	4729	
248	18	bedding	19308	16691	4729	
248	20	bedding	19374	16734	4729	
209	25	bedding	19396	16718	4729	
209	41	bedding	19225	16757	4729	
224	20	bedding	19240	16754	4729	
221	66	joint	19377	16514	4729	
270	63	joint	19344	16721	4729	
35	85	joint	19396	16711	4729	
299	87	joint	19405	16714	4729	
313	83	joint	19322	16693	4729	
13	85	joint	19309	16698	4729	
104	70	joint	19303	16698	4729	
35	81	joint	19395	16746	4729	
290	82	joint	19278	16735	4729	
117	56	joint	19279	16747	4729	
154	64	joint	19304	16724	4729	
99	51	joint	19253	16737	4729	
75	76	joint	19232	16756	4729	
288	78	joint	19230	16738	4729	
48	78	joint	19204	16737	4729	
114	78	joint	19160	16693	4729	
270	63	joint	19344	16721	4729	
35	85	joint	19396	16711	4729	
299	87	joint	19405	16714	4729	
313	83	joint	19322	16693	4729	
13	85	joint	19309	16698	4729	
104	70	joint	19303	16698	4729	
35	81	joint	19395	16746	4729	
290	82	joint	19278	16735	4729	
117	56	joint	19279	16747	4729	
154	64	joint	19304	16724	4729	
99	51	joint	19253	16737	4729	
75	76	joint	19232	16756	4729	
288	78	joint	19230	16738	4729	
48	78	joint	19204	16737	4729	
114	78	joint	19160	16693	4729	
228	25	shear	19389	16719	4729	
228	25	shear	19389	16719	4729	
285	70	fault	19384	16499	4728	ANT
285	76	fault	19535	16680	4728	
190	40	bedding	19367	16513	4728	

AZIMUTH	DIP	STRUCTURE	EASTING	NORTHING	ELEVATION	REMARK
224	19	bedding	19394	16532	4728	
235	8	bedding	19401	16510	4728	
251	19	bedding	19407	16750	4728	
251	19	bedding	19407	16750	4728	
132	87	joint	19396	16506	4728	
352	84	joint	19404	16739	4728	
28	86	joint	19505	16708	4728	
352	84	joint	19404	16739	4728	
128	70	fault	19514	16706	4727	
132	78	fault	19536	16686	4727	
261	18	bedding	19543	16684	4727	
299	86	fault	19422	16758	4726	PHE
128	68	fault	19521	16714	4726	
132	78	fault	19522	16709	4726	
144	79	fault	19526	16705	4726	
245	24	bedding	19457	16749	4726	
312	86	fault	19409	16769	4725	
118	80	fault	19547	16697	4725	
312	86	fault	19409	16769	4725	
194	89	joint	19539	16696	4725	
312	81	fault	19426	16769	4724	
312	81	fault	19426	16769	4724	
253	18	bedding	19549	16706	4724	
187	85	joint	19478	16746	4724	
209	78	sh. fracture	19540	16712	4724	
321	86	fault	19474	16761	4723	
99	78	joint	19559	16700	4723	
238	69	shear fracture	19531	16726	4723	
219	15	bedding	19449	16555	4722	
207	45	bedding	19149	16221	4722	
207	45	bedding	19149	16221	4722	
98	83	joint	19458	16582	4722	
13	87	joint	19554	16714	4722	
5	55	vein	19142	16217	4722	
5	55	vein	19142	16217	4722	
296	86	fault	19452	16581	4721	
144	71	fault	19545	16737	4721	
141	72	fault	19564	16714	4721	
228	16	fault	19561	16711	4721	
354	70	fault	19562	16709	4721	
281	79	fault	19562	16713	4721	
206	53	fault	19076	16230	4721	
10	77	joint	19461	16568	4721	
339	45	joint	19138	16225	4721	
339	45	joint	19138	16225	4721	
291	70	fault	19469	16574	4720	
288	85	fault	19475	16582	4720	
302	86	fault	19566	16716	4720	
202	31	bedding	19070	16232	4720	
98	53	joint	19149	16239	4720	
98	53	joint	19149	16239	4720	
150	80	vein	19145	16241	4720	
150	80	vein	19145	16241	4720	
132	88	fault	19573	16723	4719	
256	16	bedding	19483	16595	4719	
262	12	bedding	19563	16732	4719	
239	26	bedding	19490	16776	4719	
207	21	bedding	19078	16262	4719	
209	20	bedding	19123	16236	4719	
202	21	bedding	19128	16246	4719	
209	20	bedding	19123	16236	4719	
202	21	bedding	19128	16246	4719	
150	90	vein	19554	16744	4719	
47	77	vein	19083	16248	4719	
64	80	vein	19124	16244	4719	
64	80	vein	19124	16244	4719	
201	66	fault	19095	16262	4718	
215	28	bedding	19507	16765	4718	
207	30	bedding	19101	16245	4718	
203	30	bedding	19109	16242	4718	
207	30	bedding	19101	16245	4718	
203	30	bedding	19109	16242	4718	
203	82	vein	19572	16738	4718	
18	80	vein	19578	16727	4718	
148	82	Raven dike	19126	16270	4718	dike
138	84	fault	19572	16742	4717	
238	54	fault	19112	16276	4717	
180	29	bedding	19118	16275	4717	
195	45	bedding	19088	16279	4717	
200	30	bedding	19107	16261	4717	
200	30	bedding	19107	16261	4717	
171	40	joint	19113	16255	4717	
171	40	joint	19113	16255	4717	
304	90	vein	19565	16753	4717	
216	80	fault	19587	16742	4716	
321	85	fault	19586	16738	4716	
36	71	fault	19161	16271	4716	
37	53	fault	19151	16258	4716	
45	48	fault	19174	16266	4716	
47	63	fault	19161	16254	4716	
39	31	fault	19188	16243	4716	
32	33	fault	19196	16237	4716	CFZ

AZIMUTH	DIP	STRUCTURE	EASTING	NORTHING	ELEVATION	REMARK
33	48	fault	19211	16256	4716	CFZ
293	73	fault	19209	16262	4716	
292	65	fault	19173	16278	4716	
273	21	fault	19120	16247	4716	
202	35	bedding	19148	16277	4716	
35	32	bedding	19156	16274	4716	
161	17	bedding	19139	16263	4716	
190	32	bedding	19131	16285	4716	
12	15	bedding	19182	16264	4716	
353	13	bedding	19158	16258	4716	
187	23	bedding	19097	16246	4716	
177	30	bedding	19104	16263	4716	
205	35	bedding	19080	16261	4716	
205	35	bedding	19080	16261	4716	
193	60	joint	19144	16265	4716	
207	60	joint	19135	16270	4716	
272	66	joint	19139	16263	4716	
310	90	vein	19569	16756	4716	
351	57	shear fracture	19133	16278	4716	
115	78	shear fracture	19188	16261	4716	
286	70	fault	19193	16266	4715	
39	43	fault	19141	16198	4715	CFZ
45	43	fault	19118	16221	4715	
314	82	fault	19138	16301	4715	
87	48	fault	19132	16227	4715	
253	24	bedding	19438	16839	4715	
253	24	bedding	19438	16839	4715	
232	37	bedding	19120	16263	4715	
194	29	bedding	19144	16217	4715	
209	38	bedding	19151	16243	4715	
68	7	bedding	19183	16200	4715	
235	39	bedding	19133	16300	4715	
207	30	bedding	19143	16302	4715	
48	34	bedding	19162	16301	4715	
180	25	bedding	19087	16272	4715	
180	25	bedding	19087	16272	4715	
92	77	joint	19593	16737	4715	
177	30	joint	19128	16258	4715	
106	80	joint	19097	16214	4715	
144	88	joint	19099	16220	4715	
116	77	joint	19150	16306	4715	
85	65	joint	19139	16300	4715	
136	80	joint	19146	16297	4715	
203	85	joint	19102	16273	4715	
85	65	joint	19139	16300	4715	
136	80	joint	19146	16297	4715	
203	85	joint	19102	16273	4715	
226	39	shear	19151	16299	4715	
131	84	vein	19575	16763	4715	
254	15	fault	19592	16745	4714	
40	47	fault	19216	16265	4714	CFZ
196	39	fault	19131	16250	4714	
196	37	fault	19113	16313	4714	
261	24	bedding	19576	16770	4714	
234	62	bedding	19127	16220	4714	
223	42	bedding	19128	16305	4714	
197	43	bedding	19095	16292	4714	
197	43	bedding	19095	16292	4714	
95	84	joint	19580	16765	4714	
130	75	joint	19545	16761	4714	
259	88	joint	19125	16307	4714	
82	90	joint	19127	16304	4714	
228	55	joint	19091	16281	4714	
82	90	joint	19127	16304	4714	
228	55	joint	19091	16281	4714	
110	74	vein	19598	16750	4714	
155	85	Raven dike	19140	16245	4714	dike
259	74	fault	19599	16752	4713	
31	43	fault	19225	16279	4713	
73	45	fault	19152	16238	4713	
230	30	bedding	19514	16784	4713	
259	70	bedding	19138	16207	4713	
224	30	bedding	19112	16311	4713	
224	30	bedding	19112	16311	4713	
38	78	joint	19453	16851	4713	
38	78	joint	19453	16851	4713	
70	80	joint	19521	16781	4713	
35	80	joint	19527	16777	4713	
125	80	joint	19530	16775	4713	
190	82	joint	19546	16758	4713	
135	85	joint	19550	16746	4713	
221	88	joint	19161	16239	4713	
332	74	joint	19131	16217	4713	
283	36	joint	19139	16210	4713	
159	85	joint	19121	16308	4713	
159	85	joint	19121	16308	4713	
190	33	shear	19110	16308	4713	
134	82	vein	19463	16844	4713	
134	82	vein	19463	16844	4713	
107	88	shear fracture	19148	16248	4713	
226	88	fault	19604	16761	4712	
105	68	fault	19604	16757	4712	

AZIMUTH	DIP	STRUCTURE	EASTING	NORTHING	ELEVATION	REMARK
226	88	fault	19604	16761	4712	
105	68	fault	19604	16757	4712	
53	53	fault	19196	16297	4712	
52	62	fault	19211	16309	4712	
254	18	bedding	19527	16755	4712	
220	28	bedding	19510	16765	4712	
31	3	bedding	19232	16295	4712	
26	21	bedding	19206	16310	4712	
10	5	bedding	19197	16288	4712	
59	26	bedding	19166	16236	4712	
254	42	bedding	19095	16314	4712	
254	42	bedding	19095	16314	4712	
180	90	joint	19523	16761	4712	
130	80	joint	19514	16765	4712	
125	72	joint	19111	16316	4712	
125	72	joint	19111	16316	4712	
348	77	Raven dike	19148	16218	4712	dike
208	79	fault	19606	16759	4711	
138	78	fault	19608	16761	4711	
208	79	fault	19606	16759	4711	
138	78	fault	19608	16761	4711	
39	41	fault	19186	16222	4711	CFZ
241	16	bedding	19472	16871	4711	
241	16	bedding	19472	16871	4711	
325	7	bedding	19494	16777	4711	
228	32	bedding	19503	16782	4711	
256	45	bedding	19093	16319	4711	
256	45	bedding	19093	16319	4711	
130	90	joint	19489	16773	4711	
80	90	joint	19527	16743	4711	
234	70	joint	19505	16764	4711	
208	50	joint	19108	16328	4711	
208	50	joint	19108	16328	4711	
235	80	vein	19093	16315	4711	
217	88	sh fracture	19604	16766	4711	
217	88	sh fracture	19604	16766	4711	
141	83	fault	19613	16765	4710	
204	90	fault	19602	16773	4710	
139	84	fault	19515	16729	4710	
141	83	fault	19613	16765	4710	
204	90	fault	19602	16773	4710	
23	25	fault	19197	16216	4710	CFZ
23	31	fault	19191	16200	4710	CFZ
124	75	fault	19086	16329	4710	
124	75	fault	19086	16329	4710	
220	35	bedding	19520	16735	4710	
233	50	bedding	19089	16322	4710	
204	55	joint	19104	16336	4710	
204	55	joint	19104	16336	4710	
5	90	vein	19514	16727	4710	
355	70	fault	19197	16197	4709	CFZ
309	80	fault	19101	16350	4709	
309	80	fault	19101	16350	4709	
246	32	bedding	19086	16341	4709	
246	32	bedding	19086	16341	4709	
43	85	joint	19471	16758	4709	
114	80	joint	19096	16349	4709	
114	80	joint	19096	16349	4709	
4	18	vein	19622	16770	4709	
4	18	vein	19622	16770	4709	
132	76	Raven dike	19087	16335	4709	dike
139	83	sh fracture	19617	16765	4709	
139	83	sh fracture	19617	16765	4709	
298	75	sh fracture	19103	16335	4709	
196	76	fault	19603	16791	4708	
148	81	fault	19609	16789	4708	
168	49	fault	19504	16716	4708	
196	76	fault	19603	16791	4708	
148	81	fault	19609	16789	4708	
243	28	bedding	19502	16714	4708	
227	20	bedding	19466	16753	4708	
224	30	bedding	19505	16716	4708	
201	52	bedding	19097	16345	4708	
254	10	bedding	19081	16357	4708	
254	10	bedding	19081	16357	4708	
200	85	joint	19508	16700	4708	
303	70	fault	19507	16696	4707	PHE
295	70	fault	19504	16696	4707	PHE
290	61	fault	19097	16352	4707	
306	75	fault	19080	16367	4707	
306	75	fault	19080	16367	4707	
269	16	bedding	19615	16792	4707	
269	16	bedding	19615	16792	4707	
240	30	bedding	19492	16709	4707	
285	19	bedding	19096	16366	4707	
285	19	bedding	19096	16366	4707	
35	90	joint	19502	16695	4707	
108	85	joint	19091	16372	4707	
327	68	joint	19078	16361	4707	
108	85	joint	19091	16372	4707	
327	68	joint	19078	16361	4707	
306	90	vein	19464	16883	4707	

AZIMUTH	DIP	STRUCTURE	EASTING	NORTHING	ELEVATION	REMARK
354	74	vein	19625	16777	4707	
306	90	vein	19464	16883	4707	
354	74	vein	19625	16777	4707	
305	80	fault	19449	16737	4706	PHE
243	28	bedding	19483	16704	4706	
207	17	bedding	19088	16558	4706	
280	85	joint	19471	16882	4706	
301	90	joint	19489	16690	4706	
280	85	joint	19471	16882	4706	
111	82	joint	19087	16554	4706	
110	90	joint	19090	16376	4706	
318	80	joint	19074	16374	4706	
21	65	joint	19071	16377	4706	
110	90	joint	19090	16376	4706	
318	80	joint	19074	16374	4706	
21	65	joint	19071	16377	4706	
36	85	vein	19625	16788	4706	
36	85	vein	19625	16788	4706	
229	22	bedding	19472	16889	4705	
229	22	bedding	19472	16889	4705	
245	22	bedding	19436	16729	4705	
202	86	joint	19487	16686	4705	
52	83	joint	19444	16732	4705	
115	80	joint	19084	16393	4705	
88	85	joint	19069	16382	4705	
22	70	joint	19069	16384	4705	
115	80	joint	19084	16393	4705	
88	85	joint	19069	16382	4705	
22	70	joint	19069	16384	4705	
29	80	vein	19619	16798	4705	
29	80	vein	19619	16798	4705	
208	78	fault	19153	16662	4704	
296	73	fault	19147	16661	4704	ANT
283	74	fault	19138	16661	4704	ANT
140	64	fault	19103	16561	4704	
21	80	fault	19066	16396	4704	MAG
21	80	fault	19066	16396	4704	MAG
253	15	bedding	19149	16664	4704	
229	37	bedding	19075	16368	4704	
253	15	bedding	19085	16405	4704	
253	15	bedding	19085	16405	4704	
136	87	joint	19149	16657	4704	
305	80	joint	19094	16377	4704	
278	82	vein	19093	16370	4704	
231	71	shear fracture	19180	16652	4704	
156	85	fault	19111	16568	4703	
313	64	fault	19183	16636	4703	ANT
308	69	fault	19169	16649	4703	ANT
328	66	fault	19073	16376	4703	
45	60	fault	19085	16408	4703	
45	60	fault	19085	16408	4703	
236	26	bedding	19133	16650	4703	
209	39	bedding	19115	16570	4703	
39	83	joint	19147	16650	4703	
235	22	shear	19134	16659	4703	
28	77	fault	19157	16625	4702	
22	71	fault	19154	16624	4702	MAG
10	84	fault	19128	16554	4702	MAG
32	85	fault	19058	16415	4702	
300	50	fault	19089	16433	4702	
32	85	fault	19058	16415	4702	
300	50	fault	19089	16433	4702	
219	28	bedding	19148	16543	4702	
277	9	bedding	19164	16542	4702	
216	16	bedding	19123	16581	4702	
105	88	joint	19114	16587	4702	
145	60	joint	19077	16428	4702	
119	90	joint	19078	16416	4702	
145	60	joint	19077	16428	4702	
119	90	joint	19078	16416	4702	
19	78	fault	19130	16581	4701	
115	74	fault	19120	16573	4701	SAH
239	22	bedding	19155	16563	4701	
293	30	bedding	19082	16421	4701	
293	30	bedding	19082	16421	4701	
101	85	joint	19159	16558	4701	
8	60	joint	19089	16438	4701	
122	55	joint	19082	16432	4701	
298	65	joint	19059	16428	4701	
8	60	joint	19089	16438	4701	
122	55	joint	19082	16432	4701	
298	65	joint	19059	16428	4701	
23	77	fault	19141	16581	4700	
21	86	fault	19138	16573	4700	MAG
132	77	fault	19140	16563	4700	SAH
224	23	bedding	19511	16897	4700	
224	23	bedding	19511	16897	4700	
201	27	bedding	19143	16578	4700	
216	31	bedding	19135	16578	4700	
137	60	joint	19101	16458	4700	
246	45	joint	19097	16451	4700	
185	72	joint	19094	16450	4700	

AZIMUTH	DIP	STRUCTURE	EASTING	NORTHING	ELEVATION	REMARK
318	70	joint	19056	16433	4700	
137	60	joint	19101	16458	4700	
246	45	joint	19097	16451	4700	
185	72	joint	19094	16450	4700	
318	70	joint	19056	16433	4700	
329	81	fault	19137	16550	4699	
123	80	fault	19143	16565	4699	
220	45	bedding	19064	16457	4699	
224	25	bedding	19079	16462	4699	
228	35	bedding	19108	16477	4699	
221	30	bedding	19048	16448	4699	
220	45	bedding	19064	16457	4699	
224	25	bedding	19079	16462	4699	
228	35	bedding	19108	16477	4699	
221	30	bedding	19048	16448	4699	
21	70	sh fracture	19141	16589	4699	
145	83	fault	19152	16545	4698	
34	80	fault	19144	16599	4698	
211	80	fault	19198	16696	4698	MAG
15	85	fault	19223	16693	4698	
142	85	fault	19090	16562	4698	SAH
137	75	fault	19110	16571	4698	SAH
161	80	fault	19144	16544	4698	SAH
103	65	fault	19146	16562	4698	
131	70	fault	19167	16549	4698	
295	70	fault	19159	16661	4698	ANT
0	80	fault	19138	16575	4698	MAG
201	82	fault	19187	16699	4698	MAG
200	56	fault	19191	16710	4698	MAG
200	40	fault	19196	16724	4698	
202	60	fault	19186	16731	4698	
159	80	fault	19095	16482	4698	
159	80	fault	19095	16482	4698	
232	27	bedding	19125	16602	4698	
235	22	bedding	19221	16685	4698	
252	30	bedding	19083	16553	4698	
202	25	bedding	19143	16549	4698	
220	20	bedding	19164	16557	4698	
206	25	bedding	19140	16570	4698	
235	30	bedding	19141	16592	4698	
231	45	bedding	19152	16610	4698	
234	35	bedding	19166	16638	4698	
222	35	bedding	19187	16644	4698	
224	35	bedding	19170	16653	4698	
252	20	bedding	19158	16658	4698	
184	27	bedding	19141	16632	4698	
186	20	bedding	19129	16606	4698	
186	20	bedding	19125	16585	4698	
221	30	bedding	19093	16473	4698	
221	30	bedding	19093	16473	4698	
120	80	joint	19521	16902	4698	
120	80	joint	19521	16902	4698	
83	85	joint	19171	16550	4698	
95	85	joint	19187	16551	4698	
343	90	joint	19160	16557	4698	
32	60	joint	19158	16560	4698	
181	77	joint	19141	16568	4698	
120	90	joint	19138	16585	4698	
38	65	joint	19145	16601	4698	
90	85	joint	19147	16605	4698	
57	90	joint	19152	16616	4698	
291	80	joint	19156	16623	4698	
253	85	joint	19162	16628	4698	
337	90	joint	19145	16643	4698	
285	55	joint	19122	16578	4698	
90	70	joint	19101	16561	4698	
75	90	joint	19176	16656	4698	
75	80	joint	19173	16700	4698	
40	80	joint	19178	16712	4698	
157	80	joint	19097	16482	4698	
157	80	joint	19097	16482	4698	
251	40	shear	19219	16688	4698	
330	55	vein	19159	16668	4698	
220	80	vein	19140	16551	4698	
128	88	fault	19162	16540	4697	
125	73	fault	19168	16548	4697	
65	69	joint	19527	16904	4697	
65	69	joint	19527	16904	4697	
312	83	fault	19148	16627	4696	
227	27	bedding	19149	16635	4695	
327	90	joint	19143	16637	4695	
302	86	fault	19543	16910	4694	
302	86	fault	19543	16910	4694	
202	26	bedding	19064	16460	4694	
194	17	bedding	19052	16429	4694	
289	84	joint	19548	16892	4694	
289	84	joint	19548	16892	4694	
306	79	joint	19059	16453	4694	
294	67	fault	19551	16911	4693	
294	67	fault	19551	16911	4693	
291	67	bedding	19551	16913	4693	
291	67	bedding	19551	16913	4693	

AZIMUTH	DIP	STRUCTURE	EASTING	NORTHING	ELEVATION	REMARK
215	31	shear	19073	16449	4693	
211	33	shear	19064	16436	4693	
327	90	vein	19554	16896	4693	
327	90	vein	19554	16896	4693	
303	83	fault	19561	16898	4692	
303	83	fault	19561	16898	4692	
315	84	fault	19158	16664	4692	ANT
211	76	fault	19080	16445	4692	MAG
212	81	fault	19072	16431	4692	MAG
220	38	shear	19085	16408	4692	
198	84	fault	19173	16664	4691	MAG
9	82	fault	19068	16397	4691	MAG
184	27	bedding	19088	16438	4691	
246	79	fault	19084	16400	4690	
343	81	fault	19177	16673	4690	
257	18	bedding	19161	16681	4690	
229	27	bedding	19070	16386	4690	
49	78	joint	19572	16898	4690	
49	78	joint	19572	16898	4690	
209	38	shear	19082	16405	4690	
283	64	fault	19578	16901	4689	
283	64	fault	19576	16901	4689	
229	22	bedding	19573	16918	4689	
229	22	bedding	19573	16918	4689	
131	71	joint	19169	16682	4689	
204	77	fault	19186	16696	4686	MAG
271	87	joint	19175	16705	4686	
245	18	bedding	19683	16828	4685	
245	18	bedding	19683	16828	4685	
120	74	vein	19838	16807	4685	
120	74	vein	19838	16807	4685	
291	90	vein	19693	16801	4685	
282	52	fault	19611	16892	4684	
282	52	fault	19611	16892	4684	
285	74	fault	19597	16885	4683	
292	69	fault	19645	16858	4683	
326	65	fault	19635	16815	4683	
144	80	fault	19617	16724	4683	
111	74	fault	19636	16714	4683	
150	80	fault	19627	16710	4683	
132	73	fault	19611	16714	4683	
132	85	fault	19622	16703	4683	
116	79	fault	19649	16727	4683	
119	79	fault	19633	16738	4683	
285	75	fault	19662	16776	4683	
285	74	fault	19597	16885	4683	
292	69	fault	19645	16858	4683	
326	65	fault	19635	16815	4683	
144	80	fault	19617	16724	4683	
111	74	fault	19636	16714	4683	
150	80	fault	19627	16710	4683	
132	73	fault	19611	16714	4683	
132	85	fault	19622	16703	4683	
116	79	fault	19649	16727	4683	
119	79	fault	19633	16738	4683	
285	75	fault	19662	16776	4683	
291	27	bedding	19601	16906	4683	
247	16	bedding	19626	16886	4683	
198	26	bedding	19628	16841	4683	
242	51	bedding	19648	16847	4683	
244	16	bedding	19627	16735	4683	
256	24	bedding	19603	16694	4683	
291	27	bedding	19601	16906	4683	
247	16	bedding	19626	16886	4683	
198	26	bedding	19628	16841	4683	
242	51	bedding	19648	16847	4683	
244	16	bedding	19627	16735	4683	
256	24	bedding	19603	16694	4683	
274	21	contact	19626	16816	4683	
274	21	contact	19626	16816	4683	
92	84	joint	19597	16710	4683	
34	75	joint	19660	16734	4683	
92	84	joint	19597	16710	4683	
34	75	joint	19660	16734	4683	
300	90	vein	19652	16874	4683	
300	90	vein	19652	16874	4683	
123	90	shear fracture	19617	16700	4683	
123	90	shear fracture	19617	16700	4683	
121	85	shear fracture	19690	16789	4683	
270	16	bedding	19195	16733	4681	
237	23	bedding	19184	16734	4681	
225	70	vein	19189	16731	4681	
184	75	fault	19005	16256	4674	
263	83	fault	19008	16273	4674	
236	73	fault	19014	16273	4673	
116	79	fault	19049	16256	4673	
246	22	bedding	19040	16304	4673	
213	33	bedding	19022	16271	4673	
207	35	shear	19038	16257	4673	
219	30	bedding	19064	16253	4672	
318	84	joint	19082	16247	4672	
273	81	joint	19069	16272	4672	

AZIMUTH	DIP	STRUCTURE	EASTING	NORTHING	ELEVATION	REMARK
200	29	shear	19054	16286	4672	
231	27	bedding	19083	16234	4671	
319	80	joint	19108	16232	4671	
207	53	fault	19122	16218	4670	
208	73	fault	19116	16206	4670	
236	41	fault	19111	16208	4670	
243	25	bedding	19108	16202	4670	
205	13	bedding	19139	16211	4670	
283	85	joint	19120	16224	4670	
221	65	vein	19113	16225	4670	
215	42	bedding	19224	16438	4662	
284	82	fault	19138	16307	4661	
286	80	fault	19160	16301	4661	
68	51	fault	19233	16197	4661	
330	73	fault	19218	16438	4661	
309	60	fault	19223	16446	4661	
337	73	fault	19233	16447	4661	
53	44	fault	19329	16334	4661	
43	82	fault	19305	16318	4661	
219	33	bedding	19187	16309	4661	
202	46	bedding	19187	16345	4661	
36	24	bedding	19232	16169	4661	
8	17	bedding	19203	16211	4661	
220	31	bedding	19087	16219	4661	
233	29	bedding	19093	16225	4661	
194	42	bedding	19231	16426	4661	
248	37	bedding	19197	16312	4661	
202	42	bedding	19210	16306	4661	
233	20	bedding	19219	16338	4661	
345	7	bedding	19235	16330	4661	
62	12	bedding	19219	16307	4661	
66	28	bedding	19219	16298	4661	
70	22	bedding	19271	16269	4661	
47	52	bedding	19303	16292	4661	
23	20	bedding	19288	16300	4661	
71	26	bedding	19261	16312	4661	
195	29	bedding	19184	16296	4661	
216	25	bedding	19180	16282	4661	
222	23	bedding	19184	16276	4661	
32	16	bedding	19198	16277	4661	
9	18	bedding	19190	16259	4661	
23	31	bedding	19213	16268	4661	
54	27	bedding	19207	16253	4661	
42	10	bedding	19228	16239	4661	
33	17	bedding	19250	16249	4661	
40	3	bedding	19239	16228	4661	
55	14	bedding	19311	16349	4661	
62	23	bedding	19317	16339	4661	
52	7	bedding	19299	16324	4661	
124	70	joint	19178	16334	4661	
53	74	joint	19160	16316	4661	
280	51	joint	19155	16297	4661	
106	86	joint	19238	16193	4661	
115	85	joint	19219	16211	4661	
259	83	joint	19219	16182	4661	
26	74	joint	19209	16209	4661	
20	70	joint	19232	16423	4661	
35	55	joint	19197	16308	4661	
217	40	joint	19268	16272	4661	
227	52	joint	19307	16289	4661	
213	65	joint	19277	16309	4661	
39	48	joint	19233	16264	4661	
329	83	joint	19239	16260	4661	
216	68	joint	19198	16251	4661	
98	73	joint	19190	16267	4661	
53	70	joint	19216	16236	4661	
263	50	joint	19269	16244	4661	
60	42	joint	19222	16244	4661	
223	58	joint	19324	16348	4661	
314	86	joint	19324	16317	4661	
225	56	joint	19284	16369	4661	
221	34	shear	19183	16310	4661	
15	17	shear	19220	16174	4661	
297	84	vein	19203	16412	4661	
355	47	Raven dike	19211	16178	4661	dike
121	74	sh fracture	19191	16322	4661	
52	88	sh fracture	19224	16296	4661	
212	61	sh fracture	19247	16326	4661	
95	86	sh fracture	19272	16303	4661	
289	52	sh fracture	19320	16278	4661	
280	83	sh fracture	19257	16278	4661	
227	80	sh fracture	19206	16277	4661	
317	83	sh fracture	19227	16229	4661	
334	82	sh fracture	19213	16243	4661	
282	70	sh fracture	19259	16243	4661	
167	45	sh fracture	19265	16251	4661	
217	65	sh fracture	19322	16325	4661	
281	65	sh fracture	19281	16327	4661	
321	84	fault	19254	16436	4660	
229	37	bedding	18997	16188	4660	
221	27	bedding	19244	16438	4660	
209	32	bedding	19238	16422	4660	

AZIMUTH	DIP	STRUCTURE	EASTING	NORTHING	ELEVATION	REMARK
308	85	joint	19247	16442	4660	
147	84	fault	19015	16185	4659	
318	78	fault	19054	16220	4659	
199	83	fault	19230	16392	4659	
229	30	beddingf	19248	16417	4659	
24	8	anticline	19253	16420	4659	
53	62	fault	19017	16142	4658	
296	87	fault	19167	16322	4658	
122	73	fault	19159	16337	4658	
55	72	fault	19222	16387	4658	
35	62	fault	19238	16390	4658	
229	37	bedding	19007	16164	4658	
210	25	bedding	19275	16431	4658	
20	5	bedding	19262	16408	4658	
339	61	joint	19014	16152	4658	
106	85	joint	19027	16160	4658	
278	87	joint	19267	16401	4658	
37	84	joint	19118	16173	4658	
73	90	shear fracture	19013	16163	4658	
38	78	shear fracture	19030	16187	4658	
320	70	shear fracture	19287	16432	4658	
322	83	fault	19280	16406	4657	
209	74	fault	19237	16358	4657	
209	75	fault	19251	16382	4657	
203	28	bedding	19037	16178	4657	
198	24	bedding	19100	16249	4657	
219	34	bedding	19109	16263	4657	
230	28	bedding	19129	16295	4657	
209	39	bedding	19142	16278	4657	
229	22	bedding	19130	16249	4657	
239	8	bedding	19181	16239	4657	
230	23	bedding	19144	16220	4657	
234	22	bedding	19289	16425	4657	
230	16	bedding	19296	16420	4657	
194	20	bedding	19124	16159	4657	
100	73	joint	19041	16164	4657	
274	84	joint	19145	16281	4657	
298	87	joint	19110	16271	4657	
21	65	joint	19114	16228	4657	
323	76	joint	19143	16227	4657	
42	66	joint	19149	16215	4657	
337	83	joint	19135	16241	4657	
55	52	joint	19272	16393	4657	
190	22	shear	19125	16231	4657	
232	28	shear	19134	16227	4657	
53	2	anticline	19171	16241	4657	
336	79	Raven dike	19130	16264	4657	dike
332	76	Raven dike	19134	16270	4657	dike
299	85	shear fracture	19128	16173	4657	
294	77	fault	19171	16294	4656	
35	34	fault	19135	16156	4656	
34	67	fault	19145	16171	4656	
222	7	bedding	19258	16383	4656	
192	18	bedding	19241	16350	4656	
209	8	bedding	19135	16170	4656	
311	83	joint	19171	16227	4656	
22	66	joint	19300	16413	4656	
36	66	shear fracture	19285	16387	4656	
39	72	fault	19214	16307	4655	
24	66	fault	19228	16333	4655	
48	61	fault	19273	16372	4655	
42	87	fault	19252	16351	4655	
46	66	fault	19145	16154	4655	
74	20	fault	19083	15978	4655	
50	16	bedding	19189	16232	4655	
229	36	bedding	19095	16144	4655	
202	33	bedding	19111	16150	4655	
35	10	bedding	19255	16348	4655	
48	15	bedding	19154	16171	4655	
29	70	joint	19192	16229	4655	
323	78	Raven dike	19153	16238	4655	dike
335	86	Raven dike	19143	16243	4655	dike
332	80	shear fracture	19261	16371	4655	
275	63	shear fracture	19256	16341	4655	
23	65	shear fracture	19154	16176	4655	
133	89	fault	19326	16402	4654	SAH
65	47	fault	19119	16131	4654	
45	32	fault	19161	16168	4654	
54	11	bedding	19173	16195	4654	
80	4	bedding	19310	16380	4654	
253	28	bedding	19102	16126	4654	
37	12	bedding	19277	16369	4654	
118	88	joint	19204	16220	4654	
330	69	joint	19119	16138	4654	
337	85	joint	19073	16153	4654	
329	80	Raven dike	19161	16209	4654	dike
329	83	Raven dike	19166	16213	4654	dike
319	77	Raven dike	19180	16196	4654	dike
214	70	shear fracture	19333	16405	4654	
285	64	shear fracture	19316	16374	4654	
220	51	shear fracture	19309	16369	4654	
223	63	shear fracture	19263	16339	4654	

AZIMUTH	DIP	STRUCTURE	EASTING	NORTHING	ELEVATION	REMARK
340	70	sh fracture	19086	15982	4654	
310	83	fault	19191	16190	4653	
36	84	fault	19175	16271	4653	
38	74	fault	19185	16284	4653	
214	52	fault	19183	16268	4653	
214	63	fault	19192	16280	4653	
55	9	bedding	19328	16363	4653	
35	18	bedding	19288	16363	4653	
41	10	bedding	19169	16147	4653	
349	9	bedding	19090	15987	4653	
256	36	bedding	19074	16146	4653	
295	80	joint	19350	16400	4653	
208	54	joint	19333	16371	4653	
194	80	joint	19166	16149	4653	
43	31	shear	19168	16139	4653	
323	69	sh fracture	19175	16161	4653	
281	84	sh fracture	19182	16140	4653	
315	73	fault	19302	16383	4652	
292	72	fault	19092	15993	4652	
294	70	fault	19083	16005	4652	
245	81	fault	19078	16144	4652	
78	19	bedding	19344	16363	4652	
20	20	bedding	19279	16335	4652	
7	13	bedding	19184	16164	4652	
215	87	joint	19358	16389	4652	
289	70	sh fracture	19295	16357	4652	
204	50	sh fracture	19295	16351	4652	
132	87	fault	19364	16371	4651	SAH
133	85	fault	19361	16365	4651	SAH
38	33	fault	19352	16356	4651	
281	75	fault	19238	16289	4651	
235	38	fault	19082	16139	4651	
20	20	bedding	19368	16376	4651	
61	18	bedding	19196	16156	4651	
49	31	bedding	19188	16134	4651	
230	70	joint	19197	16160	4651	
37	13	shear	19185	16127	4651	
324	70	sh fracture	19196	16150	4651	
212	75	fault	19350	16388	4650	
23	82	bedding	19186	16122	4650	
84	15	bedding	19192	16118	4650	
32	14	shear	19207	16181	4650	
214	5	anticline	19190	16123	4650	
245	53	sh fracture	19346	16392	4650	
34	41	fault	19260	16182	4649	
281	74	fault	19260	16168	4649	
50	33	fault	19103	16132	4649	
204	73	fault	19124	16257	4649	
252	19	bedding	19156	16331	4649	
242	25	bedding	19171	16359	4649	
225	33	bedding	19196	16400	4649	
192	28	bedding	19055	16230	4649	
97	18	bedding	19072	16025	4649	
19	64	joint	19069	16215	4649	
304	87	joint	19059	16225	4649	
317	87	joint	19106	16153	4649	
336	87	joint	19180	16374	4649	
79	83	joint	19178	16369	4649	
115	72	joint	19198	16373	4649	
209	84	joint	19064	16231	4649	
291	82	joint	19045	16220	4649	
116	74	joint	19158	16279	4649	
345	87	joint	19157	16318	4649	
324	78	joint	19101	16005	4649	
92	68	joint	19086	16128	4649	
34	60	fault	19125	16124	4648	
29	42	fault	19076	16028	4648	
59	12	bedding	19221	16136	4648	
61	7	bedding	19218	16118	4648	
43	23	bedding	19103	16012	4648	
241	30	bedding	19087	16120	4648	
31	77	sh. fracture	19227	16143	4648	
292	75	fault	19121	16107	4647	
329	88	fault	19181	16163	4647	
13	78	fault	19232	16121	4647	
60	1	bedding	19115	16100	4647	
288	53	joint	19227	16131	4647	
250	10	anticline	19077	16034	4647	
123	77	sh. fracture	19118	16105	4647	
34	79	sh. fracture	19121	16101	4647	
30	63	sh. fracture	19222	16116	4647	
83	24	fault	19126	16097	4646	
340	84	fault	19189	16161	4646	
64	9	bedding	19112	16024	4646	
326	69	joint	19144	16114	4646	
33	73	sh fracture	19142	16124	4646	
80	63	sh fracture	19129	16092	4646	
28	71	fault	19289	16295	4645	
326	70	fault	19203	16150	4645	
248	14	bedding	19087	16044	4645	
32	54	fault	19257	16250	4644	
42	53	fault	19243	16222	4644	

AZIMUTH	DIP	STRUCTURE	EASTING	NORTHING	ELEVATION	REMARK
27	19	bedding	19257	16217	4644	
296	77	shear fracture	19249	16213	4644	
8	73	shear fracture	19146	16080	4644	
305	81	shear fracture	19160	16115	4644	
20	36	fault	19283	16265	4643	
103	50	fault	19181	16077	4643	
338	77	fault	19205	16118	4643	
346	78	fault	19210	16115	4643	
82	60	fault	19107	16099	4643	
64	12	bedding	19151	16076	4643	
25	23	bedding	19164	16098	4643	
284	70	joint	19097	16049	4643	
85	4	shear	19175	16103	4643	
224	27	anticline	19177	16111	4643	
322	60	shear fracture	19175	16097	4643	
280	71	fault	19309	16273	4642	
277	61	fault	19293	16278	4642	
286	70	fault	19295	16271	4642	
23	39	fault	19271	16240	4642	
29	40	fault	19261	16215	4642	
25	46	fault	19273	16206	4642	
32	41	fault	19220	16105	4642	
31	46	fault	19236	16132	4642	
60	70	fault	19128	16049	4642	
78	74	fault	19100	16044	4642	
83	15	fault	19135	16070	4642	
78	31	fault	19112	16065	4642	
50	10	bedding	19122	16038	4642	
62	26	bedding	19104	16055	4642	
75	15	bedding	19112	16080	4642	
334	87	joint	19183	16070	4642	
84	15	vein	19140	16071	4642	
52	70	shear fracture	19278	16224	4642	
76	33	fault	19097	16061	4641	
29	75	bedding	19093	16064	4641	
42	55	shear fracture	19187	16100	4641	
297	75	fault	19190	16076	4640	
32	44	fault	19197	16081	4640	
48	57	fault	19073	16060	4640	
30	4	bedding	19181	16082	4640	
13	28	bedding	19193	16084	4640	
288	78	joint	19196	16093	4640	
310	80	joint	19083	16061	4640	
43	16	bedding	19093	16047	4639	
85	64	fault	18987	15999	4638	
220	25	bedding	18986	16009	4638	
343	75	joint	18985	16002	4638	
64	86	joint	18988	16007	4638	
319	77	fault	19011	16039	4637	
73	40	fault	19020	16016	4637	
300	72	fault	19030	16031	4637	
85	48	fault	19053	16031	4637	
61	71	fault	19046	16044	4637	
231	31	bedding	18999	16028	4637	
247	37	bedding	19006	16034	4637	
325	77	joint	19001	16021	4637	
297	65	fault	19143	15981	4636	WALL
87	30	fault	19113	15960	4636	CFZ
296	66	fault	19066	16012	4636	
292	82	fault	19052	16019	4636	
244	29	bedding	19044	16058	4636	
219	40	bedding	19024	16059	4636	
273	74	joint	19050	16028	4636	
40	28	fault	19145	15987	4635	CFZ
143	19	bedding	19048	16016	4635	
23	70	joint	18830	15991	4635	
23	70	joint	18830	15991	4635	
285	55	vein	19142	16001	4635	
17	28	fault	19180	16038	4634	CFZ
242	22	bedding	19093	16117	4634	
105	20	bedding	19165	16047	4634	
155	80	joint	19173	16021	4634	
30	70	joint	19112	16091	4634	
330	65	joint	19112	16087	4634	
155	85	joint	19178	16030	4634	
61	66	joint	19056	15994	4634	
124	77	joint	18815	15991	4634	
313	52	joint	18826	15982	4634	
124	77	joint	18815	15991	4634	
313	52	joint	18826	15982	4634	
55	45	vein	19097	16109	4634	
60	65	vein	19104	16102	4634	
332	83	fault	19049	15984	4633	
170	52	fault	18799	15994	4633	
170	52	fault	18799	15994	4633	
214	22	bedding	19050	15982	4633	
185	35	bedding	18804	15997	4633	
185	35	bedding	18804	15997	4633	
243	32	bedding	19025	15976	4632	
183	33	bedding	18806	15977	4632	
183	33	bedding	18806	15977	4632	
254	77	joint	19043	15972	4632	

AZIMUTH	DIP	STRUCTURE	EASTING	NORTHING	ELEVATION	REMARK
43	35	fault	19182	16041	4631	CFZ
172	67	fault	18801	15974	4631	
172	67	fault	18801	15974	4631	
207	50	bedding	18786	15980	4631	
207	50	bedding	18786	15980	4631	
325	72	joint	19040	15965	4631	
227	63	shear	18791	15986	4631	
227	63	shear	18791	15986	4631	
130	87	joint	18831	15976	4630	
130	87	joint	18831	15976	4630	
164	33	shear	18787	15960	4629	
164	33	shear	18787	15960	4629	
71	20	bedding	19154	16022	4628	
208	35	bedding	18769	15968	4628	
202	29	bedding	18831	15966	4628	
208	35	bedding	18769	15968	4628	
202	29	bedding	18831	15966	4628	
96	85	joint	19141	16004	4625	
339	67	sh. fracture	18842	15955	4625	
339	67	sh. fracture	18842	15955	4625	
44	13	bedding	19117	16003	4624	
323	45	vein	19135	15999	4624	
50	77	vein	18830	15941	4624	
50	77	vein	18830	15941	4624	
289	82	fault	19142	15980	4623	
273	5	bedding	19102	16002	4623	
295	84	fault	19100	15997	4622	
31	72	fault	18851	15941	4622	
31	72	fault	18851	15941	4622	
335	60	joint	18844	15939	4622	
335	60	joint	18844	15939	4622	
104	3	bedding	19096	15993	4621	
339	70	vein	19137	15969	4621	
224	68	sh. fracture	18856	15927	4621	
224	68	sh. fracture	18856	15927	4621	
67	2	bedding	19094	15981	4620	
351	5	bedding	19102	15975	4620	
359	60	vein	19131	15959	4620	
308	67	sh. fracture	18859	15922	4620	
308	67	sh. fracture	18859	15922	4620	
64	33	fault	19114	15961	4619	CFZ
210	12	bedding	19112	15968	4619	
357	60	shear fracture	19128	15955	4619	
209	30	bedding	18842	15901	4617	
209	30	bedding	18842	15901	4617	
37	71	fault	18861	15895	4616	
37	71	fault	18861	15895	4616	
40	35	fault	18904	15931	4615	
45	73	fault	18914	15958	4615	
40	35	fault	18904	15931	4615	
45	73	fault	18914	15958	4615	
40	66	fault	18850	15879	4614	
224	60	fault	18866	15877	4614	
40	66	fault	18850	15879	4614	
224	60	fault	18866	15877	4614	
197	31	bedding	18910	15930	4614	
190	44	bedding	18926	15951	4614	
49	54	bedding	18916	15941	4614	
197	31	bedding	18910	15930	4614	
190	44	bedding	18926	15951	4614	
49	54	bedding	18916	15941	4614	
297	75	joint	18868	15871	4614	
297	75	joint	18868	15871	4614	
70	79	sh. fracture	18900	15957	4614	
70	79	sh. fracture	18900	15957	4614	
59	52	fault	18923	15941	4613	
59	52	fault	18923	15941	4613	
336	75	fault	19202	16415	4612	
314	78	fault	19209	16428	4612	
349	78	fault	19280	16403	4612	
335	79	fault	19309	16389	4612	
299	88	fault	19350	16379	4612	SAG
130	84	fault	19309	16403	4612	SAG
35	39	fault	19265	16282	4612	
336	75	fault	19202	16415	4612	
314	78	fault	19209	16428	4612	
349	78	fault	19280	16403	4612	
335	79	fault	19309	16389	4612	
299	88	fault	19350	16379	4612	SAG
130	84	fault	19309	16403	4612	SAG
35	39	fault	19265	16282	4612	
215	49	fault	18852	15863	4612	
215	49	fault	18852	15863	4612	
244	23	bedding	19190	16402	4612	
246	22	bedding	19221	16443	4612	
222	24	bedding	19283	16405	4612	
189	18	bedding	19319	16377	4612	
71	8	bedding	19335	16369	4612	
201	21	bedding	19291	16425	4612	
82	3	bedding	19238	16305	4612	
249	9	bedding	19241	16295	4612	
66	9	bedding	19259	16289	4612	

AZIMUTH	DIP	STRUCTURE	EASTING	NORTHING	ELEVATION	REMARK
244	23	bedding	19190	16402	4612	
246	22	bedding	19221	16443	4612	
222	24	bedding	19283	16405	4612	
189	18	bedding	19319	16377	4612	
71	8	bedding	19335	16369	4612	
201	21	bedding	19291	16425	4612	
82	3	bedding	19238	16305	4612	
249	9	bedding	19241	16295	4612	
66	9	bedding	19259	16289	4612	
202	33	bedding	18909	15969	4612	
159	19	bedding	18928	15914	4612	
202	33	bedding	18909	15969	4612	
159	19	bedding	18928	15914	4612	
138	85	joint	19210	16439	4612	
140	86	joint	19249	16432	4612	
30	75	joint	19282	16398	4612	
277	75	joint	19257	16293	4612	
138	85	joint	19210	16439	4612	
140	86	joint	19249	16432	4612	
30	75	joint	19282	16398	4612	
277	75	joint	19257	16293	4612	
206	6	anticline	19327	16371	4612	
206	6	anticline	19327	16371	4612	
216	20	anticline	18928	15948	4612	
216	20	anticline	18928	15948	4612	
317	74	shear fracture	19337	16375	4612	
331	74	shear fracture	19297	16395	4612	
331	74	shear fracture	19292	16410	4612	
317	74	shear fracture	19337	16375	4612	
331	74	shear fracture	19297	16395	4612	
331	74	shear fracture	19292	16410	4612	
331	75	fault	18926	15957	4611	
331	75	fault	18926	15957	4611	
213	88	joint	18934	15909	4611	
213	88	joint	18934	15909	4611	
298	83	shear fracture	18940	15925	4611	
298	83	shear fracture	18940	15925	4611	
327	70	fault	18848	15842	4610	
327	70	fault	18848	15842	4610	
181	35	bedding	18866	15847	4610	
181	35	bedding	18866	15847	4610	
232	76	joint	18843	15843	4610	
232	76	joint	18843	15843	4610	
310	76	joint	18845	15834	4609	
310	76	joint	18845	15834	4609	
331	70	shear fracture	18932	15964	4609	
331	70	shear fracture	18932	15964	4609	
221	56	fault	19256	16358	4608	
222	54	fault	19266	16370	4608	
80	65	fault	19272	16346	4608	
65	54	fault	19291	16339	4608	
221	56	fault	19256	16358	4608	
222	54	fault	19266	16370	4608	
80	65	fault	19272	16346	4608	
65	54	fault	19291	16339	4608	
210	32	bedding	19224	16375	4608	
54	9	bedding	19249	16357	4608	
241	16	bedding	19262	16357	4608	
284	7	bedding	19278	16361	4608	
210	40	bedding	19288	16354	4608	
230	53	bedding	19280	16339	4608	
207	35	bedding	19289	16333	4608	
49	7	bedding	19296	16329	4608	
22	26	bedding	19318	16334	4608	
210	32	bedding	19224	16375	4608	
54	9	bedding	19249	16357	4608	
241	16	bedding	19262	16357	4608	
284	7	bedding	19278	16361	4608	
210	40	bedding	19288	16354	4608	
230	53	bedding	19280	16339	4608	
207	35	bedding	19289	16333	4608	
49	7	bedding	19296	16329	4608	
22	26	bedding	19318	16334	4608	
222	71	joint	19310	16338	4608	
325	78	joint	19264	16378	4608	
47	80	joint	19238	16358	4608	
100	87	joint	19203	16373	4608	
130	77	joint	19238	16369	4608	
222	71	joint	19310	16338	4608	
325	78	joint	19264	16378	4608	
47	80	joint	19238	16358	4608	
100	87	joint	19203	16373	4608	
130	77	joint	19238	16369	4608	
321	64	shear fracture	19291	16348	4608	
321	64	shear fracture	19291	16348	4608	
60	68	shear fracture	18941	15970	4608	
60	68	shear fracture	18941	15970	4608	
203	25	bedding	18940	15991	4606	
209	26	bedding	18834	15813	4606	
203	25	bedding	18940	15991	4606	
209	26	bedding	18834	15813	4606	
166	37	bedding	18859	15813	4604	

AZIMUTH	DIP	STRUCTURE	EASTING	NORTHING	ELEVATION	REMARK
196	35	bedding	18842	15795	4604	
196	35	bedding	18842	15795	4604	
210	90	sh. fracture	18838	15801	4604	
210	90	sh. fracture	18838	15801	4604	
77	37	fault	18849	15788	4603	CFZ
217	38	bedding	18944	16005	4603	
217	38	bedding	18944	16005	4603	
12	83	sh fracture	18861	15803	4603	
329	81	fault	18960	15994	4602	
329	81	fault	18960	15994	4602	
83	48	fault	18870	15794	4601	CFZ
53	47	fault	18966	16002	4601	
53	47	fault	18966	16002	4601	
19	66	fault	18828	15808	4601	
19	66	fault	18828	15808	4601	
187	24	bedding	18957	16020	4600	
187	24	bedding	18957	16020	4600	
310	82	sh.fracture	18965	16016	4599	
310	82	sh.fracture	18965	16016	4599	
258	77	joint	18813	15794	4598	
258	77	joint	18813	15794	4598	
211	84	fault	19156	16377	4597	
218	33	bedding	19149	16396	4597	
233	31	bedding	19168	16387	4597	
50	82	joint	18804	15788	4597	
50	82	joint	18804	15788	4597	
142	80	sh fracture	19176	16375	4597	
45	48	sh fracture	19164	16403	4597	
142	80	sh.fracture	19176	16375	4597	
324	65	fault	18907	15768	4596	
77	78	joint	18980	16035	4596	
77	78	joint	18980	16035	4596	
302	80	fault	19183	16343	4595	
333	74	fault	19074	16385	4595	
354	77	fault	19071	16381	4595	
16	79	fault	19063	16384	4595	
321	80	fault	18800	15773	4595	
238	72	fault	18767	15818	4595	
56	74	fault	18773	15811	4595	
321	80	fault	18800	15773	4595	
238	72	fault	18767	15818	4595	
56	74	fault	18773	15811	4595	
217	32	bedding	18981	16041	4595	
225	32	bedding	19158	16342	4595	
217	32	bedding	18981	16041	4595	
216	20	bedding	18785	15794	4595	
52	10	bedding	18778	15798	4595	
176	18	bedding	18769	15812	4595	
216	20	bedding	18785	15794	4595	
52	10	bedding	18778	15798	4595	
176	18	bedding	18769	15812	4595	
218	26	shear	19201	16339	4595	
54	66	sh fracture	19175	16325	4595	
133	72	sh fracture	19198	16318	4595	
286	78	fault	19088	16396	4594	
341	80	fault	19088	16406	4594	
219	69	bedding	19009	15950	4594	
219	69	bedding	19009	15950	4594	
238	38	bedding	19174	16329	4594	
237	33	bedding	19215	16330	4594	
218	15	bedding	19215	16312	4594	
254	21	bedding	19057	16394	4594	
208	22	bedding	19083	16404	4594	
218	15	bedding	19215	16312	4594	
293	89	joint	19004	16033	4594	
29	70	joint	19093	16407	4594	
293	89	joint	19004	16033	4594	
339	67	joint	18752	15829	4594	
339	67	joint	18752	15829	4594	
339	48	shear	18996	16035	4594	
239	28	shear	19152	16331	4594	
234	30	shear	19213	16315	4594	
224	24	shear	19145	16411	4594	
339	48	shear	18996	16035	4594	
234	30	shear	19213	16315	4594	
101	68	sh fracture	19208	16330	4594	
315	64	fault	18937	15785	4593	
54	73	fault	19229	16306	4593	
344	75	fault	19064	16406	4593	
351	75	fault	19087	16404	4593	
54	73	fault	19229	16306	4593	
285	7	bedding	19157	16432	4593	
182	15	bedding	18748	15826	4593	
182	15	bedding	18748	15826	4593	
328	65	joint	19005	15945	4593	
328	65	joint	19005	15945	4593	
337	72	joint	19070	16407	4593	
273	86	joint	19112	16419	4593	
202	25	shear	19235	16321	4593	
214	24	shear	19125	16422	4593	
202	25	shear	19235	16321	4593	
308	40	anticline	18988	16049	4593	

AZIMUTH	DIP	STRUCTURE	EASTING	NORTHING	ELEVATION	REMARK
98	79	shear fracture	19144	16329	4593	
314	80	shear fracture	19090	16419	4593	
50	66	shear fracture	19074	16415	4593	
107	26	fault	18928	15801	4592	CFZ
331	66	fault	18998	15932	4592	
29	77	fault	19085	16428	4592	
53	80	fault	19070	16417	4592	
220	28	bedding	18994	16055	4592	
227	24	bedding	19147	16441	4592	
220	28	bedding	18994	16055	4592	
192	18	bedding	18782	15760	4592	
5	90	joint	19069	15905	4592	
23	77	joint	19108	16426	4592	
227	22	shear	19147	16447	4592	
209	34	shear	19125	16439	4592	
68	53	fault	18954	15800	4591	
332	66	fault	19007	15914	4591	
342	52	fault	18998	15926	4591	
109	77	fault	19016	16054	4591	
284	82	fault	19139	16314	4591	
109	77	fault	19016	16054	4591	
199	40	bedding	18941	15812	4591	
236	27	bedding	19125	16453	4591	
207	26	bedding	19107	16441	4591	
228	20	bedding	19098	16437	4591	
358	83	joint	18996	15926	4591	
352	87	joint	18965	15932	4591	
250	70	joint	18983	15927	4591	
327	83	joint	19131	16451	4591	
257	84	joint	18768	15772	4591	
294	77	vein	19005	16084	4591	
320	82	fault	18964	15805	4590	
340	55	fault	19005	15904	4590	
297	63	fault	19008	16087	4590	
274	79	fault	19260	16305	4590	
108	71	fault	19135	16307	4590	
284	82	fault	19122	16466	4590	
286	82	fault	19141	16461	4590	
274	79	fault	19260	16305	4590	
325	78	fault	19087	15886	4590	
218	68	bedding	18988	15913	4590	
235	78	bedding	18991	15917	4590	
80	27	bedding	18968	15925	4590	
198	12	bedding	18761	15766	4590	
209	70	beddingo	18986	15920	4590	
218	65	beddingo	18988	15917	4590	
58	70	beddingo	18991	15918	4590	
255	80	joint	19005	15911	4590	
41	49	joint	19014	16045	4590	
41	49	joint	19014	16045	4590	
223	77	fault	18971	15812	4589	
326	75	fault	18971	15907	4589	
302	83	fault	19269	16299	4589	
302	83	fault	19269	16299	4589	
223	61	bedding	18958	15823	4589	
103	45	bedding	18968	15919	4589	
265	60	bedding	18969	15910	4589	
224	33	bedding	19025	16089	4589	
250	35	bedding	19134	16301	4589	
225	23	bedding	19123	16482	4589	
268	86	joint	18974	15809	4589	
15	85	joint	18968	15916	4589	
60	90	joint	19056	15879	4589	
0	90	joint	19069	15873	4589	
350	67	joint	19133	16472	4589	
163	86	joint	18754	15761	4589	
250	10	syncline	18987	15915	4589	
295	83	vein	19065	15868	4589	
12	73	shear fracture	19033	16073	4589	
319	86	shear fracture	19128	16301	4589	
310	83	shear fracture	19136	16480	4589	
355	71	fault	18978	15815	4588	
320	70	fault	18970	15904	4588	
30	70	fault	19050	15868	4588	
105	87	fault	19133	16493	4588	
224	71	bedding	18987	15904	4588	
275	70	bedding	18971	15902	4588	
285	62	bedding	18971	15897	4588	
175	25	bedding	18995	15888	4588	
183	71	joint	19043	16095	4588	
255	84	joint	19052	16086	4588	
127	78	joint	19113	16482	4588	
37	90	joint	18763	15744	4588	
219	31	shear	19149	16291	4588	
304	80	vein	19033	16094	4588	
34	58	shear fracture	19120	16486	4588	
315	70	fault	19039	15858	4587	
24	28	fault	19139	16096	4587	
27	34	fault	19163	16107	4587	
22	32	fault	19151	16080	4587	
104	74	fault	19110	16499	4587	

AZIMUTH	DIP	STRUCTURE	EASTING	NORTHING	ELEVATION	REMARK
27	34	fault	19163	16107	4587	
22	32	fault	19151	16080	4587	
143	60	fault	19150	16247	4587	
310	80	fault	19119	16158	4587	
316	60	fault	19113	16153	4587	
312	60	fault	19109	16146	4587	
45	55	bedding	18975	15885	4587	
240	47	bedding	18998	15882	4587	
35	44	bedding	19150	16092	4587	
38	50	bedding	19141	16118	4587	
10	22	bedding	19190	16088	4587	
48	23	bedding	19169	16083	4587	
242	13	bedding	19135	16498	4587	
10	22	bedding	19190	16088	4587	
48	23	bedding	19169	16083	4587	
119	20	bedding	18757	15740	4587	
89	10	bedding	18743	15749	4587	
15	90	joint	18972	15893	4587	
17	80	joint	18975	15888	4587	
118	83	joint	19198	16092	4587	
193	58	joint	19192	16099	4587	
8	75	joint	19127	16505	4587	
118	83	joint	19198	16092	4587	
193	58	joint	19192	16099	4587	
127	90	joint	19138	16213	4587	
258	80	joint	19110	16155	4587	
301	79	vein	19046	16108	4587	
218	80	vein	19215	16078	4587	
30	77	vein	19164	16071	4587	
218	80	vein	19215	16078	4587	
30	77	vein	19164	16071	4587	
225	77	fault	18994	15834	4586	
315	50	fault	19052	15844	4586	
125	79	fault	19129	16514	4586	SAH
291	89	fault	19272	16278	4586	
290	85	fault	19282	16269	4586	
291	89	fault	19272	16278	4586	
290	85	fault	19282	16269	4586	
209	48	bedding	18972	15832	4586	
231	64	bedding	18972	15881	4586	
235	72	bedding	18978	15875	4586	
49	19	bedding	19295	16256	4586	
49	19	bedding	19295	16256	4586	
220	25	bedding	19132	16224	4586	
211	25	bedding	19106	16181	4586	
295	68	joint	18995	15865	4586	
242	45	joint	18995	15873	4586	
345	90	joint	19050	15842	4586	
16	88	joint	19103	16514	4586	
255	90	joint	19110	16184	4586	
244	85	joint	19083	16123	4586	
38	90	joint	19104	16148	4586	
36	20	shear	19302	16258	4586	
36	20	shear	19302	16258	4586	
200	67	sh fracture	19290	16254	4586	
200	67	sh fracture	19290	16254	4586	
214	80	fault	18980	15843	4585	
320	60	fault	18998	15858	4585	
23	28	fault	19131	16104	4585	
45	46	fault	19147	16112	4585	
35	65	fault	19270	16217	4585	
37	65	fault	19279	16229	4585	
29	58	fault	19244	16248	4585	
31	57	fault	19239	16235	4585	
28	42	fault	19251	16228	4585	
206	55	fault	19260	16239	4585	
201	47	fault	19278	16213	4585	
212	81	fault	19276	16214	4585	
218	80	fault	19285	16226	4585	
32	70	fault	19199	16263	4585	
307	87	fault	19172	16274	4585	
290	56	fault	19334	16262	4585	
201	58	fault	19324	16249	4585	
230	61	fault	19333	16257	4585	
32	74	fault	19330	16244	4585	
306	83	fault	19413	16321	4585	SAH
35	65	fault	19270	16217	4585	
37	65	fault	19279	16229	4585	
29	58	fault	19244	16248	4585	
31	57	fault	19239	16235	4585	
28	42	fault	19251	16228	4585	
206	55	fault	19260	16239	4585	
201	47	fault	19278	16213	4585	
212	81	fault	19276	16214	4585	
218	80	fault	19285	16226	4585	
290	56	fault	19334	16262	4585	
201	58	fault	19324	16249	4585	
230	61	fault	19333	16257	4585	
32	74	fault	19330	16244	4585	
306	83	fault	19413	16321	4585	SAH
335	75	fault	19038	15841	4585	

AZIMUTH	DIP	STRUCTURE	EASTING	NORTHING	ELEVATION	REMARK
255	53	bedding	18979	15868	4585	
225	28	bedding	19042	16151	4585	
44	42	bedding	19291	16208	4585	
17	57	bedding	19278	16228	4585	
24	12	bedding	19241	16256	4585	
226	34	bedding	19172	16289	4585	
352	10	bedding	19184	16270	4585	
207	24	bedding	19128	16531	4585	
220	24	bedding	19104	16521	4585	
74	12	bedding	19414	16335	4585	
44	42	bedding	19291	16208	4585	
17	57	bedding	19278	16228	4585	
24	12	bedding	19241	16256	4585	
74	12	bedding	19414	16335	4585	
218	20	bedding	19088	16154	4585	
142	77	joint	18975	15851	4585	
210	40	joint	19003	15856	4585	
173	80	joint	19242	16226	4585	
126	77	joint	19263	16233	4585	
129	80	joint	19298	16214	4585	
281	85	joint	19186	16291	4585	
69	85	joint	19206	16251	4585	
308	88	joint	19102	16527	4585	
290	86	joint	19120	16528	4585	
58	57	joint	19311	16245	4585	
173	80	joint	19242	16226	4585	
126	77	joint	19263	16233	4585	
129	80	joint	19298	16214	4585	
69	85	joint	19206	16251	4585	
58	57	joint	19311	16245	4585	
147	90	joint	19148	16293	4585	
215	70	joint	19112	16200	4585	
328	75	joint	19109	16192	4585	
114	80	joint	19079	16147	4585	
44	90	joint	19066	16108	4585	
217	44	vein	19290	16220	4585	
216	44	vein	19283	16209	4585	
43	48	vein	19233	16241	4585	
304	75	vein	19397	16323	4585	
304	75	vein	19410	16315	4585	
217	44	vein	19290	16220	4585	
216	44	vein	19283	16209	4585	
43	48	vein	19233	16241	4585	
304	75	vein	19397	16323	4585	
304	75	vein	19410	16315	4585	
4	84	shear fracture	19213	16249	4585	
313	73	shear fracture	19308	16250	4585	
285	73	shear fracture	19316	16279	4585	
305	75	shear fracture	19394	16319	4585	
56	54	shear fracture	19131	16245	4585	
4	84	shear fracture	19213	16249	4585	
313	73	shear fracture	19308	16250	4585	
285	73	shear fracture	19316	16279	4585	
305	75	shear fracture	19394	16319	4585	
308	66	fault	19003	15856	4584	
65	32	fault	19061	15821	4584	CFZ
149	79	fault	19137	16276	4584	dike
115	74	fault	19108	16533	4584	SAH
282	53	fault	19355	16251	4584	
283	67	fault	19349	16241	4584	
306	70	fault	19392	16314	4584	
306	69	fault	19384	16300	4584	
282	53	fault	19355	16251	4584	
283	67	fault	19349	16241	4584	
306	70	fault	19392	16314	4584	
306	69	fault	19384	16300	4584	
197	43	bedding	19013	15961	4584	
30	33	bedding	19127	16115	4584	
208	23	bedding	19099	16203	4584	
217	24	bedding	19117	16225	4584	
234	25	bedding	19140	16251	4584	
230	31	bedding	19143	16280	4584	
201	32	bedding	19114	16538	4584	
298	25	bedding	19120	16253	4584	
211	35	bedding	19142	16317	4584	
345	52	joint	18981	15858	4584	
121	77	joint	19134	16126	4584	
323	76	joint	19151	16282	4584	
52	68	joint	19122	16534	4584	
325	82	joint	19126	16271	4584	
156	80	joint	19127	16268	4584	
151	80	joint	19121	16269	4584	
192	80	joint	19134	16284	4584	
34	60	joint	19137	16294	4584	
27	65	joint	19088	16131	4584	
145	75	joint	19081	16133	4584	
212	70	joint	18738	15722	4584	
35	71	vein	19117	16110	4584	
29	85	vein	19140	16214	4584	
329	90	vein	19138	16208	4584	
20	71	vein	19152	16275	4584	
39	74	shear fracture	19120	16218	4584	

AZIMUTH	DIP	STRUCTURE	EASTING	NORTHING	ELEVATION	REMARK
41	74	sh fracture	19142	16243	4584	
328	76	sh fracture	19154	16263	4584	
197	42	sh fracture	19324	16262	4584	
304	81	sh fracture	19380	16295	4584	
197	42	sh fracture	19324	16262	4584	
304	81	sh fracture	19380	16295	4584	
67	45	fault	19042	15814	4583	CFZ
335	46	fault	19030	15818	4583	
148	83	fault	19165	16231	4583	dike
139	70	fault	19182	16204	4583	dike
50	17	fault	19223	16197	4583	
23	77	fault	19119	16507	4583	
164	59	fault	19387	16274	4583	
278	76	fault	19388	16276	4583	
50	17	fault	19223	16197	4583	
164	59	fault	19387	16274	4583	
278	76	fault	19388	16276	4583	
323	40	fault	19059	15809	4583	
232	31	bedding	19082	16155	4583	
53	21	bedding	19144	16176	4583	
197	23	bedding	19153	16213	4583	
54	24	bedding	19166	16207	4583	
14	38	bedding	19173	16202	4583	
40	16	bedding	19191	16220	4583	
42	6	bedding	19193	16204	4583	
80	13	bedding	19381	16288	4583	
80	13	bedding	19381	16288	4583	
214	22	contact	19088	16233	4583	
91	80	joint	19208	16206	4583	
209	87	joint	19376	16289	4583	
91	80	joint	19208	16206	4583	
209	87	joint	19376	16289	4583	
181	40	joint	19116	16271	4583	
216	7	anticline	19159	16212	4583	
216	7	anticline	19159	16212	4583	
218	82	sh fracture	19184	16221	4583	
56	65	fault	18974	15832	4582	
34	47	fault	19208	16189	4582	
45	33	fault	19226	16178	4582	
24	88	fault	19245	16184	4582	
49	18	fault	19240	16171	4582	
37	43	fault	19386	16236	4582	
25	41	fault	19402	16231	4582	
30	63	fault	19381	16258	4582	
232	70	fault	19107	16277	4582	
34	47	fault	19208	16189	4582	
45	33	fault	19226	16178	4582	
24	88	fault	19245	16184	4582	
49	18	fault	19240	16171	4582	
37	43	fault	19386	16236	4582	
25	41	fault	19402	16231	4582	
30	63	fault	19381	16258	4582	
200	64	bedding	18991	15824	4582	
196	15	bedding	19138	16183	4582	
22	25	bedding	19273	16178	4582	
12	22	bedding	19227	16207	4582	
37	16	bedding	19375	16270	4582	
24	37	bedding	19413	16231	4582	
22	25	bedding	19273	16178	4582	
12	22	bedding	19227	16207	4582	
37	16	bedding	19375	16270	4582	
24	37	bedding	19413	16231	4582	
77	84	joint	19252	16188	4582	
198	68	joint	19252	16151	4582	
290	83	joint	19269	16167	4582	
77	84	joint	19252	16188	4582	
198	68	joint	19252	16151	4582	
290	83	joint	19269	16167	4582	
203	30	joint	19040	16146	4582	
218	5	anticline	19144	16185	4582	
218	5	anticline	19144	16185	4582	
340	55	vein	18993	15824	4582	
198	60	sh. fracture	19263	16171	4582	
198	60	sh fracture	19263	16171	4582	
294	73	fault	19091	16159	4581	
41	73	fault	19127	16125	4581	
210	80	fault	19094	16284	4581	
211	85	fault	19096	16288	4581	
23	40	bedding	19099	16110	4581	
23	51	bedding	19108	16146	4581	
45	31	bedding	19134	16167	4581	
36	61	bedding	19143	16156	4581	
149	16	bedding	18720	15710	4581	
35	11	anticline	19094	16145	4581	
35	11	anticline	19094	16145	4581	
38	78	vein	19119	16125	4581	
56	83	vein	19128	16185	4581	
125	90	vein	19140	16211	4581	
39	78	sh. fracture	19100	16135	4581	
335	65	fault	18979	15814	4580	
298	79	fault	19098	16169	4580	
40	30	fault	19169	16148	4580	

AZIMUTH	DIP	STRUCTURE	EASTING	NORTHING	ELEVATION	REMARK
40	33	fault	19178	16158	4580	
232	23	contact	19086	16289	4580	
347	60	joint	19078	16275	4580	
341	73	joint	18704	15724	4580	
294	80	vein	19103	16169	4580	
256	66	vein	19108	16176	4580	
337	70	fault	18955	15810	4579	
34	28	fault	19189	16151	4579	
32	23	fault	19182	16140	4579	
208	90	fault	19075	16295	4579	
34	28	fault	19189	16151	4579	
32	23	fault	19182	16140	4579	
141	69	fault	18710	15706	4579	
143	69	fault	18698	15722	4579	
207	30	bedding	18948	15813	4579	
216	24	bedding	19099	16177	4579	
18	33	bedding	19188	16181	4579	
18	33	bedding	19188	16181	4579	
194	20	bedding	19069	16298	4579	
258	30	bedding	19083	16285	4579	
147	18	bedding	18706	15702	4579	
335	86	joint	19104	16195	4579	
269	76	joint	19187	16129	4579	
338	80	joint	19195	16136	4579	
269	76	joint	19187	16129	4579	
338	80	joint	19195	16136	4579	
115	70	joint	19074	16294	4579	
197	77	vein	19069	16299	4579	
316	65	fault	18940	15799	4578	
57	15	fault	19199	16130	4578	
327	79	fault	19214	16140	4578	
57	15	fault	19199	16130	4578	
327	79	fault	19214	16140	4578	
133	83	fault	18662	15758	4578	
236	30	bedding	18939	15807	4578	
70	14	bedding	19203	16121	4578	
70	14	bedding	19203	16121	4578	
51	55	joint	19062	16301	4578	
348	65	joint	19056	16289	4578	
115	15	fault	18925	15797	4577	CFZ
136	86	fault	19226	16132	4577	dike
278	85	fault	19055	16313	4577	
298	71	fault	19088	16402	4577	
136	86	fault	19226	16132	4577	dike
217	70	fault	19065	16399	4577	
43	85	fault	18873	15732	4577	
217	54	bedding	19102	16412	4577	
242	10	bedding	18879	15710	4577	
241	14	bedding	18691	15694	4577	
318	72	joint	19056	16321	4577	
121	75	joint	19053	16312	4577	
127	90	joint	19053	16317	4577	
52	90	joint	19053	16315	4577	
132	72	joint	18885	15711	4577	
118	30	fault	18935	15785	4576	CFZ
317	85	fault	19253	16098	4576	dike
34	67	fault	19033	16304	4576	MAG
22	66	fault	19091	16435	4576	MAG
17	69	fault	19111	16485	4576	MAG
317	85	fault	19253	16098	4576	dike
36	55	fault	19031	16301	4576	
143	85	fault	18663	15759	4576	CRO
125	23	bedding	18838	15820	4576	
353	24	bedding	19248	16113	4576	
353	24	bedding	19248	16113	4576	
200	20	bedding	19094	16450	4576	
143	8	bedding	18684	15740	4576	
184	62	joint	19237	16110	4576	
184	62	joint	19237	16110	4576	
110	90	joint	19051	16323	4576	
314	62	joint	18666	15688	4576	
270	81	joint	18696	15696	4576	
140	70	joint	18657	15749	4576	
294	76	fault	19055	16382	4575	
160	73	fault	19071	16404	4575	
310	68	fault	19055	16383	4575	
253	80	fault	19055	16371	4575	
218	27	bedding	19095	16464	4575	
178	10	bedding	19039	16347	4575	
179	30	bedding	19031	16325	4575	
168	25	bedding	19029	16315	4575	
188	20	bedding	19050	16368	4575	
203	20	bedding	19060	16390	4575	
208	20	bedding	19080	16417	4575	
227	24	contact	19046	16359	4575	
334	84	joint	19098	16475	4575	
46	90	joint	19088	16441	4575	
36	80	joint	19065	16398	4575	
303	73	vein	19060	16390	4575	
95	70	shear fracture	19091	16445	4575	
165	68	fault	18684	15746	4574	
231	28	bedding	19029	16327	4574	

AZIMUTH	DIP	STRUCTURE	EASTING	NORTHING	ELEVATION	REMARK
221	20	bedding	18662	15694	4574	
196	11	bedding	18673	15704	4574	
56	17	bedding	18684	15689	4574	
118	60	joint	19038	16354	4574	
185	70	joint	18686	15742	4574	
73	40	fault	18861	15779	4573	CFZ
315	75	fault	18904	15766	4573	
50	70	fault	18741	15748	4573	
144	20	bedding	18672	15733	4573	
270	55	fault	18718	15732	4572	
240	72	fault	18754	15737	4572	
125	20	bedding	18743	15729	4572	
289	56	joint	18660	15692	4572	
120	20	bedding	18734	15724	4571	
359	76	joint	18669	15674	4571	
23	55	fault	18663	15663	4570	
140	72	fault	18707	15706	4570	CRO
138	10	bedding	18671	15702	4570	
100	56	joint	18660	15691	4570	
236	90	joint	18704	15704	4570	
52	19	bedding	19145	16005	4569	
135	12	bedding	18683	15690	4569	
28	80	joint	18643	15678	4569	
55	80	fault	18623	15664	4568	
26	24	bedding	19167	16017	4568	
58	60	joint	19155	16025	4568	
268	31	fault	18646	15655	4567	
315	62	joint	18662	15634	4567	
54	85	fault	18612	15640	4566	
98	50	fault	18652	15649	4566	
300	76	joint	19183	16039	4566	
10	50	fault	18557	15619	4565	
185	60	fault	18537	15603	4564	
340	80	fault	18545	15600	4564	
105	47	fault	18645	15621	4564	
30	90	joint	18566	15605	4564	
93	41	fault	18644	15615	4563	
95	37	fault	18666	15614	4563	
215	60	fault	18515	15587	4563	
35	85	fault	19023	15698	4563	
105	40	fault	18663	15617	4563	
30	90	joint	18501	15579	4563	
75	90	joint	18523	15594	4563	
3	90	joint	18559	15601	4563	
117	85	joint	18980	15682	4563	
87	90	joint	19018	15695	4563	
105	43	vein	18645	15618	4563	
85	43	fault	18648	15606	4562	CFZ
213	80	fault	18486	15567	4562	
305	65	fault	18996	15678	4562	
35	80	fault	18989	15674	4562	
100	45	fault	18650	15609	4562	
103	28	fault	18672	15606	4562	
195	60	joint	18519	15572	4562	
55	80	joint	18972	15679	4562	
90	65	fault	18996	15671	4561	
305	60	fault	18945	15659	4561	
69	60	fault	18936	15652	4561	
354	80	fault	18864	15645	4561	
105	55	fault	18657	15598	4561	CFZ
92	90	joint	18501	15560	4561	
32	90	joint	18971	15663	4561	
45	90	joint	18842	15635	4561	
40	90	joint	18850	15639	4561	
227	50	vein	18870	15645	4561	
55	40	vein	18680	15601	4561	
72	34	fault	18661	15590	4560	CFZ
290	55	fault	18448	15542	4560	
312	75	fault	18435	15532	4560	
315	75	fault	18818	15614	4560	
105	30	fault	18684	15594	4560	CFZ
90	45	fault	18679	15588	4560	
290	80	joint	18907	15638	4560	
60	35	vein	18659	15589	4560	
15	80	sh fracture	18898	15633	4560	
356	65	fault	18867	15618	4559	
280	75	fault	18809	15611	4559	
40	32	fault	18932	15631	4559	
85	52	bedding	18756	15590	4559	
355	45	joint	18878	15625	4559	
70	90	joint	18869	15620	4559	
295	90	joint	18762	15592	4559	
350	60	joint	18886	15628	4559	
35	90	joint	18888	15628	4559	
70	50	fault	18438	15518	4558	CFZ
307	68	fault	18782	15592	4558	
35	45	fault	18730	15575	4558	
70	75	fault	18710	15575	4558	
325	55	joint	18811	15594	4558	
45	90	joint	18799	15591	4558	
302	45	fault	18938	15614	4557	
120	21	bedding	18739	15569	4557	

AZIMUTH	DIP	STRUCTURE	EASTING	NORTHING	ELEVATION	REMARK
205	75	joint	18780	15583	4557	
205	72	joint	18774	15581	4557	
75	45	fault	18943	15607	4556	
75	60	fault	18943	15603	4556	
83	85	fault	18945	15599	4556	
299	81	fault	19197	16112	4555	
290	54	fault	19260	16319	4555	
294	57	fault	19280	16312	4555	
290	80	fault	19245	16294	4555	
294	78	fault	19265	16286	4555	
297	84	fault	19239	16280	4555	
292	70	fault	19235	16275	4555	
50	73	bedding	19227	16137	4555	
39	8	bedding	19250	16305	4555	
39	10	bedding	19261	16285	4555	
55	16	bedding	19254	16271	4555	
135	88	joint	19261	16279	4555	
303	74	vein	19205	16142	4555	
136	70	Raven dike	19208	16148	4555	dike
32	26	bedding	19239	16242	4554	
152	7	bedding	19226	16265	4554	
201	8	bedding	19217	16241	4552	
71	16	bedding	19218	16221	4551	
59	78	fault	19233	16216	4549	
66	43	bedding	19237	16209	4548	
56	88	joint	19247	16216	4548	
284	87	joint	19313	16212	4547	
286	78	fault	19361	16296	4546	
298	90	fault	19325	16323	4546	
109	65	fault	19338	16337	4546	
293	85	fault	19384	16311	4546	
293	72	fault	19389	16283	4546	
17	59	bedding	19297	16211	4546	
41	35	bedding	19347	16321	4546	
51	12	bedding	19385	16307	4546	
44	26	bedding	19387	16278	4546	
31	13	bedding	19324	16340	4546	
310	74	fault	19284	16246	4545	
127	83	fault	19297	16234	4545	
289	73	fault	19299	16270	4545	
190	73	fault	19292	16256	4545	
277	78	fault	19318	16304	4545	
275	82	fault	19337	16301	4545	
285	65	fault	19352	16279	4545	
290	59	fault	19371	16274	4545	
287	70	fault	19313	16261	4545	
78	60	fault	19325	16238	4545	
37	56	fault	19353	16251	4545	
325	68	fault	19328	16288	4545	
298	78	fault	19339	16256	4545	
285	55	fault	19382	16271	4545	
303	71	fault	19375	16258	4545	
282	78	fault	19367	16244	4545	
25	58	fault	19356	16223	4545	
17	59	bedding	19301	16238	4545	
41	35	bedding	19311	16257	4545	
51	12	bedding	19318	16269	4545	
44	26	bedding	19312	16297	4545	
31	13	bedding	19320	16312	4545	
54	13	bedding	19354	16289	4545	
53	26	bedding	19366	16266	4545	
55	13	bedding	19347	16239	4545	
190	13	bedding	19343	16267	4545	
28	26	bedding	19355	16215	4545	
54	42	bedding	19299	16296	4545	
193	16	bedding	19284	16317	4545	
12	23	bedding	19284	16294	4545	
47	25	bedding	19273	16269	4545	
68	66	joint	19272	16302	4545	
234	74	joint	19301	16281	4545	
202	65	joint	19328	16311	4545	
39	66	joint	19371	16283	4545	
301	72	joint	19359	16269	4545	
238	72	joint	19322	16232	4545	
45	55	joint	19346	16215	4545	
269	87	joint	19346	16206	4545	
37	73	shear	19266	16264	4545	
237	4	anticline	19312	16291	4545	
55	33	shear fracture	19306	16246	4545	
224	65	shear fracture	19297	16297	4545	
311	72	fault	19251	16233	4544	
152	85	Raven dike	19220	16130	4543	dike

APPENDIX 2

U-Pb ZIRCON

ANALYTICAL RESULTS

Report 672 U-Pb zircon analytical results.

672-01 (Isotopic Ratios)

Analysis_#	Pb207/U235	Pb207/U235 (±1s)	Pb206/U238	Pb206/U238 (±1s)	Pb207/Pb206	Pb207/Pb206 (±1s)
6721A16	0.83122	4.21289	-0.03037	0.00881	-0.06876	0.33071
6721A14	-5.34199	6.65985	-0.00216	0.01417	9.14863	60.05191
6721A15	7.58182	8.90172	0.01767	0.00425	0.28411	0.33075
6721A25	**0.22857**	**0.0026**	**0.02957**	**0.00027**	**0.05342**	**0.00061**
6721A28	**0.21446**	**0.00238**	**0.02983**	**0.00027**	**0.05056**	**0.00057**
6721A26	**0.21772**	**0.00223**	**0.02987**	**0.00027**	**0.05138**	**0.00054**
6721A12	**0.21351**	**0.00216**	**0.03006**	**0.00027**	**0.0495**	**0.00051**
6721A27	0.4622	0.00456	0.03006	0.00027	0.10856	0.0011
6721A5	**0.2244**	**0.00262**	**0.03013**	**0.00027**	**0.04893**	**0.00056**
6721A13	**0.21583**	**0.00237**	**0.03017**	**0.00027**	**0.04929**	**0.00054**
6721A10	**0.22255**	**0.00247**	**0.03063**	**0.00027**	**0.05009**	**0.00055**
6721A9	**0.22113**	**0.00238**	**0.0308**	**0.00027**	**0.04969**	**0.00054**
6721A11	**0.2208**	**0.00221**	**0.03128**	**0.00028**	**0.0492**	**0.0005**
6721A23	**0.22374**	**0.00251**	**0.03142**	**0.00028**	**0.0505**	**0.00057**
6721A7	0.28876	0.00302	0.03154	0.00028	0.06234	0.00065
6721A24	**0.22649**	**0.00232**	**0.03166**	**0.00028**	**0.05049**	**0.00053**
6721A22	**0.22081**	**0.00242**	**0.0317**	**0.00029**	**0.05001**	**0.00055**
6721A6	**0.23471**	**0.00253**	**0.03176**	**0.00028**	**0.05075**	**0.00055**
6721A20	**0.22169**	**0.00274**	**0.032**	**0.00029**	**0.04918**	**0.0006**
6721A1	**0.2314**	**0.00242**	**0.0321**	**0.00028**	**0.04948**	**0.00052**
6721A21	**0.23056**	**0.00253**	**0.03218**	**0.00029**	**0.05079**	**0.00056**
6721A17	**0.22466**	**0.00235**	**0.03253**	**0.00029**	**0.04938**	**0.00052**
6721A2	**0.23132**	**0.00245**	**0.03253**	**0.00029**	**0.0495**	**0.00052**
6721A8	**0.26975**	**0.00277**	**0.03271**	**0.00029**	**0.05735**	**0.00059**
6721A4	**0.23753**	**0.00239**	**0.0329**	**0.00029**	**0.04968**	**0.00051**
6721A3	**0.24862**	**0.00269**	**0.03297**	**0.00029**	**0.05137**	**0.00055**
6721A19	**0.23293**	**0.00253**	**0.0332**	**0.0003**	**0.04944**	**0.00054**
6721A18	**0.23705**	**0.00245**	**0.03325**	**0.0003**	**0.05106**	**0.00054**

672-01 (Apparent Ages)

Analysis_#	Pb207/U235	Pb207/U235 (±Ma)	Pb206/U238	Pb206/U238 (±Ma)	Pb207/Pb206	Pb207/Pb206 (±Ma)
6721A16	614.3	2335.99	-198.8	58.6	0.1	3258.34
6721A14	-NaN	*******	-14	91.52	8000	0
6721A15	2182.7	1053.23	112.9	26.96	3385.7	1157.86
6721A25	**209**	**2.15**	**187.9**	**1.68**	**346.7**	**25.47**
6721A28	**197.3**	**1.99**	**189.5**	**1.69**	**220.8**	**25.65**
6721A26	**200**	**1.86**	**189.7**	**1.68**	**258**	**23.78**
6721A12	**196.5**	**1.81**	**190.9**	**1.66**	**171.5**	**23.7**
6721A27	385.8	3.17	190.9	1.69	1775.4	18.36
6721A5	**205.6**	**2.17**	**191.3**	**1.67**	**144.4**	**26.82**
6721A13	**198.4**	**1.98**	**191.6**	**1.68**	**161.8**	**25.44**
6721A10	**204**	**2.05**	**194.5**	**1.7**	**199.2**	**25.45**
6721A9	**202.9**	**1.98**	**195.5**	**1.7**	**180.4**	**24.95**
6721A11	**202.6**	**1.84**	**198.6**	**1.72**	**157.5**	**23.61**
6721A23	**205**	**2.09**	**199.4**	**1.77**	**218.2**	**25.85**
6721A7	257.6	2.38	200.2	1.74	685.7	22.2
6721A24	**207.3**	**1.92**	**200.9**	**1.78**	**217.7**	**23.98**
6721A22	**202.6**	**2.01**	**201.2**	**1.78**	**195.6**	**25.39**
6721A6	**214.1**	**2.08**	**201.6**	**1.75**	**229.4**	**24.7**
6721A20	**203.3**	**2.28**	**203.1**	**1.81**	**156.6**	**28.38**
6721A1	**211.4**	**2**	**203.7**	**1.76**	**170.6**	**24.3**
6721A21	**210.7**	**2.09**	**204.2**	**1.81**	**231.5**	**25.28**
6721A17	**205.8**	**1.95**	**206.3**	**1.81**	**165.9**	**24.49**
6721A2	**211.3**	**2.02**	**206.4**	**1.78**	**171.5**	**24.57**
6721A8	**242.5**	**2.22**	**207.5**	**1.8**	**504.7**	**22.71**
6721A4	**216.4**	**1.96**	**208.6**	**1.8**	**180.2**	**23.52**
6721A3	**225.5**	**2.19**	**209.1**	**1.81**	**257.4**	**24.57**
6721A19	**212.6**	**2.08**	**210.5**	**1.86**	**169**	**25.29**
6721A18	**216**	**2.01**	**210.8**	**1.85**	**243.7**	**23.97**

672-01 (Sorted Results)

Analysis #	Best Age (Ma)	Best Age (±Ma)	Why Rejected
6721A1	203.7	1.76	
6721A2	206.4	1.78	
6721A3	209.1	1.81	
6721A4	208.6	1.8	
6721A5	191.3	1.67	
6721A6	201.6	1.75	
6721A7			discordance
6721A8	207.5	1.8	
6721A9	195.5	1.7	
6721A10	194.5	1.7	
6721A11	198.6	1.72	
6721A12	190.9	1.66	
6721A13	191.6	1.68	
6721A14			discordance
6721A15			discordance
6721A16			discordance
6721A17	206.3	1.81	
6721A18	210.8	1.85	
6721A19	210.5	1.86	
6721A20	203.1	1.81	
6721A21	204.2	1.81	
6721A22	201.2	1.78	
6721A23	199.4	1.77	
6721A24	200.9	1.78	
6721A25	187.9	1.68	
6721A26	189.7	1.68	
6721A27			discordance
6721A28	189.5	1.69	

Analysis #	Best Age (Ma)	Best Age (±Ma)
6721A25	187.9	1.68
6721A28	189.5	1.69
6721A26	189.7	1.68
6721A12	190.9	1.66
6721A5	191.3	1.67
6721A13	191.6	1.68
6721A10	194.5	1.7
6721A9	195.5	1.7
6721A11	198.6	1.72
6721A23	199.4	1.77
6721A24	200.9	1.78
6721A22	201.2	1.78
6721A6	201.6	1.75
6721A20	203.1	1.81
6721A1	203.7	1.76
6721A21	204.2	1.81
6721A17	206.3	1.81
6721A2	206.4	1.78
6721A8	207.5	1.8
6721A4	208.6	1.8
6721A3	209.1	1.81
6721A19	210.5	1.86
6721A18	210.8	1.85
6721A7		
6721A14		
6721A15		
6721A16		
6721A27		

Analyses in red are considered unreliable:
- grains <1.0 Ga due to >10% error or significant discordance
- grains >1.0 Ga due to >20% discordance or >10% reverse discordance.

All errors are shown at the 1-sigma level, and include only measurement errors.
Systematic errors (mainly from fractionation correction) add ~3% uncertainty (2-sigma) to all ages.
Decay constants: $^{238}U=9.8485\times10^{-10}$, $^{235}U=1.55125\times10^{-10}$, $^{238}U/^{235}U=137.88$.
Isotope ratios are corrected for Pb/U fractionation by comparison with standard zircon with an age of 564 ± 4 Ma (2-sigma).

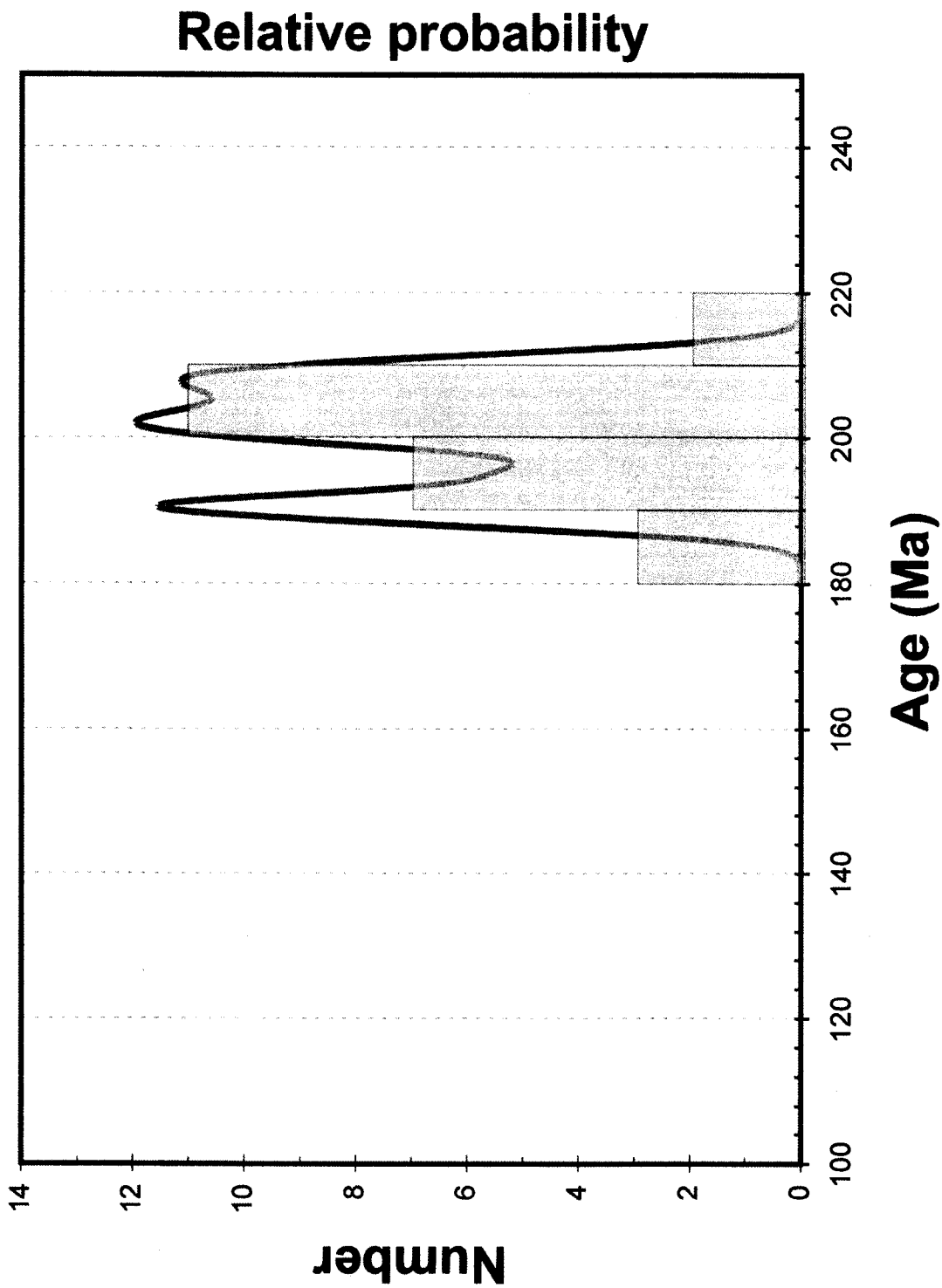

APPENDIX 3

SELECTED SAMPLES

REMARKS

SAMPLE	LEVEL	Y	X	ICP	XRD	ISOTOPES	THIN SEC	REMARKS
14	4740	16445	19310			▲		Sahegen ft.
16	4740	16438	19365			▲		Near sheated fractures
19	4740	16463	19267			▲		HW section of the Sahegen ft.
25	4740	16497	19382			▲		5 ft. from the HW section of the Antelope ft.
26	4740	16502	19387			▲		11 ft. from the HW section of the Antelope ft.
27	4740	16508	19395			▲		20 ft. from the HW section of the Antelope ft.
28	4740	16519	19412			▲		40 ft. from the HW section of the Antelope ft.
29	4710	16445	19049			▲	♦	Thermally affected by the Raven dike
30	4710	16423	19064			▲		Magpie ft. zone with some stibnite
48	4710	16275	19088			▲		
53	4720	16607	19149					Sagehen ft. zone
57	4720	16574	19120					Sahegen ft. zone
58	4720	16568	19113					Sahegen ft.zone
60	4720	16543	19152					Magpie ft. zone
63	4720	16727	19184					
64	4720	16735	19190					
69	4720	16728	19200					
70	4720	16726	19196					Magpie ft.
71	4720	16707	19191					Magpie ft.
73	4610	15822	19046			▲	♦	
74	4610	15810	19055			▲		
86	4650	15970	19136			▲		Popovich Fm.
93	4730	16705	19487			▲		Pheasant ft. Visible gold
94	4730	16711	19496			▲		
95	4730	16716	19504			▲		
96	4730	16736	19521			▲		Barite veinlets with visible gold
97	4730	16751	19529			▲	♦	Visible gold on SDrm1 bedding plane
98	4730	16725	19512			▲		Visible gold 3 ft. from a sulfide veinlet
100	4730	16763	19504			▲		
111	4720	16555	19073					Late sulfide vein+calcite @ 310,90
130	4610	15838	19045			▲		
131	4610	15849	19055	•		▲		
132	4610	15868	19066			▲	♦	
134	4610	15854	19035			▲		

137	4730	16762	19474			▲		
145	4610	15849	19054					
146	4610	15822	19062	•		▲		Canal sampling from the Contact Fault Zone
191	Tracker D.	15702	19026	•				
192	Tracker D.	15718	19040	•				Central Fault Zone
193	Tracker D.	15725	19038	•				
194	Tracker D.	15630	18644	•			♦	SDrm (exoskarn)
195	Tracker D.	15621	18645	•			♦	SDrm (exoskarn)
196	Tracker D.	15613	18641	•			♦	SDrm-Dp along the Contact Fault Zone at low angle
197	Tracker D.	15605	18652	•				Calcite stockworks along the Contact Fault Zone
198	Tracker D.	15598	18657	•				Calcite stockworks along the Contact Fault Zone
199	Tracker D.	15589	18664	•				Calcite stockworks along the Contact Fault Zone
200	Tracker D.	15589	18693	•				Calcite stockworks along the Contact Fault Zone
201	Tracker D.	15599	18683	•				Calcite stockworks along the Contact Fault Zone
202	Tracker D.	15604	18670	•			♦	Breccia zone along the Contact Fault Zone
203	4720	16611	19150	•				Magpie ft.. Mineralized breccia with Sb+barite
204	4720	16625	19158	•				
205	4720	16627	19159	•				
206	4720	16679	19165	•				
207	4720	16714	19193	•				
208	4720	16726	19198	•				
209	4720	16734	19188	•			♦	
210	4720	16764	19235	•		▲		Magpie ft.
211	4720	16766	19233	•		▲		Magpie ft.
212	4720	16771	19228	•		▲		Magpie ft.
213	4720	16773	19226	•		▲		Magpie ft.
215	4580	16266	19136	•				Raven dike.Sample for AFT
216	4580	16265	19133	•				SDrm3
217	4580	16265	19130	•				SDrm3
218	4580	16272	19136	•				Raven dike.
219	4580	16237	19157	•				Breccia along the Raven dike/fault due reactivation
224	4730	16750	19528	•				SDrm1. Strong decalcification
225	4730	16739	19523	•				SDrm1 with visible gold. Strong decalcification
226	4730	16735	19521	•				SDrm1 with visible gold. Strong decalcification
227	4730	16727	19515	•				SDrm1
228	4730	16708	19491	•				SDrm1. Pheasant ft. Strong decalcification
229	4730	16763	19544	•				SDrm1. Strong decalcification
4580As	4600	16440	19126				♦	As-minerals with stibnite along a NE-trendind structure

229	4730	16763	19544 ●				SDm1. Strong decalcification		
4580Ag	4900	16440	19126			◆	As-minerals with albrite along a NE-trending structure		
223	4880	16197	19125 ●				SDm2, 3dc		
222	4880	16174	19129 ●				SDm2, 3dc. Next to sample 163		
221	4880	16166	19130 ●				SDm2, 3dc		
220	4880	16148	19133 ●				SDm2, 3dc		

APPENDIX 4

MULTI-ELEMENT GEOCHEMICAL DATA FROM THE CHUKAR FOOTWALL DEPOSIT

LEVEL	SAMPLE	Ag ppm	Al ppm	As ppm	Au oz/ton	Au oz/ton	Ba ppm	Be ppm	Bi ppm	Ca ppm	Cd ppm	Co ppm	Cr ppm	Cu ppm	Fe ppm	Hg ppm	Li ppm	Mg ppm	Mn ppm	Mo ppm
Tracker	1		900 3732	310 248	0 0041	0 0042	1510 467	0 2761	1 5486	275000	0 4762		19 457	6 6022	7531 005			37900	707 071	4 6471
4610	2	0 752	722 5331	95 5236	0 0084	0 0082	2202 548	0 5721	3 3435	158000	0 3658		38 5324	4 3045	4379 875			82300	3104 149	7 641
4610	3		2241 293	703 4107			96 9507	0 3531	0 7089	37690 29	1 1875	9 0118	34 5179	25 4533	20145 8	0 7698		20562 65	296 9351	9 3816
4610	4	1 4975	960 5552	256 3331	0 0795	0 0808	790 7905	0 2383	1 3812	157000	0 5475		59 7157	9 6533	9386 467			81800	473 6762	7 0332
4610	5	0 553	518 6606	51 3372	0 0051	0 0052	1075 868	0 1581	1 699	46879 2	1 8857	0 6484	193 1208	11 9493	5218 891			20022 86	1166 177	17 1406
4610	6	3 408	1317 905	266 615	0 0075	0 0074	217 8867	0 4748	3 2359	149000	2 279		50 1181	34 1397	12960 16	0 6259		77500	1450 507	82 3064
4610	7	0 069	329 4792	9 1001	0 0031	0 0023	4539 421	0 1003	0 727	87800	0 2487		94 6937	2 3714	1818 715			43600	274 4587	5 8588
4610	8	1 8908	915 4189	242 1131	0 0551	0 0567	679 7648	0 247	1 0083	118000	0 6343	3 7815	46 1882	11 4956	10112 95			42000	442 7414	6 4641
4610	9	0 8006	1116 288	185 0715	0 0056	0 0051	551 433	0 6193	1 5517	186000	0 8691		30 8777	10 0821	7034 442			93300	1227 103	36 84
4730	10	0 6807	2731 672	388 7407	0 4313	0 4274	87 1903	0 3747	0 6228	45393 24	0 73	2 8212	65 2669	14 2136	13776 08	0 6331		23695 91	302 077	7 8324
4730	11	0 0394	107 4815		0 7038	0 667	744 7068	0 3063	1 7528	267000	0 0419		3 7506	0	628 4219			127000	800 9036	
4730	12	0 3096	1319 991	194 0574	0 1622	0 1572	642 1654	0 3467	1 803	112000	0 59		45 6309	18 0385	9667 689			60000	702 5786	5 422
4730	13		1678 388	72 0526	0 0373	0 0372	1165 815	0 4253	0 7256	98800	0 4462		42 2309	2 5467	6865 537			55400	567 9656	6 1847
4730	14	0 0901	2451 844	255 1391	0 158	0 1602	246 6236	0 4769	0 3338	47328 15	0 3568	1 4866	41 19	8 3769	5421 056	0 6914		25695 67	299 8284	4 8699
Tracker	190	13 5136	1053 568	234 2947	0 0235	0 0229	2982 805	1 575		88939 59			112 5453	73 2596	12081 5			45523 16	1102 913	10 8972
Tracker	191		1026 761	83 216	0 0037	0 0036	384 1399	0 5534		191000			32 4676	0	4307 187			61523 41	826 8334	22 3641
Tracker	192		139 3036		0 0018	0 0016	360 56	0 1259		358000		8 0681	10 5948	0	490 442			35572 36	712 7548	
Tracker	193	14 5803	388 5286	65 0726	0 0206	0 0211	6788 943	0 176		107689 5			102 8318	0	4593 402			15278 43	665 4539	1 9263
Tracker	194		2195 288	155 4858	0 0117	0 0116	271 1495	0 5605		65951 05			83 4472	0	7936 916			35499 33	482 428	0 696
Tracker	195		2655 213	260 4215	0 0359	0 0359	2560 783	0 5238		53463 27			72 7214	0	10569 86			29386 88	570 4268	1 7704
Tracker	196		1071 814	191 5467	0 0445	0 0447	6088 848	0 2906		50041 95			130 7285	0	6456 049			26551 95	411 796	17 0248
Tracker	197		356 5847	19 4788	0 0051	0 005	10842 26	0 0643		51867 91		15 9404	128 039	0	2341 233			16183 2	178 7813	1 445
Tracker	198		1347 729	218 6828	0 0064	0 0065	633 1382	0 7695		214000			30 4638	0	5621 423		1 0654	115000	930 7399	14 5217
Tracker	199		1340 228	348 4603	0 0083	0 0082	376 8239	1 0562		198000			21 492	0	4624 646			104000	965 0118	9 3321
Tracker	200		1341 28	261 2646	0 0039	0 0039	1163 204	0 9864		220000			34 1843	0	6757 73		1 955	115000	1201 246	12 5798
Tracker	201	28 6917	2028 203	1039 443	0 0108	0 0107	1478 644	1 2161		158000			47 0731	0	10517 5		0 2576	81300	1413 738	31 8197
Tracker	202		1109 531	190 5743	0 0226	0 0214	5069 717	0 2138		61099 99		13 5151	134 7678	0	6606 864			31385 67	366 2041	3 6994
4720	203		2540 662	1200 235	0 2283	0 2306	133 3834	0 3993		60754 62		44 0649	39 964	0	7816 55			16718 56	309 4313	4 0253
4720	204		3282 533	144 7761	0 0167	0 0158	191 407	0 6507		71638 41			77 3652	0	9748 353			37132 94	507 4721	2 3013
4720	205		3033 281	320 1589	0 0856	0 086	56 5205	0 4197		25903 88		13 1047	55 444	0	12450 23			13611 08	297 9827	4 1184
4720	206		2759 387	833 3792	0 1426	0 1417	283 6863	0 6847		104477 8			31 0488	0	12030 19			51936 68	470 8509	2 065
4720	207	5 13	1965 736	1708 692	0 7955	0 7947	483 824	0 4158		95642 29			46 5984	8 6924	22170 97	3 0649		53131 5	343 0653	9 6756
4720	208		1097 395	1500 794	0 4873	0 4768	2861 538	0 41		54625 51			65 3833	0	9756 682			28041 22	446 9773	2 8935
4720	209		2531 592	1163 711	0 03	0 0287	451 4957	1 4571		112812 3			43 1519	0	11440 84			56842 34	342 7693	7 652
4720	210		2752 435	66 4728	0 0054	0 005	785 7635	0 6837		79538 04			53 1195	0	15401 12			41076 16	291 0251	2 2644
4720	211		790 2886	141 0277	0 0209	0 0218	2018 376	0 2409		118242 1			75 45	0	3901 201			67437 98	561 727	
4720	212		3369 062	5527 624	1 0689	1 0865	379 5013	0 5993		25751 52		2 3817	37 4822	0	35691 86	23 5398		12708 59	207 2539	6 6457
4720	213		7787 162	80 2871	0 0071	0 006	92 5782	1 0258		189000			35 6396	0	12487 36		14 5245	37137 33	285 2743	0 0966
4720	214		2741 312	371 3101	0 0886	0 0892	1726 368	0 5616		84990 42			38 2892	0	13069 73			43583 41	444 6841	0 1009
4580	215		5260 22	315 415	0 0064	0 0042	542 8825	0 7389		55656 88		7 1174	59 4388	0	43574 32			28644 6	364 3239	
4580	216		3675 245	104 5738	0 0047	0 0063	114 2514	0 6968		137000		3 5754	32 0589	0	9738 304			31487 13	312 7611	2 0331
4580	217		3497 099	155 172	0 0033	0 0022	954 0543	0 693		114151 8			29 8069	0	10719 4		0 2276	36455 14	253 7096	1 1611
4580	218		2074 299	22 8244	0 0025	0 0025	1376 293	0 5978		174000			23 8702	0	7862 411			83000	448 2085	1 8582
4580	219		297 8834	29 2402	0 0159	0 0142	857 7642	1 0887		391000			16 3161	0	2641 239		0 0534	2597 556	917 3129	0 1205
4680	220		3119 723	510 3946	0 1222	0 1212	1838 83	0 3962		41342 43			56 5658	0	17870 34	2 8928		21528 56	195 8107	2 0296
4680	221		3001 488	861 6725	0 3592	0 3286	95 7205	0 2749		26065 45			41 0007	0	30609 18	5 5226		14171 78	74 4232	9 1717
4680	222		1981 938	45 851	0 0164	0 0161	403 0189	0 31		187000			21 9998	0	2396 376			103000	263 5685	1 506
4680	223		2806 123	251 0903	0 0854	0 0805	293 9795	0 1847		3726 419		6 5195	83 2047	10 4725	12299 37	4 5583	0 9743	1694 87	22 5227	3 4729
4730	224		2842 023	552 3021	1 8399	1 851	87 335	0 2374		19938 95		31 8695	25 4076	39 6422	16223 68	0 1491	0 9014	9741 356	169 983	1 6328
4730	225		3237 114	276 3022	0 2896	0 2914	201 4194	0 4663		63478 39		18 8906	30 2817	11 0262	10951 68		3 1868	34833 83	464 9435	1 1598
4730	226		1173 703	126 5324			3563 857	0 1713		34010 36			63 6586	2 6928	7365 869		2 7933	18067 6	279 2129	
4730	227		1475 82	210 2672			1166 13	0 2277		56498 7			73 9927	7 8864	20209 35		2 827	17732 98	286 6577	0 398
4730	228		2949 487	357 0858	0 2549	0 2594	191 2868	0 7873		84192 16			25 5041	20 1718	17827 15		3 3573	44568 87	654 9531	3 741
4730	229		3732 813	145 3707	0 0057	0 0041	77 3985	0 5894		159000			32 0151	6 764	9918 773		6 3032	27273 43	371 1224	0 4806
4730	230		1519 234	1326 977	0 5633	0 5678	1669 76	0 2363		37952 93		29 5715	87 1561	18 4781	7145 403	3 1198	3 1107	17777 8	323 0876	2 8083

LEVEL	SAMPLE	Ni	Pb	P	Sb	Se	Sn	Sr	Ti	Tl	V	Zn
		ppm	ppm	ppm	ppm	ppm	ppm	ppm	ppm	ppm	ppm	ppm
4610	1	35.0486	77.0903	96.1702	20.6428	5.2245	7.2206	85.4972	4.8122	8.8106	39.8034	406.6244
4610	2	15.9445	77.7434	87.3017	9.6348	4.5798	4.3171	61.1329	5.4889	4.6263	51.1402	137.1441
4610	3	32.2897	23.618	235.8189	44.8583		5.7021		7.4141	13.9474	12.2106	102.2632
4610	4	12.4558	48.8547		15.3603	2.1378	5.6227	93.742	6.1202	8.5211	23.9511	117.0528
4610	5	13.6669	50.978		18.0626	1.9402	3.9312	16.0766	4.114	4.2565	6.9918	296.1761
4610	6	70.8758	31.2997	232.299	34.1703	5.2125	5.7012	66.2773	13.4004	6.934	121.9296	331.253
4610	7	4.4726			3.6416	2.7716	3.5795	42.6454	0.8616	3.5325	1.1826	104.8357
4610	8	14.0778	42.8091		17.5846	2.2512	5.515	72.7243	5.6328	8.0939	25.9539	119.9763
4610	9	51.528	13.8939	82.0943	9.1222	3.8307	5.1294	64.048	12.9672	4.9913	109.663	216.3945
4730	10	18.8897	45.9828	60.702	22.6606	0.501	4.7413		9.2299	12.7589	17.4455	81.4017
4730	11	0.991	27.9218			4.2218	5.1499	38.716		3.9663	0.0284	144.4162
4730	12	16.0948	52.0827	56.0977	19.2417	2.1754	5.3827	34.12	5.0918	7.1508	34.2636	117.0416
4730	13	16.6578	47.5797	132.8567	6.1091	2.2225	3.9074	48.2878	6.7875	8.5008	46.7161	111.6481
4730	14	16.9362	38.5331	182.1279	14.2907	1.9281	3.7497		9.8482	10.9114	18.7138	77.8769
Tracker	190	154.409	32.0833	115.7776	82.6493	32.3112		77.0638	8.2049		148.1076	288.2055
Tracker	191	32.0606	48.4026		7.784	12.615		75.1713	9.0807	115.7403	12.6774	446.3277
Tracker	192	1.0368	90.9131		0	14.0965		236.1611		95.1532		690.2298
Tracker	193	8.6307	77.1793		24.6427	11.674		133.5152	2.9872	49.0445		246.3252
Tracker	194	11.405	29.6692		7.5033	12.5009		36.709	12.6135	40.3721	16.4322	211.015
Tracker	195	15.8146	50.4524		16.2384	15.5853		52.9988	11.1133	78.1195	11.7364	182.2769
Tracker	196	32.0098	41.3508		73.0608	13.3358		121.3961	6.9279	72.9659	5.9909	122.7339
Tracker	197	7.2081			0.1351	8.6554		178.5929	2.3061	92.7564		108.403
Tracker	198	29.1725	84.7209		32.4554	18.1292		105.7735	9.2166	58.031	25.9011	446.6763
Tracker	199	24.5654	96.8322	9.005	4.2163	14.9445		52.1402	8.7258	71.4175	34.2683	453.5391
Tracker	200	29.7376	112.9146		7.1216	20.1303		162.3828	11.8344	93.913	36.0307	476.684
Tracker	201	53.6997	53.5011		17.3623	19.3255		99.709	14.3166	64.5119	60.1855	419.3181
Tracker	202	17.3052			11.2919	11.7599		116.143	7.2567	109.852	1.5759	265.9343
4720	203	16.2577	78.6201		34.2812	12.258		29.3913	7.8049	92.0365	3.4716	190.0982
4720	204	19.3435	65.3028		16.455	14.267		38.0367	15.6351	118.9611	16.5272	257.3957
4720	205	19.107	26.5716		42.2347	15.1819		15.3169	10.7575	120.4753	6.2846	135.4333
4720	206	20.3414	49.3562		26.969	16.981		37.1017	8.5057	49.2552	8.0845	262.531
4720	207	30.8275	74.4633		158.3436	32.8036		21.8785	7.4975	161.6112	6.0375	313.897
4720	208	15.0337	63.0183		86.2961	14.658		39.837	4.3962	111.5728	4.9622	153.5165
4720	209	23.2408	26.777		11.8488	16.931		28.1827	11.3241	8.4742	102.0926	309.0517
4720	210	26.0764	46.9335		23.3841	20.9927		65.6057	17.2803	58.5496	12.3653	255.4166
4720	211	5.7185	41.8521		12.4616	14.3805		61.6568	3.2042	109.76		258.1438
4720	212	25.3049	59.2402		431.3713	38.4777		10.7368	8.8692	386.3706	14.0262	177.4454
4720	213	18.0654	64.2264	41.0739	16.0477	18.9961		190.957	88.8272	152.2671	21.4877	519.0198
4720	214	15.2154	23.4841		23.0812	20.5961		52.6813	13.7716	102.7155	2.1615	254.0846
4580	215	165.994	60.8858	445.8954	59.5476	43.4469		55.2317	21.0326		1.1955	250.3976
4580	216	15.4943	123.8674		12.5331	15.9189		156.538	16.7592	65.5043	8.4175	380.229
4580	217	13.8871	88.2949		10.5137	13.6842		122.7574	14.7561	34.5283	0.2693	315.2054
4580	218	11.8866	46.1041		9.2827	17.3237		72.5521	15.2221	23.0582	12.3622	588.6532
4580	219	4.6051	44.7618		5.4723	10.2447		78.411	0.6205	86.5723	4.1845	764.7346
4680	220	21.4934	67.3715		396.8555	18.8157		23.7482	7.6918	50.7263	0.0363	170.7023
4680	221	43.2531	72.9362		125.2097	31.9722		9.7913	5.522	148.6763		242.0446
4680	222	9.832	78.0271		5.0588	11.3896		20.2646	4.3614	77.1655		423.0484
4680	223	24.0696			27.7647	8.3449		6.2737	9.9079		2.9018	61.7346
4730	224	26.2104	47.1124	100.1926	68.6233	13.1745		11.7084	5.431			130.1551
4730	225	20.313		130.5365	26.473	10.7263		42.671	7.0208			223.9262
4730	226	7.3618	5.8638		10.4497	9.0827		31.3991	11.6528			151.9218
4730	227	13.8558	83.3059	158.3048	47.4832	18.718		61.9341	7.0552			175.3465
4730	228	33.4368	68.1308	384.4308	42.6999	23.353		64.6349	9.352		23.3585	263.4606
4730	229	16.051	116.5974		11.0396	13.1713		180.2209	11.6588			406.5428
4730	230	19.0146	48.1788		22600	12.8054		58.1738	2.4123			118.5815

APPENDIX 5

SELECTED THIN-SECTIONS

SHOWING TEXTURES, MINERALOGY,

AND CROSS-CUTTING RELATIONSHIPS

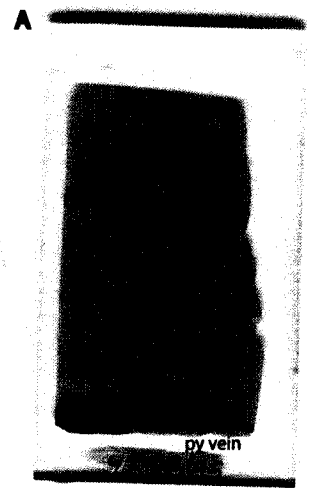

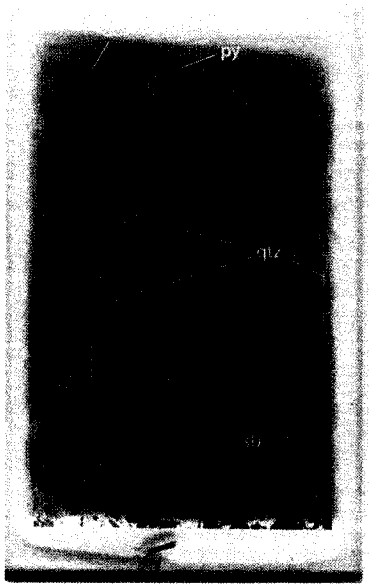

orp: orpiment
real: realgar
py: pirite
ba: barite
dol: dolomite
qtz: quartz
sb: stibnite
SDrmh: diopside hornfels

A. 4600 LEVEL. SDrm2 with stratiform orpiment cut and replaced by a realgar veinlet.
B. Hole CFU 143 (447'). SDrm2h crosscut by a barite-II vein. Microthermometric data were obtained from this vein, which mean salinities and Th values range from 1.2 to 3.4 wt percent NaCl equiv and between 118° to 197.7° C, respectively.

C. 4590 LEVEL. Mineralized fault breccia from the Magpie fault. Stibnite deposited in open spaces, producing cockcade textures. SDrm2 clasts are strongly decalcified.

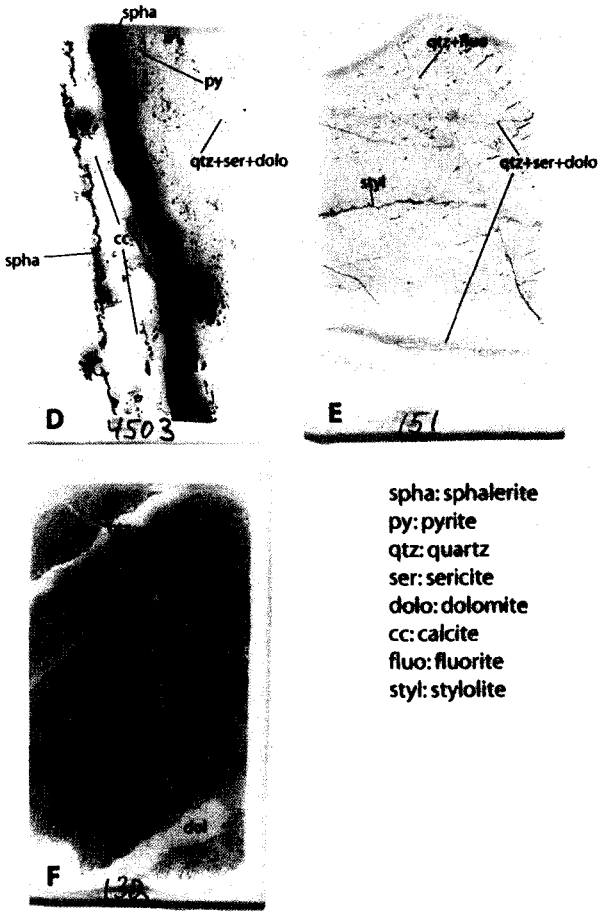

spha: sphalerite
py: pyrite
qtz: quartz
ser: sericite
dolo: dolomite
cc: calcite
fluo: fluorite
styl: stylolite

D. 4500 LEVEL. Base metal veinlets (sphalerite+galena+tennantite) crosscutting diopside hornfels hydrothermally altered to qtz+ser+dolo. Pyrite-II grains occur near the veinlets.

E. Main Decline near Tracker Exploration Drift. Two generations of veinlets are present in the diopside hornfels (SDrm1), from older to younger: (1) qtz+ser+dolo, (2) qtz+fluo. Noted that the stylolite has been cut by the latter veinlet.

F. 4610 LEVEL. Strongly decalcified and silicified SDrm1 (0.102 opt Au) with multiples generations of quartz and dolomite veinlets.

qtz: quartz
dolo: dolomite
ba: barite
sb: stibnite
bx: breccia

G. 4720 LEVEL. Similar to sample 5 (4590 level), stibnite is found in vugs in the fault breccia from the Magpie fault. Barite-I is common in this mineralized breccia, and it was deposited before stibnite.

H. 4680 LEVEL. Brecciated qtz+dolo+ba vein near a NE-striking fault in strongly decalcified SDrm2.

I. 4650 LEVEL. Planar, silty SDrm1 showing normal offset microfaulting on qtz+dolo veinlets.

L

M

L. TRACKER DECLINE. Diopside hornfels (Dp3h) hidrothermally altered. Multistage nonferroan calcite veins are associated with quartz+kaolinite alteration. Sulfide content is low.

M. 4730 LEVEL. Pseudo-rhombic crystal of arsenopyrite (Aspy-II) associated with late-ore stage barite+visible gold+marcasite+pyrite. FOV: ~3 mm.

APPENDIX 6

LOCATION MAP
OF THE QRC DRILL HOLES
IN THE CHUKAR FOOTWALL OREBODY